POLITECNICO DI MILANO

DEPARTMENT OF CHIMICA, MATERIALI E INGEGNERIA CHIMICA "G. NATTA"

DOCTORAL PROGRAMME IN MATERIALS ENGINEERING CYCLE XXXIII

IMAGE-BASED ALGORITHMS FOR STRUCTURE INVESTIGATION AND MECHANICAL MODELLING OF EXPANDED POLYMERIC MATERIALS

Doctoral dissertation of:

STEFANO TAGLIABUE

Supervisor:

LUCA ANDENA

Tutor:

CLAUDIA MARANO

Ai miei genitori,
Laura e Vittorio,
per tanta pazienza
e indiscriminato supporto.

Abstract

Expanded polymeric materials are of great importance in many engineering applications. Despite this, as of today the development of models able to describe their macroscopic mechanical behaviour considering their actual microstructure is still an open challenge.

In the following study different image-based algorithms were developed, validated and optimized for microstructure characterization and subsequent three-dimensional numerical mechanical simulations, both linear and non-linear. Microstructure was investigated through different algorithms, scalar and tensorial, to identify key parameters able to describe the internal structure. Finite element simulations were performed considering the real microstructure obtained from high-resolution X-Ray computed tomography images through the application of two different image-based approaches: a classical algorithm based on Representative Volume Elements, aimed at modelling the linear elastic behaviour of the material; a second novel approach aimed at providing an efficient and powerful numerical tool to perform non-linear simulations.

The application of algorithms for structure analysis and the image-based approaches for mechanical finite element simulations led to the identification of general relationships between expanded material microstructure and relevant macroscopic physical and mechanical properties, resulting in the formulation of a closed system of analytical equations. This framework can serve as a tool to optimize foam morphology and product final properties for widely different engineering applications, simplifying and speeding up all the prototyping phase, which usually turns out to be, from an industrial point of view, the most expensive one in terms of time and cost.

Finally, the efficiency of the numerical tool designed for non-linear mechanical simulations was analysed, opening new paths to simulations and to the extension of analytical relationships between macroscopic

mechanical parameters and microstructure quantities in the non-linear mechanical regime.

Sommario

I materiali polimerici espansi sono di grande importanza in molte applicazioni ingegneristiche. Nonostante questo, ad oggi, lo sviluppo di modelli in grado di descrivere il loro comportamento meccanico macroscopico, considerando la loro microstruttura reale, è ancora una sfida aperta.

Nel seguente studio sono stati sviluppati, validati e ottimizzati diversi algoritmi basati su immagini per la caratterizzazione della microstruttura e le successive simulazioni meccaniche numeriche tridimensionali, sia lineari che non lineari. La microstruttura è stata studiata attraverso diversi algoritmi, scalari e tensoriali, per identificare i parametri chiave in grado di descrivere la struttura interna. Le simulazioni agli elementi finiti sono state eseguite considerando la microstruttura reale ottenuta da immagini di tomografia computerizzata a raggi X ad alta risoluzione attraverso l'applicazione di due diversi approcci basati sulle immagini: un algoritmo classico basato sul Volume Rappresentativo, volto a modellare il comportamento elastico lineare del materiale ed un secondo nuovo approccio volto a fornire uno strumento numerico efficiente e potente per eseguire simulazioni non lineari.

L'applicazione di algoritmi per l'analisi della struttura e gli approcci basati sulle immagini per le simulazioni meccaniche agli elementi finiti hanno portato all'identificazione di relazioni generali tra la microstruttura del materiale espanso e le relative proprietà fisiche e meccaniche macroscopiche, portando alla formulazione di un sistema chiuso di equazioni analitiche. Questa struttura può servire come strumento per ottimizzare la morfologia della schiuma e le proprietà finali del prodotto per applicazioni ingegneristiche molto diverse, semplificando e velocizzando tutta la fase di prototipazione, che di solito risulta essere, da un punto di vista industriale, la più onerosa in termini di tempo e costi.

Infine, è stata analizzata l'efficienza dello strumento numerico pro-

gettato per le simulazioni meccaniche non lineari, aprendo nuove strade alle simulazioni e all'estensione delle relazioni analitiche tra i parametri meccanici macroscopici e le quantità della microstruttura nel regime meccanico non lineare.

Contents

List of Figures

List of Tables

Chapter 1

Structure and aim of the thesis

The work outlined in the following chapters of the present thesis is mainly focused on the development, optimization and application of different image-based algorithms whose main objectives are:

- to analyse the polymeric expanded materials internal microstructure and quantify different morpho-structural parameters able to describe the structure in a synthetic form;
- to describe the peculiar macroscopic mechanical behaviour of this particular category of materials through the application of finite element analysis, incorporating the real microstructure of the materials;
- to combine the information coming from both experimental mechanical tests and numerical simulations to understand the synergistic effects between microstructure and constituent material mechanical behaviour, in both linear and non-linear regimes;
- to formulate simple analytical equations that relate macroscopic mechanical parameters to microscopic morpho-structural characteristics and constituent material mechanical parameters; to

provide a rapid tool able to predict the mechanical behaviour of expanded polymeric materials, avoiding large and expensive experimental campaign.

The thesis is structured as follows:

- *Chapter 2* : the state of the art on expanded polymeric materials is presented; the main topics covered are: production technologies, experimental characterization techniques employed by different authors in the past decades and the main approaches adopted in the literature to model the mechanical behaviour of expanded polymeric materials in relation to their internal microstructure.

- *Chapter 3* : the experimental methods adopted to characterize the investigated materials are presented. Experimental methods aim at the characterization of constituent material properties, internal microstructure of inspected material with the use of X-Ray computed tomography and macroscopic mechanical behaviour.

- *Chapter 4* : the main image-based numerical methods implemented to analyse the set of images obtained through X-Ray computed tomography are presented and their efficiency and accuracy evaluated. The main results on structure analysis and quantification of the related parameters are also presented.

- *Chapter 5* : the first image-based approach aiming at performing linear elastic finite element simulations is presented together with the image pre-processing algorithms and results post-processing homogenization scheme. Preliminary relationships between macroscopic elastic constants and morpho-structural parameters are presented.

- *Chapter 6* : exploiting the optimized procedure outlined in the previous chapter, a methodology to study the influence of voids morphology on the macroscopic mechanical response is proposed;

an ad-hoc algorithm is also developed to artificially stretch the set of images along an arbitrary orthogonal direction to intensify the effects of morphology variation on macroscopic mechanical properties.

- *Chapter 7* : all the results of finite element simulations are combined and correlated to morpho-structural parameters, obtained from images analysis, to formulate a closed system of analytical equations useful to estimate the elastic constants necessary to describe the macroscopic mechanical behaviour according to the most suitable linear elastic constitutive law. The association between structural parameters and the most accurate linear elastic constitutive behaviour is also proposed, exploiting the definition of a newly proposed index of mechanical anisotropy combined with structure tensorial information coming from image analysis. Preliminary application of the formulated equations is also shown, applied to a completely different commercially available material with respect to the one used for model formulation.

- *Chapter 8* : the second image-based approach is shown; this method is developed with the main aim of providing a numerical tool optimized to perform non-linear mechanical simulations considering the real microstructure of the inspected samples. The model is validated through linear elastic finite element analysis, performed in the small strain deformation range, providing evidence of its efficiency and its ability to generate fictitious structures not experimentally available. In the end preliminary application to non-linear finite element simulations is shown.

- *Chapter 9* : the main results achieved during this PhD thesis are summarized and ideas for future developments of the work are proposed.

Chapter 2

Expanded polymeric materials

In the following chapter, an overview of the world of expanded polymeric materials will be given. The main fields of application will be briefly described. Production processes and technologies together with experimental characterization protocols will be summarized and at last the main modelling approaches adopted in the last decades will be considered and critically reviewed.

2.1 Introduction

Expanded materials or equivalently called cellular solids acquired in the last decades more and more importance in many fields of engineering applications due to their peculiar physical and chemical properties. These properties arise from a synergic combination of intrinsic properties specific of the constituent materials and the geometry of the internal structure [24]. The internal structure is a combination of struts, walls and voids that is the result of different production processes and technologies, which may vary for different bulk materials [31]. Thanks to the development of processing technologies [75], nowadays expanded materials can be realised with almost all the materials classes available: metals, ceramics, glasses and polymers.

Polymers are for sure the most used materials employed to realize expanded systems due to their relatively easy processing conditions, in terms of temperature and pressure, but also for their relatively high permeability to gases when they are processed in the molten state. More details about expanded polymeric materials will be given in the next section.

The resulting expanded polymeric materials are commonly classified in two categories according to their internal structure [44]:

- *Open-cell system*: when the system is constituted by an internal structure where all the voids are interconnected, and the material is organized in beam-like structures;

- *Closed-cell system*: in this case the voids are not interconnected, and the material is organized in a complex combination of beam-like and membrane-like structures. In this case, the macroscopic properties of the system are given by a combination of intrinsic properties that arise from the constituent material, the internal structure and a small contribution coming from the gas trapped inside the voids.

Another general accepted classification of these systems is based on the apparent density that these systems exhibit at the end of the process:

- *High-foaming system*: when the foam apparent density is < 100 $\mathrm{kg\,m^{-3}}$; some examples of the materials belonging to this class are: high-foamed polyethylene (PE) [70], polypropylene (PP) [11], polystyrene (PS) [51] and polyurethane (PU) [8];

- *Medium-foaming system*: in this case the foam apparent density is between 100 $\mathrm{kg\,m^{-3}}$ and 400 $\mathrm{kg\,m^{-3}}$; polyimide (PI) is one example of the used polymers for this system case;

- *Low-foaming system*: the foam belongs to this category when its apparent density is > 400 $\mathrm{kg\,m^{-3}}$; polystyrene (PS) [51] and polypropylene (PP) [11] are two examples of polymers usually foamed at this level of apparent density.

Besides the abovementioned classifications, the result of the foaming process is in general a lightweight system, if compared to the constitutive bulk polymer, that exhibits peculiar properties, mainly physical properties, which allow the use of expanded polymeric materials in many engineering application fields. The most common ones are:

- *Acoustical insulation*: the complex microstructure resulting from the expansion phase can be exploited to properly tune the damping properties of the constituent material and moreover, exploiting also the gas trapped inside closed cells, it is possible to enhance the damping properties, resulting in a system suitable to cushion the acoustic waves [77] [9] [68].

- *Thermal insulation*: exploiting the intrinsic very low thermal conductivity of polymers and the low thermal conductivity of the gas trapped inside the cells of the structure, it is possible to obtain, as a result, one class of material exhibiting the lowest

thermal conductivity among all the available classes of materials [77].

- *Structural applications*: polymeric foams are widely employed as a core material for sandwich panels used in structural applications [30]. The main interest in the applications of such systems is strictly linked to their lightweight and the mechanical properties at small deformation which can be suitable provided with a proper choice of the constituent polymer, such as semi-crystalline or rigid amorphous polymers, and the optimization of the internal structure obtained with the expansion process.

- *Buoyancy applications*: also, in this field the main characteristic exploited is the lightweight of the expanded polymeric systems with respect to bulk material and once again the performance of the buoyance system is enhanced by the gas trapped in the closed cells.

- *Shock absorption applications*: polymeric foams possess a peculiar mechanical compression behaviour, characterized by a prominent plateau, in which the stress remains almost constant over a wide range of strain [71]. This characteristic allows them to absorb a great amount of energy while limiting transferred stress levels to low values [68]: this behaviour makes polymeric foams particularly suited for packaging applications and protective devices [69].

- *Tissue engineering applications*: in recent years expanded polymeric systems have proven great efficiency in tissue engineering; the peculiar morphologies of the obtained structures and the tuneable mechanical properties [38] are exploited to build a skeleton for cellular adhesion and proliferation with the aim of constructing a favourable environment for tissue regeneration [49]. The systems mainly used in this field of application are biodegradable and non-cytotoxic systems, commonly polylactic acid (PLA),

polyglycolic acid (PGA), polycaprolactone (PCL) and others [22].

Other minor fields of application can be summarized as follows [36]:

- *Filtering systems*: these kind of systems are realized for both liquids and gases. In the case of gas filtering the selective permeability of a given polymer to different gases in closed-cell systems is exploited, while for liquid filtering systems the tortuosity and the surface tension of open-cell systems are exploited to clear liquids from different impurities.

- *Electrical insulations*: in this application, as already pointed out in the thermal insulation case, the intrinsic electrical insulator property of the polymer is exploited and enhanced by the very low electrical conductivity of the gas trapped inside the closed-cells.

- *Other applications*:

  - *Flame-retardant systems*;
  - *Water-repellent membranes*;

Among the large number of expanded polymeric systems available, the most commonly used materials can be summarized as follows, together with their main field of application:

- *Expanded polystyrene (ePS)*: surely is the most commonly used expanded polymeric system, due to its relatively easy processability and the very low cost of production. It is widely used in the realization of insulator systems, both acoustic and thermal, as a core panel in composite systems for structural application, but, above all, due to its great capability of absorbing energy [50] [51] [52], it is widely used in packaging applications and in sport equipment, such as helmets [1]. Minor applications can be found in buoyancy field.

- *Polyurethane (PU)*: these systems, both rigid and flexible, are commonly used in acoustic and thermal insulation, packaging and sports equipment [8]. In recent years PU systems were produced also in the form of auxetic structures enhancing more and more the energy absorption capability of the expanded systems [56] [79] [13].

- *Expanded polypropylene (ePP)*: since polypropylene is a semi-crystalline polymer and hence provide suitable mechanical properties, its expanded form is widely exploited in structural applications and in energy absorbing ones [1] [30] [58].

- *Polyethylene terephthalate (PET)*: also in this case the semi-crystalline nature and related mechanical properties are exploited, in the expanded system, for structural applications [46].

- *Polyvinylchloride (PVC)*: this material, due to its relatively easy foamability and hence a relatively easy tuneable internal microstructure, is widely applied in acoustic insulation field [77].

All the above-mentioned applications are made possible thanks to the development of different production technologies that will be shortly summarized in the next section. A few innovative technologies will be presented together with the classic and well-established production techniques developed in the past decades. These new techniques allow the development of new expanded polymeric systems, such as auxetic ones [79], systems presenting gradient morphologies and the so-called custom-made systems which can potentially further enlarge the range of applications in which expanded polymeric materials have great success.

2.2 Production technologies

Among the different available production technologies that may differ in some practical aspects, including the mechanical process selected or the blowing agent adopted, the classical foaming process can be easily divided into three main steps [36]:

1. *Nucleation phase (cell formation)*: in this step a blowing agent or a gas is added to the polymer in its molten state under a certain condition of pressure and temperature. The blowing agent diffuses into the molten polymer, in the case of gas addition, or a large amount of gas is produced because of a chemical reaction leading to a polymer/gas solution system. Once the system is saturated, the gas begins to flow away from the solution starting the nucleation of the voids [86].

2. *Cell growth*: thanks to the local pressure gradient between cell nuclei and the surrounded molten polymer, the cells can expand. The pressure of the gas inside the nucleus is inversely proportional to the cell diameter. The cells grow independently one from another until the pressure of neighbouring nuclei interfere. If two or more cells of equivalent size enter in contact, pressure equilibrium stabilizes the voids, instead, if smaller cells are overwhelmed by larger ones, the cells merge generating a larger void. This phenomenon leads to the generation of a large number of cells of different sizes and morphologies [15].

3. *Cell stabilization*: because of cell nucleation and consequent growth, the surface area and volume of the system continuously increase stretching the cell walls. The process is stopped before an unstable level of pressure is reached; at that time the system is frozen and the gas-polymer system is reversed toward a stable condition. Lowering the temperature, the gas does not expand anymore and the polymer returns into a solid state. Stabilization

in the molten state is usually enhanced with the addition of surfactants to the molten polymer [74].

Figure 2.1 represents a general scheme of the polymer foaming process.

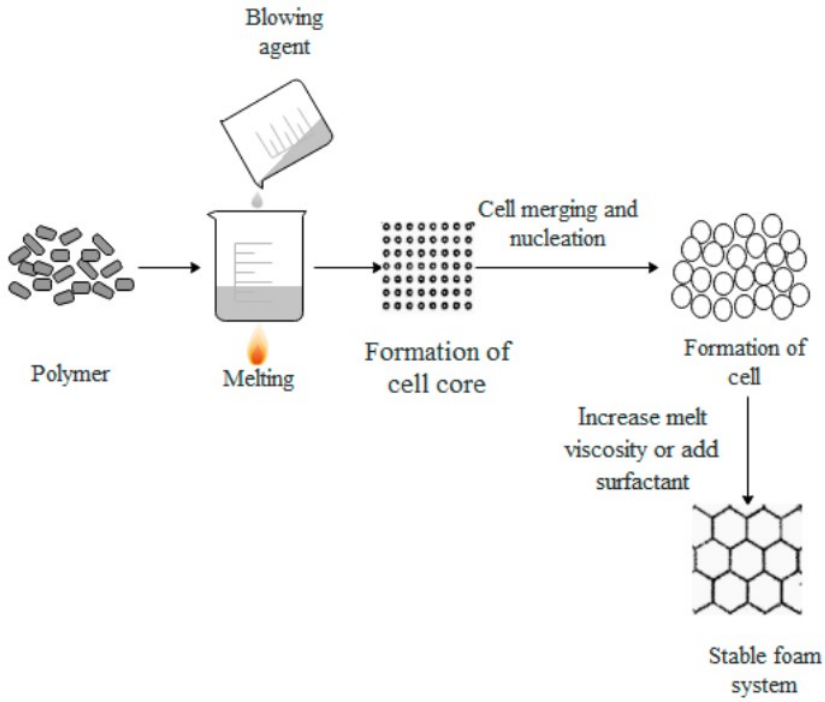

Figure 2.1: Generalized scheme representing the main physical steps involved in the foaming process; figure freely adapted from [36].

Apart from the main physical steps that occur during polymeric foam production processes, the production technologies can be classified according to the way the blowing agent is added to the system and the nature of the agent itself. The main categories reported in the literature can be summarized as follows:

- *Mechanical foaming*: the blowing agent is incorporated by mechanical means (e.g. by stirring) into the liquid or molten state polymer. This foaming technique exhibits the main advantage of excluding any chemical reaction inside the polymer, thus avoiding

the use of potentially toxic agents and excluding the presence of unreacted polymer in the final product. One of the main disadvantages is that large equipment may be required to incorporate the gas into the system, depending on the final product size.

- *Physical foaming*: all the systems that require the mixing of a low boiling point liquid and a polymer belong to this category; this process requires the mixing of the aforementioned components and the foaming process is then induced with pressurization and heating of the system. Figure 2.2 shows a simplified production scheme of the physical foaming process. Similar advantages with respect to mechanical foaming can be highlighted, first of all the use of non-toxic blowing agents (e.g. carbon dioxide and nitrogen) and the absence of chemical reactions ensuring the absence of residual blowing agent in the final product and a very low interaction between the polymeric system and the blowing agent itself; in most cases the blowing agent does not significantly modify the polymer chemistry and the final physical properties of the system. The main disadvantage is once again the need of a large equipment for the production at an industrial level [13].

- *Chemical foaming*: two main processes employed to produce foams belong to this category; the first one implies the use of a blowing agent that is once again added to the molten or liquid state polymer and through its chemical decomposition the gas is released; once the gas is released through the application of pressure and temperature the foaming process is carried on. The second system exploits a chemical reaction between two polymers with the consequent release of gas that acts as the blowing agent. The main advantages of these systems are that the reactions occur into specific ranges of temperature and pressure, with a finer control over processing conditions, and that no particular equipment is required to complete the foaming process. The main

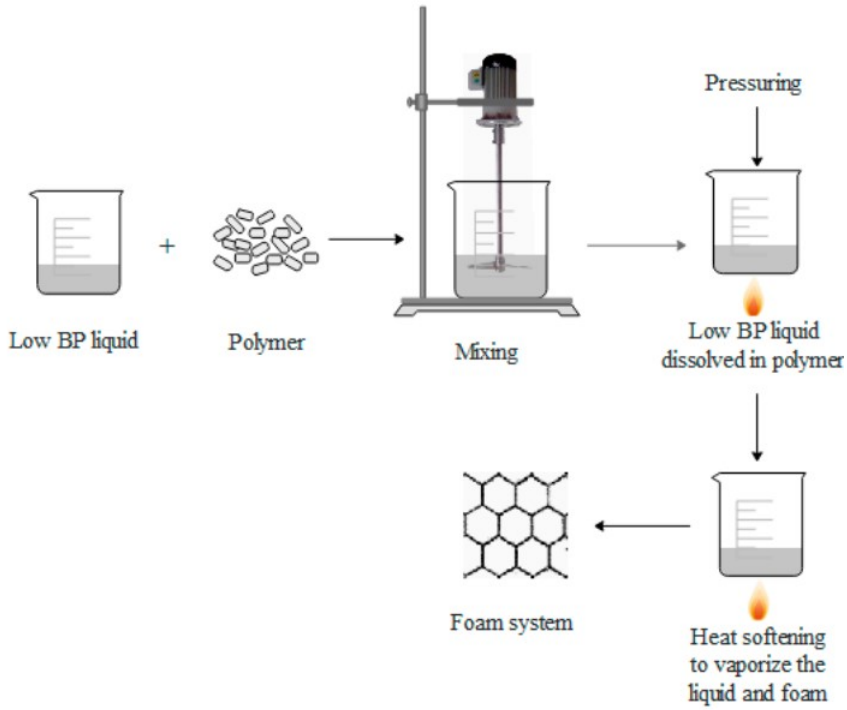

Figure 2.2: Schematic representation of physical foaming process; figure freely adapted from [36].

disadvantage is the use of chemical reactions that could occur in a non-homogeneous way across the mould, giving as a result a final product with some unreacted polymer or unfoamed product. This can compromise the final desired properties of the foam.

From an industrial point of view the previously described foaming methods can be applied in conjunction to well-established forming processes; the typically employed ones are:

- *Extrusion moulding*: generally, a polymer or polymer blend is introduced in the hopper of the extruder and processed with adequate conditions in terms of temperature, pressure, screw speed and so on [89]. At a certain position along the barrel a supercritical fluid, usually carbon dioxide or nitrogen, is introduced and dissolved into the polymer melt, decreasing its viscosity. The

control of temperature and external pressure after the superfluid is dissolved into the polymer melt, makes it possible to obtain the desired foam [39].

- *Injection moulding*: a similar process is adopted in this case; a polymer or polymer blend is processed with specific parameters of injection temperature, injection pressure, mould temperature and so on. A supercritical fluid is added and quickly dissolved into the molten polymer to obtain a gas/polymer solution. The solution is then injected into the mould experiencing a rapid pressure drop that causes a homogeneous or heterogeneous cell nucleation and consequent cell growth [7]. The final expanded system is thus strongly influenced by the properties of the molten polymer and the supercritical fluid (including its diffusivity within the molten polymer), the actual processing conditions and mould design [91].

Using these well-established processing technologies, different polymeric systems with a sufficiently homogeneous internal structure can be foamed at an industrial level with an adequate control of the process parameters. The main expanded polymeric systems can be classified as follows:

- *Thermosetting resins*: these materials are usually foamed through a chemical process, since they are available in a liquid state as two separate components that react together [6]. The main systems used are epoxy or phenolic resins [47], polyester and polyurethane (PU) [21].

- *Thermoplastic polymers*: usually foamed with a physical process, since at a sufficiently high temperature they behave like a viscous fluid [93]. The most used polymers are polyethylene (PE), polypropylene (PP) [90], polystyrene (PS) [85], polyvinylchloride (PVC) and poly(methyl methacrylate) (PMMA) [62].

- *Rubbers*: these polymers are foamed with physical or mechanical foaming process [5]. An example of foamed rubber are silicone rubber, natural rubber (NR) [32], ethylene-propylene diene monomer rubber (EPDM) [53] and styrene-butadiene rubber (SBR) [34].

Besides well-established technologies that allow to obtain expanded polymeric materials characterized by a homogeneous internal microstructure, in recent years new technologies were proposed at the research level to obtain heterogeneous foams, in terms both of cell structure and constituent materials [95].

Many researchers proposed the use of 3D printing technologies to produce cellular structures with optimized and regular geometries. This procedure found a large application in custom-made products in many fields of applications, from biomedical to aerospace engineering, but also in rapid prototyping, when the optimized structure under design needs to be validated experimentally [40].

Other authors recently proposed an enhanced physical foaming method based on the precise control of the supercritical fluid concentration profile inside the molten polymer; a specific boundary pressure profile, variable in time, is applied to obtain a controlled heterogeneous morphology within a single expanded product. This allows to properly tune the macroscopic properties of the foam by adjusting the distribution of properties at a local level in accordance with the morphology of a specific region [88].

Another relatively recent technology, mainly regarding PU systems, allows the production of auxetic structures [79]. Auxetic structures have the peculiar characteristic to increase their size in all directions when stretched along a single one, as opposed to conventional materials which exhibit a lateral contraction [18] [56]. This kind of structures and their peculiar characteristics greatly enrich the possible applications of expanded polymeric materials, in particular for applications in which energy absorption is essential (i.e. protective devices or packaging) [76].

Last but not least, many authors tried to introduce controlled

heterogeneities in the produced expanded polymeric materials acting not only on the structure but also on the constituent material, introducing a certain degree of anisotropy with the addition of micro-fillers [28] [61] [95].

Given the variety of available technologies and polymeric systems, each characterised by its own peculiar physical properties, the experimental characterisation of these systems acts as a fundamental step between their production and real-life use. In the past decades, strong efforts have been made by many authors to fill the gap between production and applications. The main experimental methods developed all share the common aim of relating the measured macroscopic physical properties to the internal structure of the foam [67]. In the next section the main approaches and related empirical models will be discussed with a particular focus on the mechanical properties exhibited by expanded polymeric materials, which is one of the main aspects considered in the present thesis.

2.3 Experimental mechanical characterization

Polymeric expanded materials, as reported in previous paragraphs, exhibit many peculiar physical properties, whether they be mechanical, thermal, electrical or others; it is widely reported in the literature that the exhibited macroscopic properties are always the result of a synergic combination between the geometrical structure, strictly linked to the production technology adopted, and the properties related to the constituent material chosen for the manufacturing of the expanded material [24]. Many authors developed different experimental methods in the past decades to demonstrate this synergistic contribution to the overall macroscopic behaviour.

In the present work the attention will be focused on the macroscopic mechanical behaviour of expanded polymeric materials. Figure 2.3 qualitatively shows the characteristic uniaxial compressive behaviour of this class of material [24]. This curve is commonly divided into three main regions [26] [25] [1]:

I *Elastic region*: also called low-strain region; in this range the material exhibits a linear or quasi-linear mechanical behaviour up to a certain stress level where the structure begins to collapse. The extent of this region is strictly related to the constituent material, but is commonly exhibited in the range within 0 % and 5 % of compressive strain for the majority of polymeric expanded materials. This range is exploited in practical applications mainly for thermal insulation, acoustic damping and structural applications, where the foam typically acts as a core in composite sandwich panels. From a mechanical point of view, the tuneable apparent stiffness of the structure and the almost completely elastic and thus, recoverable strains and stresses, are exploited [26].

II *Collapse region*: also called plateau region, in this region expanded

polymeric materials display their maximum energy absorption capability, since the strain increases at an almost constant stress value. This next-to-ideal macroscopic response is strictly related to an internal progressive collapse of the voids [25]. The microscopic bending of the foam structures, including cell walls in case of closed-cell systems, are mainly responsible of this peculiar deformation behaviour [45]. A proper use of this region allows to design expanded materials for energy absorption applications, such as sports equipment and packaging [1].

III *Densification region*: the third region begins when all the internal structures are collapsed and cell walls enter in contact with each other. This region is characterized by a steep increase in the stress level with small increases in strain. Since the effect of the internal structure is negligible in this region, many authors assume, as a first approximation, the compressive behaviour approaching that of the bulk constituent material. This region is not fully exploited in practical applications since the original internal structure becomes not relevant to the macroscopic response and the energy absorption properties become that of the constituent material [55]. Research interests lie in the determination of the onset of this region, with the aim of maximizing the previous high-absorption region [12].

The macroscopic compressive behaviour displayed by polymeric foams has been widely reported by many authors also in other simple stress states, above all simple shear tests [59] [63]. Also, in this configuration, the microscopic deformation mechanisms contribute to a similar macroscopic mechanical response characterized by the above described regions [51] [52]. One simple stress state in which the overall mechanical response exhibits a different trend is uniaxial tension; in this case the stress versus strain curve is characterized by an elastic region, similar to the one depicted in figure 2.3, followed by a progressive damage and failure of the material [29]. The plateau region is completely absent,

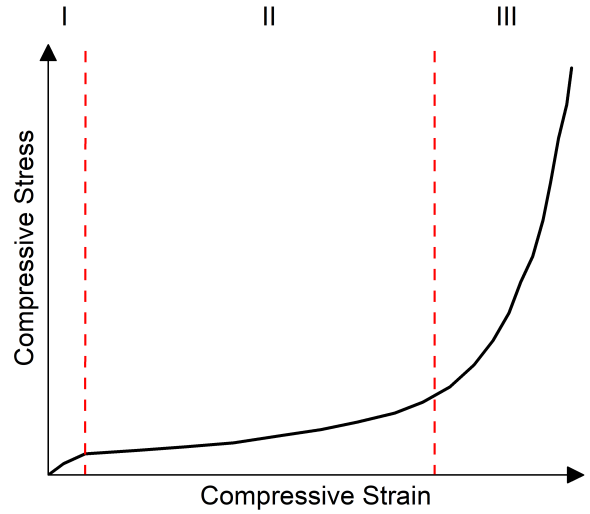

Figure 2.3: Qualitative uniaxial compressive behaviour of expanded polymeric materials.

except for elastomeric foams, but even if present, it is strictly related to the intrinsic mechanical behaviour of the constituent material and it is not caused by a progressive collapse of the internal structure like in other stress states. This is the main reason why expanded materials are mainly used and designed in compression rather than tension [58].

Since the structure gives a fundamental contribution to the macroscopic mechanical response for this class of materials, a great effort in the recent scientific literature has been devoted to develop experimental methods (and the related equipment) capable of inspecting the geometrical structure of the foams and its evolution following deformation. This second aspect is of great importance to correlate microscopic deformation mechanisms with the macroscopic mechanical behaviour [16] [17]. The experiments are made possible thanks to the development of new technologies capable of accurately measure strain distribution in the tested samples. Many authors proposed the application of digital image correlation (DIC) [8], bidimensional or three-dimensional correlation [37], in order to achieve this goal. The technique consists in recording with one or more cameras the sample that undergoes the mechanical

test, appropriately covered with a suitable pattern or exploiting the intrinsic pattern given by the structure of the material when affordable, and evaluate the deformations by correlating the evolution of the recorded images with respect to the reference one, representing the undeformed state. With this kind of tests, localizations on the strain field within the sample can be detected to highlight local structure collapse and structure bending [37].

Other authors proposed the use of in-situ scanning electron microscopy (SEM) [66], confocal microscopy [2] or X-Ray computed tomography (CT) [83] to quantify structure deformation at the microscopical level in a total three-dimensional view, obtaining a more realistic picture of the internal structure during the test [56] [20]. The methods consist in compressing at a certain level of strain the specimen under test and then, keeping the strain level constant, performing a reconstruction of the structure using one of the aforementioned techniques. Unfortunately, these methods are very expensive in terms of test duration and equipment costs and frequently collide with the viscoelastic nature of the constituent polymers. In fact, the image acquisition time is usually incompatible with the characteristic time of the material under test and so the structure continuously modifies during the step of three-dimensional structure inspection, unless very long resting times are provided after each compression step [15].

Besides the fundamental contribution of the internal structure to the macroscopic mechanical response, other physical aspects, intrinsic of the nature of constituent material, have been considered over the years. One above all is the viscoelastic nature of polymeric materials, which plays a fundamental role also in the mechanical response of expanded material [87]. As an example, many authors reported the preserved dependence of the mechanical response on the test velocity and consequently on the strain rate, or stress rate, applied during the test [92]. This dependence is in any case different from the one measured on the bulk constituent polymer since during the foaming process the

polymer is highly oriented in the micro-structure and consequently the free volume and chain mobility, two of the main factors responsible for the viscoelastic nature of polymers, are modified. Another aspect widely studied in the literature is the dependence of the mechanical response on the temperature, which again strongly influences material viscoelasticity [45]. Related to these aspects different techniques were exploited in the past years, such as impact testing, performed to cover a wide range of test speeds, or the integration of environmental chambers able to control temperature and humidity. Many authors also combined these experimental techniques with the imaging techniques previously described [77].

The last aspect, always related to the viscoelastic nature of polymeric materials, faced by many authors in the past decades is the aforementioned effect of foaming process on the constituent material properties [10] [94]. This is another fundamental factor that, together with the foam structure, contributes to the macroscopic mechanical behaviour [81]. The main experimental approach adopted consists in studying the effect of the process variables, mainly temperature and pressure, on the employed polymer and try to apply the modified behaviour to describe the contribution of the constituent polymer on the overall mechanical response [96]. This indirect approach is mainly motivated by the fact that once the polymer is foamed it is practically impossible to characterize a single structure with conventional experimental tests, due to the small characteristic dimensions, in the order of few microns, of the internal structures of the foam. Recently some author proposed the use of nanoindentation to characterize the constituent material and through the application of suitable homogenization models obtain the macroscopic constituent material behaviour [84]. This approach turned out to be suitable for expanded materials whose constituent material belongs to the family of metals or ceramic, but in case of polymers many challenges still need to be overcome.

Empirical models

One of the main outcome of the researches developed in the past years and described in previous paragraphs, is the development of some empirical models that correlate structural parameters, suitable for the description of the internal microstructure, with selected macroscopic mechanical properties exhibited by polymeric foams; amongst them, the apparent stiffness, the stress and related strain plateau value, the dependence on the applied strain or stress rate, the densification stress onset and related strain and many others. The common approach followed in this category of models consists in the research of correlations between structural and global parameters suitable to describe the macroscopic mechanical response. These empirical correlations are always dependent on a certain number of constants that are usually determined through a suitable fitting procedure performed on experimental data, coming from laboratory tests. The determination of these constants for the specific system under study allows the generalization and application of the empirical relation to the specific expanded polymeric material.

One of the most famous sets of equations, constituting an empirical model, is the one proposed by Gibson and Ashby in their masterpiece *"Cellular solid"* [24]; in their book the authors summarized a huge number of experimental data obtained on different expanded polymeric systems. Their characterization regarded both structure and mechanical tests. For what concerns the structure they propose a description based on some concentrated parameters, such as the apparent foam density, the mean structure thickness, the wall thickness in the case of closed-cell systems, the internal microstructure of foams. The mechanical properties are summarized through the usual quantities applied in the description of bulk material mechanical behaviour, but with the meaning of apparent quantities. Through the application of dimensional analysis, they established some empirical relationships that correlate internal structure and bulk material properties with the macroscopic

ones. Here a couple of examples are reported:

$$\frac{E^*}{E_S} = C_1\,\phi^2\left(\frac{\rho^*}{\rho_S}\right)^2 + C_2\;(1-\phi)\;\frac{\rho^*}{\rho_S} + C_3\,\frac{p_0\,(1-2\nu^*)}{E_s\,(1-\frac{\rho^*}{\rho_S})} \tag{2.1}$$

in this equation, developed to describe the apparent stiffness (E^*) of closed-cell foams, its value is normalized to the stiffness of constituent material (E_S) and empirically related to structure parameters such as the solid volume fraction (ϕ) and the apparent density (ρ^*), once again normalized to the bulk density (ρ_S). All the quantities are linked with three constants (C_1, C_2 and C_3) that have to be determined by fitting experimental data. Another reported example concerns the plateau stress value for closed-cell systems:

$$\frac{\sigma^*_{pl}}{\sigma_{y,\,S}} = D_1\left(\phi\,\frac{\rho^*}{\rho_S}\right)^{\frac{3}{2}} + D_2\;(1-\phi)\;\frac{\rho^*}{\rho_S} + D_3\,\frac{p_0 - p_{at}}{\sigma_{y,\,S}} \tag{2.2}$$

also, in this example the quantities related to the foam structure are linked to the mechanical parameters, plateau stress (σ^*_{pl}) and the yielding stress of constituent material ($\sigma_{y,\,S}$), with three empirical constants (D_1, D_2 and D_3) that can be determined by data fitting.

Another example of empirical model is the one proposed by Nagy and co-authors [60] and successfully applied in many experimental works [80]. The construction procedure is similar to the one employed by Ashby and it aims at the description of strain rate dependence of polymeric foams. Also in this case the authors performed an extended experimental campaign of mechanical characterization at different strain rates on different polymeric systems and, exploiting all the obtained data, they identified an empirical relation:

$$\sigma\,(\varepsilon) = \sigma_0\,(\varepsilon)\,\left(\frac{\dot{\varepsilon}}{\dot{\varepsilon}_0}\right)^{n(\varepsilon)} \tag{2.3}$$

In this case $\sigma_0(\varepsilon)$ represents the material stress-strain behaviour in

a reference strain rate ($\dot{\varepsilon}_0$) and the exponent $n(\varepsilon)$ determines the dependence of the overall stress-strain curve on the strain rate. Nagy and co-authors found that this exponent exhibits a linear dependence on the actual level of strain. The main drawback also in this case is the dependence of the model on the specific tested system and its application requires a large amount of experimental data in order to perform fitting operations and to compute relevant model parameters.

Other empirical approaches consist in the definition of a single scalar parameter, also called synthetic parameter, or a curve able to describe a particular aspect of the mechanical response of expanded polymeric materials. Some examples are:

- *Cushioning factor*: a method to visualize in a more direct way the energy absorption of expanded polymeric materials plotting the peak stress normalized to the absorbed energy with respect to the stress level itself [64].

- *Janssen factor*: relates the impact peak deceleration, measured during an experimental impact test, to the theoretical value of an ideal foam that is capable to absorb all the nominal impact energy at constant deceleration [3]. The factor is usually plotted as a function of specific absorbed energy (energy absorbed per unit volume) [72].

- *Rusch diagram*: these are refined approaches with respect to the cushion factor that consist in plotting the normalized peak stress, with respect to foam apparent stiffness, as a function of specific absorbed energy [72].

- *Maiti diagram*: is considered the ultimate refinement of Rusch approach in which the energy per unit volume is plotted against the actual stress level, both quantities normalized with respect to foam apparent stiffness. This procedure repeated for different apparent densities of the same polymeric system, allows the

construction of an envelope curve, corresponding to the different densification onset, that can be used to select the proper foam density for a certain application [55].

Besides the variable level of complexity of empirical models, the approach with which they are constructed mainly suffer from the large amount of experimental data necessary to properly tune the parameters of the model and the high dependency on the specific system under design. These are some of the many reasons that led many authors in the past years to look for more general approaches to develop numerical tools that would more effectively guide the development of expanded systems and design of new products that incorporate these kind of materials. The main approaches adopted will be discussed in the next section.

2.4 Modelling approaches

Many authors in the past years researched models of general validity, independent from the specific system under study for what concerns structure contribution; the ability to suitably describe and predict mechanical behaviour of expanded polymeric materials is of great interest in view of the wide range of engineering applications in which these systems are employed and also, within a given field of application, the different working conditions in which they could be exploited. These numerical models are for sure powerful tools during the design phase of new expanded polymeric system or the development of new devices or components that incorporate these systems. They also facilitate the optimization phase of new devices reducing the mandatory prototyping step that usually involves extended and expensive experimental characterization studies [19].

The general approach adopted in these models differs from empirical ones since few systems are selected and subjected to a thorough study in order to obtain general laws suitable to describe the largest number of possible different systems. The main goal of these models is to fully understand the synergic contribution of microscopic structure and constituent material behaviour to the macroscopic one.

Among the large number of models proposed by many authors in the past decades, three main categories can be distinguished based on the theoretical approach adopted:

- *Analytical models*
- *Voronoi tessellation models*
- *Image-based models*

These three categories will be briefly summarized in the next sections and the most popular models reported in literature will be described as examples.

2.4.1 Analytical models

The main hypothesis underlying this kind of approach is the assumption of a regular internal structure of the expanded material, with a spatial repetition of a regular solid or of a combination of them. The regular solid is usually referred to as the unit cell [24]. Figure 2.4 summarizes the main regular solids adopted in the past decades to describe the internal structure of the foams [27]. Once the proper polyhedron is selected it is considered like a structure made of beams or beams and membranes in the case of closed-cell systems. Through the application of the classic elastic theory or, as an alternative, the virtual work principle, it is possible to analyse the structure under simple load conditions and to obtain closed relationships that correlate the elastic constants that describe the beam linear elastic behaviour and the characteristic geometrical dimensions of the chosen solid [82]. This turns out to be an advantageous approach since it always gives closed analytical relationships between geometry and constituent material, with constant coefficients that can be computed from geometrical considerations, strictly related on the characteristic lengths of the solid chosen, and therefore no extended experimental tests and consequent fitting is required like in an empirical model. Some authors also exploit this approach trying to derive some closed relationships also in the case of non-linear mechanical behaviour of both the structure and its constituent material [33].

The main disadvantage of this approach is that the real structure of expanded materials is oversimplified; the regular polyhedrons are not suitable to reproduce the complexity of real structures and implicitly neglect many irregularities that occur in real samples, and play an essential role in determining their properties [96] [99]. This usually leads to a closed relationship that overestimates the real response of expanded materials in terms of apparent moduli and strength. Another drawback of this kind of model lies in the fact that closed analytical

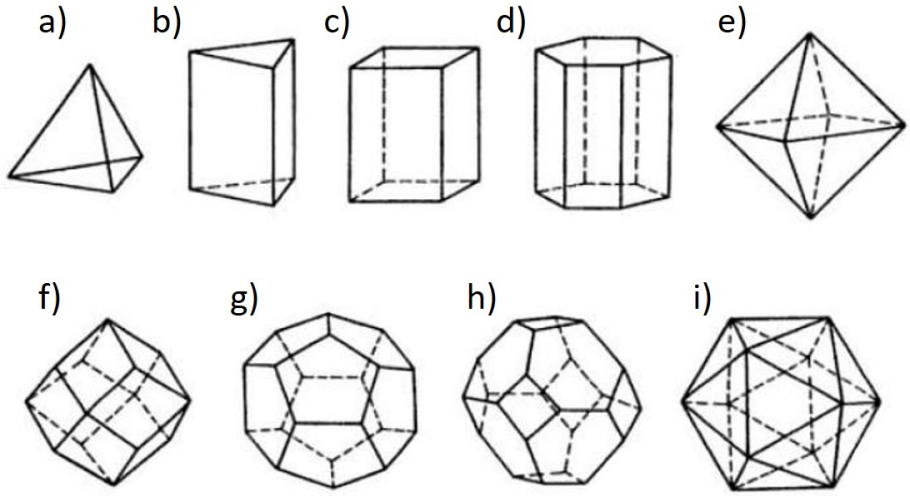

Figure 2.4: Three-dimensional polyhedral cells commonly used to represent the internal structure of expanded polymeric materials; in order a) tetrahedron, b) triangular prism, c) rectangular prism, d) hexagonal prism, e) octahedron, f) rhombic dodecahedron, g) pentagonal dodecahedron, h) tetrakaidekahedron and i) icosahedron. Image freely adapted from [24].

relationships are derivable only in the simple case of loading conditions linked with properly defined boundary conditions (symmetry or periodic ones are usually selected); these relationships are obtained almost always under the strong hypothesis of a homogeneous linear elastic constituent material. Only few analytical solutions are available for the case of non-elastic constituent materials [48].

In the following paragraph the two most famous and widely used models will be briefly summarized. For a complete model derivation please refer to the referenced works [24] [97].

Ashby hexahedral unit cell

Ashby model [24] assumes a hexahedral structure as a unit cell suitable to represent the internal structure of expanded materials. Two cases can be distinguished, as reported in figure 2.5: one represents

open-cell systems, with beam-like structures, and one for closed-cell systems, where additionally to beams also membrane elements are employed to describe the structure. The characteristic lengths of the unit cell selected are the length of the beam and its thickness, while in addition for closed-cell systems membrane thickness is added as a characteristic length.

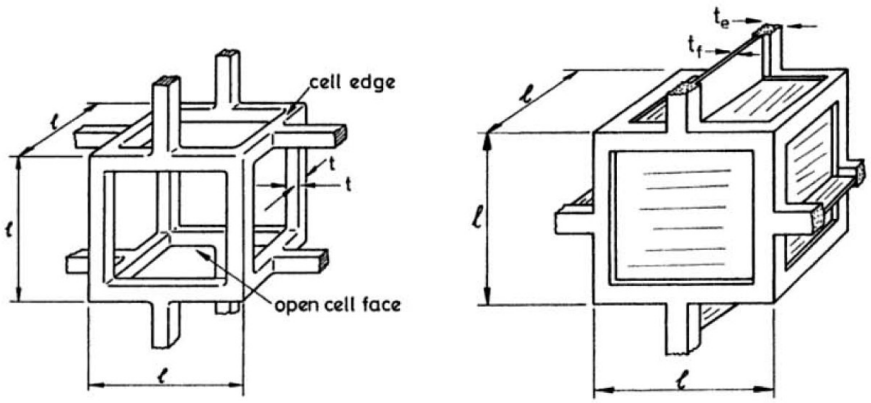

(a) *Ashby hexahedral open cell* **(b)** *Ashby hexahedral closed cell*

Figure 2.5: Ashby hexahedral unit cell used to skeletonize the internal structure of expanded polymeric materials; open-cell systems (right) and closed-cell systems (left). Image freely adapted from [24].

Through the application of linear elastic beam-membranes theory and under the hypothesis of homogeneous linear elastic constituent material, the structure behaviour is analytically computed. The simple applied load condition is uniaxial compression. The relationships obtained are outlined in equations 2.4 - 2.5:

Open-cell

$$\begin{cases} \frac{E^*}{E_S} \approx \left(\frac{\rho^*}{\rho_S}\right)^2 \\ \frac{\rho^*}{\rho_S} \approx \left(\frac{t_e}{l}\right)^2 \end{cases} \tag{2.4}$$

Closed-cell

$$\begin{cases} \frac{E^*}{E_S} \approx \phi^2 \left(\frac{\rho^*}{\rho_S}\right)^2 + (1-\phi)\ \frac{\rho^*}{\rho_S} + \frac{p_0\ (1-2\nu^*)}{E_S\ (1-\frac{\rho^*}{\rho_S})} \\ \frac{\rho^*}{\rho_S} \approx 1.2\ \left(\frac{t_e^2}{l^2} + 0.7\,\frac{t_f}{l}\right) \end{cases} \tag{2.5}$$

where ρ^* is the apparent density of the foam, ρ_S is the density of bulk constituent material, E^* is the apparent modulus of the foam and E_S is the Young modulus of the constituent material; ϕ is the solid volume fraction, t_e is the beam thickness, t_f is the wall (membrane) thickness and l is the beam length. p_0 is the pressure of the fluid inside the closed-cell and ν^* is the apparent Poisson's ratio of the foam.

Closed relationships can be obtained only through simplified geometrical considerations; they uniquely relate microscopic structure parameters and macroscopic mechanical parameters.

Besides linear elastic solutions, Ashby is one of the authors that proposed closed solutions also for non-linear mechanical behaviour of foams; his studies range from elastic buckling to plastic collapse and densification. The other main aspect faced by the author is the induced anisotropy in the foam structure and its effect on the macroscopic mechanical response. This last aspect will be dealt with in later chapters of this thesis.

Zhu tetrakaidekahedral unit cell

The other main analytical model widely used by many authors in the past decades is the one proposed by Zhu [97]. The theoretical background and mathematical approach are the same proposed by Ashby and all the other authors that follow the road of analytical models.

In this case, the chosen polyhedron is the tetrakaidekahedron, selected according to lord Kelvin studies and mathematical demonstrations, being the polyhedron that better optimizes the occupation of a certain prescribed volume in space and the ideal spatial configuration,

among the approximately $1.5 * 10^9$ possibilities, is the one reported in figure 2.6.

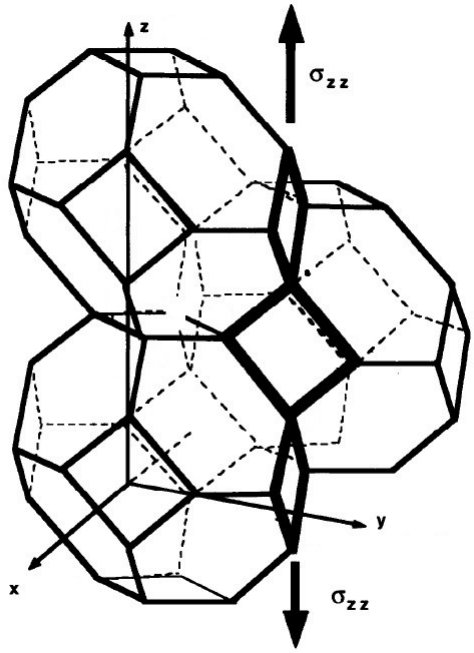

Figure 2.6: Zhu unit cell, composed of three tetrakaidekahedrons arranged in space in the configuration that best optimize the occupied volume. Image freely adapted from [97].

The relationships outlined in equations 2.6 - 2.7 describe the apparent stiffness along the macroscopically uniaxial compression direction and the apparent shear stiffness in the cross-sectional plane with respect to the load application direction:

$$\frac{1}{E_Z} = \frac{1}{6\sqrt{2}} \left(\frac{12L^2}{E_S A} + \frac{L^4}{E_S I} \right) \tag{2.6}$$

$$\frac{1}{G_{XY}} = \frac{2\sqrt{2}L^2}{E_S A} + \frac{\sqrt{2}L^4}{6E_S I} \left(\frac{8E_S I + G_S J}{5E_S I + G_S J} \right) \tag{2.7}$$

in this relationship the Young modulus (E_Z) and shear modulus (G_{XY}) of the foam are related to the equivalent mechanical constant of the constituent material (E_S and G_S) through geometrical parameters such

as the cell edge length (L), the cross-sectional area of the unit-cell (A), the second moment of inertia (I) and the polar moment of inertia (J).

Zhu, like Ashby, proposed a refinement of the model including geometrical anisotropy and non-linear aspects of the mechanical behaviour [82].

2.4.2 Voronoi tessellation

This kind of approach is mainly based on classical voids nucleation theory of foaming processes; for the sake of brevity the nucleation theory is not reported, but interested readers are addressed to the relevant scientific literature [42] [41]. Nucleation theory serves as a basis to generate a certain number of randomly distributed structures that occupy a certain volume in three-dimensional models or a certain area in bidimensional models [78]. Figure 2.7 and 2.8 display a couple of examples of the structures generated with nucleation theory approach.

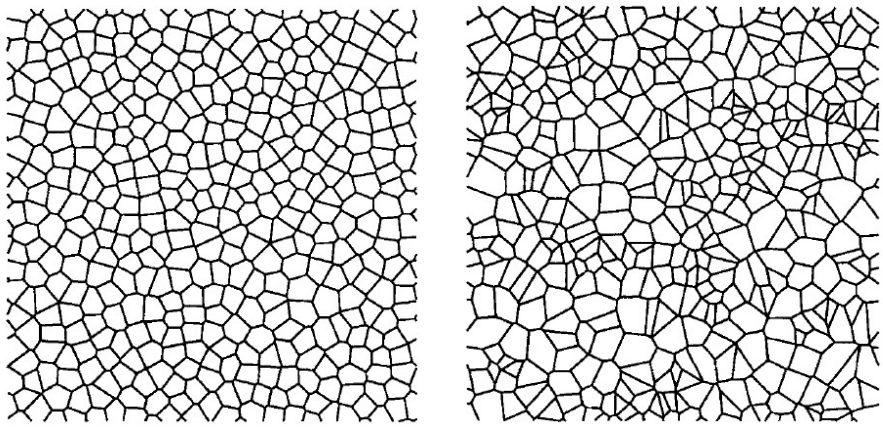

(a) *Bidimensional example of regular Voronoi tessellation*

(b) *Bidimensional example of irregular Voronoi tessellation*

Figure 2.7: Examples of bidimensional Voronoi tessellation. Image freely adapted from [100].

These random structures serve as a basis for numerical simulations in order to compute the macroscopic properties exhibited by the inspected

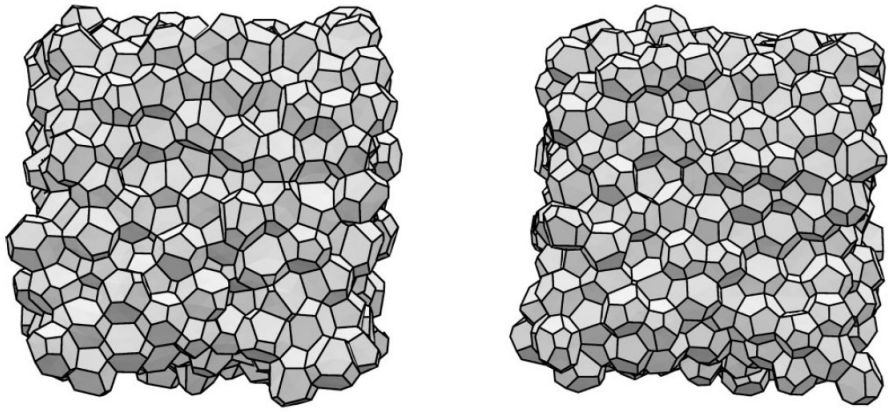

Figure 2.8: Three-dimensional examples of Voronoi tessellation. Image freely adapted from [44].

structure [98].

The main advantage of this approach is the possibility to generate a large number of different structures constituted by an adequate number of cells in order to perform a statistical analysis on the macroscopic properties as a function of small variations in the microstructure or on the properties of the constituent material. This approach also allows to perform parametric studies changing one variable at a time and studying the consequent effect on the macroscopic property of interest. Different studies were performed in the past decades with the aim of studying the effect of cell geometrical irregularities or the presence of defects inside the structure [100].

The main drawbacks of this approach can be summarized as follows [78]:

- A large number of cells has to be generated in order to have a sample representative of the real behaviour of expanded materials. Usually this collides with the available numerical resources and related time request to perform simulations. This is a crucial aspect that the present approach has in common with image-based approaches; suitable numerical solutions has to be implemented

to optimize the available numerical resources and to obtain results in a reasonable amount of time.

- The structures generated are generally unrelated to the real ones since they are based on classical nucleation theory; real foaming process typically divert from this theory in a sensible manner and hence the synthetic structures do not correspond to the real ones.

- Generally speaking, bidimensional Voronoi tessellation cannot be used to represent real structures, since it neglects mechanisms and cell interactions that occur in laboratory test on a three-dimensional sample. They are certainly cheaper from a computational point of view, in terms of time and numerical resources, but give an unacceptable overestimation of the mechanical properties obtained and so they are not suitable tools to describe and predict the real behaviour of expanded materials.

2.4.3 Image-based models

The third approach presented became available in recent years thanks to the development of new experimental techniques able to inspect the real geometry of expanded polymeric materials with a sufficiently high resolution [57]. The main step performed in the present approach is the acquisition of the real geometry, usually as a set of digital images, and convert this information into numerical tools, such as finite element mesh, finite volume or voxel volume elements and level sets elements, to perform numerical simulations considering the real structure experimentally inspected [54].

Among the different imaging techniques, the most frequently used are X-Ray computed tomography (CT), synchrotron computed tomography or solid state nuclear magnetic resonance (ss-NMR) which are techniques able to inspect from a three-dimensional perspective the internal microscopic structure [43]. Figure 2.9 displays an example of

converted images into a finite element mesh; the preservation of the real structure is clearly visible in the reconstruction. Many authors exploit also bidimensional imaging techniques, such as scanning electron microscopy (SEM), optical or confocal microscopy and transmission electron microscopy (TEM) performing the imaging procedure on different slices of sample adequately prepared, usually with the use of a microtome [14].

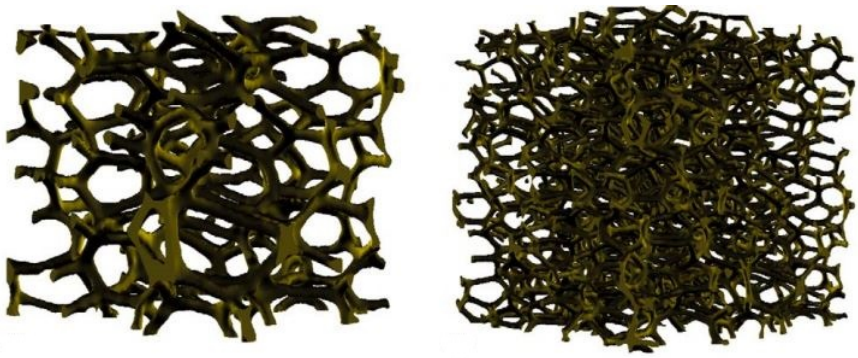

Figure 2.9: Reconstruction of two open-cell polyurethane foams starting from a set of images representing the internal structure obtained with high-resolution X-ray computed tomography. Image freely adapted from [12].

The main advantage of this method is the absence of any simplifying hypothesis made on the structure [12], since the real one is directly considered without neglecting any possible defect coming from the foaming process or the necessity to a priori distinguish between open-cell or closed-cell systems [65].

The main drawbacks are, from an experimental point of view, the very long time of image acquisition required and the small volume that could be inspected without decreasing too much the resolution, with the actually available technologies. From a computational point of view, the difficulties arise from the large amount of data generated during the image acquisition phase and the vast numerical resources, in terms of computational power and time, required to perform analysis on a reconstructed volume representative of the real samples [73] [54] [4].

Authors during the past years proposed different solutions to reduce the physical resources required and simulation time without losing too much in terms of accuracy and efficiency. Some author proposed the use of bidimensional images to compute quantities representative of the three-dimensional inspected structure and to model the macroscopic mechanical response, but this turned out to be an excessive simplification since the deformation mechanisms experienced by the expanded material in a bidimensional simulation are not representative of the real three-dimensional ones, as already pointed out in the Voronoi tessellation section [92]. These simulations give as a result an excessive overestimation of the mechanical properties with respect to the real behaviour of the expanded material. Other authors proposed the use of simplified elements, such as Timoshenko beams, collapsing each structure into its inertial axis [35]. This solution surely reduces the simulation time and resources required, but once again gives as a result an overestimation of the real behaviour, since simplified elements are characterized by fewer degrees of freedom with respect to standard solid elements and hence the deformation mechanisms are over constrained. Another approach proposed in literature is the use of suitable homogenization schemes to obtain the macroscopic properties starting from a simulated sub-domain, that usually requires a limited computational effort; this approach is suitable but with many different approximations since the structures of real foams are characterized by a very limited degree of geometrical regularity; yet, this is one of the most promising approaches in this field [23].

Despite the many highlighted drawbacks, this kind of modelling approach is the most promising one in the field of polymeric foams properties modelling. Since it is relatively new, many challenges are still to be overcome and many complementary tools have to be developed or optimized yet.

In the present thesis the image-based approach has been selected; numerical tools have been developed and macroscopic constitutive

relationships been sought to reliably and efficiently describe and predict expanded polymeric materials behaviour.

2.5 References

[1] L. Andena et al. “Compression of polystyrene and polypropylene foams for energy absorption applications: A combined mechanical and microstructural study”. en. In: *Journal of Cellular Plastics* 55.1 (Jan. 2019), pages 49–72. DOI: 10.1177/0021955X18806794. URL: http://journals.sagepub.com/doi/10.1177/0021955X18806794.

[2] E.W. Andrews et al. “Size effects in ductile cellular solids. Part II: experimental results”. en. In: *International Journal of Mechanical Sciences* (2001), page 13.

[3] M. Avalle, G. Belingardi, and R. Montanini. “Characterization of polymeric structural foams under compressive impact loading by means of energy-absorption diagram”. en. In: *International Journal of Impact Engineering* 25.5 (May 2001), pages 455–472. DOI: 10.1016/S0734-743X(00)00060-9. URL: https://linkinghub.elsevier.com/retrieve/pii/S0734743X00000609.

[4] P. Babin et al. “Mechanical properties of bread crumbs from tomography based Finite Element simulations”. en. In: *Journal of Materials Science* 40.22 (Nov. 2005), pages 5867–5873. DOI: 10.1007/s10853-005-5021-x. URL: http://link.springer.com/10.1007/s10853-005-5021-x.

[5] J. Bai et al. “Control of the cell structure of microcellular silicone rubber/nanographite foam for enhanced mechanical performance”. en. In: *Materials & Design* 133 (Nov. 2017), pages 288–298. DOI: 10.1016/j.matdes.2017.07.064. URL: https://linkinghub.elsevier.com/retrieve/pii/S0264127517307402.

[6] M. Bakir et al. “Aromatic thermosetting copolyester nanocomposite foams: High thermal and mechanical performance lightweight structural materials”. en. In: *Polymer* 123 (Aug. 2017), pages 311–

320. DOI: 10.1016/j.polymer.2017.07.030. URL: https://linkinghub.elsevier.com/retrieve/pii/S0032386117306894.

[7] R.C.N. Barbosa, R.D.S.G. Campilho, and F.J.G. Silva. "Injection mold design for a plastic component with blowing agent". en. In: *Procedia Manufacturing* 17 (2018), pages 774–782. DOI: 10.1016/j.promfg.2018.10.128. URL: https://linkinghub.elsevier.com/retrieve/pii/S2351978918312460.

[8] R. Belda et al. "Some Practical Considerations for Compression Failure Characterization of Open-Cell Polyurethane Foams Using Digital Image Correlation". en. In: *Sensors* 20.15 (July 2020), page 4141. DOI: 10.3390/s20154141. URL: https://www.mdpi.com/1424-8220/20/15/4141.

[9] M. Benanti. "2015 Properties Cellular Polymeric Materials Related to Structure". en. Phd Thesis. Politecnico di Milano: Politecnico di Milano, 2015.

[10] M. Bocciarelli et al. "Assessment of the shock adsorption properties of bike helmets: a numerical/experimental approach". en. In: *Computer Methods in Biomechanics and Biomedical Engineering* 23.5 (Apr. 2020), pages 169–181. DOI: 10.1080/10255842.2019.1709451. URL: https://www.tandfonline.com/doi/full/10.1080/10255842.2019.1709451.

[11] R. Bouix, P. Viot, and J. Lataillade. "Polypropylene foam behaviour under dynamic loadings: Strain rate, density and microstructure effects". en. In: *International Journal of Impact Engineering* 36.2 (Feb. 2009), pages 329–342. DOI: 10.1016/j.ijimpeng.2007.11.007. URL: https://linkinghub.elsevier.com/retrieve/pii/S0734743X08000791.

[12] A.D. Brydon et al. "Simulation of the densification of real open-celled foam microstructures". en. In: *Journal of the Mechanics and Physics of Solids* 53.12 (Dec. 2005), pages 2638–2660. DOI:

10.1016/j.jmps.2005.07.007. URL: https://linkinghub.elsevier.com/retrieve/pii/S0022509605001298.

[13] S. Chen, W. Zhu, and Y. Cheng. "Multi-Objective Optimization of Acoustic Performances of Polyurethane Foam Composites". en. In: *Polymers* 10.7 (July 2018), page 788. DOI: 10.3390/polym10070788. URL: http://www.mdpi.com/2073-4360/10/7/788.

[14] Y. Chen et al. "Micro-CT based finite element models of cancellous bone predict accurately displacement once the boundary condition is well replicated: A validation study". en. In: *Journal of the Mechanical Behavior of Biomedical Materials* 65 (Jan. 2017), pages 644–651. DOI: 10.1016/j.jmbbm.2016.09.014. URL: https://linkinghub.elsevier.com/retrieve/pii/S1751616116303204.

[15] N.P. Daphalapurkar et al. "Tomography and Simulation of Microstructure Evolution of a Closed-Cell Polymer Foam in Compression". en. In: *Mechanics of Advanced Materials and Structures* 15.8 (Dec. 2008), pages 594–611. DOI: 10.1080/15376490802470523. URL: http://www.tandfonline.com/doi/abs/10.1080/15376490802470523.

[16] V.S. Deshpande, M.F. Ashby, and N.A. Fleck. "Foam topology: bending versus stretching dominated architectures". en. In: *Acta Materialia* 49.6 (Apr. 2001), pages 1035–1040. DOI: 10.1016/S1359-6454(00)00379-7. URL: https://linkinghub.elsevier.com/retrieve/pii/S1359645400003797.

[17] V.S. Deshpande and N.A. Fleck. "Multi-axial yield behaviour of polymer foams". en. In: *Acta Materialia* 49.10 (June 2001), pages 1859–1866. DOI: 10.1016/S1359-6454(01)00058-1. URL: https://linkinghub.elsevier.com/retrieve/pii/S1359645401000581.

[18] O. Duncan et al. “A Comparison of Novel and Conventional Fabrication Methods for Auxetic Foams for Sports Safety Applications”. en. In: *Procedia Engineering* 147 (2016), pages 384–389. DOI: 10.1016/j.proeng.2016.06.323. URL: https://linkinghub.elsevier.com/retrieve/pii/S1877705816307706.

[19] W. Ehlers and B. Markert. “A macroscopic finite strain model for cellular polymers”. en. In: *International Journal of Plasticity* 19.7 (July 2003), pages 961–976. DOI: 10.1016/S0749-6419(02)00088-8. URL: https://linkinghub.elsevier.com/retrieve/pii/S0749641902000888.

[20] J.A. Elliott et al. “In-situ deformation of an open-cell flexible polyurethane foam characterised by 3D computed microtomography”. en. In: (), page 9.

[21] N. Esmaeili et al. “Bio-based thermosetting epoxy foam: Tannic acid valorization toward dye-decontaminating and thermoprotecting applications”. en. In: *Journal of Hazardous Materials* 357 (Sept. 2018), pages 30–39. DOI: 10.1016/j.jhazmat.2018.05.045. URL: https://linkinghub.elsevier.com/retrieve/pii/S0304389418304011.

[22] F.A.O. Fernandes et al. “Comparing the mechanical performance of synthetic and natural cellular materials”. en. In: *Materials & Design* 82 (Oct. 2015), pages 335–341. DOI: 10.1016/j.matdes.2015.06.004. URL: https://linkinghub.elsevier.com/retrieve/pii/S0264127515003548.

[23] F. Fischer et al. “Numerical Simulation of Mechanical Properties of Cellular Materials Using Computed Tomography Analysis”. en. In: *Journal of Cellular Plastics* 45.5 (Sept. 2009), pages 441–460. DOI: 10.1177/0021955X09339340. URL: http://journals.sagepub.com/doi/10.1177/0021955X09339340.

[24] L.J. Gibson and M.F. Ashby. *Cellular Solids*. en.

[25] L. Gong and S. Kyriakides. “Compressive response of open cell foams Part II: Initiation and evolution of crushing”. en. In: *International Journal of Solids and Structures* 42.5-6 (Mar. 2005), pages 1381–1399. DOI: 10.1016/j.ijsolstr.2004.07.024. URL: https://linkinghub.elsevier.com/retrieve/pii/S0020768304004317.

[26] L. Gong, S. Kyriakides, and W.Y. Jang. “Compressive response of open-cell foams. Part I: Morphology and elastic properties”. en. In: *International Journal of Solids and Structures* 42.5-6 (Mar. 2005), pages 1355–1379. DOI: 10.1016/j.ijsolstr.2004.07.023. URL: https://linkinghub.elsevier.com/retrieve/pii/S0020768304004305.

[27] L. Gong, S. Kyriakides, and N. Triantafyllidis. “On the stability of Kelvin cell foams under compressive loads”. en. In: *Journal of the Mechanics and Physics of Solids* 53.4 (Apr. 2005), pages 771–794. DOI: 10.1016/j.jmps.2004.10.007. URL: https://linkinghub.elsevier.com/retrieve/pii/S0022509604001899.

[28] A.R. Hamilton et al. “Evaluation of the anisotropic mechanical properties of reinforced polyurethane foams”. en. In: *Composites Science and Technology* 87 (Oct. 2013), pages 210–217. DOI: 10.1016/j.compscitech.2013.08.013. URL: https://linkinghub.elsevier.com/retrieve/pii/S0266353813003175.

[29] P. Hard af Segerstad and S. Toll. “Open-cell cellular solids: A constitutive equation for hyperelasticity with deformation induced anisotropy”. en. In: *International Journal of Solids and Structures* 45.7-8 (Apr. 2008), pages 1978–1992. DOI: 10.1016/j.ijsolstr.2007.11.003. URL: https://linkinghub.elsevier.com/retrieve/pii/S0020768307004787.

[30] A. Heidari and M. Fasihi. “Cell structure-impact property relationship of polypropylene/thermoplastic elastomer blend foams”.

en. In: *Express Polymer Letters* 13.5 (2019), pages 429–442. DOI: 10.3144/expresspolymlett.2019.36. URL: http://www.expresspolymlett.com/letolt.php?file=EPL-0009644&mi=c.

[31] N. C. Hilyard and A. Cunningham, editors. *Low density cellular plastics: Physical basis of behaviour*. en. Dordrecht: Springer Netherlands, 1994. DOI: 10.1007/978-94-011-1256-7. URL: http://link.springer.com/10.1007/978-94-011-1256-7.

[32] D. Huang et al. "Experimental investigations on the effects of bottom ventilation on the fire behavior of natural rubber latex foam". en. In: *Applied Thermal Engineering* 133 (Mar. 2018), pages 201–210. DOI: 10.1016/j.applthermaleng.2018.01.044. URL: https://linkinghub.elsevier.com/retrieve/pii/S1359431117305896.

[33] W.Y. Jang, A.M. Kraynik, and S. Kyriakides. "On the microstructure of open-cell foams and its effect on elastic properties". en. In: *International Journal of Solids and Structures* 45.7-8 (Apr. 2008), pages 1845–1875. DOI: 10.1016/j.ijsolstr.2007.10.008. URL: https://linkinghub.elsevier.com/retrieve/pii/S0020768307004118.

[34] Z. Ji et al. "Improved dimensional stability of styrene butadiene rubber/ethylene vinyl acetate composite foams with skeleton support structure based on alternately cross-linking process". en. In: *Polymer* 157 (Nov. 2018), pages 103–110. DOI: 10.1016/j.polymer.2018.10.028. URL: https://linkinghub.elsevier.com/retrieve/pii/S0032386118309510.

[35] J. Jiao and N. Huber. "Effect of nodal mass on macroscopic mechanical properties of nanoporous metals". en. In: *International Journal of Mechanical Sciences* 134 (Dec. 2017), pages 234–243. DOI: 10.1016/j.ijmecsci.2017.10.011. URL: https://linkinghub.elsevier.com/retrieve/pii/S0020740317317010.

[36] F. Jin et al. “Recent Trends of Foaming in Polymer Processing: A Review”. en. In: *Polymers* 11.6 (June 2019), page 953. DOI: 10.3390/polym11060953. URL: https://www.mdpi.com/2073-4360/11/6/953.

[37] A. Jung et al. “Correlative digital image correlation and infrared thermography measurements for the investigation of the mesoscopic deformation behaviour of foams”. en. In: *Journal of the Mechanics and Physics of Solids* 130 (Sept. 2019), pages 165–180. DOI: 10.1016/j.jmps.2019.06.009. URL: https://linkinghub.elsevier.com/retrieve/pii/S0022509618311542.

[38] H. Kang, C.Y. Lin, and S.J. Hollister. “Topology optimization of three dimensional tissue engineering scaffold architectures for prescribed bulk modulus and diffusivity”. en. In: *Structural and Multidisciplinary Optimization* 42.4 (Oct. 2010), pages 633–644. DOI: 10.1007/s00158-010-0508-8. URL: http://link.springer.com/10.1007/s00158-010-0508-8.

[39] M. Keshtkar et al. “Extruded PLA/clay nanocomposite foams blown with supercritical CO2”. en. In: *Polymer* 55.16 (Aug. 2014), pages 4077–4090. DOI: 10.1016/j.polymer.2014.06.059. URL: https://linkinghub.elsevier.com/retrieve/pii/S0032386114005539.

[40] R.A. Ketcham and T.M. Ryan. “Quantification and visualization of anisotropy in trabecular bone: anisotropy in trabecular bone”. en. In: *Journal of Microscopy* 213.2 (Jan. 2004), pages 158–171. DOI: 10.1111/j.1365-2818.2004.01277.x. URL: http://doi.wiley.com/10.1111/j.1365-2818.2004.01277.x.

[41] J. Köll and S. Hallström. “Generation of periodic stochastic foam models for numerical analysis”. en. In: *Journal of Cellular Plastics* 50.1 (Jan. 2014), pages 37–54. DOI: 10.1177/0021955X13503848. URL: http://journals.sagepub.com/doi/10.1177/0021955X13503848.

[42] J. Köll and S. Hallström. "Influence from polydispersity on the morphology of Voronoi and equilibrium foams". en. In: *Journal of Cellular Plastics* 53.2 (Mar. 2017), pages 199–214. DOI: 10.1177/0021955X16644892. URL: http://journals.sagepub.com/doi/10.1177/0021955X16644892.

[43] A.M. Kraynik. "The Structure of Random Foam". en. In: *Advanced Engineering Materials* 8.9 (Sept. 2006), pages 900–906. DOI: 10.1002/adem.200600167. URL: http://doi.wiley.com/10.1002/adem.200600167.

[44] A.M. Kraynik, D.A. Reinelt, and F. van Swol. "Structure of random monodisperse foam". en. In: *Physical Review E* 67.3 (Mar. 2003), page 031403. DOI: 10.1103/PhysRevE.67.031403. URL: https://link.aps.org/doi/10.1103/PhysRevE.67.031403.

[45] A. Krundaeva et al. "Dynamic compressive strength and crushing properties of expanded polystyrene foam for different strain rates and different temperatures". en. In: *Polymer Testing* 55 (Oct. 2016), pages 61–68. DOI: 10.1016/j.polymertesting.2016.08.005. URL: https://linkinghub.elsevier.com/retrieve/pii/S0142941816304275.

[46] J. Lambert et al. "Extraction of relevant physical parameters from 3D images of foams obtained by X-ray tomography". en. In: *Colloids and Surfaces A: Physicochemical and Engineering Aspects* 263.1-3 (Aug. 2005), pages 295–302. DOI: 10.1016/j.colsurfa.2005.01.002. URL: https://linkinghub.elsevier.com/retrieve/pii/S0927775705000324.

[47] B. Li et al. "New foaming formulations for production of biophenol formaldehyde foams using raw kraft lignin". en. In: *European Polymer Journal* 111 (Feb. 2019), pages 1–10. DOI: 10.1016/j.eurpolymj.2018.12.011. URL: https://linkinghub.elsevier.com/retrieve/pii/S0014305718319098.

[48] K. Li, X.L. Gao, and G. Subhash. “Effects of cell shape and cell wall thickness variations on the elastic properties of two-dimensional cellular solids”. en. In: *International Journal of Solids and Structures* 42.5-6 (Mar. 2005), pages 1777–1795. DOI: 10.1016/j.ijsolstr.2004.08.005. URL: https://linkinghub.elsevier.com/retrieve/pii/S0020768304004536.

[49] C.Y. Lin, N. Kikuchi, and S.J. Hollister. “A novel method for biomaterial scaffold internal architecture design to match bone elastic properties with desired porosity”. en. In: *Journal of Biomechanics* 37.5 (May 2004), pages 623–636. DOI: 10.1016/j.jbiomech.2003.09.029. URL: https://linkinghub.elsevier.com/retrieve/pii/S0021929003003683.

[50] C. Ling, P. Cardiff, and M.D. Gilchrist. “Mechanical behaviour of EPS foam under combined compression-shear loading”. en. In: *Materials Today Communications* 16 (Sept. 2018), pages 339–352. DOI: 10.1016/j.mtcomm.2018.07.001. URL: https://linkinghub.elsevier.com/retrieve/pii/S2352492818301880.

[51] C. Ling et al. “Deformation response of EPS foam under combined compression-shear loading. Part I: Experimental design and quasi-static tests”. en. In: *International Journal of Mechanical Sciences* 144 (Aug. 2018), pages 480–489. DOI: 10.1016/j.ijmecsci.2018.06.014. URL: https://linkinghub.elsevier.com/retrieve/pii/S0020740318305794.

[52] C. Ling et al. “Deformation response of EPS foam under combined compression-shear loading. Part II: High strain rate dynamic tests”. en. In: *International Journal of Mechanical Sciences* 145 (Sept. 2018), pages 9–23. DOI: 10.1016/j.ijmecsci.2018.06.015. URL: https://linkinghub.elsevier.com/retrieve/pii/S0020740318306143.

[53] H. Liu and Y. Kang. “Superhydrophobic and superoleophilic modified EPDM foam rubber fabricated by a facile approach for

oil/water separation". en. In: *Applied Surface Science* 451 (Sept. 2018), pages 223–231. DOI: 10.1016/j.apsusc.2018.04.179. URL: https://linkinghub.elsevier.com/retrieve/pii/S0169433218311504.

[54] E. Maire. "X-ray tomography applied to the characterization of cellular materials. Related finite element modeling problems". en. In: *Composites Science and Technology* 63.16 (Dec. 2003), pages 2431–2443. DOI: 10.1016/S0266-3538(03)00276-8. URL: https://linkinghub.elsevier.com/retrieve/pii/S0266353803002768.

[55] S.K. Maiti, L.J. Gibson, and M.F. Ashby. "Deformation and energy absorption diagrams for cellular solids". en. In: *Acta Metallurgica* 32.11 (Nov. 1984), pages 1963–1975. DOI: 10.1016/0001-6160(84)90177-9. URL: https://linkinghub.elsevier.com/retrieve/pii/0001616084901779.

[56] S.A. McDonald et al. "In situ 3D X-ray microtomography study comparing auxetic and non-auxetic polymeric foams under tension". en. In: *physica status solidi (b)* 248.1 (Jan. 2011), pages 45–51. DOI: 10.1002/pssb.201083975. URL: http://doi.wiley.com/10.1002/pssb.201083975.

[57] M.D. Montminy, A.R. Tannenbaum, and C.W. Macosko. "The 3D structure of real polymer foams". en. In: *Journal of Colloid and Interface Science* 280.1 (Dec. 2004), pages 202–211. DOI: 10.1016/j.jcis.2004.07.032. URL: https://linkinghub.elsevier.com/retrieve/pii/S0021979704006824.

[58] D. T. Morton et al. "Mechanical response of low density expanded polypropylene foams in compression and tension at different loading rates and temperatures". en. In: *Materials Today Communications* 23 (June 2020), page 100917. DOI: 10.1016/j.mtcomm.2020.100917. URL: https://linkinghub.elsevier.com/retrieve/pii/S2352492819313911.

[59] Y. Mosleh et al. “Decoupling shear and compression properties in composite polymer foams by introducing anisotropy at macro level”. en. In: *Journal of Reinforced Plastics and Composites* 37.10 (May 2018), pages 657–667. DOI: 10.1177/0731684418758926. URL: http://journals.sagepub.com/doi/10.1177/0731684418758926.

[60] A. Nagy, W.L. Ko, and U.S. Lindholm. “Mechanical Behavior of Foamed Materials Under Dynamic Compression”. en. In: *Journal of Cellular Plastics* 10.3 (May 1974), pages 127–134. DOI: 10.1177/0021955X7401000306. URL: http://journals.sagepub.com/doi/10.1177/0021955X7401000306.

[61] P.H. Nam et al. “Foam processing and cellular structure of polypropylene/clay nanocomposites”. en. In: *Polymer Engineering & Science* 42.9 (Sept. 2002), pages 1907–1918. DOI: 10.1002/pen.11083. URL: http://doi.wiley.com/10.1002/pen.11083.

[62] B. Notario et al. “Dielectric behavior of porous PMMA: From the micrometer to the nanometer scale”. en. In: *Polymer* 107 (Dec. 2016), pages 302–305. DOI: 10.1016/j.polymer.2016.11.030. URL: https://linkinghub.elsevier.com/retrieve/pii/S0032386116310230.

[63] P.R. Onck, E.W. Andrews, and L.J. Gibson. “Size effects in ductile cellular solids. Part I: modelling”. en. In: *International Journal of Mechanical Sciences* (2001), page 19.

[64] U.E. Ozturk and G. Anlas. “Finite element analysis of expanded polystyrene foam under multiple compressive loading and unloading”. en. In: *Materials & Design* 32.2 (Feb. 2011), pages 773–780. DOI: 10.1016/j.matdes.2010.07.025. URL: https://linkinghub.elsevier.com/retrieve/pii/S0261306910004607.

[65] U. Pérez-Ramírez et al. “Micro-computed tomography image-based evaluation of 3D anisotropy degree of polymer scaffolds”. en. In: *Computer Methods in Biomechanics and Biomedical Engineering* 18.4 (Mar. 2015), pages 446–455. DOI: 10.1080/10255842.2013.818663. URL: http://www.tandfonline.com/doi/abs/10.1080/10255842.2013.818663.

[66] C. Richert and N. Huber. “Skeletonization, Geometrical Analysis, and Finite Element Modeling of Nanoporous Gold Based on 3D Tomography Data”. en. In: *Metals* 8.4 (Apr. 2018), page 282. DOI: 10.3390/met8040282. URL: http://www.mdpi.com/2075-4701/8/4/282.

[67] M.A. Rodriguez-Perez, M. Álvarez-Láinez, and J.A. de Saja. “Microstructure and physical properties of open-cell polyolefin foams”. en. In: *Journal of Applied Polymer Science* 114.2 (Oct. 2009), pages 1176–1186. DOI: 10.1002/app.30283. URL: http://doi.wiley.com/10.1002/app.30283.

[68] M.A. Rodriguez-Perez and J.A. de Saja. “Dynamic mechanical analysis applied to the characterisation of closed cell polyolefin foams”. en. In: *Polymer Testing* 19.7 (Aug. 2000), pages 831–848. DOI: 10.1016/S0142-9418(99)00054-9. URL: https://linkinghub.elsevier.com/retrieve/pii/S0142941899000549.

[69] M.A. Rodriguez-Perez et al. “Foaming of EVA starch blends: Characterization of the structure, physical properties, and biodegradability”. en. In: *Polymer Engineering & Science* 52.1 (Jan. 2012), pages 62–70. DOI: 10.1002/pen.22046. URL: http://doi.wiley.com/10.1002/pen.22046.

[70] M.A. Rodriguez-Perez et al. “Mechanical Behaviour at Low Strains of LDPE Foams with Cell Sizes in the Microcellular Range: Advantages of Using These Materials in Structural Elements”. en. In: *Cellular Polymers* 27.6 (Nov. 2008), pages 347–

362. DOI: 10.1177/026248930802700602. URL: http://journals.sagepub.com/doi/10.1177/026248930802700602.

[71] M.A. Rodriguez-Perez et al. "Mechanical Behaviour at Low Strains of LDPE Foams with Cell Sizes in the Microcellular Range: Advantages of Using These Materials in Structural Elements". en. In: *Cellular Polymers* 27.6 (Nov. 2008), pages 347–362. DOI: 10.1177/026248930802700602. URL: http://journals.sagepub.com/doi/10.1177/026248930802700602.

[72] K. C. Rusch. "Energy-absorbing characteristics of foamed polymers". en. In: *Journal of Applied Polymer Science* 14.6 (June 1970), pages 1433–1447. DOI: 10.1002/app.1970.070140603. URL: http://doi.wiley.com/10.1002/app.1970.070140603.

[73] E. Sadek and N. Fouad. "Finite element modeling of compression behavior of extruded polystyrene foam using X-ray tomography". en. In: *Journal of Cellular Plastics* 49.2 (Mar. 2013), pages 161–191. DOI: 10.1177/0021955X13477436. URL: http://journals.sagepub.com/doi/10.1177/0021955X13477436.

[74] C. Saiz-Arroyo et al. "Structure-property relationships of medium-density polypropylene foams: Structure-property relationships of medium-density PP foams". en. In: *Polymer International* 62.9 (Sept. 2013), pages 1324–1333. DOI: 10.1002/pi.4424. URL: http://doi.wiley.com/10.1002/pi.4424.

[75] M. Sauceau et al. "New challenges in polymer foaming: A review of extrusion processes assisted by supercritical carbon dioxide". en. In: *Progress in Polymer Science* 36.6 (June 2011), pages 749–766. DOI: 10.1016/j.progpolymsci.2010.12.004. URL: https://linkinghub.elsevier.com/retrieve/pii/S0079670010001280.

[76] T. Shepherd et al. "Validation of a Finite Element Modeling Process for Auxetic Structures under Impact". en. In: *physica status solidi (b)* 257.10 (Oct. 2020), page 1900197. DOI: 10.1002/

pssb.201900197. URL: https://onlinelibrary.wiley.com/doi/10.1002/pssb.201900197.

[77] A. Shi, G. Zhang, and C. Zhao. "Study of Rigid Cross-Linked PVC Foams with Heat Resistance". en. In: *Molecules* 17.12 (Dec. 2012), pages 14858–14869. DOI: 10.3390/molecules171214858. URL: http://www.mdpi.com/1420-3049/17/12/14858.

[78] M.J. Silva and L.J. Gibson. "The effects of non-periodic microstructure and defects on the compressive strength of two-dimensional cellular solids". en. In: *International Journal of Mechanical Sciences* 39.5 (May 1997), pages 549–563. DOI: 10.1016/S0020-7403(96)00065-3. URL: https://linkinghub.elsevier.com/retrieve/pii/S0020740396000653.

[79] C.W. Smith, J.N. Grima, and K.E. Evans. "A novel mechanism for generating auxetic behaviour in reticulated foams: missing rib foam model". en. In: *Acta Materialia* 48.17 (Nov. 2000), pages 4349–4356. DOI: 10.1016/S1359-6454(00)00269-X. URL: https://linkinghub.elsevier.com/retrieve/pii/S135964540000269X.

[80] L. Sorrentino, M. Aurilia, and S. Iannace. "A simple method to predict high strain rates mechanical behavior of low interconnected cell foams". en. In: *Polymer Testing* 26.7 (Oct. 2007), pages 878–885. DOI: 10.1016/j.polymertesting.2007.06.004. URL: https://linkinghub.elsevier.com/retrieve/pii/S0142941807000852.

[81] C. Soyarslan et al. "3D stochastic bicontinuous microstructures: Generation, topology and elasticity". en. In: *Acta Materialia* 149 (May 2018), pages 326–340. DOI: 10.1016/j.actamat.2018.01.005. URL: https://linkinghub.elsevier.com/retrieve/pii/S1359645418300363.

[82] R.M. Sullivan, L.J. Ghosn, and B.A. Lerch. "A general tetrakaidecahedron model for open-celled foams". en. In: *International Journal of Solids and Structures* 45.6 (Mar. 2008), pages 1754–1765. DOI: 10.1016/j.ijsolstr.2007.10.028. URL: https://linkinghub.elsevier.com/retrieve/pii/S0020768307004465.

[83] S. Tagliabue et al. "An image-based approach for structure investigation and 3D numerical modelling of polymeric foams". en. In: *Journal of Polymer Research* 28.3 (Mar. 2021), page 75. DOI: 10.1007/s10965-021-02438-9. URL: https://link.springer.com/10.1007/s10965-021-02438-9.

[84] S. Tagliabue et al. "Micro-CT based finite element models for elastic properties of glass–ceramic scaffolds". en. In: *Journal of the Mechanical Behavior of Biomedical Materials* 65 (Jan. 2017), pages 248–255. DOI: 10.1016/j.jmbbm.2016.08.020. URL: https://linkinghub.elsevier.com/retrieve/pii/S1751616116302806.

[85] N. Tang et al. "Mechanical performance of polystyrene foam (EPS): Experimental and numerical analysis". en. In: *Polymer Testing* 73 (Feb. 2019), pages 359–365. DOI: 10.1016/j.polymertesting.2018.12.001. URL: https://linkinghub.elsevier.com/retrieve/pii/S0142941818315046.

[86] C. Tekoglu et al. "Size effects in foams: Experiments and modeling". en. In: *Progress in Materials Science* 56.2 (Feb. 2011), pages 109–138. DOI: 10.1016/j.pmatsci.2010.06.001. URL: https://linkinghub.elsevier.com/retrieve/pii/S0079642510000393.

[87] T.A. Tervoort et al. "A Constitutive Equation for the Elasto-Viscoplastic Deformation of Glassy Polymers". en. In: (), page 23.

[88] M. Trofa, E. Di Maio, and P. Maffettone. "Multi-graded foams upon time-dependent exposition to blowing agent". en. In: *Chemical Engineering Journal* 362 (Apr. 2019), pages 812–817. DOI:

10.1016/j.cej.2019.01.077. URL: https://linkinghub.elsevier.com/retrieve/pii/S1385894719300841.

[89] G. Wang et al. "Lightweight and tough nanocellular PP/PTFE nanocomposite foams with defect-free surfaces obtained using in situ nanofibrillation and nanocellular injection molding". en. In: *Chemical Engineering Journal* 350 (Oct. 2018), pages 1–11. DOI: 10.1016/j.cej.2018.05.161. URL: https://linkinghub.elsevier.com/retrieve/pii/S1385894718309768.

[90] J. Wang and D. Chen. "Flexural properties and morphology of microcellular-insert injection molded all-polypropylene composite foams". en. In: *Composite Structures* 187 (Mar. 2018), pages 403–410. DOI: 10.1016/j.compstruct.2017.12.083. URL: https://linkinghub.elsevier.com/retrieve/pii/S0263822317319189.

[91] L. Wang et al. "Fabrication of lightweight microcellular foams in injection-molded polypropylene using the synergy of long-chain branches and crystal nucleating agents". en. In: *Polymer* 128 (Oct. 2017), pages 119–127. DOI: 10.1016/j.polymer.2017.09.025. URL: https://linkinghub.elsevier.com/retrieve/pii/S003238611730887X.

[92] J.G.F. Wismans et al. "Computed Tomography-based Modeling of Structured Polymers". en. In: *Journal of Cellular Plastics* 45.2 (Mar. 2009), pages 157–179. DOI: 10.1177/0021955X08100045.

[93] S. Wu et al. "Visualization observation of cells growth in low-density polyethylene foaming processes". en. In: *Polymer Testing* 63 (Oct. 2017), pages 367–374. DOI: 10.1016/j.polymertesting.2017.08.039. URL: https://linkinghub.elsevier.com/retrieve/pii/S0142941817304336.

[94] L.M. Yang and V.P.W. Shim. "A visco-hyperelastic constitutive description of elastomeric foam". en. In: *International Journal of Impact Engineering* 30.8-9 (Sept. 2004), pages 1099–1110.

DOI: 10.1016/j.ijimpeng.2004.03.011. URL: https://linkinghub.elsevier.com/retrieve/pii/S0734743X04000661.

[95] W. Zhai et al. "Heterogeneous nucleation uniformizing cell size distribution in microcellular nanocomposites foams". en. In: *Polymer* 47.21 (Oct. 2006), pages 7580–7589. DOI: 10.1016/j.polymer.2006.08.034. URL: https://linkinghub.elsevier.com/retrieve/pii/S003238610600989X.

[96] H.X. Zhu, J.R. Hobdell, and A.H. Windle. "Effects of cell irregularity on the elastic properties of open-cell foams". en. In: *Acta Materialia* 48.20 (Dec. 2000), pages 4893–4900. DOI: 10.1016/S1359-6454(00)00282-2. URL: https://linkinghub.elsevier.com/retrieve/pii/S1359645400002822.

[97] H.X. Zhu, J.F. Knott, and N.J. Mills. "Analysis of the elastic properties of open-cell foams with tetrakaidecahedral cells". en. In: *Journal of the Mechanics and Physics of Solids* 45.3 (Mar. 1997), pages 319–343. DOI: 10.1016/S0022-5096(96)00090-7. URL: https://linkinghub.elsevier.com/retrieve/pii/S0022509696000907.

[98] H.X. Zhu, S.M. Thorpe, and A.H. Windle. "The geometrical properties of irregular two-dimensional Voronoi tessellations". en. In: *Philosophical Magazine A* 81.12 (Dec. 2001), pages 2765–2783. DOI: 10.1080/01418610010032364. URL: http://www.tandfonline.com/doi/abs/10.1080/01418610010032364.

[99] H.X. Zhu and A.H. Windle. "Effects of cell irregularity on the high strain compression of open-cell foams". en. In: *Acta Materialia* 50.5 (Mar. 2002), pages 1041–1052. DOI: 10.1016/S1359-6454(01)00402-5. URL: https://linkinghub.elsevier.com/retrieve/pii/S1359645401004025.

[100] H.X. Zhu et al. "The effects of regularity on the geometrical properties of Voronoi tessellations". en. In: *Physica A: Statistical Mechanics and its Applications* 406 (July 2014), pages 42–58. DOI:

10.1016/j.physa.2014.03.012. URL: https://linkinghub.elsevier.com/retrieve/pii/S0378437114002064.

Chapter 3

Experimental characterization

In the following chapter the materials, the experimental techniques and related methods selected will be outlined. Basic correlations between macroscopic mechanical behaviour and morpho-structural characteristics will be presented and will serve as a basis for the analysis proposed in the next chapters. The results obtained using different experimental techniques will be used in future chapters to justify various numerical assumptions and hypothesis, and will be used as a fundamental tool to prove the validity and accuracy of the numerical models developed.

3.1 Materials

The expanded polymeric system selected is a commercially available closed-cell foam, mainly used as a core in sandwich panels for structural applications. The constituent material is polyethylene terephthalate (PET), a semi-crystalline thermoplastic polymer, and the foam was available in four different nominal densities. Samples were produced by *3A Composites* through extrusion foaming process and were supplied in the form of sheets of nominal dimensions $150\,x\,100\,x\,10$ mm. Table 3.1 lists the four materials together with their nominal densities and the codes with which they will appear in the present thesis.

Table 3.1: PET foam nominal densities.

Code	**Nominal apparent density** $[\mathrm{kg\,m^{-3}}]$
PET 80	80
PET 100	100
PET 130	130
PET 320	320

3.2 Experimental methods

A few experimental techniques were selected to characterize the physical properties of the foams and their constituent material. The latter was characterized through differential scanning calorimetry (DSC) to quantify its degree of crystallinity but no mechanical tests could be performed due to the difficulties, already outlined in chapter 2 section 2.3, to obtain suitable specimens without re-processing the material. The apparent density of the expanded material was measured using a gas pycnometer while mechanical tests were performed to sample the macroscopic mechanical behaviour of the selected materials.

3.2.1 Density

A gas pycnometer was selected as the most suitable experimental technique to measure the apparent densities of the material. The working principle of this technique is based on Boyle law for perfect gases in isothermal condition. The device consists of two chambers, the measuring and the reference one, both of known volume. The sample is introduced in the measurement chamber; the system is closed, pressurized, thermally equilibrated and consequently the measurement chamber equilibrates with the reference one. Measuring the difference in the equilibrium pressure between the two chambers allows to measure the volume of the sample and consequently the density once the sample mass is known [3].

The instrument used in this thesis was a *Pycnomatic ATC Thermo Scientific* gas pycnometer and the measurements were carried out following *ASTM D6226* standard as a guideline [1]. Three cubic specimens of 10 mm side length for each foam were prepared with a band saw. The samples size was reputed adequate since they had a sufficient number of cells to be representative of the overall material; moreover, the samples were cut randomly along the extruded sheet to increase the statistical validity of the results. Measurements were conducted in pure helium atmosphere (Helium 5.0, purity grade) at 23°C and at an equilibrium pressure of 2 kPa. The extra-small configuration, available on the instrument and corresponding to a measurement volume of 4 cm^3, was selected in order to improve accuracy. Three consecutive measurements were performed on each specimen.

3.2.2 Differential Scanning Calorimetry (DSC)

Differential scanning calorimetry (DSC) was performed to quantify the degree of crystallinity of the foam constituent polymer. The measurement was performed on a heat flux technology machine, *Mettler Toledo – DSC 3*. The technique consists in measuring the heat

difference required to maintain at the same temperature, under specific environment conditions, the crucible containing the sample and an empty reference one.

The measurements were performed in accordance with *ISO 11357-3* standard, taken as a guideline [2]. Two samples for each material, weighting between 5 and 10 mg, were heated under pure nitrogen atmosphere from 30 °C to 300 °C with a constant heating rate of 10 $^{\circ}\mathrm{C}\,\mathrm{min}^{-1}$. The crystallinity degree was computed by normalizing the measured melting enthalpy with respect to the theoretical value of a pure PET crystal (140 $\mathrm{J}\,\mathrm{g}^{-1}$) [4].

3.2.3 Uniaxial compression

The same samples geometry adopted for gas pycnometer measurements was adopted also for mechanical testing. Also in this case the volume tested is considered representative of the whole foam since enough cells are included. This hypothesis was confirmed by some preliminary tests performed on specimens of nominal dimensions $15\,x\,15\,x\,10$ mm and $20\,x\,20\,x\,10$ mm that gave results comparable with those of the selected geometry. Samples prepared with a band saw (*Proxxon 24260*) had their outer surfaces sanded to maximize surface planarity.

Mechanical tests were performed with an electromechanical dynamometer *Instron 1185R5800* equipped with a 10 kN load cell, under crosshead displacement control and parallel plates configuration. Tests were carried out in a controlled environment at 23 °C and 50 % of relative humidity. Tests were performed with two main objectives:

- Characterize the macroscopic mechanical response at large strain of the selected expanded material and identify the three characteristic regions highlighted in chapter 2 section 2.3.

- Once the elastic region had been identified, the apparent stiffness of the foams along the three main orthogonal directions of

the cubic specimen was measured with the aim of quantifying mechanical anisotropy.

For what concerns the first objective, tests were conducted up along the thickness of the sheets to a nominal strain of 50 %. Once the elastic region was identified subsequent tests were conducted up to 2 % strain, along the three orthogonal directions of each specimen. Three specimens per density were tested at 50 % of nominal strain and three more specimens where characterized in the elastic region with the protocol just described. All the mechanical tests were carried out at a quasi-static strain rate equal to 0.005 s^{-1} which corresponds to a nominal crosshead displacement of 3 $mm\,min^{-1}$. Moreover, crosshead displacement data were corrected according to machine compliance, independently measured with ad hoc tests performed with the same setup. In the specific case a stainless-steel bar, $30\,x\,30\,x\,80$ mm, was compressed in the same configuration and the machine compliance computed according to equation 3.1:

$$C_M = \frac{s_R}{F} - \frac{L_R}{(b_R\,d_R)\;E_R} \tag{3.1}$$

C_M is the compliance of the machine, s_R is the displacement, F is the force associated to each value of s_R, L_R is the initial distance between plates, b_R and d_R are the cross-section dimensions of the reference sample and E_R is the Young modulus of the reference material ($2.1 * 10^5$ MPa for stainless steel). It was also verified that compliance was constant within the whole force range.

3.3 Results and discussion

3.3.1 Density

Figure 3.1 displays the results obtained from gas pycnometer analysis; the plotted values of apparent measured densities ($\rho^*_{Measured}$) are corrected values according to the procedure suggested in *ASTM D6226* standard [1]. To consider the contribution of cells that were opened during sample preparation, the measured volume was compared with the apparent external one, measured with a parallel plate micrometre before gas pycnometer analysis was performed, and consequently the volume of closed cells that were opened was computed and the volume consequently corrected. Moreover, specimens were randomly taken around the sheets of material to increase the validity of the data obtained, since some inhomogeneities could be expected from an industrial product.

Irrespective of the applied correction, the measured apparent densities are systematically higher than nominal ones; the straight dashed line in figure 3.1 represents the ideal correspondence between nominal apparent density ($\rho^*_{Nominal}$) and the measured one. Obtained results are considered reliable for two main reasons: the first one arises from the very good reproducibility obtained for each material, displayed by the error bars which are smaller than the symbols used to plot mean measured values. The second reason lies in the fact that helium gas was used to improve the accuracy and sensibility of measurements; thanks to the very low dimensions of helium atoms (in the order of hundreds picometers), the smallest molecular atom gas used in this kind of measures, it is possible to detect any defect that is present in the sample under test (e.g. not perfectly closed cells which create a percolation path for the gas or some region that is not completely expanded during the foaming process). The explanation for the systematic discrepancy between nominal values of apparent densities and measured ones has to be researched in the internal microscopic structure that will be the

topic of next chapters, especially for sample PET 100 on which higher values than PET 130 were measured. In any case this tests already prove at this stage that the knowledge of the real internal structure is a crucial aspect in foam experimental characterization, as already extensively pointed out in chapter 2.

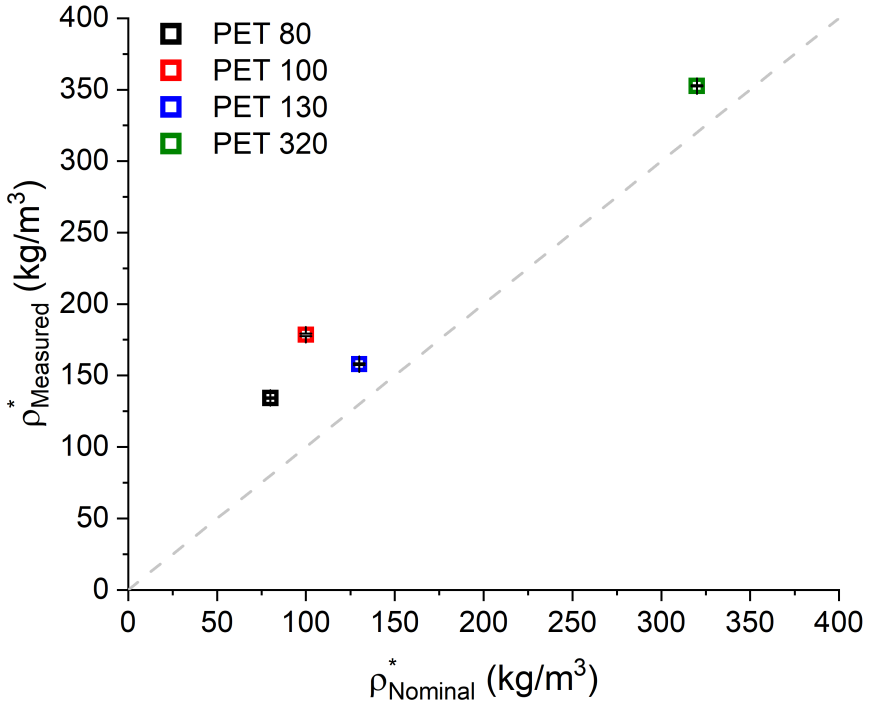

Figure 3.1: Gas pycnometer analysis results in terms of nominal density (x-axis) and measured apparent density (y-axis); the dashed line represents the ideal correspondence between the nominal value and the measured one.

3.3.2 Differential Scanning Calorimetry (DSC)

Figure 3.2 reports the results obtained through differential scanning calorimetry (DSC) whose aim was to estimate the degree of crystallinity of the constituent material (PET) as processed to give the foam samples under investigation.

On the left of figure 3.2, the thermogram obtained for the four materials is reported and an evident melting peak is detectable. The specific melting enthalpy was obtained from the area of the peak. Even if the sample mass is comprehensive of constituent material mass and trapped gas mass, the second term was considered negligible. The specific melting enthalpy of the four materials was the same proving the identical nature of the constituent bulk polymer (melting at 240 °C, which is a reasonable value for pure PET). The values were then converted in a crystallinity degree through the normalization with respect to the theoretical value of PET 100% crystallinity (140 $\mathrm{J\,g^{-1}}$) [4] and the results are shown on the right of figure 3.2. As can be seen the values are quite low, around 5%; error bars are not reported in the graph since the experimental dispersion was negligible. These results will allow in future chapter to consider, as a first approximation, the constituent material as almost completely amorphous. Moreover, the almost identical values obtained for the four PET materials strengthen the hypothesis that the characteristics of the foamed constituent material are the same, irrespective of the density.

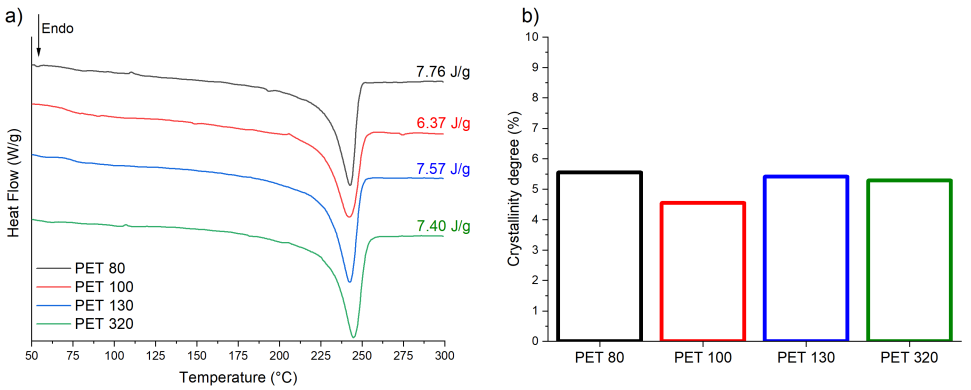

Figure 3.2: Differential scanning calorimetry results: a) thermograms measured for each material and specific melting enthalpy reported near each curve; b) crystallinity degree computed through the normalization of the specific enthalpy with respect to the reference value of 140 $\mathrm{J\,g^{-1}}$ [4].

3.3.3 Uniaxial compression

The results described in this paragraph will be presented in the form of nominal stress ($\sigma_{nominal}$) versus nominal strain ($\varepsilon_{nominal}$) plots. These two quantities were computed as follows: the stress by dividing the measured force by the cross-sectional original area of the untested specimen, while the strain was evaluated by dividing the machine displacement, corrected according to machine compliance, by the specimens' initial height.

The results of the first set of tests, conducted up to a nominal strain of 50 %, are displayed in figure 3.3 from which error bars are omitted for the sake of clarity. The stress versus strain plot clearly exemplifies the peculiar macroscopic compressive mechanical behaviour of expanded polymeric materials, already discussed in chapter 2 section 2.3. A quasi-linear elastic region is detectable in the range of nominal strain between 0 % and about $5 - 7$ %; this region is then followed by a plateau up to about 40 % nominal strain and for material PET 320 and PET 130 the onset of the subsequent densification region is also visible.

Following the identification of the elastic region a second set of tests was performed, along the three main orthogonal directions of each cubic specimen; relevant stress versus strain results are depicted in figure 3.4 as average curves, with a shaded area associated with the experimental semi-dispersion. In the graphs the orthogonal directions are identified as X, Y (direction orthogonal to the sheet plane) and Z.

From each test the apparent macroscopic stiffness (E^*) was computed by performing a linear fit of the stress versus strain curve in the range of strain between 0 % and 2 % and the results are summarized in figure 3.5. The results clearly highlight how the macroscopic mechanical response become more and more isotropic with the increase of apparent density. In particular is evident from figure 3.5 that PET 80 and PET 100 exhibit apparent stiffnesses which are statistically

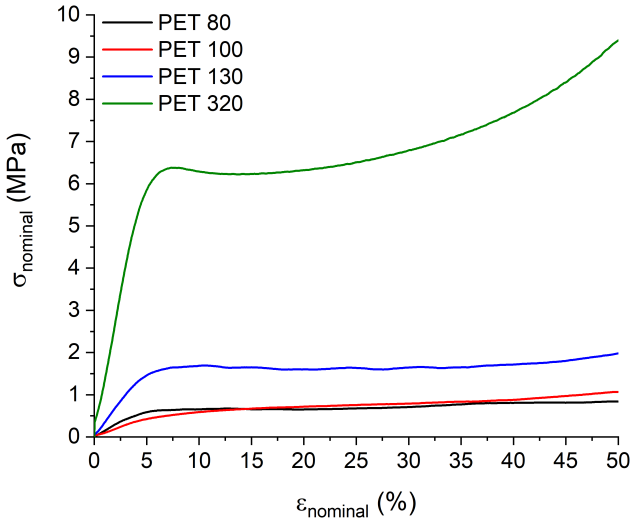

Figure 3.3: Nominal stress ($\sigma_{nominal}$) versus nominal strain ($\varepsilon_{nominal}$) graph representing the macroscopic compressive mechanical behaviour of the four expanded materials.

different along the three orthogonal directions while PET 130 and PET 320 exhibit apparent stiffnesses which are almost the same along the three directions. This observed phenomenon could be strictly correlated to the internal microstructure of the samples: increasing the apparent density the internal structure also becomes more isotropic and this is macroscopically exhibited in the mechanical response.

At last a basic correlation between the mean apparent stiffness ($E^*_{Mean} = \frac{E^*_X + E^*_Y + E^*_Z}{3}$) and the apparent measured densities ($\rho^*_{Nominal}$) is reported in figure 3.6. A clear expected dependence of the apparent stiffness on the density is obtained, but not enough points are present to define a specific trend. The graph simply wants to highlight once again the importance of microstructure inspection since its contribution, together with constituent material properties, is unavoidable in the study of expanded polymeric materials.

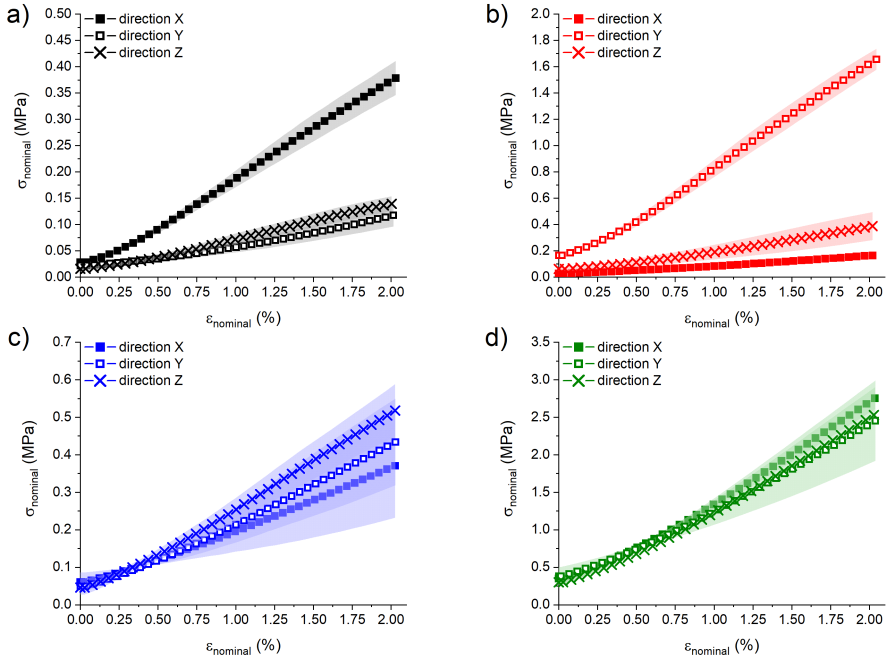

Figure 3.4: Mean nominal stress versus nominal strain for each orthogonal direction (X, Y and Z) of the tested cubic specimens. Values are reported for a) PET 80, b) PET 100, c) PET 130 and d) PET 320. **Note that different scales had to be used**.

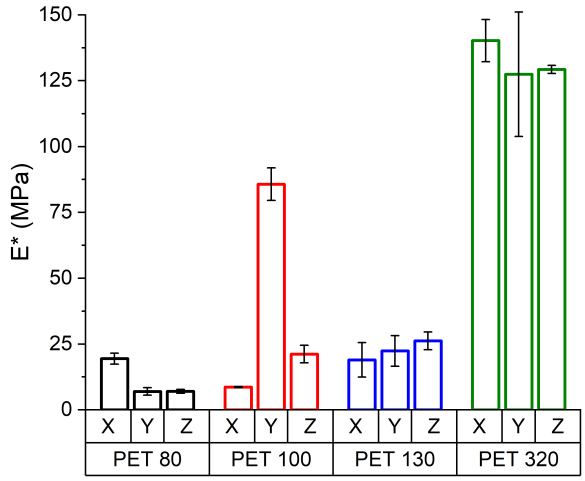

Figure 3.5: Apparent macroscopic stiffness (E^*) along three main orthogonal directions (X, Y and Z). Mean values and associated error bars are reported.

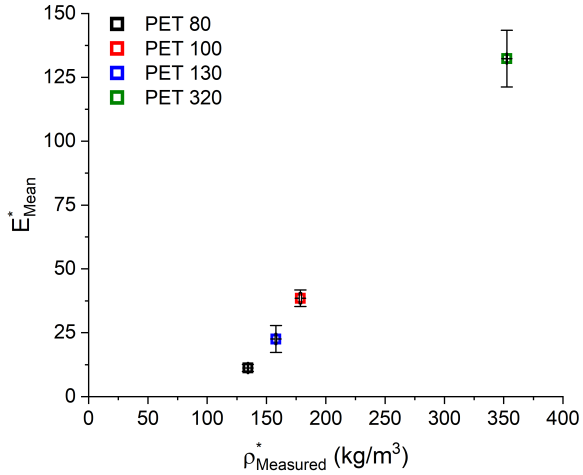

Figure 3.6: Apparent mean stiffness versus measured apparent density; mean values with error bars for both x and y axis are reported. X-error bars are smaller than the symbol representing mean values.

3.4 Concluding remarks

Experimental results presented in the present chapter will be extensively used in the following ones to support and validate numerical models developed along the research work, both in terms of numerical predictions and of the relationships between microstructure parameters and macroscopic mechanical behaviour that will be constructed.

Beside the aforementioned preamble, a preliminary methodological conclusion can be stated: experimental results, from gas pycnometer to mechanical tests, clearly prove the importance of inspecting the internal structure to fully understand the foams macroscopic behaviour, as widely reported in literature and extensively demonstrated in chapter 2. It is impossible to pretend to build any model, descriptive or predictive, on this particular class of material without having an insight on the structure to fully understand the synergistic effect between constituent material properties and structure itself which give rise to the measured macroscopic properties.

3.5 References

[1] D20 Committee. *Test Method for Open Cell Content of Rigid Cellular Plastics*. en. Technical report. ASTM International. DOI: 10.1520/D6226-21. URL: http://www.astm.org/cgi-bin/resolver.cgi?D6226-21.

[2] ISO Committee. *Plastics - Differential Scanning Calorimetry (DSC) - Part 3: Determination of temperature and enthalpy of melting and crystallization*. en. Technical report. ISO International.

[3] S. Tamari. "Optimum design of the constant-volume gas pycnometer for determining the volume of solid particles". en. In: *Measurement Science and Technology* 15.3 (Mar. 2004), pages 549–558. DOI: 10.1088/0957-0233/15/3/007. URL: https://iopscience.iop.org/article/10.1088/0957-0233/15/3/007.

[4] B. Wunderlich. "Thermal analysis of polymers". en. In: *THERMAL ANALYSIS OF POLYMERS* (1973), page 20.

Chapter 4

Structure analysis

In this chapter the main topic of structure investigation and its quantitative description is faced. The experimental methods and numerical algorithms adopted are described. For the sake of clarity, the chapter is structured in four main parts: in the first a brief overview on the most commonly used imaging techniques reported in scientific literature is given together with an extensive description of the physical principles behind the application of X-Ray computed tomography, the technique selected for structure analysis in the present thesis. The second part is focused on the theoretical aspects of the algorithms employed for structure investigation; images binarization algorithms will be considered together with the main tensorial algorithms employed for structure parameter quantification. In the third part, the materials together with experimental details will be presented and in the last part the main results on structure analysis, comprehensive of some comparisons between the different numerical algorithms, will be outlined. Results presented in this chapter will be widely exploited in the following ones when macroscopic mechanical properties and microstructure will be correlated.

4.1 Introduction

As already briefly pointed out in chapter 3, structure inspection is a crucial aspect in the field of expanded polymeric materials to fully understand the synergistic effect between structure itself and constituent material properties that gives rise to the already described macroscopic behaviour. Thanks to the development of new experimental techniques and related laboratory equipment, structure inspection has become more and more accessible and accurate.

The most commonly used imaging techniques reported in scientific literature can be grouped according to the dimensionality of the resulting images:

- *Bidimensional (2D) imaging techniques*: to this group mainly belong all the microscopical techniques, such as Scanning Electron Microscopy (SEM), optical microscopy (OM) and confocal microscopy (CM) [1]. The output is a bidimensional image reproducing a cross-section of the internal structure [42]. A couple of examples are reported in figures 4.1 and 4.2. The main advantage of this group of techniques is the relatively short time required for the acquisition of the images while the main drawbacks reside in the complexity of adequate sample preparation and the nature of the images themselves. Many authors report in their scientific works that using measurements taken from a bidimensional image to compute quantities representative of an intrinsic three-dimensional structure leads to a misleading interpretation of the real complexity of the structure itself and usually results in an overestimation of the macroscopic properties associated to a mechanical model, such as the ones reported in chapter 2 [19].

- *Three-dimensional (3D) imaging techniques*: the complex internal architecture can be investigated as a whole and reconstructed in three dimensions through the use of different available techniques, such as X-Ray computed tomography (CT) [52] [57], synchrotron

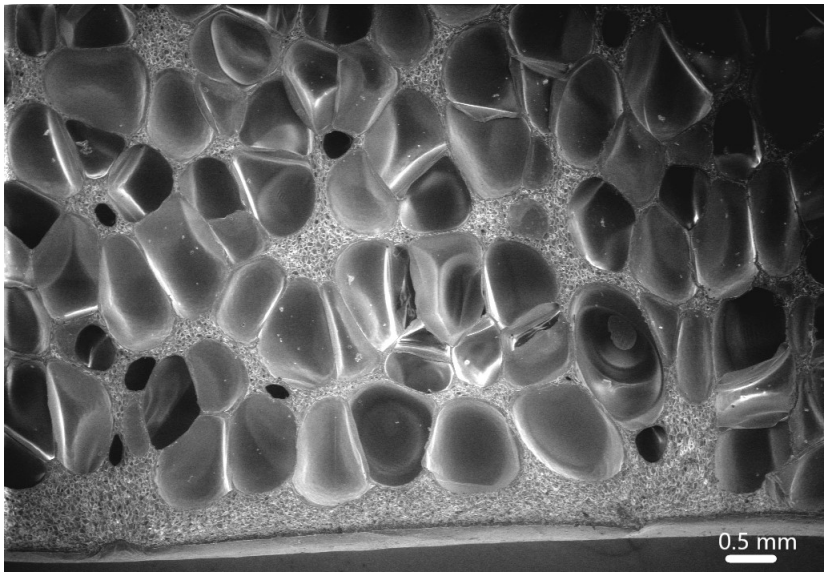

Figure 4.1: High resolution Scanning Electron Microscopy (SEM) image depicting the cross-section of an expanded polystyrene foam. Two different levels of the hierarchical internal structure are clearly detectable in the bidimensional image.

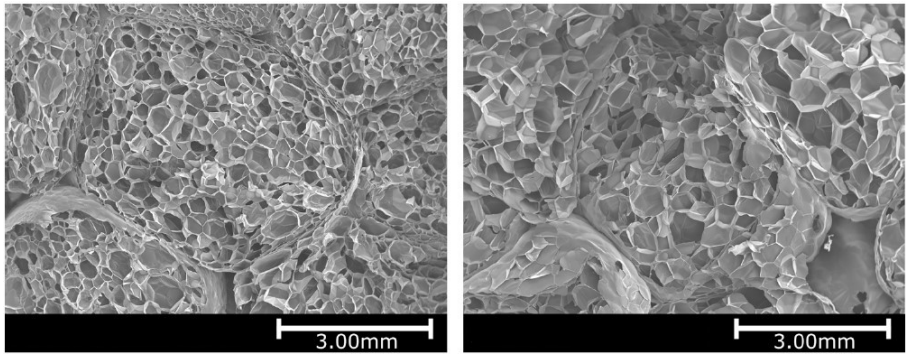

Figure 4.2: Low magnification Scanning Electron Microscopy (SEM) image depicting the cross-section of a sintered bead expanded polypropylene (PP) system. The complexity of the internal structure is clearly detectable but quantification of wall thickness would result in a wrong estimation of the real three-dimensional architecture. Image freely adapted from [36].

radiation tomography, magnetic resonance imaging (MRI) or solid-state nuclear magnetic resonance (ss-NMR) [13]. The main

advantages provided with this kind of inspection are the relatively simple sample preparation, the preservation of the integrity of the sample during the analysis and above all the possibility to obtain three-dimensional information representing the real internal architecture of the investigated samples [46]. The main drawbacks reside in the very long image acquisition time, the large amount of data generated at the end of analysis and the small volume inspected if a very high resolution is selected; for example, a resolution of a hundred nanometres can be achieved with conventional detectors on a total volume in the order of a few hundreds of micrometres using a synchrotron radiation tomography. Using this kind of imaging approach, it is mandatory to always look for a good compromise between desired resolution and total volume reconstructed, ensuring that the latter is large enough to represent the real material under test [16]. Figure 4.3 reports an example of the set of images obtained and the associated volume reconstruction [18].

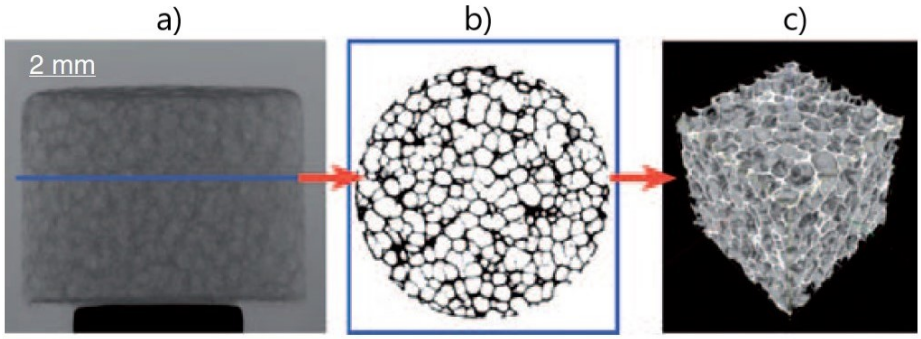

Figure 4.3: X-Ray computed tomography of an expanded polyvinylchloride (PVC) system: a) acquisition of the X-Ray projections along different planes that intersect the inspected volume; b) image reconstruction of the cross-section; c) three-dimensional volume reconstruction. Image freely adapted from [18].

Due to the motivations explained in the above paragraph, in this work a three-dimensional imaging technique was selected for structure

investigation, in the specific case X-Ray computed tomography as described in the experimental section. In the following paragraph a brief description of the physical principles behind this experimental technique, the most commonly used setup and the materials employed to realize the different components of a CT instrument will be provided.

4.2 X-Ray computed tomography (CT)

X-Ray computed tomography has been developed long after the discovery of X-Ray radiation, performed by Röntgen in 1895. The scientist obtained a picture of his own hand in which soft tissues were clearly distinguishable by hard tissues (bones). This fact led to the consequent investigation of material X-Ray attenuation and absorption properties. The first applications of this newly discovered phenomenon were all developed in medical field, due to the possibility of inspecting the inside of a human body without performing an invasive inspection.

New technologies and materials have allowed in the past twenty years the development of equipment at laboratory scale to perform the same inspection on material samples and products. Among the main fields of application in material science certainly belongs internal damage inspection, such as for defects in metals or in composite materials generated during production process [48]. Another field is the analysis of expanded materials: their complex and random internal three-dimensional structure can be inspected and reconstructed with very high precision in a non-destructive way [29]. Continuous improvement of available X-Ray sources and detectors has allowed the development of more and more accurate systems with increased resolution, down to a few microns for commercially available devices. Last generation nano computed tomography provide an even superior resolution in the order of a few hundred nanometres [58]; this high resolution was achievable, up to few years ago, only through synchrotron radiation, equivalent to X-Ray radiation but characterized by a very tiny source,

essential for minimizing penumbral blurring and maximizing spatial coherence for phase imaging [49].

4.2.1 Physical principle

The main physical principle on which the experimental technique is based is, as already written, the attenuation of X-Rays of wavelength, λ, through a homogeneous material, which is described by equation 4.1:

$$\frac{I}{I_0} = e^{-\mu x} \tag{4.1}$$

where I_0 is the intensity of the incoming X-Ray radiation, I is the intensity of the attenuated beam after crossing a homogeneous material of thickness x and characterized by a linear attenuation coefficient μ. Equation 4.1 can be rewritten in terms of material properties, in the specific case in terms of density, ρ:

$$\frac{I}{I_0} = e^{-\frac{\mu}{\rho}\rho x} \tag{4.2}$$

Equation 4.2 highlights the importance of specific attenuation coefficient, representative of the number of atoms encountered by the beam while passing through the material inspected. Moreover, writing the equation in a differential form:

$$\frac{dI}{I} = -\frac{\mu}{\rho}\,\rho\,dx \tag{4.3}$$

is clearly shown that the attenuation phenomenon is a space-dependent one, occurring progressively in each space interval dx crossed by the X-Ray beam. The minimum space increment in which the space can be divided is strictly dependent on the laboratory equipment used and on the specific material investigated and basically represents the spatial resolution of the acquired data. Writing the absorption equation in an integral form and explicitly writing the dependence of the specific

attenuating coefficient, μ_{sp}, on the spatial coordinate s, it is evident that summing up all the space increments of the attenuation along the direction of X-Ray propagation the attenuated intensity can be computed as follows:

$$I = I_0 \, e^{-\int \mu_{sp}(s) ds} \tag{4.4}$$

where $\mu_{sp}(s)$ is the specific linear absorption coefficient at position s along the projected ray $\mathbf{s}$. The crucial step that allows volume inspection and reconstruction is to assign the correct value of β to each position along the X-Ray and along all the other rays crossing the material, knowing only the values of the line integral for the various orientations of $\mathbf{s}$.

This reconstruction consists in locating and defining the different contributions to attenuation by measuring $\frac{I}{I_0}$ for many different X-Rays directions ($\mathbf{s}$) and many different positions for a given direction ($\mathbf{s}$). Acquiring a sufficient number of these matrices of values for a sufficient number of properly chosen directions ($\mathbf{s}$), graphically represented as a bidimensional image that reproduces an internal cross-section oriented in direction ($\mathbf{s}$) of the material, allowing the reconstruction of the volume through which the X-Rays traverse.

The above reported definition is usually summarized with the term projection. For each projections several samples are acquired and consequently different images are averaged to increase the signal noise ratio and obtain high-quality images representing cross-sections of the inspected material [49].

The number of samples per projection and the number of projections needed to reconstruct an inspected material or product strictly depend on the nature and geometry of the inspected sample itself and on the size of the features that are to be detected and resolved during the reconstruction [49].

4.2.2 Experimental apparatus

From a practical point of view the necessary equipment to perform the analysis can be summarized in the following three essential elements, also exemplified in figure 4.4 [9]:

- *X-Ray source*: usually also referred to as X-Ray tube, it contains a vacuum section wherein a filament is heated up to a specific temperature, called thermionic emission temperature, at which electrons are emitted. Through the application of an electrical potential between the filament, the cathode, and the target material, acting as the anode, electrons are accelerated and discharged on the target. Tungsten is commonly used for the filament due to its high atomic number. The interaction of the beam electrons with electrons and nuclei of the anode results in a characteristic bremsstrahlung emission of X-Rays, giving a continuous energy spectrum. The main drawback is that most of the energy is dissipated into thermal energy due to the interaction between cathode and anode electrons.

  The intensity of the X-Ray beam is directly related to the applied current which controls the number of released electrons. The applied electrical potential is commonly used as an indicator of X-Ray quality or, in other words, of the penetration capability of the electron beam with respect to the sampled material.

  New generation sources, for example solid-anode microfocus X-Ray tubes or metal-jet-anode microfocus X-Ray tubes, provide enhanced resolution, in the order of 1 µm, thanks to the optimization of the X-Ray beam focus [48].

- *Sample movement stage*: a mechanical platform that, depending on the system adopted, possesses different degree of freedom, usually rotation around an axis and translation along one or two directions orthogonal to the X-Ray direction. It allows an

accurate movement of the sample to collect different projections since another main aspect that strongly affects the efficiency of the measurement is the distance between X-Ray source and detector since X-Rays intensity is reduced proportionally to the reciprocal square of the distance travelled. Another crucial degree of freedom of the movement stage is the one that allows a fine positioning of the sample with respect to the source and the detector; this position directly determines the final voxel size (X_S), usually referred to as tomographic system resolution. This quantity strictly depends on detector pixel size (p_S) and on the desired level of magnification (M) as reported in equation 4.5:

$$X_S = \frac{p_S}{M} \tag{4.5}$$

- *X-Ray detector*: it is the component that collect X-Ray attenuated projections; generally, one- or two-dimension detector are employed, based on different semiconductor technologies: photodiode arrays, charge injection devices, charge coupled devices (CCD) and the recently introduced complementary metal-oxide semiconductor (CMOS) transistors technology. In general, the photons are not detected directly, but the array is coupled with an X-Ray sensitive media that scintillate when X-Ray photons are absorbed. Crucial aspects in detector construction are its sensitivity, the noise to signal ratio, its resolution and pixel size, which strictly determine the maximum resolution of the reconstructed final image [59].

The three main components can be arranged in many different experimental setups; the most commonly used in the scientific literature are depicted in figure 4.5; they can be summarized in four configurations:

- *Pencil beam systems*: they are usually called first generation systems; in this kind of setup a pinhole collimator from a point-like source generates a narrow, pencil-like beam, that scan the

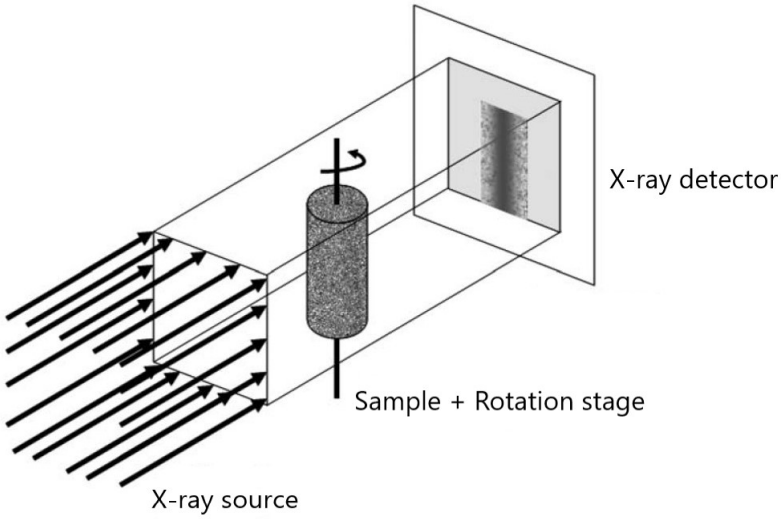

Figure 4.4: Schematic representation of the main components needed to perform an X-Ray computed tomography volume inspection and reconstruction. In the example reported the movement stage is a rotating stage and the source is a parallel beam configuration. Picture freely adapted from [9].

object in different projections thanks to the rotation stage that allows to acquire projections along different angle of the sample. Due to the zero-dimensional nature of the detector system, the movement stage also allows a horizontal or vertical translation in order to reconstruct different section of the inspected sample.

- *Fan beam systems*: this system only use a rotation movement apparatus; a flat fan of X-Ray beams is generated by a point-like source, passes through the object and the scatter shield and is collected by a one-dimensional detector system. These systems allow the collection of the entire view simultaneously.

- *Parallel beam systems*: in this case parallel X-Ray beams are generated by a bidimensional source and once the sample is crossed they are collected by a bidimensional detector. The main advantage of these systems is the possibility to collect straightforwardly and rapidly data for multiple slices, since the

projection of a single slice is completely independent from the other simultaneously acquired, due to the intrinsic nature of source and detector.

- *Cone beam systems*: is the equivalent three-dimensional system of the bidimensional fan beam; in this setup the X-Ray beams diverge from a point-like source, cross the sample and are collected by an area detector system. In this case each row of the detector, except for the central line, during a scan receives information from more than one projection and due to this overlapping set of information the reconstruction algorithm provides an approximation of the real inspected volume.

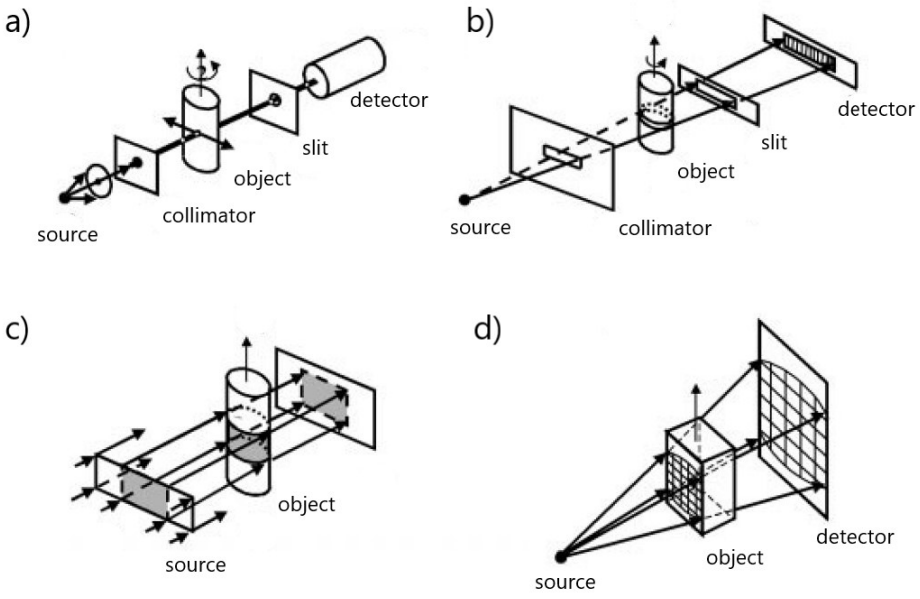

Figure 4.5: Schematic representation of the most used configurations commonly used during X-ray computed tomography acquisition experiment; a) pencil beam system, b) fan beam system, c) parallel beam system and d) cone beam system. Image freely adapted from [49].

4.3 Theoretical background

In this section the main theoretical background which is behind the development of the applied algorithms will be outlined starting with binarization algorithms, going through Hildebrand and Rüegsegger algorithm, applied to quantify the mean volumetric structure thickness of the inspected samples, and concluding with global and local algorithms implemented to quantify material spatial distribution in the volumes inspected as vectorial quantities.

4.3.1 Binarization algorithms

Binarization is a crucial and fundamental step that has to be faced every time the analogue output of an X-Ray computed tomography analysis, a set of grey-level images representing the structure, has to be analysed. It is widely reported in the literature that quantitative measurements performed on an image give more accurate results if the image is binarized, in other words converted from grey levels to an array of Boolean values, where 0 represents the background and 1 represents the solid material [61]. This process prevents uncertainty in the measurements deleting the so-called grey level transition region between background and inspected material [21]. Recently some authors developed algorithms that work directly on grey-level images, but some open challenges, above all the procedure to weight the measure performed in the transition region, still have to be overcome [41].

The selection of the proper binarization algorithm is fundamental since it affects all the subsequent quantitative measurements performed. The application of the wrong approach could lead to an artificial alteration of the real structure inspected. For this reason, many authors in literature proposed some experimental protocols as a guideline that help in the selection of the proper algorithm depending on the specific features of the image or set of images that have to be analysed [60] [54].

One of the main aspects that guides the choice of the most suit-

able binarization algorithm that has to be selected, is the grey-level histogram that can be computed for a bidimensional image or a set of images representing a volume. In general, the histograms that are obtained from set of images coming from X-Ray computed tomography analysis performed on expanded polymeric materials can be grouped in two main categories [29]:

- *Bimodal distribution*: the histogram is characterized by two peaks; one is centred around low grey-level values, representing background and noise, and the other is centred around high grey-level values, representing the material imaged. For this kind of distribution global binarization algorithms are usually preferred since are very efficient in computing the proper binarization threshold and are relatively cheap in terms of numerical resources, even when large amounts of data are analysed [39].

- *Monomodal distribution*: the histogram is characterized by a single peak, usually centred around low grey-level values, representing background and noise, and a large tail distributed around high grey-level values, representing the presence of material. In this case the so-called local methods are preferred, since the absence of a second peak could lead to the selection of an unsuitable threshold with global methods. Local methods are based on the evaluation of local gradient of grey-levels and consequently require longer time and greater numerical resources to be implemented when large amounts of data are analysed [37].

Figure 4.6 displays a qualitative example of the above-mentioned histogram classes.

In the following paragraphs the theoretical background of the two selected binarization algorithms will be outlined. In the specific case the Otsu algorithm, one of the gold-standard global methods widely applied in the field of image analysis, and the local Watershed algorithm method are described.

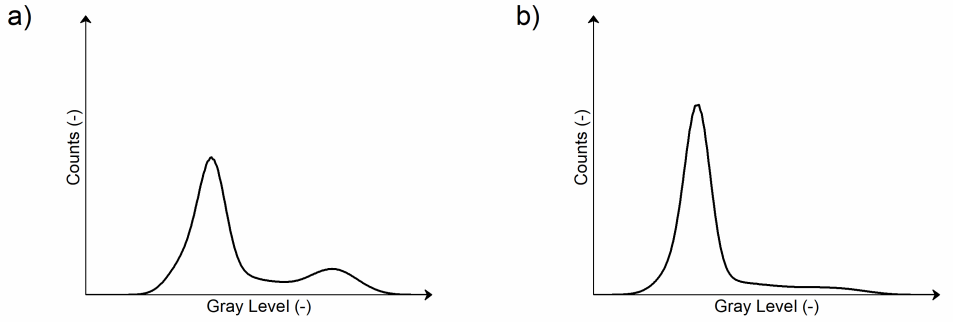

Figure 4.6: Qualitative examples of the two main classes of histogram usually obtained from set of images coming from X-ray computed tomography inspection of expanded polymeric materials; a) bimodal distribution and b) monomodal distribution.

Global method: Otsu algorithm

As already pointed out the algorithm is based on the analysis of the grey-level histogram of the image or set of images under the hypothesis that the grey-level distribution is represented by a bimodal histogram [39]. The objective of the algorithm is the research of a proper threshold that maximizes the separation of the two histogram peaks, as depicted in figure 4.7. With this analytical approach a clear distinction between pixels belonging to the solid material and the ones representing the background is obtained.

Assuming that the pixels of a given image can be represented by a certain grey-level, L, which is an integer number ranging from 1 to 2^n and n is the image depth in bits, the number of pixels corresponding to level i can be denoted as n_i and the total number of pixels N is directly computed as the summation of all the classes n_i. For the sake of simplicity, the histogram is considered normalized and regarded as a probability distribution, expressed with equation 4.6:

$$p_i = \frac{n_i}{N} \qquad \text{with} \quad p_i \geq 0 \quad \text{and} \quad \sum_{i=1}^{L} p_i = 1 \tag{4.6}$$

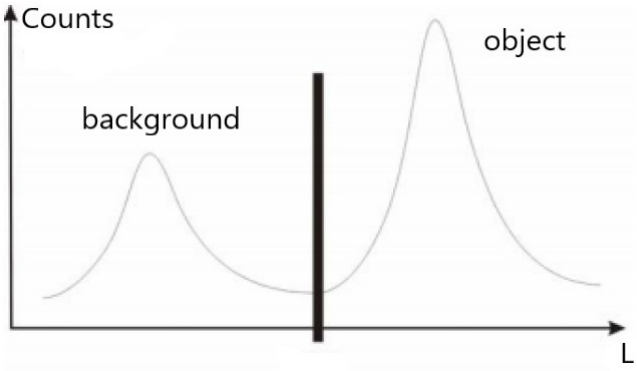

Figure 4.7: Optimal threshold that maximize the separation between the two peaks of the grey-level distribution deleting less pixel representing the object as possible. Image freely adapted from [23].

The classes of pixels are divided into two groups, called C_0 and C_1 (representing background and material respectively), by application of a threshold s: C_0 denotes all the pixels with levels $[1, \ldots, s]$ while C_1 denotes pixels with levels $[s+1, \ldots, L]$. The probability that a pixel belongs to one of these groups is:

$$P_0 = \sum_{j=1}^{s} p(j) \tag{4.7}$$

$$P_1 = \sum_{j=s+1}^{L} p(j) = 1 - P_0 \tag{4.8}$$

From the two probability distributions mean values (m_0 and m_1) can be computed with the associated class variances (σ_0^2 and σ_1^2):

$$m_0 = \sum_{j=1}^{s} j \, \frac{p(j)}{P_0}, \qquad m_1 = \sum_{j=s+1}^{L} j \, \frac{p(j)}{P_1} \tag{4.9}$$

$$\sigma_0^2 = \sum_{j=1}^{s} (j - m_0)^2 \, \frac{p(j)}{P_0}, \qquad \sigma_1^2 = \sum_{j=s+1}^{L} (j - m_1)^2 \, \frac{p(j)}{P_0} \tag{4.10}$$

The evaluation of the global mean grey value, wholly considering

the image, can be computed as follows:

$$m = P_0\, m_0 + P_1\, m_1 \quad \text{with statistical condition} \quad P_0 + P_1 = 1 \tag{4.11}$$

Once the two probability distributions are defined, thanks to the computation of the above described zeroth- and second-order cumulative moments, three additional variances can be computed:

$$\sigma_W^2 = P_0\, \sigma_0^2 + P_1\, \sigma_1^2 \tag{4.12}$$

$$\sigma_B^2 = P_0\, P_1\, (m_1 - m_0)^2 \tag{4.13}$$

$$\sigma_T^2 = \sum_{j=1}^{L} (j - m)^2\, p(j) \tag{4.14}$$

which represent the within-class variance, the between-class variance and the total variance of levels respectively. Once these quantities are computed, the problem is reduced to an optimization problem, searching for a threshold s which maximizes a suitable objective function $\eta(s)$, for example the one defined in equation 4.15:

$$\eta\,(s) = \frac{\sigma_B^2(s)}{\sigma_T^2} \tag{4.15}$$

In this case, the ideal threshold value is the one that maximizes the between-class variance: as the variance increases the two classes are better separated thus minimizing the within-class variance, used as an indication of the homogeneity of a single class alone; the lower this value gets, the more homogeneous the class is.

Once the optimal threshold is determined, the correct assignment of each pixel to the correct class can be performed and the actual binarization process take place. All the pixels belonging to the *"Object class"* will be converted in a Boolean value equal to 1 and the others into a 0 value.

Local method: Watershed algorithm

The local algorithm selected is based on functional watershed applied to a continuous function defined by Schmitt in 1994. Up to his publication the watershed concept was strictly applied only to morphological segmentation, hence in a discrete form, and there was no theoretical background for continuous functions. His analytical formulation allowed the development of newer and more efficient algorithms for image analysis. The complete analytical set of equations and related demonstration is not reported, since it is beyond the scope of the present work, but references could address interested readers to the complete works [37].

The general concept on which the algorithm is based relies on considering an image as a topographical surface; this is achieved by considering the grey-level of a pixel (pixel intensity) as an altitude. Once the topographical profile is drawn, places of high variation in the pixel intensity values are the starting points for contour research, for example boundaries between background and material or between two different material phases. The variation is then computed through the evaluation of local grey-level gradient. The consequent research of the so-called crest lines of the gradient image could be performed through the application of watershed transform itself. The basic watershed idea is to attribute an influence zone to each of the regional minima of an image, or in other words in finding a connected plateau from which it is possible to reach a point of lower grey level by an always descending path. The watershed is consequently defined as the boundaries of these influence zones. The idea can be easily explained with a one-dimensional example; the steps that are needed to construct the watershed are as follows:

1. Regional minima of the imaged surface are detected.

2. Image is imaginarily immersed into a lake and so the water progressively floods the basins corresponding to the various minima;

to prevent the merging of two different water zones, coming from different minima, some virtual dams are constructed.

3. Once the image is virtually totally immersed in water and all the dams, corresponding to local minima are built, the watershed transform of the image is built.

In the case of one-dimensional example, the watershed profile is determined in a straightforward manner, while the situation is more complicate for bidimensional images, even if the basic idea of water and dams is preserved. Figure 4.8 provide a visualization of the waterflood process in the case of a bidimensional example. In 2D some attention has to be payed to the plateau regions of the image (iso-level curves in topographical notation); to avoid possible errors coming from these regions, different solutions are proposed in literature, among which the most common ones employed and implemented in commercial algorithms are based on second order partial derivatives or on the study of local Hessian matrix that discriminate local minima from other characteristic points, such as saddle points, typical of bidimensional functions.

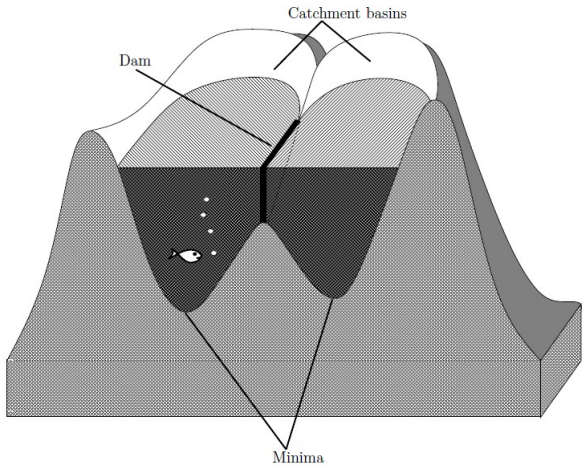

Figure 4.8: Graphical qualitative example of watershed construction in bidimensional case. Image freely adapted from [37].

The main challenge of bidimensional images is the unique determination of the watershed image profile, in other words the profile defined by the virtual constructed basins. Schmitt proved that this problem "simply" reduces to the solution of the eikonal equation, in which f is an analytical function that describe the perimeter of the catchment basin and g is the function that satisfies the research of minima, once again a continuous function:

$$\text{finding } f \text{ such as } \|\nabla f\| = g \tag{4.16}$$

This equation is numerically solved through the application of different numerical solutions developed in the past 20 years. The main approaches, widely used in computer graphics, are:

- *Watershed by flooding*: the above-mentioned main and first approach developed [3].
- *Watershed by topographic distance*: it is based on the image of a drop of water falling on a topographic relief that proceeds towards the nearest minimum following the steepest descent path.
- *Inter-pixel watershed*: in which a discrete research of local minima is proposed implementing the integral concept of Lebesgue [5].
- *Topological watershed*: based on the analytically demonstrated theorem that states that a function W is a watershed of another function F if and only if $W \leq F$ and W preserves the contrast between the regional minima of F [4] [11].
- *Meyer's flooding watershed algorithm*: suitably developed and optimized for very large data analysis [3] [2].
- *Optimal spanning forest algorithms*: also called watershed cuts, provide an optimization and co-implementation of the ideas at the basis of watershed by flooding and topographic distance [12].

Besides the large number of numerical solutions proposed by different authors to solve the eikonal equation, the main advantage of applying the local algorithm is its independence on the bimodal nature of the image histogram. Conversely, due to the large number of calculations required to numerically solve the eikonal equation on a large set of images or a very high-resolution single image, it requires longer time and greater numerical resources with respect to global methods.

4.3.2 Hildebrand and Rüegsegger algorithm

In 1997 Hildebrand and Rüegsegger proposed an algorithm, that has become in the last 20 years one of the gold-standard methods, to compute the average volumetric thickness of structures starting from a three-dimensional set of images. The main advantage and novelty of the proposed algorithm resides in its complete independence on the nature of the system or material imaged; it depends only on the image quality and resolution. In their work the authors also demonstrated the greater accuracy of measurements performed on three-dimensional image sets with respect to those performed on lower dimension images and then extrapolated in 3D space [22].

The system-independent algorithm assumes that for primitive geometrical objects, such as plates, cylinders and spheres, the mean volumetric thickness is uniquely defined by geometrical considerations. For generic structures the fundamental element required is a well-defined weighting of the mean value, that ensures the existence of a unique mean value for objects characterized by a varying structure thickness. To fulfil these requirements the authors proposed a new definition of local structure thickness; considering $\Omega \subset R^3$, where Ω is the set of all points of the spatial structure under investigation, and $\mathbf{p} \in \Omega$ an arbitrary point of the structure, the local thickness, $\tau(\mathbf{p})$, can be defined as the diameter of the largest sphere which contains the point, $\mathbf{p}$, and

which is completely inside the structure:

$$\tau(\mathbf{p}) = 2 \max\left(\{r \mid \mathbf{p} \in sph(\mathbf{x}, r) \subseteq \Omega, \mathbf{x} \in \Omega\}\right) \tag{4.17}$$

in which $sph(\mathbf{x}, r)$ is a set of points inside a sphere with centre $\mathbf{x}$ (position vector) and radius r.

Figure 4.9 displays a graphical representation of the requirement expressed by equation 4.17.

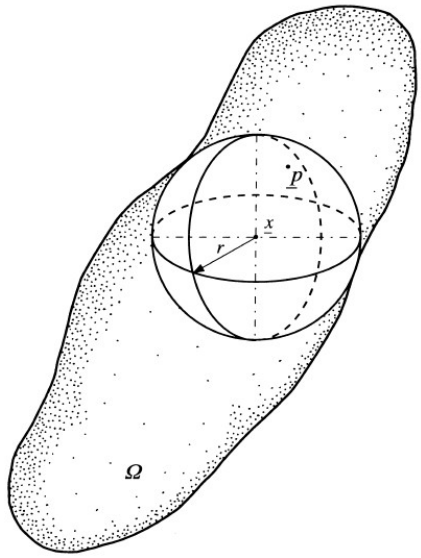

Figure 4.9: Local thickness of a generic structure, Ω, determined by fitting maximal spheres to the structure. Picture freely adapted from [22].

Since the local thickness is defined for each point of the three-dimensional structure, from here on called volume-based local thickness, the arithmetic mean value of the local thickness over all the points belonging to the inspected structure can be defined as:

$$\langle \boldsymbol{\tau} \rangle = \frac{1}{Vol(\Omega)} \iiint_{\Omega} \boldsymbol{\tau}\,(\mathbf{x})\; d^3\mathbf{x} \quad with \quad Vol\,(\Omega) = \iiint_{\Omega} d^3\mathbf{x} \tag{4.18}$$

and the maximum local thickness can be defined with an equation similar to 4.18. The same quantities can be computed through a

different approach that considers local thickness distribution from a probabilistic distribution point of view, but is not reported here since beyond the scope of this thesis; interested readers are addressed to the scientific literature listed in the references section [22] [25].

Besides the continuous formulation, that assumes the presence of a continuous closed domain Ω, a discrete form was also proposed by the authors with the aim of converting the continuous formulation into numerical algorithms, applicable to discrete systems such as the set of images obtained from X-Ray computed tomography where the hypothesis of continuity of the structure is not always verified and the 3D volume is described by a set of discrete voxels. The key is the conversion of the continuous expression given in equation 4.17 into a different form, as a function of structure distance map, D_{map}. Distance map is calculated by the distance transformation [17], assigning to every point in the structure the Euclidean distance from that point to the nearest background point; this is a discrete formulation of the radius of the sphere described previously. Distance transformations is defined, with a similar structure and quantities with respect to equation 4.19, as:

$$D_{map}(\mathbf{q}) = \max\left(\{r > 0 \mid sph(\mathbf{q}, r) \subseteq \Omega, \mathbf{q} \in \Omega\}\right) \tag{4.19}$$

Consequently, the local thickness can be rewritten as:

$$\tau\left(\mathbf{p}\right) = 2 \max_{\mathbf{q} \in X(\mathbf{p})} \left(D_{map}\left(\mathbf{q}\right)\right) \tag{4.20}$$

where $X(\mathbf{p})$ represents the centre points of all the spheres with a radius equal to their corresponding distance value and including the point $\mathbf{p}$:

$$X\left(\mathbf{p}\right) = \{\mathbf{x} \in \Omega \mid \mathbf{p} \in sph\left(\mathbf{x}, D_{map}\left(\mathbf{x}\right)\right)\} \tag{4.21}$$

The calculation of the local thickness is thereby split in two consequent steps:

1. Calculation of the distance map, which can be carried out effi-

ciently on discrete data since the fitting of spheres in one point is independent from the neighbouring ones and so the procedure is suitable for parallel processing.

2. Evaluation of the distance ridge as the set of the centre points of all nonredundant spheres; this step can be efficiently performed by numerical methods with local inclusion tests only for neighbouring voxels.

The efficiency of the proposed algorithm, when applied to discrete systems, intrinsically depends on image resolution and implicitly has a sensitivity equal to the voxel side dimension. Poor image quality, affected by noise, can lead to underestimation of the true imaged local thickness.

4.3.3 Fabric tensor evaluation algorithms

The general definition of a fabric tensor unifies all the algorithms developed in the past years that aim at modelling through tensors both anisotropy and orientation of an inspected material [35]. The main fields in which these algorithms were developed are biomedical engineering and medicine, mainly to determine the internal structure dimensions and orientation of trabecular bone [24]. Fabric tensors are generally considered as semi-global measurements in the sense that they are computed in relatively large neighbourhoods, considered as quasi-homogeneous domains [10] [27]. These algorithms were successfully applied in the past years also in other fields, such as material science and geology. In general, also for this fields of application, it has been shown that microstructural architecture of most materials can be accurately modelled by means of second-order tensors [28].

These algorithms are generally divided into two main groups:

- *Mechanics-based methods*: the fabric tensor is indirectly determined from mechanical properties; in other words, first the tensor

that describes the mechanical behaviour is determined and then the fabric tensor is built up from an analytical set of equations [43]. This approach usually involves different approximations and numerical challenges [40], since it is not easy to experimentally identify the constitutive matrix of a material [33].

- *Morphology-based methods*: the fabric tensor is directly computed from the morphology of the internal material structure. This approach is generally less severe from a computational point of view with respect to the previous one; moreover, the resulting fabric tensors are not dependent on numerical simulations parameters, such as boundary conditions or homogenization schemes. Conversely, the results of mechanical simulations have to be correlated in a second step to the generated fabric tensors [6].

In addition, morphology-based methods are generally classified in sub-groups according to the approach adopted to analyse images in order to quantify the fabric tensor:

- *Boundary-based methods*: these algorithms exploit the interface between phases of the inspected material to estimate fabric tensors. The most famous approaches belonging to this category are Mean Intercept Length (MIL) [34] [35] and Global Gradient Structure Tensor (GST) [32] [51]. The main limitation of these methods consists in the strict dependence of anisotropy on the interface of material phases and the result is greatly affected by the regularity of the analysed structure; if the inspected set of images represent a completely regular structure the algorithm is not able to identify with great accuracy the principal direction of material distribution.

- *Volume-based methods*: this approach aims at overcoming the main limitation of boundary-based methods. The anisotropy is computed from measures directly performed inside one of the

phases. The idea is similar to the Hildebrand and Rüegsegger algorithm presented in the previous paragraph [38]. The most commonly used algorithms are Star Volume Distribution (SVD), Star Length Distribution (SLD) and Sampling Sphere Orientation Distribution (SSOD) [45].

- *Texture-based methods*: these methods exploit texture analysis tools to compute the fabric tensors. Among different algorithms, for example, Fractal Dimension (FD) [30] models are based on the hypothesis that the volume investigated is built on a fractal, or auto similar, structure, and involve directional measurements of fractal characteristic dimensions to create orientation distributions which afterwards are approximated through tensors. Another widely applied algorithm is the spatial Autocorrelation Function (ACF) [56] that is directly applied on grey-scale level images, measuring directional texture features (e.g. the voids in expanded polymeric materials) to build the fabric tensor [32]. The main assumption in this kind of approach is that the inspected structure is quasi-regular, from a mathematical point of view.

- *Alternative methods*: a recently developed group of algorithms describes from a polar point of view the structure inspected, evaluating polar moments [44] that describe the structure and other features present in the inspected samples [26] (e.g. voids in the case of expanded polymeric materials [47] or short glass fibres in the case of composite materials [53]) [8].

In the present work two algorithms have been selected: Mean Intercept Length (MIL), which is considered the gold-standard algorithm in the field of image analysis and fabric tensor computation, and spatial Autocorrelation Function (ACF). The choice of two algorithms taken from different groups has the objective of comparing and validating the results coming from approaches based on different assumptions when applied to expanded polymeric materials, to provide a more robust

analysis. Moreover, the validity of the ACF approach is still openly questioned in the literature and so its use in the present study has also the aim of investigating its validity in comparison with the reference MIL algorithm [50].

In the following paragraphs the two selected algorithms will be described in detail for what concerns their theoretical formulation; for the MIL algorithm the generalized formulation proposed by Moreno and co-authors is considered [34], while for spatial autocorrelation function the formulation proposed by Wald is reported [56]. Readers interested in other algorithms can refer to the referenced works listed at the end of this chapter.

Mean Intercept Length (MIL)

As previously mentioned Mean Intercept Length (MIL) belongs to the sub-group of boundary-based algorithms, in which the interface between phases of the inspected material is used to estimate the fabric tensor [34].

Generally speaking MIL is defined with respect to a particular orientation as the mean distance between a change from one phase to the other along that direction; this value is inversely proportional to the number of intercepts between a set of parallel lines and the interfaces between phases. A bidimensional representation is reported in figure 4.10.

The classical procedure to compute MIL consist of different steps:

1. A family of lines parallel to a specified direction, $\mathbf{v}$, are traced, with $\mathbf{v}$ being a unitary vector;

2. The number of intersections, $C(\mathbf{v})$, between the lines and the interface between the two phases is counted;

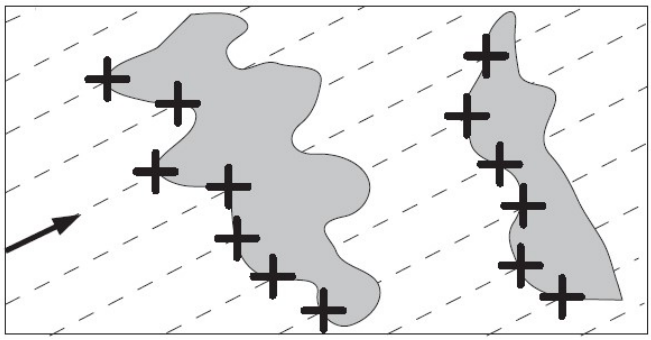

Figure 4.10: Example of a bidimensional computation of intercepts between a set of parallel lines and the interface between phases. Image freely adapted from [34].

3. The MIL with respect to $\mathbf{v}$, $MIL(\mathbf{v})$, can be computed as:

$$MIL\,(\mathbf{v}) = \frac{h}{C(\mathbf{v})} \tag{4.22}$$

where h is the summation of the length of all traced lines.

The MIL evaluated along different $\mathbf{v}$ can be plotted in a so-called rose-diagram which usually give an ellipse-like shape for the majority of materials. It is then possible to estimate with small errors the characteristic dimensions of such an ellipse with any fitting algorithm, for example least-squares fitting. In 2D images, thanks to the duality between ellipses centred at the origin and positive semidefinite second-order tensors, the MIL tensor, **MIL**, can be computed as the $2\,x\,2$ matrix that represents the estimated ellipse. The same procedure can be extended to set of images that represent three-dimensional structures, with a greater computational effort; in the 3D case the MIL for different orientations has to be fitted to an ellipsoid and the results can be used to compute the $3\,x\,3$ matrix that represents such an ellipsoid.

Besides its classical formulation the MIL definition can be extended to a more general closed one. The generalization is built on 2D images. Considering the situation reported in figure 4.11, which shows a squared region of interest where the interface between phases is represented

by a line, l, with an associated unitary normal, $\mathbf{u}$; the dashed lines represent a specific direction, $\mathbf{v}$, and are separated from one another by a certain distance, ϵ. It is possible to show that:

$$C(\mathbf{v}) = \frac{l}{v}\, t(\mathbf{v}, -\mathbf{u}) \tag{4.23}$$

where t is usually referred to as half-cosine function. In general, $C(\mathbf{v}) \neq C(-\mathbf{v})$, since only bright to dark interfaces, or vice versa, are considered.

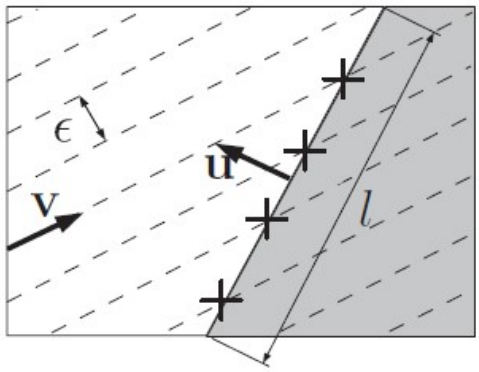

Figure 4.11: Graphical example of MIL computation for a linear interface, length l and normal $\mathbf{u}$, between phases. Separation between testing lines parallel to $\mathbf{v}$ is denoted with ϵ. Figure freely adapted from [34].

For sufficiently small values of ϵ, the results reported in equation 4.23 can be generalized to any shape of interface between phases:

$$C(\mathbf{v}) = \frac{1}{\epsilon} \int_L t(\mathbf{v}, -\mathbf{s})\, dL \tag{4.24}$$

in which L is the perimeter of the interface between phases and $\mathbf{s}$ is the normal at every point of the interface. The equation can be rewritten in a different form:

$$C(\mathbf{v}) = \frac{1}{\epsilon} \int_L \int_0^{2\pi} t(\mathbf{v}, -\mathbf{u}_\theta)\, \delta(-\mathbf{u}_\theta, -\mathbf{s})\, d\theta dL \tag{4.25}$$

where δ is the unit impulse function and $\mathbf{u}_\theta = (\cos\theta\ \sin\theta)^T$. The

integral can be simplified with the application of the Extended Gaussian Image (EGI). The EGI at a specific direction $\mathbf{u}_\theta, G(\mathbf{u}_\theta)$, is given by:

$$G\left(\mathbf{u}_\theta\right) = \int_L \delta(\mathbf{u}_\theta, -\mathbf{s})\, dL \tag{4.26}$$

and consequently, equation 4.26 can be rewritten, substituting EGI:

$$C\left(\mathbf{v}\right) = \frac{1}{\epsilon}\int_0^{2\pi} t\left(\mathbf{v}, -\mathbf{u}_\theta\right) G\left(-\mathbf{u}_\theta\right)\, d\theta \tag{4.27}$$

The last equation shows that C is equivalent to the angular convolution between the mirrored EGI and the smoothing half-cosine kernel t and so can be used to estimate the MIL tensor:

$$\mathbf{MIL} = \omega \int_0^{2\pi} \frac{\mathbf{v}_\theta \mathbf{v}_\theta^T}{C(\mathbf{v}_\theta)^2}\, d\theta \tag{4.28}$$

where $\mathbf{v}_\theta = (\cos\theta\ \sin\theta)^T$ and ω is a constant. This is an alternative expression, with respect to classical definition that considers the ellipse fitting procedure; this alternative is valid since the **MIL** is proportional to the covariance matrix. Equation 4.28 proves once again that **MIL** is inversely proportional to $C(\mathbf{v}_\theta)$. One important thing to notice is that **MIL** can be computed only if $C(\mathbf{v}_\theta) > 0$, but this is ensured if L is a set of closed contours.

The generalized closed formulation can be extended to the three-dimensional case:

$$C\left(\mathbf{v}\right) = \frac{1}{\epsilon^2}\int_\Omega t\left(\mathbf{v}, -\mathbf{s}\right)\, d\Omega \tag{4.29}$$

in which Ω is the interface surface between phases. Applying a similar procedure to the 2D case, the final expression for **MIL** computation is:

$$\mathbf{MIL} = \omega \int_0^{\pi}\int_0^{2\pi} \frac{\mathbf{v}_{\theta,\phi}\mathbf{v}_{\theta,\phi}^T}{C(\mathbf{v}_{\theta,\phi})^2} \sin\left(\phi\right) d\theta d\phi \tag{4.30}$$

with $\mathbf{v}_{\theta,\phi}$ a vector in the unitary sphere given in spherical coordinates and $\sin\left(\phi\right) d\theta d\phi$ the surface element of the unitary sphere in spherical

coordinates.

Once the closed formulation is stated, the correspondence between the covariance matrix and the ellipsoid is also demonstrated; hence there is a strict correspondence between the axis lengths of the ellipsoid and the eigenvalues of the covariance matrix, used to determine ellipsoid orientation. With this correspondence is it possible to compute a scalar quantity representing the degree of structural anisotropy (DA):

$$DA = \frac{\lambda_{max}}{\lambda_{min}} \tag{4.31}$$

or alternatively

$$DA = 1 - \frac{\lambda_{min}}{\lambda_{max}} \tag{4.32}$$

so, in this case DA assumes value raging from 0, isotropic material distribution (isotropic structure), and 1, anisotropic material distribution (anisotropic structure).

In both equations 4.31 and 4.32 λ_i represent the eigenvalues of the covariance matrix.

Autocorrelation function (ACF)

The Autocorrelation function (ACF) method belongs to the so-called texture-based ones and it exploits a texture pattern, present in the set of images obtained during material inspection, to determine spatial material distribution and anisotropy. When applied to expanded polymeric materials the texture feature selected is the voids distribution. This can be done under the hypothesis that the inspected sample possesses a quasi-regular structure that can be described through a suitable fabric tensor [56].

Given a profile $\rho_{\theta,\varphi,c}$ along direction $[\theta, \varphi]$ and centred at the point c, and a shift length $\Delta r \in R$, the spatial autocorrelation function is a statistical measure of the profile's reappearance at a distance Δr along $[\theta, \varphi]$. For example, the one-dimensional spatial function is defined as

the convolution of $\rho_{\theta,\varphi,c}$ with its mirrored complex conjugate, $\rho^*_{\theta,\varphi,c}$:

$$ACF\,(\Delta r) = \left\langle \rho_{\theta,\varphi,c}\ \rho_{\theta,\varphi,c+\Delta r} \right\rangle = \int_{-\infty}^{+\infty} \rho^*_{\theta,\varphi,c}\ \rho_{\theta,\varphi,c+\Delta r}\, dr \qquad (4.33)$$

Since the operation of autocorrelation returns only the power information it is possible to prove that the operation is nonlinear and irreversible. Moreover, if $\rho_{\theta,\varphi,c}$ is a real function, then $ACF(\Delta r)$ is symmetric and also real, which is the case of real intensity images. An example of computation of 1D spatial autocorrelation function is reported in figure 4.12.

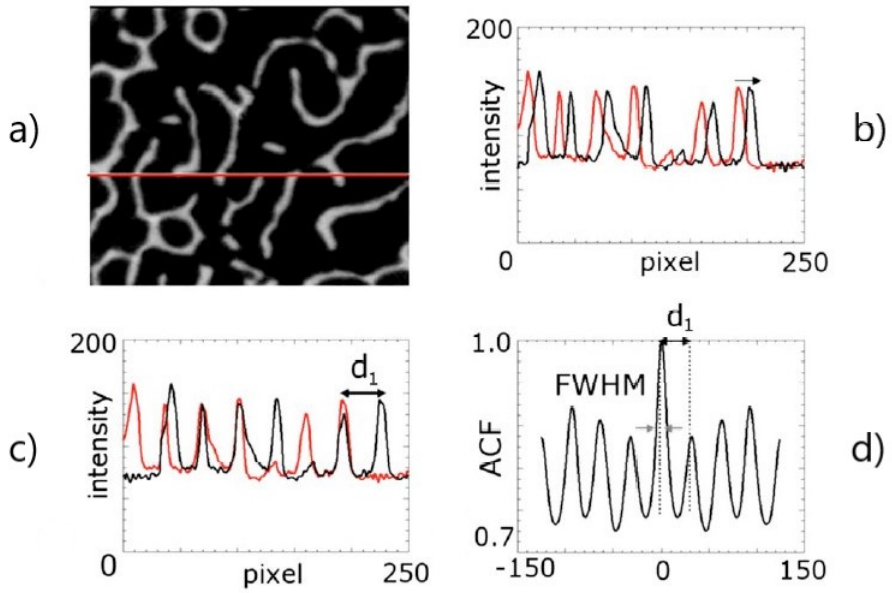

Figure 4.12: Example of 1D spatial autocorrelation function computation along a generic test line; a) image slice from an X-Ray computed tomography analysis of trabecular bone with a generic test line reported in red, b) original intensity function ($\rho_{\theta,\varphi,c}$, in red) and its shifted counterpart ($\rho_{\theta,\varphi,c+\Delta r}$, in black), c) maxima overlap of the two intensity functions at a certain shift length d_1 and d) Autocorrelation function. Figure freely adapted from [56].

The one-dimensional expression reported in equation 4.33 can be

extended to any higher dimensions performing the integration over the entire domain of the input function; area in the case of 2D and volume for 3D. In the case of a multidimensional function, the shift direction becomes a vector, $\boldsymbol{\Delta r}$. In the case of three-dimensional functions, the shift vector $\boldsymbol{\Delta r} = [\Delta x, \Delta y, \Delta z] = \boldsymbol{i}_{\theta,\varphi}\, \Delta r$ is defined by the Cartesian vector or the unit vector $\boldsymbol{i}_{\theta,\varphi}$ and magnitude Δr. The ACF function can be consequently denoted as $\boldsymbol{ACF}(\Delta x, \Delta y, \Delta z)$ in Cartesian coordinates or $\boldsymbol{ACF(\Delta r)}$ in spherical coordinates. Usually the spherical coordinates system is preferred since the texture features distribution can be represented, like in the MIL algorithm, with a Rose diagram plot [34].

Integration over the entire sample volume for each $\boldsymbol{\Delta r}$ is usually computationally very expensive, both in terms of time and physical resources; a solution is to perform calculations in the Fourier domain by the use of convolution theorem which states that $\boldsymbol{ACF(\Delta r)}$ is equivalent to the inverse Fourier transform of the Fourier power spectrum:

$$\boldsymbol{ACF}\left(\boldsymbol{\Delta r}\right) = \int_{-\infty}^{+\infty} \left|S(\mathbf{k})\right|^2 e^{i\mathbf{k}\cdot r}\, d^3\mathbf{k} \tag{4.34}$$

in which $\mathbf{k}$ is the spatial wave vector and $S(\mathbf{k})$ is the k-space signal measured.

From a numerical point of view the algorithm can be implemented, in a three-dimensional space, rewriting the analytical definition:

$$\boldsymbol{ACF}\left(x, y, z\right) = \frac{1}{L\,M\,N} \sum_{l=0}^{L} \sum_{m=0}^{M} \sum_{n=0}^{N} V^*\left(l, m, n\right)\, V(x+l, y+m, z+n) \tag{4.35}$$

where V^* denotes the complex conjugate of V, which are coincident since V is real; as shown for the 1D case. The ACF is then computed applying both convolution integral and Fast Fourier Transform:

$$\boldsymbol{ACF} = IFFT(S\left(\mathbf{k}\right)) \tag{4.36}$$

in which $IFFT$ represents the inverse of the Fast Fourier Transform and $S(\mathbf{k})$ represents, as reported in equation 4.35, the power spectrum in the frequency domain computed as the product between the Fourier Transform of V and its conjugate:

$$S(\mathbf{k}) = FFT(V)\ \ FFT^{*}(V) \tag{4.37}$$

At last, similarly to what is performed with the MIL algorithm, the anisotropy tensor is once again defined as the optimally fitting ellipsoid to the rose diagram. The ellipsoid principal axes ($\mathbf{a}_{ACF}$, $\mathbf{b}_{ACF}$ and $\mathbf{c}_{ACF}$) can be easily computed and the relative magnitudes define the degree of structural anisotropy:

$$DA = \sqrt{1 - \left(\frac{|\mathbf{a}_{ACF}|}{|\mathbf{c}_{ACF}|}\right)^{2}} \tag{4.38}$$

in which is assumed that $|\mathbf{a}_{ACF}| \leq |\mathbf{b}_{ACF}| \leq |\mathbf{c}_{ACF}|$, which are the magnitudes of the principal axes of the ellipsoid.

4.4 Materials and methods

4.4.1 Materials

The material referred to in the present chapter are the same ones investigated in chapter 3; moreover, the same cubic specimens, having 10 mm side length, used for gas pycnometer analysis have been used also for X-Ray computed tomography. This choice was made to have a direct feedback on the apparent density measured with two different experimental techniques on the same specimens, given the intrinsic variability from sample to sample observed for each material. Two specimens for each foam density were analysed and referred to in the subsequent paragraphs as specimens A and B.

4.4.2 X-Ray computed tomography (CT)

All the tomographic acquisitions were made in collaboration with *ENEA, Division for Sustainable materials, Research centre of Brindisi*. Acquisitions were performed using a *GE Phoenix Nanotom CT system* equipped with a 180 kV /15 W nano focus X-Ray tube and a 12-bit $2300\,x\,2300$ pixel *Hamamatsu* flat panel detector. A molybdenum target, suitable for weak absorbing specimen, like the ones investigated in the present work, was used for all the analyses. The accelerating voltage and the beam current of the X-Ray tube were set at 50 kV and 180 µA, respectively. The number of projections was 2400. Voxel size was set at 3 µm for each sample, corresponding to a geometric magnification of about 17 times. The exposure time for each projection and the total scan time were 1 s and 4.5 h, respectively. Volume reconstruction was carried out with the application *Phoenix datos|x 2*. The software enables to transform the series of acquired X-Rays projections, as the sample revolves 360°, in a resulting stack of slices representing the actual digital volumetric reconstruction, through the filtering back projection algorithm whose description is beyond the scope of the present thesis

work; interested readers are referenced to [7] [31]. The size of the resulting sets of images was $1300\,x\,1300\,x\,1300$ voxels, corresponding to an investigated volume of 3.9^3 mm^3.

4.4.3 Structure analysis

Images sets acquired with X-Ray computed tomography were used as a basis for structure analysis, performed in terms of solid volume fraction, structure volumetric mean thickness, pores characteristic dimensions and volume anisotropy distribution. Each image represents a virtual slice of the acquired CT volume.

Image analysis is performed through the use of a custom-developed algorithm, developed with *Matlab R2019b*, while the 3D visualization and analysis software *Avizo 8 Fire Edition* was used for the analysis of voids. To characterize the cell foam features the following general processing steps were performed:

- Denoising of grey-scale images by median filter;
- Binarization of the images, through the application of a suitable algorithm (Otsu or Watershed);
- Mean structure volumetric thickness quantification;
- Pore separation and labelling, subsequent removal of all the pores touching the borders of the inspected volume and calculation of cell features.

Ideally, the resulting set of binarized images should represent a closed-cell system hence the binarization algorithm adopted should minimize material erosion without artificially introducing a percolation path between closed adjacent cells. From the resulting binarized set of images the solid volume fraction, from now uniquely identified as ϕ, and the strictly related void volume fraction $1-\phi$, commonly addressed

to as macro porosity, can be easily computed as follows:

$$\phi = \frac{\#\ Voxel_{Full}}{\#\ Voxel_{Tot}} \tag{4.39}$$

where $\#\ Voxel_{Tot}$ is the total number of voxels within the analysed volume and $\#\ Voxel_{Full}$ is the total number of voxels associated with the presence of solid material in the binarized image after the binarization stage (Boolean value equal to 1). From equation 4.40 the apparent density, ρ^*, of the inspected samples can be computed as follows:

$$\rho^* = \rho_S \left(\frac{\#\ Voxel_{Full}}{\#\ Voxel_{Tot}} \right) + \rho_{Air} \left(1 - \frac{\#\ Voxel_{Full}}{\#\ Voxel_{Tot}} \right) \tag{4.40}$$

in which ρ_S is the density of the constituent material solid (PET), assumed equal to 1340 $\mathrm{kg\,m^{-3}}$ (average density of amorphous PET) and ρ_{Air} is the density of the gas trapped inside the closed cells, in this case taken as 1.2 $\mathrm{kg\,m^{-3}}$ (air density for $T = 25°\mathrm{C}$ and $p = 0.1$ MPa).

The choice of the proper binarization algorithm is hence based on two complementary criteria: mathematical criterion, based on the shape of the histogram as presented in the theoretical background section, and on a physical criterion; the apparent density computed from binarized images is compared with the value obtained from gas pycnometer analysis and if the value is in the same order of magnitude of the experimentally measured the binarization algorithm is considered adequate, otherwise it is changed or adjusted to obtain a more realistic value of apparent density for each inspected specimen.

Mean volumetric structure thickness and pores size were investigated to identify foams' internal cells characteristic dimensions, in a similar way to what performed by Ashby and Zhu and outlined in chapter 2. The mean volumetric structure thickness was calculated using the algorithm of Hildebrand and Rüegsegger implemented in the custom-made *Matlab* algorithm while the labelling analysis tool of *Avizo* was used for cell measurements. Cell measurements was performed in terms

of:

- Volume of the void;
- Equivalent diameter of the void, defined as the diameter of a regular sphere with the same volume of the inspected non-regular solid;
- Sphericity of the void, defined as how closely the shape of an object resembles that of a perfect sphere; is computed through the ratio of the surface area of a sphere with the same volume as the given particle to the surface area of the particle itself, as defined by Wadell in 1935 [55].

The analysis of anisotropy was accomplished using two custom made algorithms. The first one was implemented in *Matlab* to compute MIL on the set of images, according to the procedure proposed in section 4.3.3. The second one was implemented using the *VTK library* to compute spatial autocorrelation function according to a procedure widely reported in the literature: each sphere was divided into triangular facets defined by recursively subdividing the faces of an octahedron and then projecting them outward to the sphere surface. Computing the orientation of all the analysed voids and plotting them in an orthogonal three-dimensional reference system is possible to visualize voids distribution with the widely used rose diagrams [16]. In both approaches, MIL and ACF, a least square fitting algorithm was employed to fit the ellipsoid represented in the rose diagram; the number of orientations chosen for both analyses was 2049.

4.5 Results and discussion

In figure 4.13 the grey-level set of images obtained at the end of X-Ray computed tomography inspection and reconstruction are reported. Images are reported for each specimen A inspected for any given density; similar sets were obtained also for samples B.

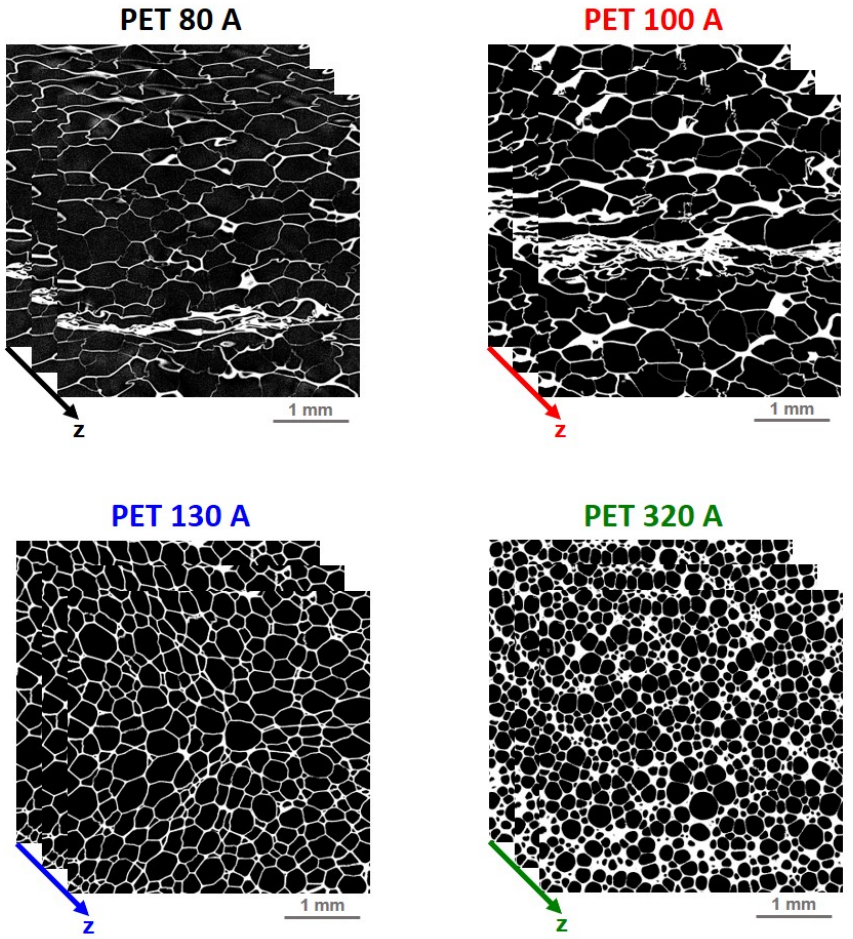

Figure 4.13: Greyscale set of images obtained from X-ray computed tomography analysis; the results are referred to sample A for each inspected density.

4.5.1 Image binarization

Each set of images was segmented using both Watershed and Otsu algorithms in order to compare the two according to analytical and physical selection criteria. Once the images had been binarized solid volume fraction ϕ and related apparent density was computed and relevant results are shown in figure 4.14; plotted against the apparent densities measured through gas pycnometer analysis, as presented in chapter 3 section 3.3.1. Results are for each sample A of any material density, on which these binarization test are performed. Once the proper algorithm was selected, it has been applied systematically to all samples.

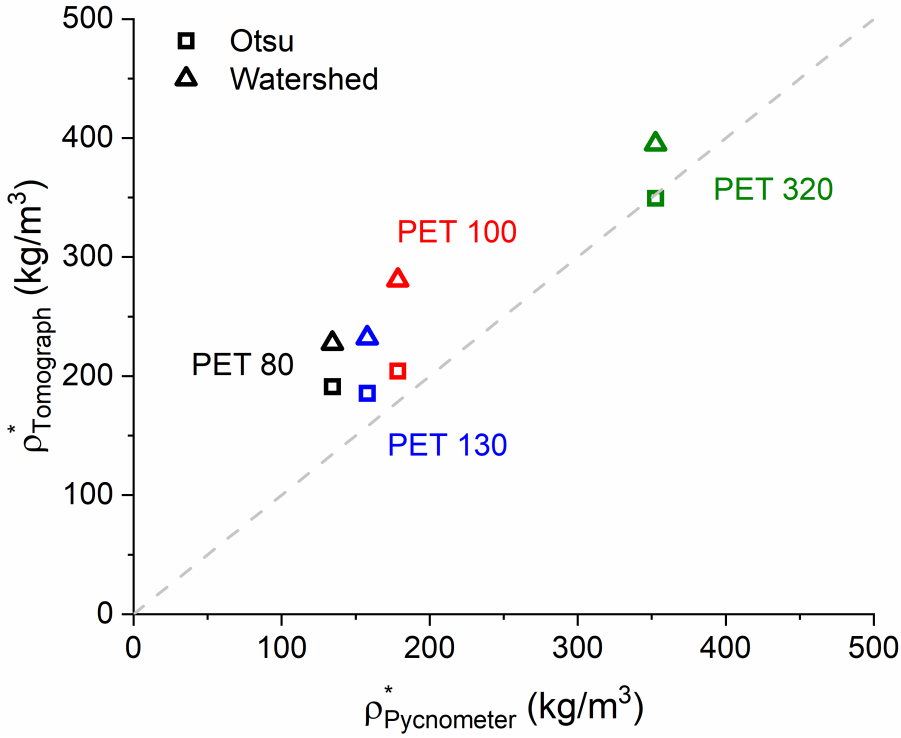

Figure 4.14: Apparent density computed from image analysis as a function of that measured with gas pycnometer analysis; dashed grey line represents the ideal correspondence between the two values. Results are referred to sample A for each inspected density.

Irrespective of the chosen algorithm, the apparent density measured with X-Ray computed tomography is systematically higher than the one obtained from gas pycnometry, with the only exception of PET 320. This result can be easily explained because of the presence of a significantly denser inner region, clearly visible in the set of images shown in figure 4.13 and not directly detectable with gas pycnometer. For what concerns material PET 320 the choice of the binarization algorithm is straightforward from both analytical and physical considerations: the histogram of the set of images representing the inspected structure has a bimodal shape which obviously leads to the choice of Otsu binarization algorithm; moreover, as can be seen from the graph, the watershed algorithm is highly conservative in this case and it adds artificial material to the binarized images. In addition, Otsu algorithm is suitable enough to preserve the internal closed structure without creating an artificial percolation path between adjacent closed cells. Analogous considerations can be made for the other samples, in these three cases (PET 80, PET 100 and PET 130) the histogram of the images is monomodal, leading the preference to Watershed algorithm; in these cases Otsu's algorithm is not conservative enough to preserve the internal structure, it does not preserve the integrity of closed cells, since the ideal threshold is not uniquely determined, due to the nature of the histogram, while is preserved through the application of the Watershed one. Moreover, the discrepancy between the two measures is justified by the presence of dense regions. For what concerns PET 130 Watershed algorithm is in any case preferred since the thin wall of the internal structure, in same cases 1 pixel in length, are not detected by Otsu's algorithm.

Aside from considerations which are specific to the individual specimens inspected in the present thesis, the results highlight the importance of the proper choice of the binarization algorithm during image processing. The correct choice is a fundamental step that, if not properly investigated, can introduce significant errors during subsequent phases,

in addition to the intrinsic errors of the tomographic reconstruction.

4.5.2 Structure analysis

Once the set of images were properly binarized they were used for an accurate reconstruction and to perform quantitative measurements on the foam samples. In figure 4.15 the cross sections taken along the X-Z plane (sheet plane) of the different samples, as cut from the material sheets, are shown. Two samples (sample A and B) are shown for each density, typically both sharing a distinctive appearance. Some qualitative differences are clearly detectable from the observation of the images. Sample PET 80 A exhibits a densification area, not present in sample B, which also influences the shape of neighbouring cells; a similar feature is also present in both samples of PET 100. On the other hand, sample PET 130 B possesses a slightly coarser structure when compared with its counterpart. While the peculiar feature observed for sample PET 80 A is probably fortuitous, variations in structure within different regions of the same sheet can generally occur on a product industrially realised on a large scale, as demonstrated by PET 130 A and PET 130 B.

The repeatability of the tomographic analysis was ascertained through the evaluation of concentrated structural scalar parameters: solid volume fraction, ϕ, mean structure volumetric thickness, mean equivalent pore diameter, D_{eq}, and pore sphericity. The comparison is graphically reported in figure 4.16 for all the tested samples. For a more homogeneous comparison among all the samples, the wall thickness and the volume fraction were measured with the caution to exclude the densification areas, to prevent an artificial increase of the relevant quantities: taking the average volumetric thickness as an example, the values would have been equal to 32.1 µm (instead of 23.6 µm), 33.1 µm (instead of 25.2 µm) and 25.8 µm (instead of 22.0 µm) for PET 100 A, PET 100 B and PET 80 A, respectively.

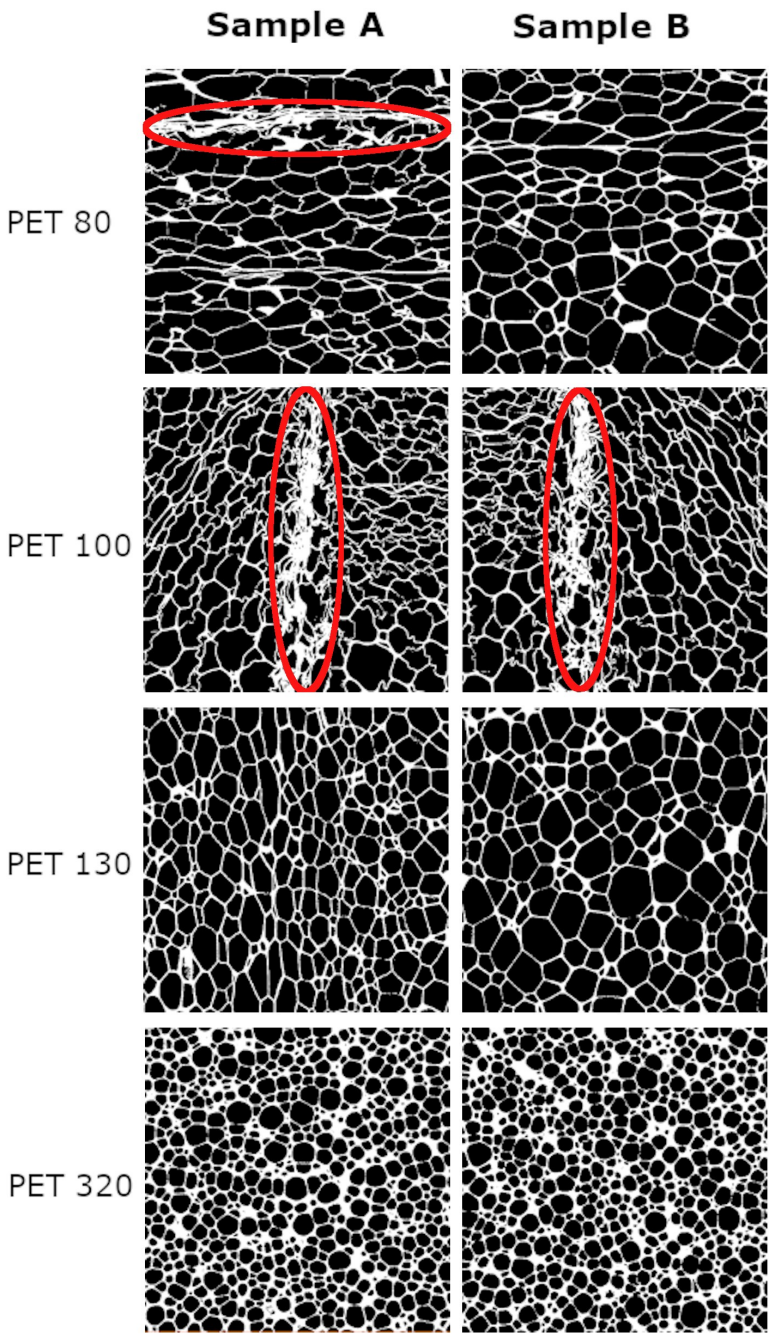

Figure 4.15: Tomographic cross-sections, related to the X-Z plane of observation, for all the specimens inspected with the X-Ray computed tomography; densification regions are highlighted with red ellipses.

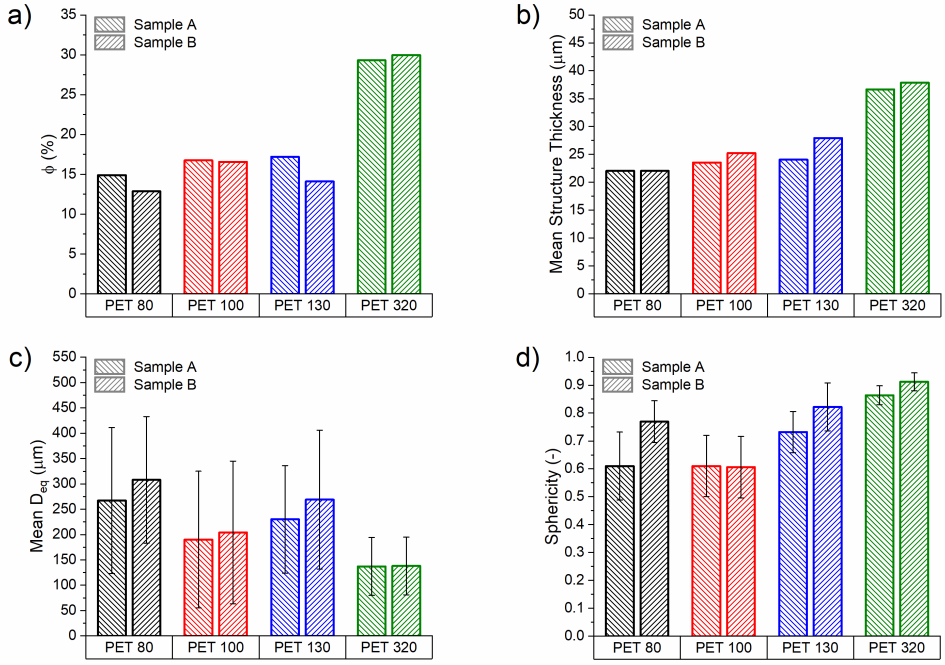

Figure 4.16: Comparison of structural parameters obtained from CT for two samples of the four investigated expanded polymeric materials: a) solid volume fraction, ϕ, b) mean structure volumetric thickness, c) mean equivalent pores diameter, D_{eq}, and d) pores sphericity. The dispersions reported come from the statistical analysis performed on the pores.

All foams gave similar results (about 15%) in terms of ϕ, with the exception of PET 320 for which a nearly double value was found; the measurements between samples of the same foam are in any case in very good agreement for PET 100 and PET 320, while minor differences are detectable in the case of the two other materials, but they are explained by the qualitative differences described previously. Besides these differences the evaluation of the mean volumetric structure thickness, performed on really different morphologies with the same algorithm, from a numerical point of view, supports the main hypothesis at the basis of Hildebrand and Rüegsegger algorithm: the independence of

algorithm results on the procedure itself. The results reported in figure 4.16 are obtained without the selection of any parameter for the application of the numerical procedure.

D_{eq} and pores sphericity were obtained through the analysis of individual voids within the reconstructed volume. The number of cells analysed for each sample is reported in table 4.1; from the analysis of the cells a statistical distribution can be computed and an example is reported in figures 4.17 and 4.18 for samples A of each analysed density. Similar results were obtained on samples B. Continuous distributions are obtained through a Gaussian fit of the data, since the distribution had proven to be non-normal.

Table 4.1: Number of cells analysed for each sample inspected with X-Ray computed tomography.

Sample	**Number of cells**
PET 80 A	1635
PET 80 B	1402
PET 100 A	3087
PET 100 B	2626
PET 130 A	3125
PET 130 B	1928
PET 320 A	16678
PET 320 B	16541

From both graphs, the distributions, from which mean values and error bars reported in figure 4.16 are computed as the median and the inter-quartile distance respectively, are clearly visible. It is also possible to qualitatively observe a progressive horizontal restriction in voids morphology distributions with respect to an increasing density. This anticipate the quantitative results presented in the next section, clearly visible in the rose diagram computed with fabric tensor algorithms: the morphologies become more and more regular with increasing density, confirming also the hypothesis built on the mechanical results presented

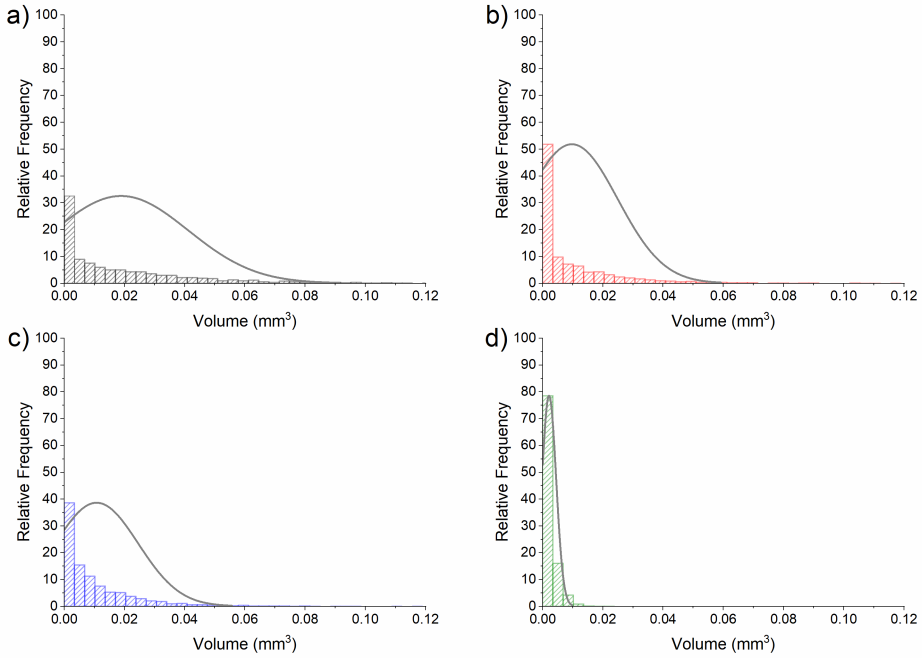

Figure 4.17: Statistical distribution of the volumes of the analysed cells; for each plot continuous distribution (grey line) is superimposed to the histogram for a clearer visualisation of the distribution itself: a) PET 80, b) PET 100, c) PET 130 and d) PET 320.

in chapter 3 paragraph 3.3.3. Moreover, given the high ratio between the size of the analysed volume (about four millimetres) and typical cell size, in terms of D_{eq}, (a few hundreds of microns), the concentrated parameters computed from this structural analysis are considered representative of the whole structure. This consideration strongly supports the search for correlations between these structural parameters and other macroscopic quantities.

As a first step, the solid volume fraction was related to macroscopic apparent densities, the first quantity compute through X-Ray computed tomography and the second determined through gas pycnometer analysis. Figure 4.19 shows relevant data in a double logarithmic plot: despite a relatively large dispersion in solid volume fraction data, ϕ, a linear relationship can clearly be identified between the apparent

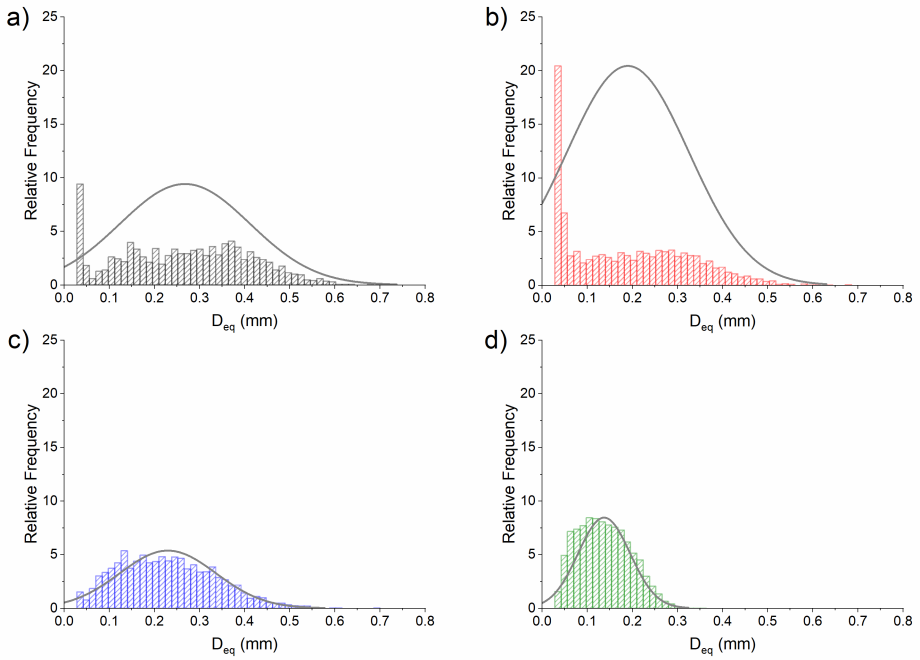

Figure 4.18: Statistical distribution of the equivalent diameters of the analysed voids; for each plot continuous distribution (grey line) is superimposed to the histogram for a clearer visualisation of the distribution itself: a) PET 80, b) PET 100, c) PET 130 and d) PET 320.

density ρ^* and ϕ, which leads to the following equation:

$$\frac{\rho^*}{\rho_S} \approx (\phi)^m \quad \text{with} \quad m = 1.185 \tag{4.41}$$

where ρ_S is the bulk solid density and m is the slope of the dashed line shown in figure 4.19, obtained with a linear fit.

Another relationship was found between the relative density and a characteristic dimension of the cells: the ratio between the mean structure thickness and the equivalent diameter of the pores, as proposed by Gibson and Ashby [20] (see chapter 2 paragraph 2.4.1). Also, in this case a linear fit of the data, as shown in figure 4.20, was performed. A similar relation to the one reported in equation 4.41 can thus be

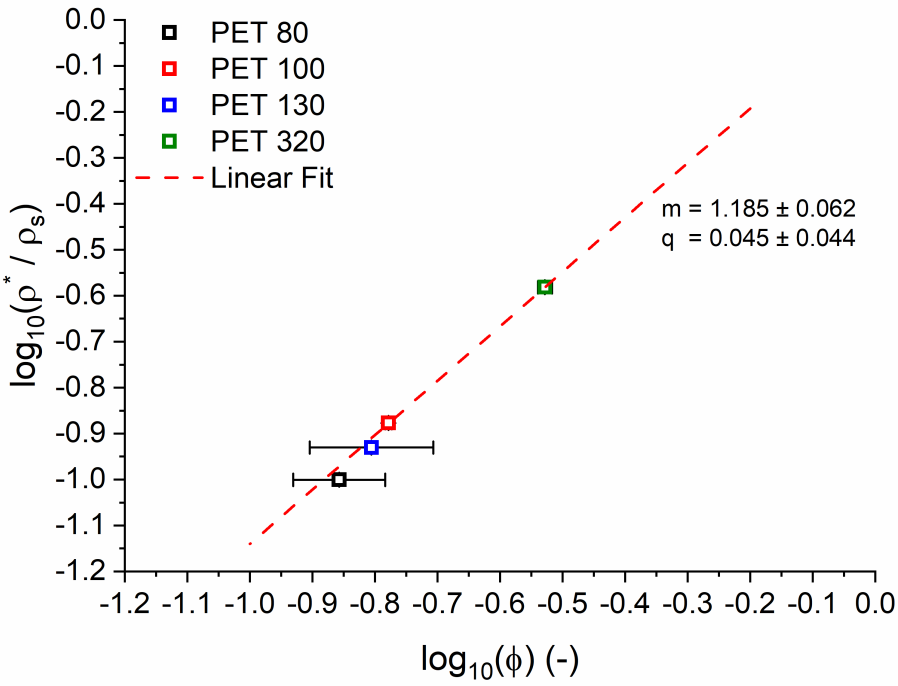

Figure 4.19: Double logarithmic plot of the relative density (y-axis) versus solid volume fraction of the four foams investigated; the dashed line represents a linear fit of the data.

identified:

$$\frac{\rho^*}{\rho_S} \approx \left(\frac{Th}{D_{eq}}\right)^n \quad \text{with} \quad n = 0.781 \tag{4.42}$$

where ρ^* is once again the measured apparent density, ρ_S is PET solid density, Th is the average volumetric structure thickness, D_{eq} is the mean equivalent diameter of the measured pores and n is the slope of the dashed lines reported in Figure 4.20.

Both linear fits were accomplished with an r^2-value greater than 0.99, indicating that the identified relationships can be considered valid from a statistical point of view. The quite high horizontal dispersion, computed as the interquartile difference of the Gaussian distribution, reported in figure 4.18 is strictly related to the statistical analysis performed on the voids, which descends from the wide difference in foam morphologies highlighted in the inspected samples.

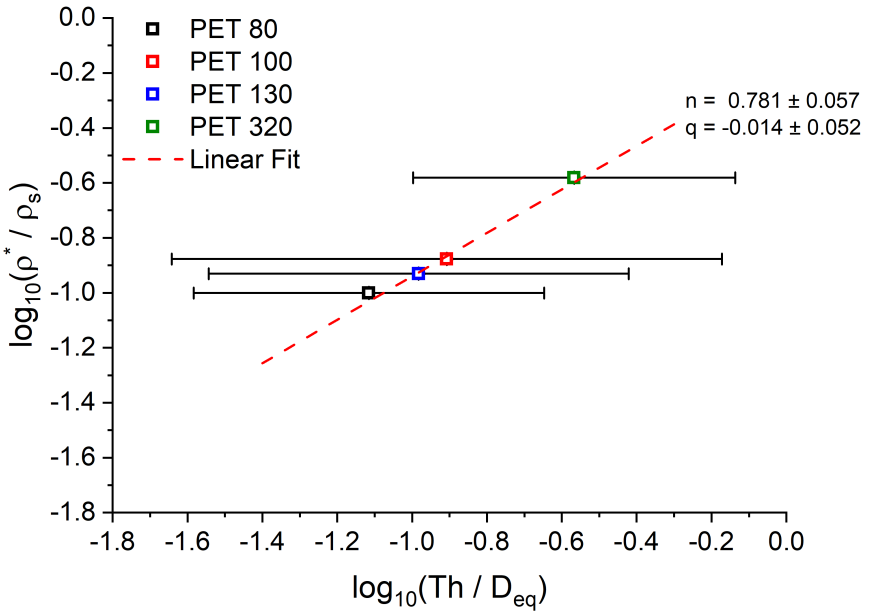

Figure 4.20: Double logarithmic plot of the relative density (y-axis) versus the ratio of mean structure thickness and the equivalent diameter of the pores; the dashed line represents a linear fit of the data.

4.5.3 Structure anisotropy

The other main aspect, faced in the present chapter, is the analysis of global sample anisotropy accomplished through the application of the MIL and ACF algorithms.

The results of anisotropy analysis for all the examined samples are summarized in figure 4.21 with the values of the degree of anisotropy (DA) evaluated with both MIL and ACF algorithms.

Three eigenvalues (λ_i) and the direction of the corresponding eigenvectors, where Θ is the inclination angle and φ the azimuth, are reported explicitly in table 4.2. The eigenvectors are listed following a descending order of the corresponding eigenvalue. In general, a strong agreement between the data computed by ACF and by MIL is evident and also there is a good repeatability between sample A and sample B. The results obtained for DA are systematically higher for ACF calculation

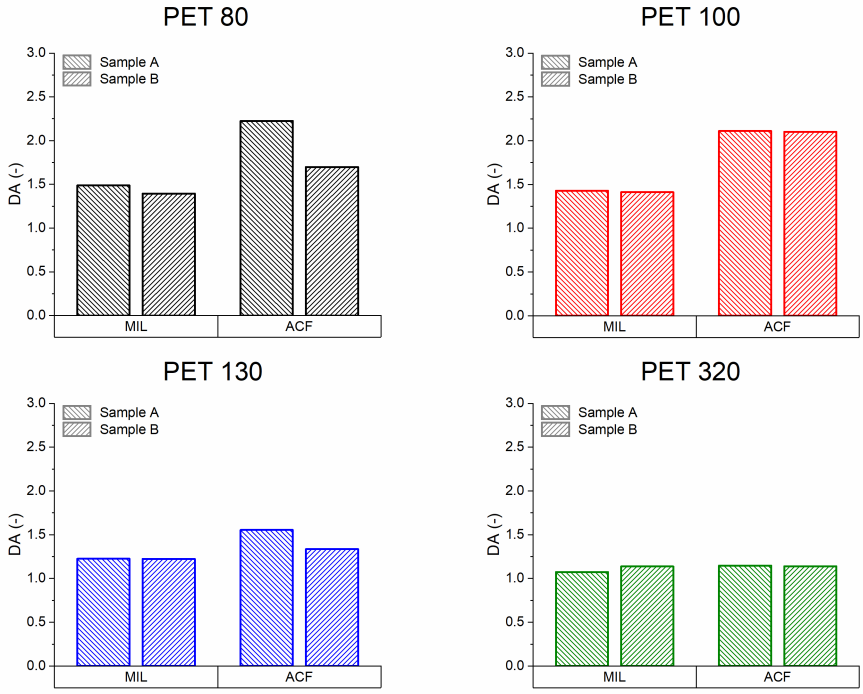

Figure 4.21: Comparison of degree of anisotropy index (DA) evaluated with both MIL and ACF algorithms for each inspected sample; two samples for each density.

with respect to MIL values, but this fact is expected and widely reported in literature [14] [15] [50]; it is strictly related to the analytical approach adopted (research of interface of material interphases for MIL and spatial autocorrelation of characteristic texture features, supposed to be quasi-regular, for ACF).

The reported results also show that the degree of anisotropy is inversely correlated with the nominal density of the expanded polymeric materials. This finding confirms once again the observations performed in the previous paragraph on the statistical distribution of voids and the hypothesis performed in chapter 3 on mechanical results. The internal structure becomes more and more isotropic with increasing foam density and consequently the mechanical response of the material along the three main orthogonal directions of the tested specimens.

Table 4.2: Anisotropy analysis results: degree of anisotropy, eigenvalues and eigenvectors are reported for all the investigated specimens; all the values are computed through mean intercept length and autocorrelation functions algorithms.

	DA	I eigenvector (Θ, φ)	II eigenvector (Θ, φ)	III eigenvector (Θ, φ)	λ_{max}	λ_{med}	λ_{min}
PET 80 Sample A							
MIL	1.487	(88.42°, 0.84°)	(63.53°, 91.64°)	(153.47°, 87.69°)	425.907	331.573	286.375
ACF	2.225	(88.21°, 1.53°)	(67.82°, 92.26°)	(157.74°, 87.16°)	72.634	44.205	32.637
PET 80 Sample B							
MIL	1.395	(88.41°, 5.75°)	(89.70°, 95.76°)	(178.38°, 16.51°)	583.664	528.576	418.419
ACF	1.698	(88.07°, 1.45°)	(88.40°, 217.40°)	(2.51°, 141.81°)	52.269	40.586	30.782
PET 100 Sample A							
MIL	1.429	(88.52°, 89.46°)	(37.53°, 357.52°)	(127.49°, 0.59°)	336.913	248.922	235.791
ACF	2.111	(87.36°, 89.16°)	(28.92°, 354.37°)	(118.77°, 0.61°)	87.178	47.926	41.293
PET 100 Sample B							
MIL	1.412	(89.53°, 91.62°)	(148.31°, 2.38°)	(58.31°, 1.33°)	348.550	263.480	246.888
ACF	2.102	(89.01°, 92.51°)	(158.22°, 5.01°)	(68.25°, 2.12°)	94.823	56.394	45.108
PET 130 Sample A							
MIL	1.225	(5.06°, 146.28°)	(91.03°, 68.00°)	(85.04°, 338.09°)	355.922	297.295	290.599
ACF	1.554	(4.66°, 139.76°)	(91.78°, 72.16°)	(85.69°, 342.30°)	56.256	37.929	36.203
PET 130 Sample B							
MIL	1.224	(21.29°, 93.75°)	(68.76°, 278.01°)	(91.44°, 7.45°)	574.447	524.876	469.473
ACF	1.336	(7.95°, 98.62°)	(82.12°, 286.02°)	(91.01°, 15.88°)	56.582	46.635	42.352
PET 320 Sample A							
MIL	1.073	(81.51°, 1.77°)	(171.09°, 19.58°)	(87.31°, 92.17°)	174.569	170.255	162.740
ACF	1.148	(88.14°, 1.21°)	(177.59°, 40.57°)	(88.47°, 91.26°)	57.606	56.033	50.197
PET 320 Sample B							
MIL	1.138	(89.67°, 351.31°)	(178.60°, 67.69°)	(88.64°, 81.31°)	204.650	200.029	179.862
ACF	1.140	(89.54°, 344.61°)	(178.08°, 60.93°)	(88.13°, 74.63°)	61.329	59.914	53.810

Both PET 320 specimens are in fact characterized by small and more spherical voids and have a degree of anisotropy close to 1. On the other hand, PET 80 and PET 100, characterized by elongated cells and a high variability of voids morphologies, exhibited the most anisotropic behaviour. Material distribution can be visually summarized with the Rose diagrams reported in figure 4.22. The eigenvectors are also reported, drawn in light blue colour, with their length proportional to the relevant eigenvalues.

At last the MIL algorithm, in the version proposed by Wald [56],

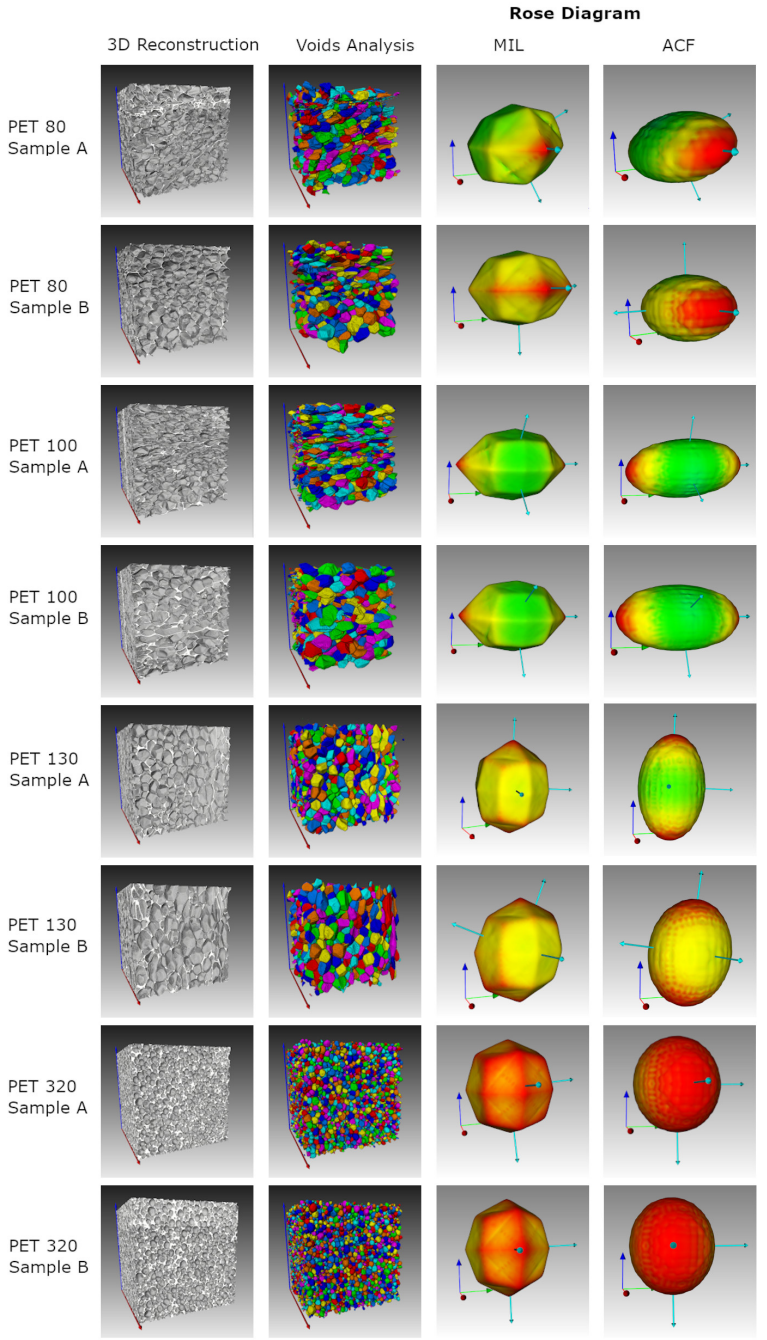

Figure 4.22: Graphical representation of anisotropy analysis results in terms of Rose diagrams, which represent the orientation of the structure in a cartesian 3D coordinate system. Diagrams are reported for all inspected specimens analysed with both MIL and ACF.

was applied to compute the mean structure thickness along different orientations, $Th(\boldsymbol{v})$, for PET 320 sample A, whose fabric tensor turned out to be the most isotropic one among the other inspected foams. The obtained average value:

$$\bar{Th} = \frac{1}{N} \sum_{v=1}^{N} Th\,(v) = 39.1\ \mu m \tag{4.43}$$

is in very good agreement with the one computed with Hildebrand and Rüegsegger algorithm, reported in figure 4.16. This result alone is not surprising due to the isotropic nature of the inspected structure, but computing the same quantity with the ACF algorithm, a very similar result is obtained:

$$\bar{Th} = \frac{1}{N} \sum_{v=1}^{N} FWHM\,(v) = 38.4\ \mu m \tag{4.44}$$

showing that on isotropic structures the results of the three algorithms, based on very different hypothesis, are comparable; the equivalence of ACF and MIL algorithms, which is still today a topic of discussion in literature, is thus supported by the present research. The same analysis can not be easily performed on the other inspected samples, due to the anisotropic nature of the structure and the strong dependence of the above computed quantities on the nature of inspected structure; this dependency is not considered in the Hildebrand and Rüegsegger algorithm. A modified version of MIL and ACF algorithms, objective that goes behind the aim of the present work, could also demonstrate the equivalence of the two approaches for less isotropic structures.

4.6 Concluding remarks

In this chapter an image-based approach for expanded polymeric materials internal structure inspection and quantification has been proposed. From a general point of view, in the present chapter the good

accuracy and repeatability of three-dimensional measures, performed with different and ad-hoc algorithms, is reported, proving, as reported by many authors in literature, the superiority of three-dimensional measurements with respect to bidimensional ones. 3D approaches offer the possibility to analyse different aspects of the real inspected structure, such as material spatial distribution or voids characteristic dimensions; this would be impossible with a bidimensional approach except with the application of some algorithms, that extrapolate three-dimensional geometries from 2D measurements, which always determine an overestimation of the dimensions of real structure features or introduce artefacts that are not representative of the true inspected structure.

The importance of accurately inspecting the internal microstructure to study the macroscopic properties exhibited by this class of materials and correlating them with constituent material properties and internal structure itself has been stressed again. Moreover, the equivalence of two different algorithms, MIL and ACF, has been demonstrated for the study of spatial material distribution. The general proposed approach has also proven to be accurate and repeatable despite inspected structures having qualitatively different morphologies and the intrinsic variability between samples exhibiting low macroscopic apparent densities (PET 80 and PET 100).

The results presented in this chapter will be widely exploited in the following ones where numerical algorithms for mechanical modelling and structure versus macroscopic mechanical properties will be presented.

4.7 References

[1] E.W. Andrews et al. “Size effects in ductile cellular solids. Part II: experimental results”. en. In: *International Journal of Mechanical Sciences* (2001), page 13.

[2] R. Barnes. “Parallel Priority-Flood depression filling for trillion cell digital elevation models on desktops or clusters”. en. In: *Computers & Geosciences* 96 (Nov. 2016), pages 56–68. DOI: 10.1016/j.cageo.2016.07.001. URL: https://linkinghub.elsevier.com/retrieve/pii/S0098300416301704.

[3] R. Barnes, C. Lehman, and D. Mulla. “Priority-Flood: An Optimal Depression-Filling and Watershed-Labeling Algorithm for Digital Elevation Models”. en. In: *Computers & Geosciences* 62 (Jan. 2014). arXiv: 1511.04463, pages 117–127. DOI: 10.1016/j.cageo.2013.04.024. URL: http://arxiv.org/abs/1511.04463.

[4] G. Bertrand. “On Topological Watersheds”. en. In: *Journal of Mathematical Imaging and Vision* 22.2-3 (May 2005), pages 217–230. DOI: 10.1007/s10851-005-4891-5. URL: http://link.springer.com/10.1007/s10851-005-4891-5.

[5] S. Beucher and F. Meyer. “The Morphological Approach to Segmentation: The Watershed Transformation”. en. In: *Mathematical Morphology in Image Processing*. Edited by Edward R. Dougherty. 1st edition. CRC Press, Oct. 2018, pages 433–481. DOI: 10.1201/9781482277234-12. URL: https://www.taylorfrancis.com/books/9781482277234/chapters/10.1201/9781482277234-12.

[6] J. Bigun. “Optimal Orientation Detection of Linear Symmetry”. en. In: (), page 15.

[7] N.K. Bose. “Multidimensional digital signal processing: problems, progress, and future scopes”. en. In: *PROCEEDINGS OF THE IEEE* 78.4 (1990), page 8.

[8] B. Brunet-Imbault et al. “A new anisotropy index on trabecular bone radiographic images using the fast Fourier transform”. en. In: *BMC Medical Imaging* (2005), page 11.

[9] A.D. Brydon et al. “Simulation of the densification of real open-celled foam microstructures”. en. In: *Journal of the Mechanics and Physics of Solids* 53.12 (Dec. 2005), pages 2638–2660. DOI: 10.1016/j.jmps.2005.07.007. URL: https://linkinghub.elsevier.com/retrieve/pii/S0022509605001298.

[10] T.E. Ciarelli et al. “Variations in Three-Dimensional Cancellous Bone Architecture of the Proximal Femur in Female Hip Fractures and in Controls”. en. In: (), page 9.

[11] M. Couprie, L. Najman, and G. Bertrand. “Quasi-Linear Algorithms for the Topological Watershed”. en. In: *Journal of Mathematical Imaging and Vision* 22.2-3 (May 2005), pages 231–249. DOI: 10.1007/s10851-005-4892-4. URL: http://link.springer.com/10.1007/s10851-005-4892-4.

[12] J. Cousty et al. “Watersheds, minimum spanning forests, and the drop of water principle”. en. In: (), page 46.

[13] N.P. Daphalapurkar et al. “Tomography and Simulation of Microstructure Evolution of a Closed-Cell Polymer Foam in Compression”. en. In: *Mechanics of Advanced Materials and Structures* 15.8 (Dec. 2008), pages 594–611. DOI: 10.1080/15376490802470523. URL: http://www.tandfonline.com/doi/abs/10.1080/15376490802470523.

[14] F. De Pascalis and M. Nacucchi. “Relationship between the anisotropy tensor calculated through global and object measurements in high-resolution X-ray tomography on cellular and

composite materials". en. In: *Journal of Microscopy* 273.1 (Jan. 2019), pages 65–80. DOI: 10.1111/jmi.12762. URL: https://onlinelibrary.wiley.com/doi/abs/10.1111/jmi.12762.

[15] F. De Pascalis and M. Nacucchi. "Volume orientation: a practical solution to analyse the orientation of fibres in composite materials". en. In: *Journal of Microscopy* 276.1 (Oct. 2019), pages 27–38. DOI: 10.1111/jmi.12832. URL: https://onlinelibrary.wiley.com/doi/abs/10.1111/jmi.12832.

[16] F. De Pascalis et al. "Quantitative characterisation of low-density, high performance polymeric foams using high resolution X-ray computed tomography and laser confocal microscopy". en. In: *NDT & E International* 83 (Oct. 2016), pages 123–133. DOI: 10.1016/j.ndteint.2016.06.010. URL: https://linkinghub.elsevier.com/retrieve/pii/S0963869516300573.

[17] P.F. Felzenszwalb and D.P. Huttenlocher. "Distance transforms of sampled functions". en. In: *Theory of Computing* 8.1 (2012), pages 415–428. DOI: 10.4086/toc.2012.v008a019. URL: http://www.theoryofcomputing.org/articles/v008a019.

[18] F. Fischer et al. "Numerical Simulation of Mechanical Properties of Cellular Materials Using Computed Tomography Analysis". en. In: *Journal of Cellular Plastics* 45.5 (Sept. 2009), pages 441–460. DOI: 10.1177/0021955X09339340. URL: http://journals.sagepub.com/doi/10.1177/0021955X09339340.

[19] Q. Fu et al. "Toward Strong and Tough Glass and Ceramic Scaffolds for Bone Repair". en. In: *Advanced Functional Materials* 23.44 (Nov. 2013), pages 5461–5476. DOI: 10.1002/adfm.201301121. URL: http://doi.wiley.com/10.1002/adfm.201301121.

[20] L.J. Gibson and M.F. Ashby. *Cellular Solids*. en.

[21] T.P. Harrigan and R.W. Mann. “Characterization of microstructural anisotropy in orthotropic materials using a second rank tensor”. en. In: *Journal of Materials Science* 19.3 (Mar. 1984), pages 761–767. DOI: 10.1007/BF00540446. URL: http://link.springer.com/10.1007/BF00540446.

[22] T. Hildebrand and P. Rüegsegger. “A new method for the model-independent assessment of thickness in three-dimensional images”. en. In: *Journal of Microscopy* 185.1 (Jan. 1997), pages 67–75. DOI: 10.1046/j.1365-2818.1997.1340694.x. URL: https://onlinelibrary.wiley.com/doi/abs/10.1046/j.1365-2818.1997.1340694.x.

[23] N. C. Hilyard and A. Cunningham, editors. *Low density cellular plastics: Physical basis of behaviour*. en. Dordrecht: Springer Netherlands, 1994. DOI: 10.1007/978-94-011-1256-7. URL: http://link.springer.com/10.1007/978-94-011-1256-7.

[24] J. Homminga et al. “The osteoporotic vertebral structure is well adapted to the loads of daily life, but not to infrequent “error” loads”. en. In: (2004), page 7.

[25] R.A. Ketcham and T.M. Ryan. “Quantification and visualization of anisotropy in trabecular bone: anisotropy in trabecular bone”. en. In: *Journal of Microscopy* 213.2 (Jan. 2004), pages 158–171. DOI: 10.1111/j.1365-2818.2004.01277.x. URL: http://doi.wiley.com/10.1111/j.1365-2818.2004.01277.x.

[26] J.H. Kinney and J.S. St. “An orientation distribution function for trabecular bone”. en. In: (2005), page 9.

[27] J.M. Kreider and S.A. Goldstein. “Trabecular Bone Mechanical Properties in Patients with Fragility Fractures”. en. In: *Clinical Orthopaedics and Related Research* 467.8 (2009), page 9.

[28] P. Launeau. “Two- and three-dimensional shape fabric analysis by the intercept method in grey levels”. en. In: (2010), page 10.

[29] E. Maire. “X-ray tomography applied to the characterization of cellular materials. Related finite element modeling problems”. en. In: *Composites Science and Technology* 63.16 (Dec. 2003), pages 2431–2443. DOI: 10.1016/S0266-3538(03)00276-8. URL: https://linkinghub.elsevier.com/retrieve/pii/S0266353803002768.

[30] S. Majumdar et al. “Fractal analysis of radiographs: Assessment of trabecular bone structure and prediction of elastic modulus and strength”. en. In: *Medical Physics* 26.7 (1999), page 12.

[31] R.M. Mersereau and A.V. Oppenheim. “Digital reconstruction of multidimensional signals from their projections”. en. In: *PROCEEDINGS OF THE IEEE* (1974), page 29.

[32] J. Millard. “Power Spectral Analysis of Vertebral Trabecular Bone Structure from Radiographs: Orientation Dependence and Correlation with Bone Mineral Density and Mechanical Properties”. en. In: (), page 8.

[33] M. Moakher. “On the Averaging of Symmetric Positive-Definite Tensors”. en. In: (), page 24.

[34] R. Moreno, M. Borga, and O. Smedby. “Generalizing the mean intercept length tensor for gray-level images: Generalizing the mean intercept length tensor”. en. In: *Medical Physics* 39.7Part2 (July 2012), pages 4599–4612. DOI: 10.1118/1.4730502. URL: http://doi.wiley.com/10.1118/1.4730502.

[35] R. Moreno, M. Borga, and O. Smedby. “Techniques for Computing Fabric Tensors: A Review”. en. In: *Visualization and Processing of Tensors and Higher Order Descriptors for Multi-Valued Data*. Edited by Carl-Fredrik Westin, Anna Vilanova, and Bernhard Burgeth. Series Title: Mathematics and Visualization. Berlin, Heidelberg: Springer Berlin Heidelberg, 2014, pages 271–292. DOI: 10.1007/978-3-642-54301-2_12. URL:

http://link.springer.com/10.1007/978-3-642-54301-2_12.

[36] D. T. Morton et al. “Mechanical response of low density expanded polypropylene foams in compression and tension at different loading rates and temperatures”. en. In: *Materials Today Communications* 23 (June 2020), page 100917. DOI: 10.1016/j.mtcomm.2020.100917. URL: https://linkinghub.elsevier.com/retrieve/pii/S2352492819313911.

[37] L. Najman and M. Schmitt. “Watershed of a continuous function”. en. In: *Signal Processing* 38.1 (July 1994), pages 99–112. DOI: 10.1016/0165-1684(94)90059-0. URL: https://linkinghub.elsevier.com/retrieve/pii/0165168494900590.

[38] A. Odgaard. “Three-Dimensional Methods for Quantification of Cancellous Bone Architecture”. en. In: 20.4 (), page 14.

[39] N. Otsu. “A Threshold Selection Method from Gray-Level Histograms”. en. In: (), page 5.

[40] D.H. Pahr and P.K. Zysset. “Influence of boundary conditions on computed apparent elastic properties of cancellous bone”. en. In: (), page 14.

[41] J. Pinto et al. “Characterization of the cellular structure based on user-interactive image analysis procedures”. en. In: *Journal of Cellular Plastics* 49.6 (Nov. 2013), pages 555–575. DOI: 10.1177/0021955X13503847. URL: http://journals.sagepub.com/doi/10.1177/0021955X13503847.

[42] C. Richert and N. Huber. “Skeletonization, Geometrical Analysis, and Finite Element Modeling of Nanoporous Gold Based on 3D Tomography Data”. en. In: *Metals* 8.4 (Apr. 2018), page 282. DOI: 10.3390/met8040282. URL: http://www.mdpi.com/2075-4701/8/4/282.

[43] B. Rietbergen and A. Odgaard. “Direct mechanics assessment of elastic symmetries and properties of trabecular bone architecture”. en. In: (), page 6.

[44] C. Rossi et al. “DTI of trabecular bone marrow”. en. In: *Magnetic Resonance Imaging* (2005), page 4.

[45] P.K. Saha and F.W. Wehrli. “A robust method for measuring trabecular bone orientation anisotropy at in vivo resolution using tensor scale”. en. In: *Pattern Recognition* (2004), page 10.

[46] R. Schlimper, M. Rinker, and R. Schäuble. “Prediction of material behaviour of closed cell rigid foams via mesoscopic modelling”. en. In: (), page 11.

[47] G.E. Schröder-Turk et al. “Minkowski Tensor Shape Analysis of Cellular, Granular and Porous Structures”. en. In: *Adv. Mater.* (2011), page 19.

[48] S.R. Stock. “Recent advances in X-ray microtomography applied to materials”. en. In: *International Materials Reviews* 53.3 (May 2008), pages 129–181. DOI: 10.1179/174328008X277803. URL: http://www.tandfonline.com/doi/full/10.1179/174328008X277803.

[49] S.R. Stock. “X-ray microtomography of materials”. en. In: *International Materials Reviews* 44.4 (Apr. 1999), pages 141–164. DOI: 10.1179/095066099101528261. URL: http://www.tandfonline.com/doi/full/10.1179/095066099101528261.

[50] Z. Tabor. “On the equivalence of two methods of determining fabric tensor”. en. In: *Medical Engineering & Physics* 31.10 (Dec. 2009), pages 1313–1322. DOI: 10.1016/j.medengphy.2009.09.003. URL: https://linkinghub.elsevier.com/retrieve/pii/S135045330900191X.

[51] Z. Tabor and E. Rokita. “Quantifying anisotropy of trabecular bone from gray-level images”. en. In: *Quantifying anisotropy of trabecular bone from gray-level images* 40 (2007), pages 966–972. DOI: 10.1016/j.bone.2006.10.022.

[52] S. Tagliabue et al. “An image-based approach for structure investigation and 3D numerical modelling of polymeric foams”. en. In: *Journal of Polymer Research* 28.3 (Mar. 2021), page 75. DOI: 10.1007/s10965-021-02438-9. URL: https://link.springer.com/10.1007/s10965-021-02438-9.

[53] “Tensorial Minkowski functionals and anisotropy measures for planar patterns”. en. In: *Journal of Microscopy* (2009), page 19.

[54] P. Viot, E. Plougonven, and D. Bernard. “Microtomography on polypropylene foam under dynamic loading: 3D analysis of bead morphology evolution”. en. In: *Composites Part A: Applied Science and Manufacturing* 39.8 (Aug. 2008), pages 1266–1281. DOI: 10.1016/j.compositesa.2007.11.014. URL: https://linkinghub.elsevier.com/retrieve/pii/S1359835X0700262X.

[55] H. Wadell. “Volume, Shape, and Roundness of Quartz Particles”. en. In: *Journal of Geology* 43 (1935), page 30. DOI: 10.1086/624298.

[56] M.J. Wald et al. “Spatial autocorrelation and mean intercept length analysis of trabecular bone anisotropy applied to in vivo magnetic resonance imaging: Spatial autocorrelation and mean intercept length analysis”. en. In: *Medical Physics* 34.3 (Feb. 2007), pages 1110–1120. DOI: 10.1118/1.2437281. URL: http://doi.wiley.com/10.1118/1.2437281.

[57] J.G.F. Wismans et al. “Computed Tomography-based Modeling of Structured Polymers”. en. In: *Journal of Cellular Plastics* 45.2 (Mar. 2009), pages 157–179. DOI: 10.1177/0021955X08100045.

[58] P.J. Withers. “X-ray nanotomography”. en. In: *Materials Today* 10.12 (Dec. 2007), pages 26–34. DOI: 10.1016/S1369-7021(07)70305-X. URL: https://linkinghub.elsevier.com/retrieve/pii/S136970210770305X.

[59] M.J. Yaffe and J.A. Rowlands. “X-ray detectors for digital radiography”. en. In: *Physics in Medicine and Biology* 42.1 (Jan. 1997), pages 1–39. DOI: 10.1088/0031-9155/42/1/001. URL: https://iopscience.iop.org/article/10.1088/0031-9155/42/1/001.

[60] J.P. Yang. “Image-Based Procedure for Biostructure Modeling”. en. In: *Journal of Nanomechanics and Micromechanics* 4.3 (Sept. 2014). DOI: 10.1061/(ASCE)NM.2153-5477.0000086. URL: http://ascelibrary.org/doi/10.1061/%28ASCE%29NM.2153-5477.0000086.

[61] P.K. Zysset, R.W. Goulet, and S.J. Hollister. “A Global Relationship Between Trabecular Bone Morphology and Homogenized Elastic Properties”. en. In: *Journal of Biomechanical Engineering* 120.5 (Oct. 1998), pages 640–646. DOI: 10.1115/1.2834756. URL: https://asmedigitalcollection.asme.org/biomechanical/article/120/5/640/398235/A-Global-Relationship-Between-Trabecular-Bone.

Chapter 5

Statistical approach for finite element mechanical modelling

In the following chapter the first of two image-based approaches developed in the present thesis is presented. The aim of both models is to provide efficient numerical tools which allow to perform numerical simulations considering the real structure of inspected samples and the constituent material properties, to study the macroscopic mechanical behaviour of expanded polymeric materials possessing a wide range of structures. The first approach presented is targeted at faithfully describing the linear elastic macroscopic mechanical behaviour in the range of finite small strains [21]; the approach is based on the Representative Volume Element (RVE) methodology, already widely employed in composite simulation [3]. A brief overview of the selected methodology is presented followed by the theoretical background regarding linear elastic constitutive laws and homogenization scheme; in the specific case Gurson model and the marching cube algorithm are outlined. Then the methodology adopted in this chapter is described and the main macroscopic mechanical results obtained are presented together with model validation. At last, a few basic structural-mechanical relationships are provided, strengthened, with respect to previous chapters, by the increased amount of data obtained through numerical simulations.

5.1 Introduction

As already widely pointed out in chapter 2, image-based approaches, developed in the past years, are the most promising path to understand and model macroscopic behaviour of expanded polymeric materials [27]. They present the possibility to include in the model the real structure of expanded polymeric materials inspected with one of the available imaging techniques, preferably a three-dimensional imaging analysis, such as X-ray computed tomography (CT) [23], nuclear resonance imaging (NRI) or others [9]. This advantage is at the same time one of the most challenging aspects, since considering the real structure and topology of the inspected samples usually requires a large amount of numerical resources, and in most cases, this prevents straightforward use of high-resolution images [16]. To overcome this issue, in the past years different numerical approaches were proposed in literature by many authors, among which the most commonly used one is a macroscopic homogenization scheme based on Representative Volume Elements (RVE) [7] [2]. Homogenization schemes, applied in the mechanics field, generally employ the continuum mechanics theoretical framework to describe the global mechanical behaviour of a heterogeneous media [28]. While being microscopically heterogeneous, these heterogeneities are assumed to be much smaller than some representative characteristic length at the macro-scale. Hence the heterogeneous material exhibits a macroscopically homogeneous behaviour within the single RVE; the global behaviour can then be reconstructed by applying suitable periodicity conditions [11]. Considering this hypothesis, the problem of equilibrium of a complex heterogeneous media is redefined at a smaller scale domain as a boundary value problem, in terms of stress and strain tensor fields, and then it is transferred back to the macroscopic scale as an equivalent homogeneous material in which its behaviour can be described by the related constitutive equations of continuum mechanics [22]. In general, the application of the RVE approach requires the ap-

plication of a suitable homogenization scheme to compute macroscopic stress and strain and the identification of a characteristic size of the representative element itself [14]; the latter must comply with the Hill principle, for compatibility of energetic and mechanical equivalence of the effective properties [12]. Figure 5.1 shows an explicative graphical sketch of the RVE approach applied in a bidimensional case.

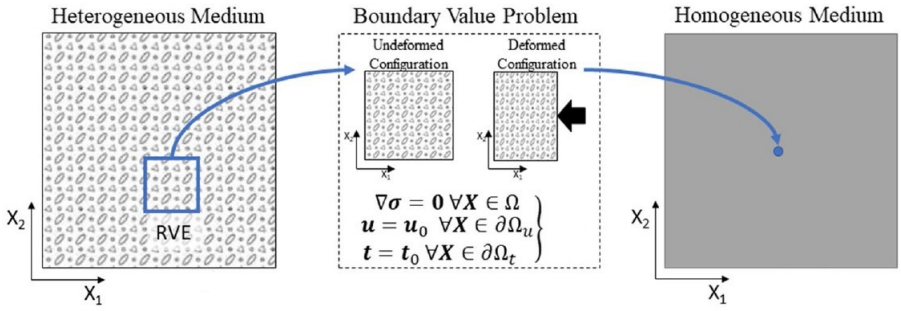

Figure 5.1: Schematic representation of the steps required to apply Representative Volume Element approach to heterogeneous solids; a bidimensional example is reported. Image freely adapted from [3].

In the present chapter a modified Representative Volume Element (RVE) approach will be presented with the aim of providing a suitable numerical tool to perform finite element analysis, starting from image inspection of expanded polymeric materials, and consequently describe and predict macroscopic mechanical behaviour. For the sake of clarity in the next section the theoretical background of different algorithms, necessary to apply the RVE approach, will be briefly presented: first of all, a description of linear elastic constitutive laws [28], used to describe elastic behaviour of solids; then marching cube algorithm [15], adopted to convert images into finite element mesh; finally, Gurson model, which is the homogenization scheme selected to compute macroscopic stress and strain [10]. Generality of the algorithms will be adapted to the specific case of the macroscopic mechanical behaviour of expanded polymeric materials in the practical section.

5.2 Theoretical background

5.2.1 Linear elastic constitutive laws

The linear elastic behaviour of a solid can be described in compact tensorial form as follows [28]:

$$\sigma_{ij} = C_{ijkl}\varepsilon_{kl} \tag{5.1}$$

in which σ_{ij} is the stress tensor, ε_{kl} is the strain tensor and C_{ijkl} is the fourth rank tensor that relates the strain to the stress, usually referred to as stiffness tensor.

In principle, for a generic anisotropic elastic material the relationship between strain and stress is descripted through 81 elastic constants. It can be proven that the stiffness tensor in the linear elastic case exhibits the following properties:

- *Bi-univocity*
- *Linearity*, usually referred to as directly proportionality
- *Invertibility*: the relation can be written also in terms of the compliance tensor, S_{klij};

$$\varepsilon_{kl} = S_{klij}\sigma_{ij} \quad with \quad \boldsymbol{C} = \boldsymbol{S}^{-1} \tag{5.2}$$

Moreover, the 81 elastic constants are straightforwardly reduced to 36 due to the symmetry of strain and stress tensors (major symmetry). Another reduction on the number of elastic constants can be performed based on energetic considerations, computing the work performed by a field stress for a given strain field, whose validity can be shown also in the case of independence of the two fields. This theorem reduces the maximum number of independent elastic constants to 21, necessary to fully describe the linear elastic behaviour of a generic anisotropic elastic material, usually referred to as triclinic.

Writing equation 5.1 in an extended tensorial form, using Voigt notation, is possible to attribute a physical meaning to each term of the elastic tensor:

$$\begin{Bmatrix} \sigma_{11} \\ \sigma_{22} \\ \sigma_{33} \\ \tau_{23} \\ \tau_{13} \\ \tau_{12} \end{Bmatrix} = \begin{bmatrix} C_{11} & C_{12} & C_{13} & C_{14} & C_{15} & C_{16} \\ C_{12} & C_{22} & C_{23} & C_{24} & C_{25} & C_{26} \\ C_{13} & C_{23} & C_{33} & C_{34} & C_{35} & C_{36} \\ C_{14} & C_{24} & C_{34} & C_{44} & C_{45} & C_{46} \\ C_{15} & C_{25} & C_{35} & C_{45} & C_{55} & C_{56} \\ C_{16} & C_{26} & C_{36} & C_{46} & C_{56} & C_{66} \end{bmatrix} \begin{Bmatrix} \varepsilon_{11} \\ \varepsilon_{22} \\ \varepsilon_{33} \\ \gamma_{23} \\ \gamma_{13} \\ \gamma_{12} \end{Bmatrix} \tag{5.3}$$

in the extended tensorial form σ_{ii} and ε_{ii} represent normal stresses and strains while τ_{ij} and γ_{ij} represent shear stresses and the corresponding strains. Given a generic strain field as an input and a stress field as output, the components of the elastic tensor can be physically interpreted as follows:

- C_{11}, C_{22} and C_{33} represent the direct effect of normal strains components on the material response;
- C_{44}, C_{55} and C_{66} represent the direct effect of shear strains components on the material response;
- C_{12}, C_{13} and C_{23} represent the coupled effect of normal strains and normal stresses on the material response;
- C_{45}, C_{46} and C_{56} represent the coupled effect of shear strains and shear stresses on the material response;
- C_{14}, C_{15}, C_{16}, C_{24}, C_{25}, C_{26}, C_{34}, C_{35} and C_{36} represent the coupled effect of normal strains and shear stresses, or vice versa, on the material response.

Each elastic component of the stiffness (or compliance) matrix must be identified with a specific experiment, which means that for a generic

anisotropic elastic solid 21 experiments have to be performed to fully characterize the material response.

Additional symmetries allow to further reduce the number of independent component necessary to fully describe the linear elastic behaviour. Figure 5.2 graphically exemplifies the different categories of linear elastic materials and the related constitutive laws identified in the past decades, according to the number of symmetry planes.

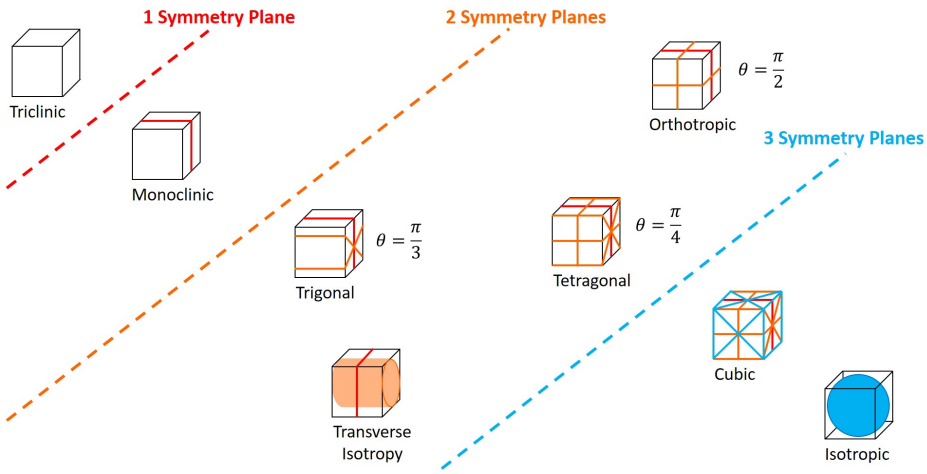

Figure 5.2: Graphical representation of linear elastic constitutive laws based on the number of minor symmetries identified in the material; they range from triclinic (no symmetries) up to isotropic (complete symmetry).

With an increasing number of symmetry planes, the number of independent components decreases and so does the number of experiments necessary to identify the elastic constants of the material.

One of the most common elastic constitutive laws is the orthotropic one; this class of materials is characterized by two minor symmetries, as given by three mutually orthogonal planes of symmetry. In this case, due to the presence of major and minor symmetries, all the components of the stiffness matrix representing coupled effects are equal to zero apart from coupled normal strains and stresses. The constitutive law

in tensorial form can be consequently written as:

$$\begin{Bmatrix} \sigma_{11} \\ \sigma_{22} \\ \sigma_{33} \\ \tau_{23} \\ \tau_{13} \\ \tau_{12} \end{Bmatrix} = \begin{bmatrix} C_{11} & C_{12} & C_{13} & 0 & 0 & 0 \\ C_{12} & C_{22} & C_{23} & 0 & 0 & 0 \\ C_{13} & C_{23} & C_{33} & 0 & 0 & 0 \\ 0 & 0 & 0 & C_{44} & 0 & 0 \\ 0 & 0 & 0 & 0 & C_{55} & 0 \\ 0 & 0 & 0 & 0 & 0 & C_{66} \end{bmatrix} \begin{Bmatrix} \varepsilon_{11} \\ \varepsilon_{22} \\ \varepsilon_{33} \\ \gamma_{23} \\ \gamma_{13} \\ \gamma_{12} \end{Bmatrix} \tag{5.4}$$

The independent components are consequently reduced to nine and these nine elastic constants can be defined:

- *Three Young moduli* (E_1, E_2 and E_3) representing the stiffness of the material along the three main orthogonal directions;
- *Three Poisson coefficients* (ν_{12}, ν_{13} and ν_{23});
- *Three Shear moduli* (G_{12}, G_{13} and G_{23}).

The constitutive relation can be consequently rewritten as a function of the aforementioned elastic constants. For the sake of clarity, the equation is now written in terms of compliance, whose expressions are simpler:

$$\begin{Bmatrix} \varepsilon_{11} \\ \varepsilon_{22} \\ \varepsilon_{33} \\ \gamma_{23} \\ \gamma_{13} \\ \gamma_{12} \end{Bmatrix} = \begin{bmatrix} \frac{1}{E_1} & -\frac{\nu_{21}}{E_2} & -\frac{\nu_{31}}{E_3} & 0 & 0 & 0 \\ -\frac{\nu_{12}}{E_1} & \frac{1}{E_2} & -\frac{\nu_{32}}{E_3} & 0 & 0 & 0 \\ -\frac{\nu_{13}}{E_1} & -\frac{\nu_{23}}{E_2} & \frac{1}{E_3} & 0 & 0 & 0 \\ 0 & 0 & 0 & \frac{1}{G_{23}} & 0 & 0 \\ 0 & 0 & 0 & 0 & \frac{1}{G_{13}} & 0 \\ 0 & 0 & 0 & 0 & 0 & \frac{1}{G_{12}} \end{bmatrix} \begin{Bmatrix} \sigma_{11} \\ \sigma_{22} \\ \sigma_{33} \\ \tau_{23} \\ \tau_{13} \\ \tau_{12} \end{Bmatrix} \tag{5.5}$$

In the tensorial notation, only for formal reasons three more Poisson coefficients are introduced, but they are not independent constants due to the following symmetry relations:

$$\frac{\nu_{12}}{E_1} = \frac{\nu_{21}}{E_2}; \quad \frac{\nu_{13}}{E_1} = \frac{\nu_{31}}{E_3}; \quad \frac{\nu_{23}}{E_2} = \frac{\nu_{32}}{E_3} \tag{5.6}$$

From an experimental point of view the nine elastic constants can be determined by performing six experimental tests:

- uniaxial compression tests along three main orthogonal directions ($1-1$, $2-2$ and $3-3$) of the tested sample from which Young moduli and Poisson ratios are measured;
- simple shear tests along the three coordinate planes ($1-2$, $2-3$ and $1-3$) from which the shear moduli are measured.

Other simpler elastic models are widely used in literature to describe the mechanical behaviour of materials; the two most commonly used are transversely isotropic, widely employed for composite materials, and fully isotropic, for homogeneous materials.

Transversely isotropic materials are characterized by a complete in-plane symmetry and hence the independent components of stiffness matrix are reduced to five (and so the related elastic constants):

- *Two Young moduli* (E_p and E_t) representing the in-plane and out of plane stiffness;
- *Two Poisson ratios* (ν_p and ν_{pt});
- *One Shear modulus* (G_{tp}).

The related tensorial relation can be written as follows:

$$\begin{Bmatrix} \varepsilon_{11} \\ \varepsilon_{22} \\ \varepsilon_{33} \\ \gamma_{23} \\ \gamma_{13} \\ \gamma_{12} \end{Bmatrix} = \begin{bmatrix} \frac{1}{E_p} & -\frac{\nu_p}{E_p} & -\frac{\nu_{tp}}{E_t} & 0 & 0 & 0 \\ -\frac{\nu_p}{E_p} & \frac{1}{E_p} & -\frac{\nu_{tp}}{E_t} & 0 & 0 & 0 \\ -\frac{\nu_{pt}}{E_p} & -\frac{\nu_{pt}}{E_p} & \frac{1}{E_t} & 0 & 0 & 0 \\ 0 & 0 & 0 & \frac{1}{G_{tp}} & 0 & 0 \\ 0 & 0 & 0 & 0 & \frac{1}{G_{tp}} & 0 \\ 0 & 0 & 0 & 0 & 0 & \frac{1}{G_p} \end{bmatrix} \begin{Bmatrix} \sigma_{11} \\ \sigma_{22} \\ \sigma_{33} \\ \tau_{23} \\ \tau_{13} \\ \tau_{12} \end{Bmatrix} \tag{5.7}$$

in which the subscript p and t refer to the in-plane and out of plane elastic constants, respectively.

Also, in this case for the sake of notation consistency it appears that more constants that the minimum number are introduced, but once again a symmetry relation can be written:

$$\frac{\nu_{pt}}{E_p} = \frac{\nu_{tp}}{E_t} \tag{5.8}$$

Moreover, a further relation can be analytically demonstrated:

$$G_p = \frac{E_p}{2\left(1+\nu_p\right)} \tag{5.9}$$

At last, the simplest linear elastic constitutive law, applied to materials characterized by an infinite number of symmetry planes, is the isotropic one. In this case only two components of the stiffness matrix, or equivalently the compliance matrix, are independent. Two elastic constants are thus defined:

- *Young modulus* (E);
- *Poisson coefficient* (ν).

The tensorial relationship becomes:

$$\begin{Bmatrix} \varepsilon_{11} \\ \varepsilon_{22} \\ \varepsilon_{33} \\ \gamma_{23} \\ \gamma_{13} \\ \gamma_{12} \end{Bmatrix} = \begin{bmatrix} \frac{1}{E} & -\frac{\nu}{E} & -\frac{\nu}{E} & 0 & 0 & 0 \\ -\frac{\nu}{E} & \frac{1}{E} & -\frac{\nu}{E} & 0 & 0 & 0 \\ -\frac{\nu}{E} & -\frac{\nu}{E} & \frac{1}{E} & 0 & 0 & 0 \\ 0 & 0 & 0 & \frac{1}{G} & 0 & 0 \\ 0 & 0 & 0 & 0 & \frac{1}{G} & 0 \\ 0 & 0 & 0 & 0 & 0 & \frac{1}{G} \end{bmatrix} \begin{Bmatrix} \sigma_{11} \\ \sigma_{22} \\ \sigma_{33} \\ \tau_{23} \\ \tau_{13} \\ \tau_{12} \end{Bmatrix} \tag{5.10}$$

Once again, an analytical relationship can be demonstrated to hold between E and G:

$$G = \frac{E}{2\left(1+\nu\right)} \tag{5.11}$$

Analogously to what described for orthotropic materials, similar experiments have to be performed to measure the elastic constants of

the material under investigation, but the number of experiments is reduced accordingly to the required number of elastic constants.

5.2.2 Marching cube algorithm

The marching cube algorithm was developed in 1987 in the field of computer graphics with the aim of providing a tool to build three-dimensional volume rendering starting from a series of images [15] [26] [25]; the first application of the algorithm was proposed in the medical field to visualise in three dimensions the results of medical analyses such as Nuclear Resonance Imaging (NRI) or Axially Computed Tomography (CT) [2]. Subsequently it was applied in different engineering fields in which image analysis and volumetric reconstruction is of crucial importance [9].

Starting from a set of images it is possible to convert it into a three-dimensional mesh uniquely identified through labelling of elements and their corresponding nodes. First of all, in the case of a set of images, representing a volume, the unitary space subdivision should be defined: in this case the space is discretized into voxels (volumetric pixels), graphically represented with a hexahedron uniquely identified by its eight vertices and centroid, corresponding to the bidimensional pixel coordinates. Starting from the bidimensional image and considering each pixel as a centroid of a voxel, it is possible to construct around each centroid a three-dimensional hexahedral structure whose side length is equal to the image resolution; a graphical example is reported in figure 5.3.

This procedure can be applied to each pixel of an image or equivalently a set of images obtaining as a result a three-dimensional rendering of the inspected volume. Considering now a set of images of dimensions $I\,x\,J\,x\,K$, the first step to be performed is the discretization of the space, represented by the set of images, and the definition of an artificial reference system to uniquely identify the spatial coordinates of

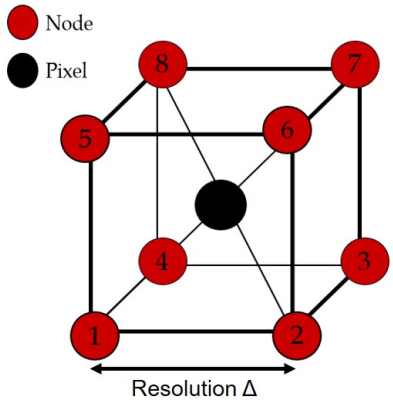

Figure 5.3: Three-dimensional discretization and representation of a voxel with a hexahedral element and symmetrically constructed around the pixel of a bidimensional image considered as the centroid of the voxel.

the centroids (i, j, k). A graphical representation is depicted in figure 5.4.

The second step consists in the node numbering, considering that the set of images is comprehensive of a total number of nodes (N) variable in each direction of the global coordinate system and equal to: $N_i = I + 1$ along i direction, $N_j = J + 1$ along j direction and

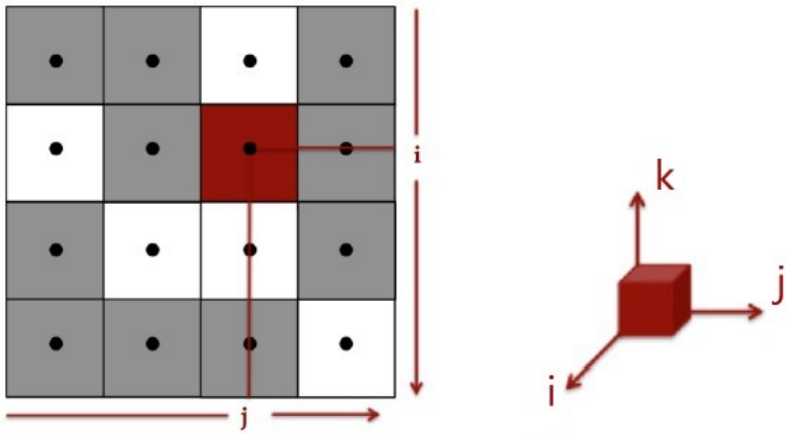

Figure 5.4: Bidimensional discretization of an image and unique identification of each pixel, through a coordinate system.

$N_k = K + 1$ along k direction. The numbering procedure is performed with a global and systematic approach with respect to the reference system, starting along i direction, then j and at last k, as depicted in figure 5.5. The operation of node numbering is performed only around pixels exhibiting the presence of material in the inspected volume; "empty" pixels are discarded in the procedure.

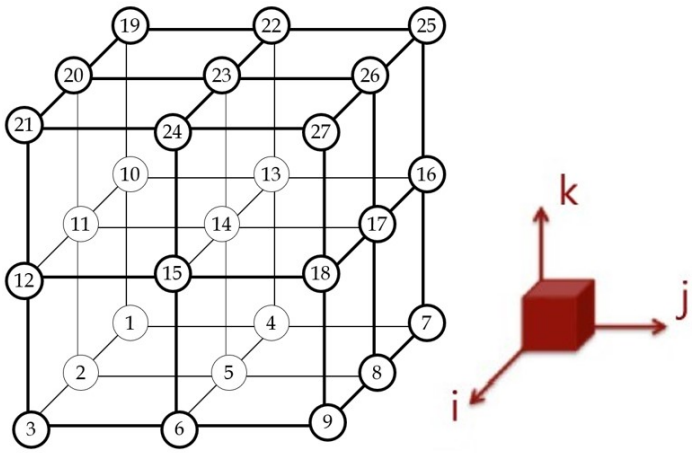

Figure 5.5: Graphical example of global nodes numbering around each pixel representing the presence of material in the inspected volume.

The numbering procedure is performed through a set of equations that uniquely identify each node in the global system, with eight nodes

for each pixel as depicted in figure 5.3:

$$\begin{cases} Node_1 = (N_i\, N_j)\,(k-1) + N_i\,(j-1) + (i+1) \\ Node_2 = Node_1 + N_i \\ Node_3 = Node_2 - 1 \\ Node_4 = Node_1 - 1 \\ Node_5 = Node_1 + (N_i\, N_j) \\ Node_6 = Node_2 + (N_i\, N_j) \\ Node_7 = Node_3 + (N_i\, N_j) \\ Node_8 = Node_4 + (N_i\, N_j) \end{cases} \tag{5.12}$$

The third and last step consists in the extraction of nodes coordinates with respect to the global coordinate system; this is performed in two sub-steps that consist in the introduction of a local coordinate system, centred in each pixel and with the axes parallel to the global coordinate system, and the computation of local coordinates of the nodes, taking the side length of the hexahedron equal to the image resolution; the coordinates are then converted according to the global coordinate system knowing the position of each centroid, to which the node is associated; in figure 5.6 a representation of the two coordinate systems is depicted. This last step can be analytically written as follows for a generic node in position (i, j, k):

$$i = \begin{cases} \Delta\,(i-1) + \frac{\Delta}{2} & if \quad a > 0 \\ \Delta\,(i-1) - \frac{\Delta}{2} & if \quad a < 0 \end{cases} \tag{5.13}$$

$$j = \begin{cases} \Delta\,(j-1) + \frac{\Delta}{2} & if \quad b > 0 \\ \Delta\,(j-1) - \frac{\Delta}{2} & if \quad b < 0 \end{cases} \tag{5.14}$$

$$k = \begin{cases} \Delta\,(k-1) + \frac{\Delta}{2} & if \quad c > 0 \\ \Delta\,(k-1) - \frac{\Delta}{2} & if \quad c < 0 \end{cases} \tag{5.15}$$

in which Δ denotes image resolution and a, b and c denote the local coordinates of the node.

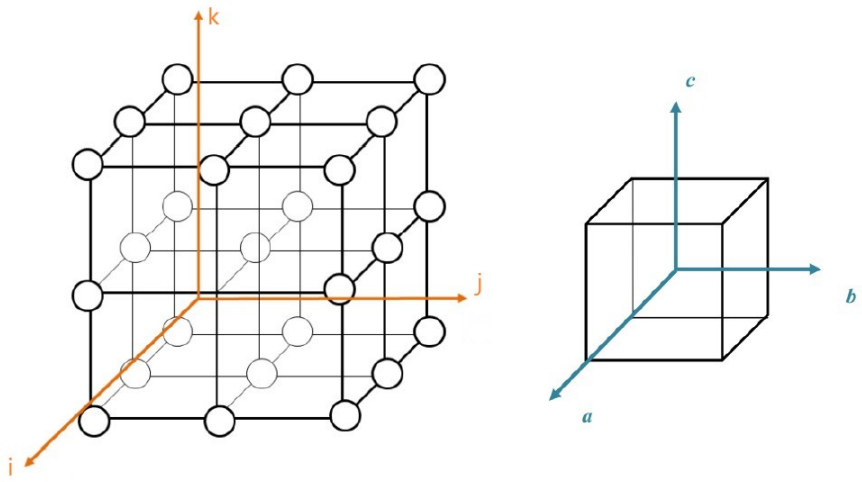

Figure 5.6: Graphical representation of global and local coordinate systems adopted for nodes coordinates computation.

Thanks to the descripted procedure each set of images can be easily and uniquely converted into a three-dimensional representation of the volume inspected. Voxels are uniquely identified through the so-called incidence and coordinates matrices: the first one is a matrix containing the number of each pixel associated with the eight nodes number of the associated voxel while the second is a matrix containing the global coordinates of each node.

5.2.3 Gurson model

Gurson model was developed in 1975 with the aim of providing a yielding criterion for porous ductile materials and in the following years it was adapted and modified also for the description of various mechanical aspects of cellular materials, since it considers the presence and the possible voids nucleation in the computation of strain and stress fields [19] [1]. The formulation proposed in this section is the

original model derived by Gurson [10]; in the following paragraphs it will be employed in a discrete and simplified version aimed at its implementation in finite element modelling post-processing.

The model is based on the main assumption of small strain fields inside the inspected discrete volume or otherwise called volume of interest. The material is assumed to be constituted by at least two phases, matrix and inclusions, in the specific case voids; moreover, the non-linear behaviour of the matrix is assumed incompressible and rigid-perfectly plastic. The second phase, referred to as inclusions, which triggers the nucleation of voids in the matrix, and especially at its interface with the second phase, is considered completely unbonded from the surrounding matrix material since the very beginning of the deformation process. Hence, the second phase can be approximated as cavities with stress-free boundary and consequently the dilatant behaviour of the volume, V, is caused by the presence of the cavity themselves.

The macroscopic strain rate tensor can be expressed by subdividing the contributions of the matrix volume, called Ω, and of the void volume, $V - \Omega$, as:

$$\dot{E}_{ij} = \frac{1}{V} \int_V \dot{\varepsilon}_{ij} \, dV = \frac{1}{V} \left[\int_\Omega \dot{\varepsilon}_{ij} \, dV + \int_{V-\Omega} \dot{\varepsilon}_{ij} \, dV \right] \tag{5.16}$$

in which capital letters refer to macroscopic quantities and lowercase letters refer to microscopic, or local, quantities.

Applying the Green theorem to equation 5.16 the equation can be expressed as:

$$\dot{E}_{ij} = \frac{1}{V} \int_V \dot{\varepsilon}_{ij} \, dV = \frac{1}{V} \left[\int_\Omega \dot{\varepsilon}_{ij} \, dV + \frac{1}{2} \int_{\partial\Omega_i} (v_i n_j^{'} + v_j n_i^{'}) \, dS \right] \tag{5.17}$$

where $\partial\Omega_i$ is the profile of the interface between matrix and the cavity, $n^{'}$ is the unit outward normal to the void surface and v is the field velocity; equation 5.17 requires that the velocity field is continuous with

its first derivative inside the integration volume. The second term at the right-hand side of the equation highlights the contribution responsible for the dilatant behaviour of the volume.

The macroscopic plastic dissipation can be defined as:

$$\dot{W} \equiv \langle \dot{w} \rangle = \frac{1}{V} \int_V \sigma_{ij} \dot{\varepsilon}_{ij} \, dV = \frac{1}{V} \int_\Omega \sigma_{ij} \dot{\varepsilon}_{ij} \, dV = \frac{1}{V} \int_{\partial V} \sigma_{ij} v_i n_j \, dS \tag{5.18}$$

where $\langle \square \rangle$ stands for the volume average operator and the integration is performed only over the rigid ideally-plastic matrix volume, Ω, due to the null strength properties of the void. In the equation the plastic dissipation is defined as the doubly contracted product of the microscopic stress, σ_{ij}, and microscopic strain rate tensors, $\dot{\varepsilon}_{ij}$. Moreover, within the incompressible matrix material the hydrostatic part of the stress tensor does not play a role, hence it can be substituted by its deviatoric component.

At the microscale, it is assumed that the matrix yield surface is convex and the requirement is fulfilled by the J_2 yield condition. The maximum work principle thus states that:

$$\dot{w} - \dot{w}^* \equiv \left(\sigma_{ij} - \sigma^*_{ij} \right) \dot{\varepsilon}_{ij} \geq 0 \quad for \quad \forall \dot{\varepsilon_{ij}} \neq 0 \tag{5.19}$$

where σ_{ij} represents a plastic stress state, $\dot{\varepsilon}_{ij}$ is the relevant strain rate as given by the associated flow rules, σ^*_{ij} is a state of stress which lies within or upon the yield surface, $\dot{w}$ and w^* are the microscopic plastic dissipation associated with σ_{ij} and σ^*_{ij} respectively.

At this point the no-correlation postulate of Bishop and Hill is introduced: it is assumed that no correlation between the components of the microscopic stress tensor σ_{ij} and the components of the velocity field v_i over any plane section, S_A, of the volume occurs. The condition is satisfied if the strain or the stress states are uniform in the volume.

This statement implies that:

$$\frac{1}{S_A}\int_{S_A}\sigma_{ij}v_i\,dS = \frac{1}{S_A}\int_{S_A}\sigma_{ij}\;dS\cdot\frac{1}{S_A}\int_{S_A}v_i\,dS \tag{5.20}$$

Applying equation 5.19 to equation 5.18 leads to:

$$\dot{W} = \frac{1}{V}\int_V \sigma_{ij}\dot{\epsilon}_{ij}\,dV = \Sigma_{ij}\dot{E}_{ij} \tag{5.21}$$

in which Σ_{ij} is the macroscopic resultant stress tensor over the plane section.

By means of the virtual work principle, for a given stress state σ_{ij} which satisfies the equilibrium conditions and a strain rate state $\dot{\varepsilon}_{ij}$ associated to the velocity field v_i the following relation holds true:

$$\dot{W}^A - \dot{W}^* \equiv \left(\Sigma_{ij}^A - \Sigma_{ij}^*\right)\dot{E}_{ij} = \frac{1}{V}\int_V \left(\sigma_{ij}^A - \sigma_{ij}^*\right)\dot{\varepsilon}_{ij}\,dV \geq 0 \tag{5.22}$$

where σ_{ij}^* is a stress state that does not violate the yield condition in the volume, while σ_{ij}^A and Σ_{ij}^A are the actual microscopic and macroscopic stress tensors, respectively. This equation represents the macroscopic maximum work principle deduced from the microscopic maximum work principle and from the no-correlation postulate. Hence, the macroscopic yield function inherits the properties of the local one for the matrix material.

The macroscopic stress at yielding can be obtained by exploiting the associativity property of the macroscopic flow rules as:

$$\Sigma_{ij}^A = \frac{\partial\dot{W}}{\partial\dot{E}_{ij}} \tag{5.23}$$

This last equation defines the actual response, Σ_{ij}^A, of the porous material under the applied loading conditions. When an approximate velocity field, linear in $\dot{E}_{ij}$, is introduced for the matrix material, the approximate effective yield function possesses the properties of convexity and normality as well. Due to the linearity of the velocity field in the

macroscopic strain rate tensor, the effective dissipation can be expressed as follow:

$$\dot{W} = \dot{W}\left(v_i\left(\dot{E}_{ij}\right)\right) = \frac{\partial \dot{W}}{\partial \dot{E}_{ij}}\dot{E}_{ij} \tag{5.24}$$

The approximate macroscopic stress tensor at yielding can be defined analogously to the actual one:

$$\Sigma_{ij} = \frac{\partial \dot{W}}{\partial \dot{E}_{ij}} = \frac{1}{V}\int_V \left[\sigma_{kl}\frac{\partial \dot{\varepsilon}_{kl}}{\partial \dot{E}_{ij}} + \frac{\partial \sigma_{kl}}{\partial \dot{E}_{ij}}\dot{\varepsilon}_{kl}\right] dV = \frac{1}{V}\int_V \sigma_{kl}\frac{\partial \dot{\varepsilon}_{kl}}{\partial \dot{E}_{ij}}\, dV \tag{5.25}$$

in the equation the term $\frac{\partial \sigma_{kl}}{\partial \dot{E}_{ij}}\dot{\varepsilon}_{kl}$ disappears because of the local associated flow rules.

By analogy with equation 5.23 normality at the macroscopic scale has been proven and furthermore, the maximum work principle at the macroscale follows directly from convexity of the matrix constitutive behaviour and from the linearity of the approximate strain rate tensor within the volume.

Finally, it can be demonstrated that the approximate yield function always lies on or outside the actual one. To show this fact, the maximum plastic work principle is written as:

$$\dot{W} - \dot{W}^A \equiv \left(\Sigma_{ij} - \Sigma_{ij}^A\right)\dot{E}_{ij} = \frac{1}{V}\int_V (\sigma_{ij} - \sigma_{ij}^A)\dot{\varepsilon}_{ij}\, dV \geq 0 \tag{5.26}$$

Since both Σ_{ij} and Σ_{ij}^A are work conjugate pairs with $\dot{E}_{ij}$, which has the direction of the outward normal to the yield loci, both approximate and actual, at, respectively, Σ_{ij} and Σ_{ij}^A, Σ_{ij} is consequently an upper bound for the actual stress tensor at yielding.

5.3 Materials and methods

5.3.1 Materials

The sets of images representative of the inspected expanded polymeric structure already described in chapter 4 will be considered in the present one; they will be used for structure analysis and also as a basis for finite element simulations. The general procedure adopted in the following sections is based on the Representative Volume Element (RVE) approach previously described.

5.3.2 Representative Volume Element (RVE) approach

The first step to apply the RVE approach consists in subdividing the total volume inspected with X-Ray computed tomography into smaller sub-domains [20]. In the specific case the total volume inspected and reconstructed with CT analysis is represented by a set of images of total dimension $1300\,x\,1300\,x\,1300$ pixel which corresponds, with the employed resolution of 3 µm, to a volume of 3.9^3 mm^3. The criteria adopted to select the proper dimension of the RVE are:

- *Upper limit* is set according to the resources available for numerical simulations; considering that each pixel representative of the presence of material will be converted into a hexahedral finite element the limit in this case is a volume of $400\,x\,400\,x\,400$ pixel (1.35^3 mm^3) which in general corresponds to an average value of "solid" pixels, in the order of 10^7, which roughly translates into a similar number of finite elements.

- *Lower limit* is determined according to two considerations: the first is a mathematical condition considering that the sub-domain should not contain only solid material or vice versa it should not be completely empty; for the inspected sets of images a volume of

$50\,x\,50\,x\,50$ pixel (0.153 mm^3) was enough to prevent this. The second reason is based on the physical consideration that the RVE selected should contain a minimum number of cells comprised between 5 and 10; according to the literature, this number ensures that the RVE is representative of the whole inspected volume. In this case the characteristic length of RVE range from $200\,x\,200\,x\,200$ pixels (0.63 mm^3) for PET 320 to $250\,x\,250\,x\,250$ pixels (0.753 mm^3) for PET 80. The second criterion gives in this case the resulting minimum dimension of the RVE selected for numerical simulation.

Table 5.1 summarizes the characteristic dimension of the RVE selected for each set of images and the corresponding number of subdomains in which the whole set is divided:

Table 5.1: Number of cells analysed for each sample inspected with X-Ray computed tomography.

Sample	**RVE [Pixel]**	**RVE** [mm]	**Number of domains**
PET 80 A PET 80 B	$250\,x\,250\,x\,250$	$0.75\,x\,0.75\,x\,0.75$	140
PET 100 A PET 100 B	$250\,x\,250\,x\,250$	$0.75\,x\,0.75\,x\,0.75$	140
PET 130 A PET 130 B	$200\,x\,200\,x\,200$	$0.60\,x\,0.60\,x\,0.60$	275
PET 320 A PET 320 B	$200\,x\,200\,x\,200$	$0.60\,x\,0.60\,x\,0.60$	275

5.3.3 Structure analysis

Each subdomain was analysed with the algorithms presented in chapter 4 to compute microstructure features, such as solid volume fraction (ϕ), mean volumetric structure thickness, voids equivalent diameter (D_{eq}) and voids sphericity. For what concerns structural anisotropy analysis the different approaches presented in the previous

chapter were adopted. Autocorrelation function (ACF) method was not applied in the case of small RVE having not enough texture features since in this case the application of this tensorial algorithm could give misleading results. Mean Intercept Length (MIL) was in this case implemented in the version proposed by Moreno and co-authors [18]: the number of interfaces between material phases was computed along lines parallel to the three orthogonal directions of the Cartesian reference system and along lines inclined at $\pm \frac{\pi}{4}$ in the coordinate planes $x - y$, $x - z$ and $y - z$. The anisotropy index was computed as:

$$DA = 1 - \frac{\lambda_{min}}{\lambda_{max}} \tag{5.27}$$

in which λ_i are the eigenvalues of the second order tensor representing spatial material distribution, obtained through the MIL algorithm.

Once the structural analysis was performed on each domain, the results were combined in a bi-variate statistical distribution to highlight the frequency distribution of sub-domains having specified morpho-structural characteristics in terms of two parameters. In the specific case the two variables selected for the statistical analysis are:

- *Solid volume fraction*: this quantity is selected since it is the main physical parameter that influences the macroscopic mechanical response of expanded polymeric materials as proven by many authors in the scientific literature and already shown by the experimental tests in chapter 3 [8].

- *Degree of anisotropy*: this variable was considered as a scalar index of the anisotropic macroscopic mechanical response of the domain selected; as shown in chapter 3, the tested samples exhibit an increasing degree of mechanical anisotropy with decreasing apparent density and hence solid volume fraction. It is expected that this index is strictly correlated to spatial material distribution and therefore is one of the crucial parameters to select the most adequate sub-domain to reproduce the macroscopic mechanical

response of the whole inspected material. It is expected that structural degree of anisotropy is a good indicator to predict different mechanical response in different spatial directions of the inspected sub-domain.

The bin selected for bi-variate statistical analysis was 0.05 for both adimensional quantities selected (which vary between 0 and 1).

Structure analysis and bi-variate statistical analysis were performed using a custom-made *Matlab R2019b* code on a personal computer with 2 cores and 16 GB RAM.

5.3.4 Finite element modelling

From the result of bi-variate statistical distribution, from the most occurring subdomain with given solid volume fraction and degree of anisotropy, two sub-domains were selected to validate the RVE approach, comparing the results with those obtained in chapter 3 from experimental tests.

The identified sub-domains were processed with a custom-made code, implemented in *Matlab R2019b*, and converted into a finite element mesh with the marching cube algorithm. Effectively a one to one conversion, each pixel representing the presence of material (Boolean value equal to 1) was converted into a finite element. This operation was performed after a filtering one that removes all the elements not connected with the main structure identified in the RVE, to prevent errors during finite element simulations. Once the incidence and coordinates matrices were generated they were imported into the commercial software *ABAQUS 2018*. The elements type selected for all the simulations was C3D8, a linear cubic finite element with full integration; this choice was performed with the aim of including all the degree of freedom in the simulation without any limitation provided by the choice of other finite elements (e.g. beam elements or shell elements). Full integration was selected to give the highest accuracy in numerical simulation results.

Once the sub-domain had been imported into the commercial finite element code, six linear elastic simulations were performed on each domain representing elementary loading conditions, with the aim of computing the stiffness matrix of the system [24]. Figure 5.7 depicts qualitatively the six simple stress states simulated on each sub domain:

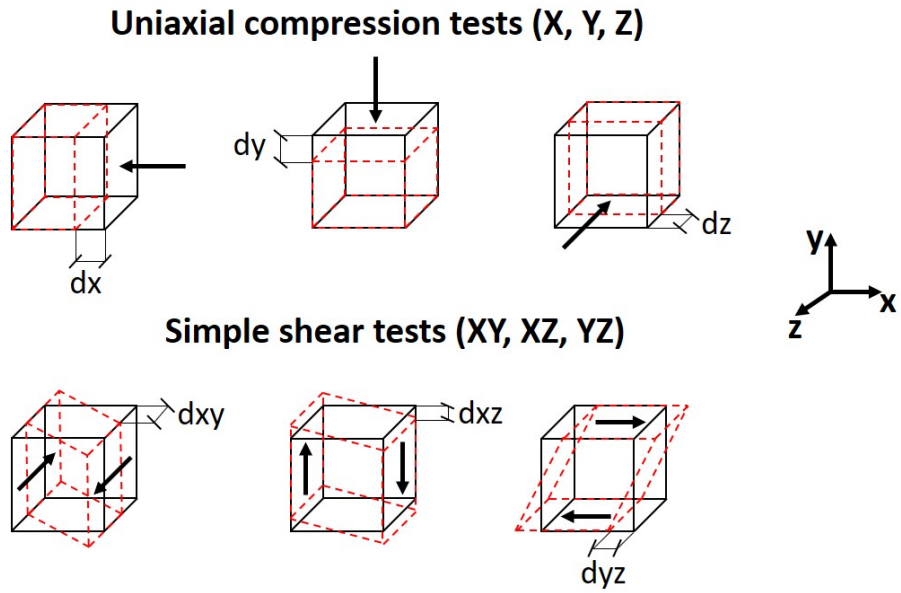

Figure 5.7: Qualitative representation of the six simple stress states simulated on each sub domain.

Simulations were performed imposing a displacement, corresponding to a macroscopic strain of 1%, on one face of the cubic RVE and constraining the displacement on the opposite face. For each simulation the boundary conditions adopted on the faces not directly involved in the simple stress state simulation were symmetry boundary conditions, under the hypothesis that the selected RVE is the unit cell of which the macroscopic expanded material is made of [6] [7]. The adopted solution scheme was implicit static general and the constituent material considered linear elastic with the elastic constants reported in table 5.2:

Values were taken from literature data concerning amorphous polyethylene terephthalate (PET); this choice is justified by the crystallinity

Table 5.2: Linear elastic parameters.

Parameter	Value
Young's modulus (E)	2900 MPa
Poisson's ratio ν	0.4

degree measurements presented in chapter 3.

The results of each simulation underwent a post-processing analysis performed with a custom-made *Python 2* code in which Gurson model had been numerically implemented. Since finite element simulations are performed in small strain linear elastic regime, yielding does not occur in the material and hence the only quantities that needs to be homogenized through the application of Gurson model are stress and elastic strain fields; this is achieved implementing the following numerical equations, derived from Gurson model [27]:

$$\Sigma_{i,j} \equiv \langle \sigma_{i,j} \rangle = \frac{1}{V} \int_V \sigma_{i,j}\, dV = \frac{1}{V_{Tot}} \sum_{k=1}^{\#\, elements} \sigma_{i,j}^k V^k \tag{5.28}$$

$$\begin{aligned} E_{i,j} \equiv \langle \varepsilon_{i,j} \rangle &= \frac{1}{V} \left[\int_V \varepsilon_{i,j}\, dV + \int_{\partial V} \nabla \boldsymbol{u} \cdot \boldsymbol{n}\, dS \right] = \\ &= \frac{1}{V_{Tot}} \left[\sum_{k=1}^{\#\, elements} \varepsilon_{i,j}^k V^k + \sum_{w=1}^{\#\, elements\, ext} \boldsymbol{u}^w \cdot \boldsymbol{n}^w S^w \right] \end{aligned} \tag{5.29}$$

in which $\Sigma_{i,j}$ and $E_{i,j}$ are the macroscopic stress and strain while $\sigma_{i,j}$ and $\varepsilon_{i,j}$ the correspondent microscopic quantities; $\langle \square \rangle$ indicates the average volumetric operator. $\nabla \boldsymbol{u}$ is the displacement gradient and $\boldsymbol{n}$ is the unit vector normal to the surface to which the gradient refers to. In the discrete form, the stress is computed over all the finite element present in the mesh while the strain is computed once again on all the finite elements for what concerns the volumetric component and only on elements representing the interface with voids for what concerns the surface component. In the discrete case, V_{Tot} is the total volume

of the RVE (material and voids), V^k is the volume of k-th element in the deformed configuration and S^w is the area of w-th element in the deformed configuration.

Once the tensors representing macroscopic stresses and strains were computed the macroscopic stiffness tensor of the RVE was assembled:

$$\begin{Bmatrix} \Sigma_{11} \\ \Sigma_{22} \\ \Sigma_{33} \\ \Sigma_{23} \\ \Sigma_{13} \\ \Sigma_{12} \end{Bmatrix} = \begin{bmatrix} C_{11} & C_{12} & C_{13} & C_{14} & C_{15} & C_{16} \\ C_{12} & C_{22} & C_{23} & C_{24} & C_{25} & C_{26} \\ C_{13} & C_{23} & C_{33} & C_{34} & C_{35} & C_{36} \\ C_{14} & C_{24} & C_{34} & C_{44} & C_{45} & C_{46} \\ C_{15} & C_{25} & C_{35} & C_{45} & C_{55} & C_{56} \\ C_{16} & C_{26} & C_{36} & C_{46} & C_{56} & C_{66} \end{bmatrix} \begin{Bmatrix} E_{11} \\ E_{22} \\ E_{33} \\ 2E_{23} \\ 2E_{13} \\ 2E_{12} \end{Bmatrix} \tag{5.30}$$

each column of the tensor filled with the results of one simulation:

- The first three columns represent the result of uniaxial compression tests along the three main orthogonal directions; in order, X, Y and Z;
- The fourth column is the simple shear test along the coordinate plane $Y - Z$;
- The fifth column is the simple shear test along the coordinate plane $X - Z$;
- The sixth column is the simple shear test along the coordinate plane $X - Y$.

The computed matrix can be inverted to obtain the compliance matrix, and elastic constants can be easily extracted with the relations provided into previous paragraphs. For each domain the elastic constants at the present stage were computed under the hypothesis of an orthotropic material. The elastic constants obtained (E_1, E_2 and E_3) were compared against experimental results for the purpose of model validation.

The second step after the validation of the approach consisted in verifying that each sub-domain belonging to one specific bin of the distribution exhibited the same macroscopic mechanical response; this check was performed by selecting all the sub-domains belonging to a bin of the distribution and applying the above descripted procedure.

Once these two steps were performed, a total number of 100 sub-domains, with different morpho-structural characteristics, were selected; the same aforementioned procedure was applied to increase the number of available experimental and numerical data to seek valid relationships between microstructure parameters and macroscopic elastic constants.

All the pre-processing and post-processing operations were performed on a personal computer with 2 cores and 16 GB RAM, while finite element simulations were performed on a Linux machine with 24 cores and 49 GB RAM; the total number of finite elements ranged from a minimum of $9 * 10^5$ up to a maximum of $3.5 * 10^6$ elements and so the related number of free nodes varied from $2 * 10^6$ up to $6 * 10^6$. The average CPU time needed for a single simulation varied between 6 and 32 hours depending on the total number of free nodes in the finite element mesh.

5.4 Results and discussion

5.4.1 Model validation

Figure 5.8 shows the results obtained from the bi-variate statistical analysis performed on each inspected sample; the figure refers only to sample A of each analysed density, but similar results were obtained for sample B.

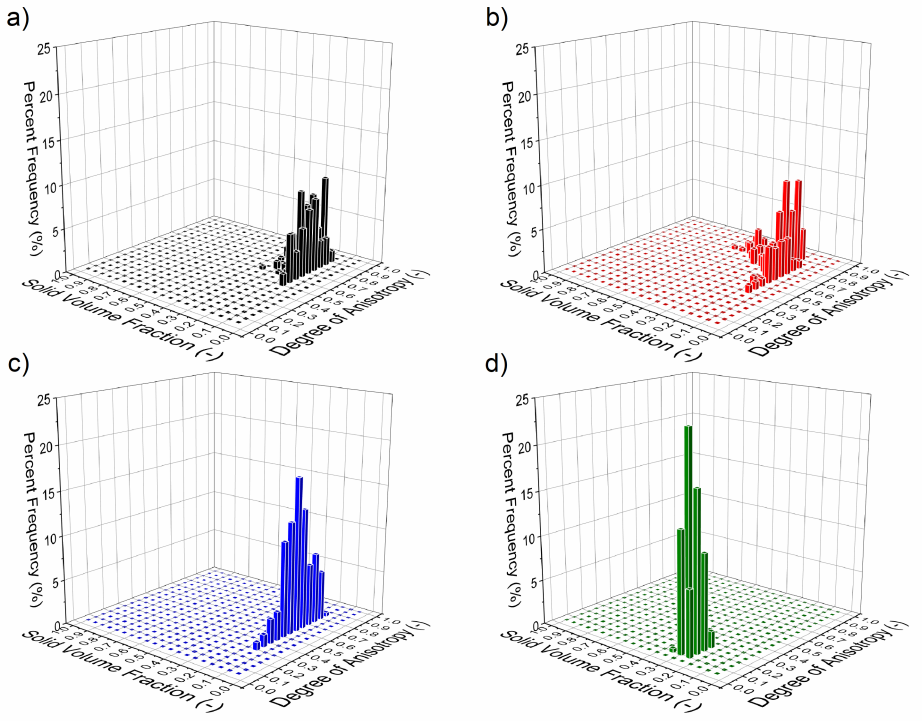

Figure 5.8: 3D histograms representing the results of bi-variate statistical distribution performed on each sample density; figure refers to sample A of each inspected density: a) PET 80, b) PET 100, c) PET 130 and d) PET 320.

From the graph a decrease of the dispersion of the distribution with increasing density is clearly visible, in accordance with the observations already reported in the previous chapter.

Table 5.3 summarizes the results of bi-variate statistical distribution in terms of the highest frequency of domains having given morpho-

structural characteristics:

Table 5.3: Bi-variate statistical distribution results.

Sample	Solid Volume Fraction (%)	Degree of Anisotropy (-)	Percent frequency (%)
PET 80 A	$15-20$	$0.90-0.95$	10
PET 80 B	$15-20$	$0.85-0.90$	10
PET 100 A	$20-25$	$0.75-0.80$	10
PET 100 B	$20-25$	$0.85-0.90$	10
PET 130 A	$15-20$	$0.60-0.65$	10
PET 130 B	$15-20$	$0.65-0.70$	10
PET 320 A	$30-35$	$0.15-0.20$	10
PET 320 B	$30-35$	$0.15-0.20$	10

From the most frequent class of each sample, one sub-domain was converted into a finite element mesh and figure 5.9 shows an example of the corresponding reconstructed geometry; the high level of details that can be reproduced with the marching cube algorithm from a high-resolution set of images, in this case obtained with X-Ray computed tomography, is evident.

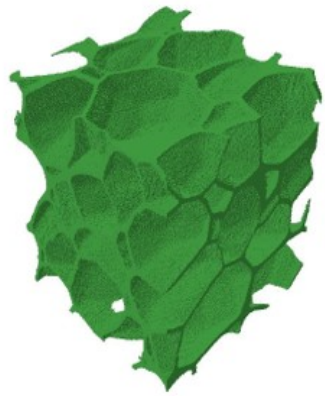

Figure 5.9: Example of Representative Volume Element (RVE) reconstructed from the set of images, obtained with X-Ray computed tomography, applying the marching cube algorithm; the sample refers to a sub-domain belonging to PET 130 sample B ($\phi = 16.78\%$ and $DA = 0.66$).

The results of simulation post-processing, in terms of elastic constants and in the specific case the three apparent Young moduli (E_1^*, E_2^*

and E_3^*), are displayed in figure 5.10 and compared with experimental data already obtained in chapter 3.

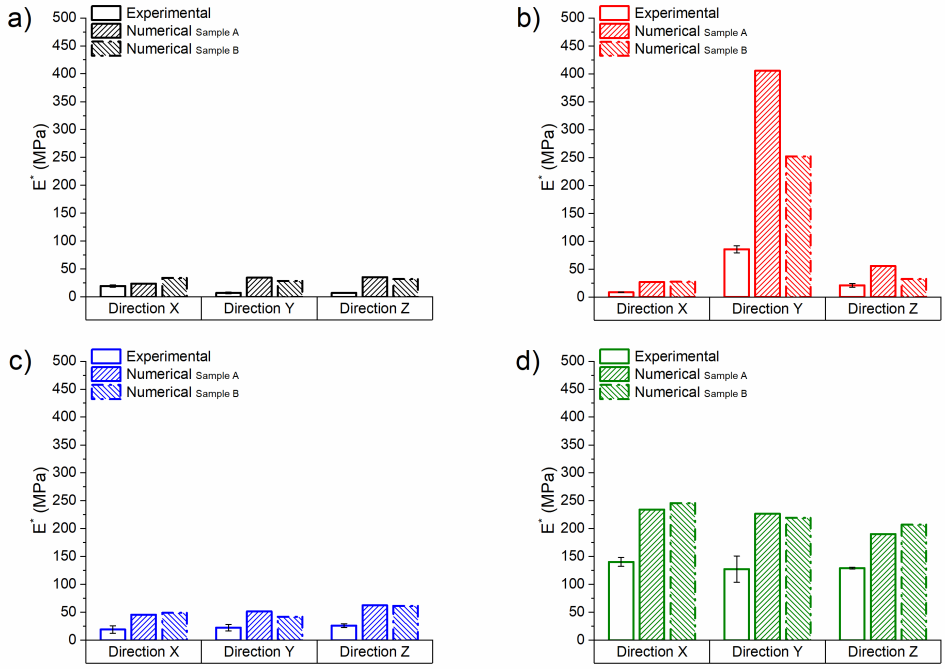

Figure 5.10: Comparison between apparent experimental and numerical stiffness evaluated along the three main orthogonal directions (X, Y and Z) of the foams. Experimental data shows average values and dispersion of five samples for each foam density; for numerical simulations, individual results obtained for each reconstructed sample are shown.

Experimental and numerical results are in fair agreement, with the exception of the Y direction for samples PET 100 A and B; this discrepancy was attributed to the densification region identified in the set of images obtained from X-Ray computed tomography analysis. During the reconstruction of the sub-domain including the densification region a relatively large number of very small voids, that go undetected in the CT scans, were neglected; this error leads to a significant over-estimation of the apparent stiffness in Y direction. Nevertheless, the

apparent stiffnesses obtained from the simulation are systematically higher than the experimental ones; this fact can be explained with the choice of symmetry boundary conditions enforced in the finite element simulations [21]: the repetition in space of the simulated elementary unit cell leads to the overestimation of the macroscopic mechanical response. The real structure, as shown by the bi-variate statistical analysis is made of a great variety of sub-domains, each group characterized by specific value of solid volume fraction, ϕ, and structural degree of anisotropy; assuming the internal microstructure made up of a single sub-domain leads to compute a stiffer macroscopic mechanical response since all the sub-domains characterized by a lower value of solid volume fraction are neglected. Another minor reason could be attributed to the selected Young modulus of the constituent material, taken from the literature for amorphous PET; this value could be higher than the actual one of the PET with which the inspected expanded polymeric material is made of, but the impossibility to mechanically characterize the constituent material forced the adoption of literature data [17] [13].

Besides these minor differences, the results confirm what was already observed in chapter 3 with experimental tests.

The last validation step was made with the aim of testing all the sub-domains belonging to one category of the bi-variate statistical distribution to verify that they exhibit a similar macroscopic mechanical response. The results, once again in terms of apparent stiffness along three orthogonal directions, are displayed in figure 5.11 and refer to all the sub-domains belonging to a bin category that exhibits the same values of solid volume fraction, ϕ, and degree of structural anisotropy, DA.

A small variation of the apparent stiffnesses is reported along the three main orthogonal directions (X, Y and Z) for all the sub-domains belonging to the selected bin of the bi-variate statistical distribution. This result proves that the dimension of the bin selected is adequate to group the RVE according to their microstructural characteristics and

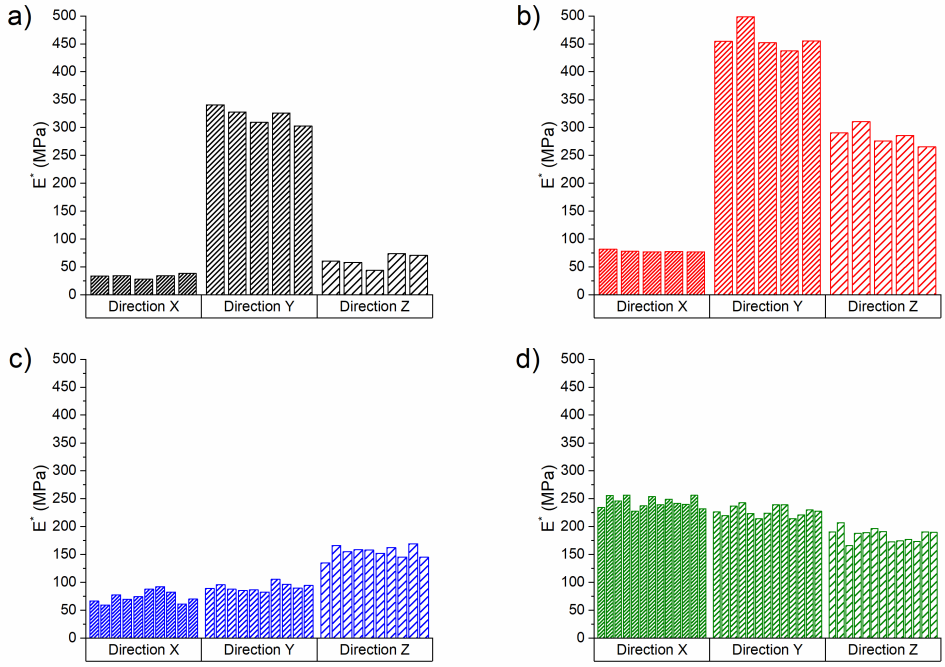

Figure 5.11: Apparent stiffness evaluated along three main orthogonal directions (X, Y and Z) for all the sub-domains belonging to a specific bin of the bi-variate statistical distribution; a) PET 80 sample A for ϕ bin 15% − 20% and DA bin 0.90 − 0.95, b) PET 100 sample B for ϕ bin 20% − 25% and DA bin 0.85 − 0.90, c) PET 130 sample B for ϕ bin 15% − 20% and DA bin 0.65 − 0.70, a) PET 320 sample A for ϕ bin 30% − 35% and DA bin 0.15 − 0.20.

that the two variables selected, solid volume fraction and structural anisotropy degree are good parameters to characterize the macroscopic mechanical behaviour of the different sub-domains. The small variations detected among the different sub-domains can be attributed to small variations of solid volume fraction inside the bin of the distribution and the different voids morphology included in the sub-domains.

5.4.2 Porous solids and Cellular solids

Figure 5.12 displays the correlation between the average apparent stiffness, computed as the average of the three Young moduli ($E^*_{Mean} = \frac{E^*_1+E^*_2+E^*_3}{3}$, normalized with respect to the constituent material bulk modulus (E_S) used in the finite element simulations, and the void volume fraction of the samples ($1-\phi$). Experimental data, numerical data used for model validation and numerical data obtained from sub-domains representing virtual foam structures outside the available experimental range are plotted. For the experimental data the void volume fraction is estimated with equation 4.41 relating normalized apparent density and solid volume fraction (ϕ). All the available experimentally tested samples are considered separately since it is clear from the graph that a variation in the microstructure, in terms of void volume fraction in this specific case, leads to a more or less significant variation of the normalized apparent stiffness. In the plot the star-like point represents the ideal bulk (not foamed) polymer, having 0% void volume fraction.

Combining the information coming from numerical simulations performed on numerical structures and the ones obtained from experimental tests and numerical simulations performed on RVE representing real tested structures, a bilinear trend could be highlighted on the graph, with a change in slope around 80% of void volume fraction value. This variation in the sensitivity of the apparent stiffness to the void volume fraction is consistent with a transition in the deformation mechanism from an axially dominated to a bending dominated one [5]. The value of 80% void volume fraction is consistent with scientific literature [4] [8] and here is proposed as a threshold value that distinguishes two classes of expanded polymeric material: the so-called porous solids, subjected to a balanced combination of axial and bending deformation mechanisms under loading, and the so-called cellular solids, whose main deformation mechanism is dominated by bending. This distinction is

clearly not sharp: in the case of the experimentally tested samples, all the densities clearly belong to the cellular solid group except for PET 320 which is in the transition region. Another aspect of great importance is that in the cellular solid regions the dependence of the apparent stiffness on the void volume fraction is very strong: the accurate determination of the internal microstructure characteristics thus becomes a crucial aspect in the study of macroscopic mechanical response of these materials.

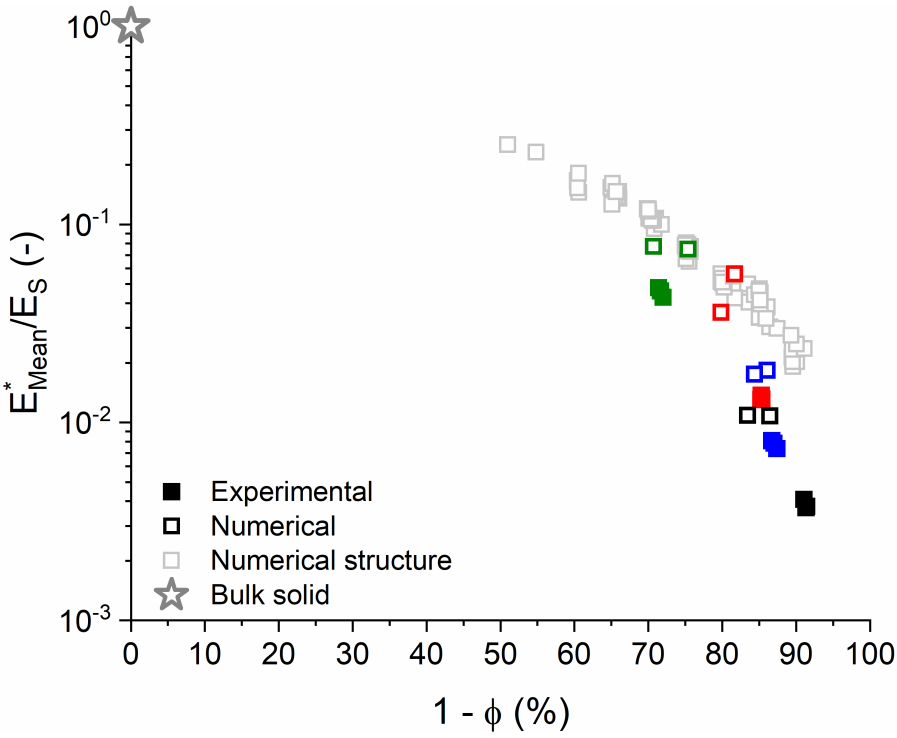

Figure 5.12: Normalized mean apparent stiffness ($\frac{E^*_{Mean}}{E_S}$) as a function of void volume fraction ($1-\phi$). Filled coloured symbols represent experimental mechanical tests and empty coloured symbols are the corresponding numerical simulations; empty grey symbols are the results obtained from numerical simulation performed on sub-regions that do not have corresponding experimental data.

The existence of two distinct regions in the previous graph is further supported by the results displayed in figure 5.13. In this graph the dif-

ferent deformation contributions, computed during the post-processing of simulation results by applying Gurson model, are plotted, once again, as a function of void volume fraction. In the graph the red dashed line represents the macroscopic strain, applied through the correspondent displacement in finite element simulation, while the symbols represent the two deformation mechanisms separated using Gurson model: volumetric deformation (orange) and surface deformation (green). Also, in this case, the star symbols represent the bulk material, whose void volume fraction is equal to 0%, with a purely volumetric deformation mechanism. A trend of increasing surface component with increasing void volume fraction is clearly visible, with the volumetric component vanishing as the void fraction approaches 100%. The main deformation contribution becomes the surface one around a void volume fraction value equal to 80%. A similar threshold value, similar to the one found in figure 5.12, is highlighted and hence this fact justifies the adoption of this value as a threshold to discriminate between cellular and porous-like solids.

Figure 5.14 shows the normalized apparent Young moduli as a function of structural anisotropy degree (DA). It is clearly visible that for increasing values of DA the values in the three directions diverge, implying a progressively more anisotropic mechanical behaviour. Conversely, for low values of DA, it appears that the expanded material can be described by a simpler model, such as for example transversely isotropic or even fully isotropic.

This result confirms the validity of the approach based on a linear elastic constitutive model coupled with the scalar structural anisotropy parameter, in this chapter evaluated with Mean Intercept Length (MIL) algorithm, able to relate the macroscopic mechanical behaviour to the relevant morpho-structural features of the foams. This aspect will be deeply studied and discussed in chapter 7.

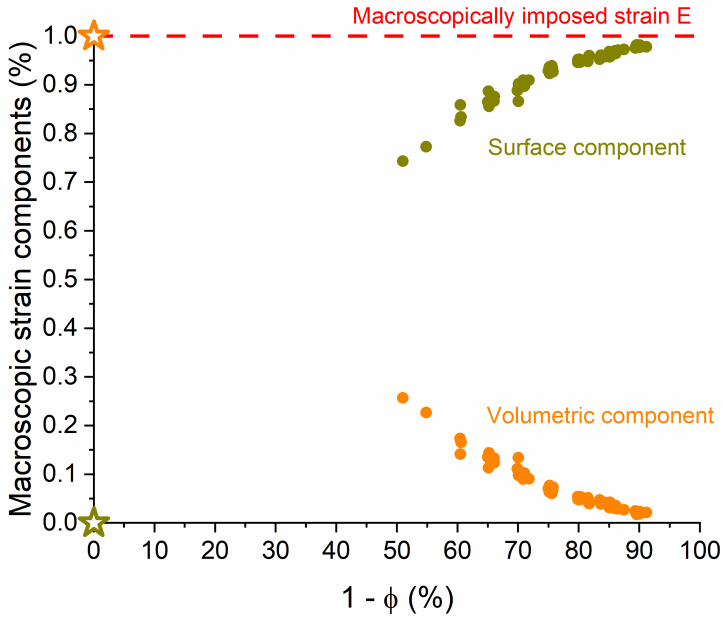

Figure 5.13: Deformation components of the simulated sub-domains as a function of void volume fraction; the two contributions derive from the application of Gurson model. Dashed red line represents the macroscopic strain applied as a boundary condition in finite element modelling.

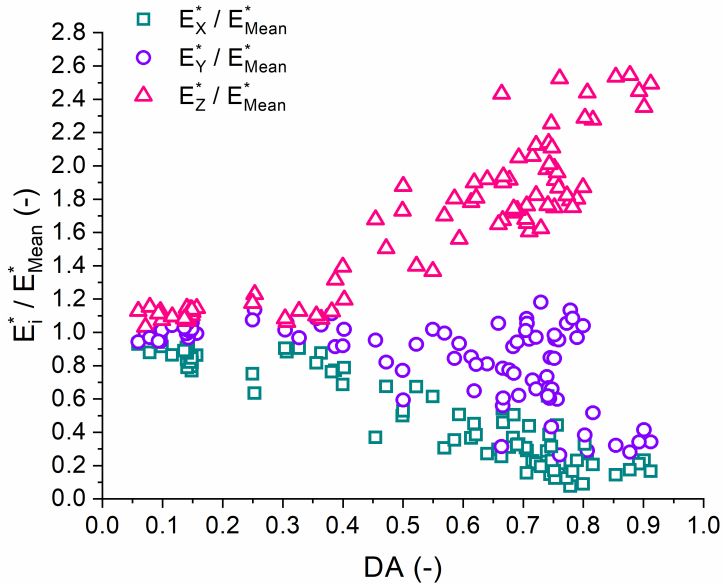

Figure 5.14: Young moduli normalized with respect to their mean values as a function of structural anisotropy degree (DA).

5.4.3 Structure – Mechanical behaviour basic relationships

In this section the correlations between average elastic constants and void volume fraction are shown and they are compared with the predictions of two of the most popular analytical models, Ashby and Zhu, already presented in chapter 2. The attention is focused on data obtained from sub-domains exhibiting a void volume fraction $(1-\phi)$ greater than 60%, hence considering the transition region between porous and cellular solids and covering almost all the region assigned to cellular solids, characterized by void volume fraction values greater than 80%.

Figure 5.15 displays the average apparent Young modulus ($E^*_{Mean} = \frac{E^*_1+E^*_2+E^*_3}{3}$), normalized with respect to the Young modulus of bulk constituent polymer (E_S), as a function of $1-\phi$. The two dashed lines represent the prediction of Ashby [8] and Zhu [29] analytical models, already described in chapter 2. It is clearly visible how the Ashby prediction, built on a simplified hexahedral unit cell, foresees higher values with respect to the computed one, which accounts for the geometrical irregularity of the systems under investigation. Conversely the Zhu model, even if aimed at the description of open cell foams, well captures the trend of experimental data.

Figure 5.16, analogously to the previous one, displays the average apparent Poisson coefficient ($\nu^*_{Mean} = \frac{\nu^*_{12}+\nu^*_{13}+\nu^*_{23}}{3}$) as a function of void volume fraction $(1-\phi)$. Also, in this case the predictions of Ashby and Zhu analytical models are plotted. The experimental Poisson coefficients are not reported since they were not measured. The results obtained are apparently independent from the void volume fraction, as described by Ashby model, even if, once again, the latter overestimates the average value; Ashby derived a constant Poisson coefficient equal to $\frac{1}{3}$ while the average value found was around 0.25. Zhu model instead implies a dependence of the Poisson coefficient which decreases from

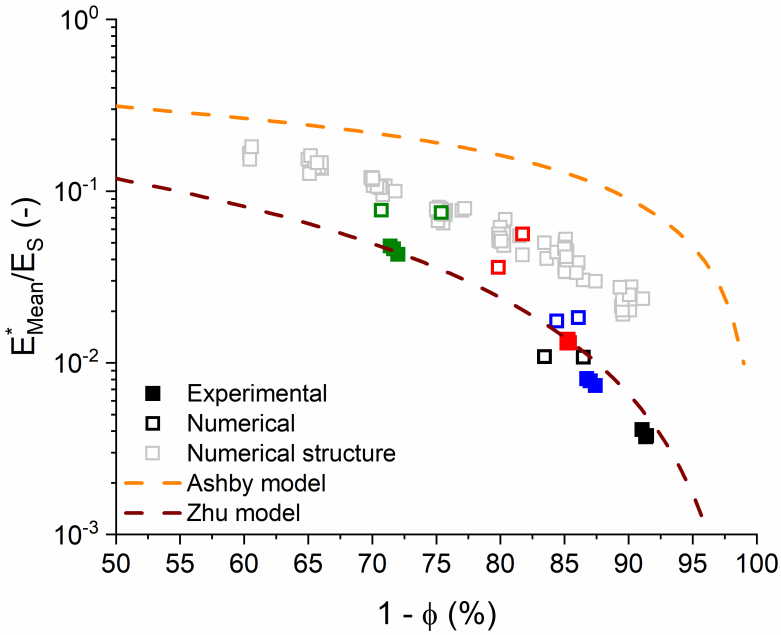

Figure 5.15: Normalized mean apparent stiffness ($\frac{E^*_{Mean}}{E_S}$) as a function of void volume fraction ($1-\phi$). Filled coloured symbols represent experimental mechanical tests and empty coloured symbols are the corresponding numerical simulations; empty grey symbols are the results obtained from numerical simulation performed on sub-regions that do not have corresponding experimental data. Dashed lines represent the analytical prediction made with Ashby model (orange line) and Zhu model (brown line).

0.5, for a solid material, to 0, for a void volume fraction equal to 0%. The classical boundaries of macroscopic Poisson coefficient for a linear elastic solid must not be considered in the case of cellular materials, given their heterogeneous, anisotropic nature. The macroscopic linear elastic regime will be investigated more in depth in chapter 7.

For the sake of completeness, in figure 5.17 average apparent shear modulus ($G^*_{Mean} = \frac{G^*_{12}+G^*_{13}+G^*_{23}}{3}$), normalized with respect to the shear modulus of bulk constituent polymer (G_S), as a function of void volume fraction ($1-\phi$) is reported with the prediction of analytical models. Bulk shear modulus is computed from equation 5.11, since the constituent

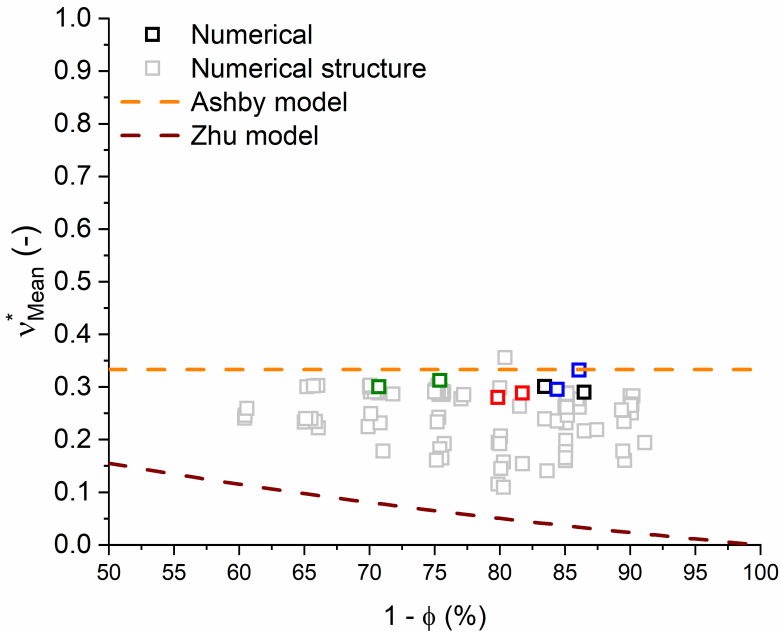

Figure 5.16: Mean apparent Poisson coefficient (ν^*_{Mean}) as a function of void volume fraction ($1-\phi$). Filled coloured symbols represent experimental mechanical tests and empty coloured symbols are the corresponding numerical simulations; empty grey symbols are the results obtained from numerical simulation performed on sub-regions that do not have corresponding experimental data. Dashed lines represent the analytical prediction made with Ashby model (orange dashed line) and Zhu model (brown line).

material is assumed linear elastic isotropic, and is taken equal to 1036 MPa. Results are qualitatively similar to those displayed for the Young modulus.

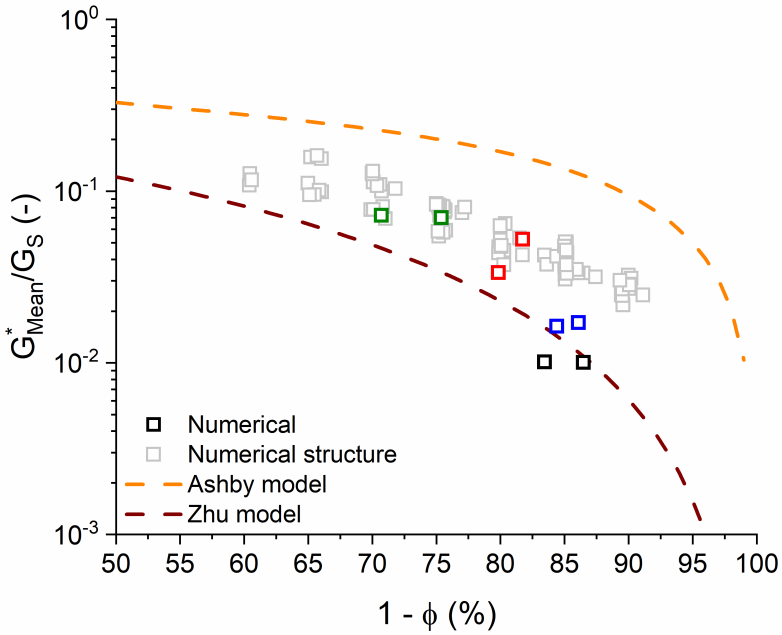

Figure 5.17: Normalized mean shear modulus ($\frac{G^*_{Mean}}{G_S}$) as a function of void volume fraction ($1-\phi$). Filled coloured symbols represent experimental mechanical tests and empty coloured symbols are the corresponding numerical simulations; empty grey symbols are the results obtained from numerical simulation performed on sub-regions that do not have corresponding experimental data. Dashed lines represent the analytical prediction made with Ashby model (orange dashed line) and Zhu model (brown line).

5.5 Concluding remarks

In the present chapter a first image-based numerical approach developed and optimized along this PhD thesis work was presented. The well consolidated representative volume element approach was adapted and optimized to the specific material category inspected in the present work. The aim of developing an efficient tool to model the macroscopic mechanical response of expanded polymeric materials, considering the real complex microstructure and the constitutive material mechanical properties, was reached. The approach is focused on finite strain

mechanical modelling, with the aim of finding correlations between elastic constants and suitable scalar parameters used to describe the complex and irregular microstructure of such class of materials. During the approach validation a satisfactory agreement between experimental and numerical results was obtained and hence the model was used to simulate macroscopic mechanical behaviour of additional geometries to increase the range of data on which correlations are built. Moreover, an unexpected fair agreement between the results obtained and Zhu analytical model has been found, proving that the image-based approach developed is a valid tool to compute macroscopic mechanical information on expanded polymeric materials, even if the two systems reported, open-cell systems for Zhu model and closed-cell systems analysed in the present thesis, are compared. The results also confirm the fundamental importance of knowing and inspecting the real complexity of internal microstructure to understand the macroscopic behaviour of expanded polymeric materials.

Some limitations in the approach are still present, since, as shown in previous paragraphs, the model overestimates the real macroscopic mechanical response of the inspected material. A possible improvement could be achieved through the implementation of periodic or semi-periodic boundary conditions in finite element simulation. This aspect was not faced in the present work due to the complexity of the finite element mesh obtained from X-Ray computed tomography scans and the objective was beyond the scope of the present thesis. Moreover, from a numerical point of view, the implementation of this kind of boundary conditions would lead to a greater request of numerical resources, compromising the efficiency of the developed approach. Another possible improvement concerns the constituent material of the inspected foams; in the present approach it is considered linear elastic isotropic, while it is well known and reported in the literature that polymeric materials are quite sensitive to process parameters, such as temperature and pressure. During the foaming process significant ori-

entation phenomena are expected in the amorphous phase. This could require the use of a more complex constitutive law, such as transversely isotropic constitutive law, to describe the mechanical behaviour of the polymer of which the foams are made of. This change would also lead to a significant increase of the numerical resources required to perform simulations starting from high-resolution images.

In the following chapters the presented image-based approach will be employed to further study other aspects of expanded polymeric materials; in the next chapter the effect of voids morphology on macroscopic mechanical response will be investigated, while in chapter 7 a deeper investigation of elastic constants and structural parameters relationships is presented with the aim of identifying the most suitable linear elastic constitutive model able to the describe macroscopic mechanical behaviour exploiting only structure quantities, computed through the application of different algorithms, such as the ones presented in chapter 4.

5.6 References

[1] E.W. Andrews et al. “Size effects in ductile cellular solids. Part II: experimental results”. en. In: *International Journal of Mechanical Sciences* (2001), page 13.

[2] S.K. Boyd and R. Müller. “Smooth surface meshing for automated finite element model generation from 3D image data”. en. In: *Journal of Biomechanics* 39.7 (Jan. 2006), pages 1287–1295. DOI: 10.1016/j.jbiomech.2005.03.006. URL: https://linkinghub.elsevier.com/retrieve/pii/S0021929005001442.

[3] M. Campillo et al. “Development of an RVE using a DEM–FEM scheme under modified approximate periodic boundary condition to estimate the elastic mechanical properties of open foams”. en. In: *Engineering with Computers* (Mar. 2021). DOI: 10.1007/s00366-021-01355-1. URL: http://link.springer.com/10.1007/s00366-021-01355-1.

[4] V.S. Deshpande, M.F. Ashby, and N.A. Fleck. “Foam topology: bending versus stretching dominated architectures”. en. In: *Acta Materialia* 49.6 (Apr. 2001), pages 1035–1040. DOI: 10.1016/S1359-6454(00)00379-7. URL: https://linkinghub.elsevier.com/retrieve/pii/S1359645400003797.

[5] V.S. Deshpande and N.A. Fleck. “Multi-axial yield behaviour of polymer foams”. en. In: *Acta Materialia* 49.10 (June 2001), pages 1859–1866. DOI: 10.1016/S1359-6454(01)00058-1. URL: https://linkinghub.elsevier.com/retrieve/pii/S1359645401000581.

[6] F. Fritzen et al. “Computational homogenization of porous materials of Green type”. en. In: *Computational Mechanics* 52.1 (July 2013), pages 121–134. DOI: 10.1007/s00466-012-0801-z. URL: http://link.springer.com/10.1007/s00466-012-0801-z.

[7] D. Garoz et al. “Consistent application of periodic boundary conditions in implicit and explicit finite element simulations of damage in composites”. en. In: *Composites Part B: Engineering* 168 (July 2019), pages 254–266. DOI: 10.1016/j.compositesb.2018.12.023. URL: https://linkinghub.elsevier.com/retrieve/pii/S1359836818337776.

[8] L.J. Gibson and M.F. Ashby. *Cellular Solids*. en.

[9] R.E. Guldberg, S.J. Hollister, and G.T. Charras. “The Accuracy of Digital Image-Based Finite Element Models”. en. In: *Journal of Biomechanical Engineering* 120.2 (Apr. 1998), pages 289–295. DOI: 10.1115/1.2798314. URL: https://asmedigitalcollection.asme.org/biomechanical/article/120/2/289/399907/The-Accuracy-of-Digital-ImageBased-Finite-Element.

[10] A.L. Gurson. “Continuum theory of ductile rupture by void nucleation and growth: Part I - Yield criteria and flow rules for porous ductile media”. en. In: *Continuum theory of ductile rupture by void nucleation and growth: Part I - Yield criteria and flow rules for porous ductile media* 39 (Sept. 1975), page 63.

[11] S.J. Hollister and N. Kikuchi. “A comparison of homogenization and standard mechanics analyses for periodic porous composites”. en. In: *Computational Mechanics* 10.2 (1992), pages 73–95. DOI: 10.1007/BF00369853. URL: http://link.springer.com/10.1007/BF00369853.

[12] A. Khare, R. MacKenzie, and M.B. Paranjape. “On the Coleman-Hill theorem”. en. In: *Physics Letters B* 343.1-4 (Jan. 1995), pages 239–243. DOI: 10.1016/0370-2693(94)01420-H.

[13] E.T.J. Klompen et al. “Modeling of the Postyield Response of Glassy Polymers: Influence of Thermomechanical History”. en. In: *Macromolecules* 38.16 (Aug. 2005), pages 6997–7008. DOI:

10.1021/ma050498v. URL: https://pubs.acs.org/doi/10.1021/ma050498v.

[14] V. Kouznetsova, M.G.D. Geers, and W.A.M. Brekelmans. "Multi-scale constitutive modelling of heterogeneous materials with a gradient-enhanced computational homogenization scheme". en. In: *International Journal for Numerical Methods in Engineering* 54.8 (July 2002), pages 1235–1260. DOI: 10.1002/nme.541. URL: http://doi.wiley.com/10.1002/nme.541.

[15] W.E. Lorensen and H.E. Cline. "Marching cubes: a high resolution 3D surface construction algorithm". en. In: *Marching cubes: a high resolution 3D surface construction algorithm* 21 (July 1987), page 7.

[16] H.E.H. Meijer and L.E. Govaert. "Multi-Scale Analysis of Mechanical Properties of Amorphous Polymer Systems". en. In: *Macromolecular Chemistry and Physics* 204.2 (Feb. 2003), pages 274–288. DOI: 10.1002/macp.200290080. URL: http://doi.wiley.com/10.1002/macp.200290080.

[17] H.G.H. van Melick, L.E. Govaert, and H.E.H. Meijer. "Localisation phenomena in glassy polymers: influence of thermal and mechanical history". en. In: *Polymer* 44.12 (June 2003), pages 3579–3591. DOI: 10.1016/S0032-3861(03)00089-2. URL: https://linkinghub.elsevier.com/retrieve/pii/S0032386103000892.

[18] R. Moreno, M. Borga, and O. Smedby. "Generalizing the mean intercept length tensor for gray-level images: Generalizing the mean intercept length tensor". en. In: *Medical Physics* 39.7Part2 (July 2012), pages 4599–4612. DOI: 10.1118/1.4730502. URL: http://doi.wiley.com/10.1118/1.4730502.

[19] P.R. Onck, E.W. Andrews, and L.J. Gibson. "Size effects in ductile cellular solids. Part I: modelling". en. In: *International Journal of Mechanical Sciences* (2001), page 19.

[20] L. Riaño and Y. Joliff. “An Abaqus™ plug-in for the geometry generation of Representative Volume Elements with randomly distributed fibers and interphases”. en. In: *Composite Structures* 209 (Feb. 2019), pages 644–651. DOI: 10.1016/j.compstruct.2018.10.096. URL: https://linkinghub.elsevier.com/retrieve/pii/S0263822318315472.

[21] M. Shakoor et al. “On the choice of boundary conditions for micromechanical simulations based on 3D imaging”. en. In: *International Journal of Solids and Structures* 112 (May 2017), pages 83–96. DOI: 10.1016/j.ijsolstr.2017.02.018. URL: https://linkinghub.elsevier.com/retrieve/pii/S0020768317300732.

[22] R.J.M. Smit, W.A.M. Brekelmans, and H.E.H. Meijer. “Prediction of the mechanical behavior of nonlinear heterogeneous systems by multi-level finite element modeling”. en. In: *Computer Methods in Applied Mechanics and Engineering* 155.1-2 (Mar. 1998), pages 181–192. DOI: 10.1016/S0045-7825(97)00139-4. URL: https://linkinghub.elsevier.com/retrieve/pii/S0045782597001394.

[23] S. Tagliabue et al. “An image-based approach for structure investigation and 3D numerical modelling of polymeric foams”. en. In: *Journal of Polymer Research* 28.3 (Mar. 2021), page 75. DOI: 10.1007/s10965-021-02438-9. URL: https://link.springer.com/10.1007/s10965-021-02438-9.

[24] S. Tagliabue et al. “Micro-CT based finite element models for elastic properties of glass–ceramic scaffolds”. en. In: *Journal of the Mechanical Behavior of Biomedical Materials* 65 (Jan. 2017), pages 248–255. DOI: 10.1016/j.jmbbm.2016.08.020. URL: https://linkinghub.elsevier.com/retrieve/pii/S1751616116302806.

[25] G. Taubin. “A signal processing approach to fair surface design”. en. In: *Proceedings of the 22nd annual conference on*

Computer graphics and interactive techniques - SIGGRAPH '95. Not Known: ACM Press, 1995, pages 351–358. DOI: 10.1145/218380.218473. URL: http://portal.acm.org/citation.cfm?doid=218380.218473.

[26] G. Taubin. "Geometric Signal Processing on Polygonal Meshes". en. In: (), page 11.

[27] K. Terada et al. "Simulation of the multi-scale convergence in computational homogenization approaches". en. In: *International Journal of Solids and Structures* 37.16 (Apr. 2000), pages 2285–2311. DOI: 10.1016/S0020-7683(98)00341-2. URL: https://linkinghub.elsevier.com/retrieve/pii/S0020768398003412.

[28] A. Zaoui. "Continuum Micromechanics: Survey". en. In: *Journal of Engineering Mechanics* 128.8 (Aug. 2002), pages 808–816. DOI: 10.1061/(ASCE)0733-9399(2002)128:8(808). URL: http://ascelibrary.org/doi/10.1061/%28ASCE%290733-9399%282002%29128%3A8%28808%29.

[29] H.X. Zhu, J.F. Knott, and N.J. Mills. "Analysis of the elastic properties of open-cell foams with tetrakaidecahedral cells". en. In: *Journal of the Mechanics and Physics of Solids* 45.3 (Mar. 1997), pages 319–343. DOI: 10.1016/S0022-5096(96)00090-7. URL: https://linkinghub.elsevier.com/retrieve/pii/S0022509696000907.

Chapter 6

Morphology influence on macroscopic mechanical response

In the following chapter the numerical approach developed and optimized in the previous chapter will be applied with the aim to study the effect of microstructure morphology on the macroscopic mechanical response of expanded polymeric materials. An approach similar to that proposed by Ashby and Zhu will be adopted and adapted for the specific randomly distributed structures inspected along the present thesis work.

6.1 Introduction

In the scientific literature many works are reported concerning the effect of microscopic structure morphology on the macroscopic mechanical response of expanded polymeric materials, following different approaches [18] [5] [10] [8] [14].

Many authors proposed the application of parametric analysis; they started from the simulation of regular structures, made up of regular unit cell [2], such as Ashby hexahedral cell or Kelvin cell [6], and varied one structural parameter at a time. Among the different considered parameters are the mean thickness of cell structures (beams and/or walls), the total length of the unit cell, the volume of the void and many others [4].

The main limitation of this approach is its inadequacy to deal with irregular structures, such as the real ones characterizing typical expanded polymeric materials [15] [17]. The main difficult resides in finding a reasonable number of suitable scalar parameters to describe such irregular structures [11]. Two different approaches, deterministic and statistical, are commonly adopted. Another problem consists in the difficulty to change only one variable at a time: usually changing a parameter describing the microstructure, for example the mean structure thickness, also implies the change of other related variables, such as the apparent density or the related solid volume fraction, which in turn strongly influences the macroscopic mechanical behaviour of polymeric foams, as widely demonstrated in previous chapter [9].

In the present chapter an approach similar to the one proposed by Ashby and Zhu on regular structures is proposed and suitably modified for its application to irregular and randomly distributed microstructures, like the one already showed in previous chapters. The analytical approach proposed by Ashby [3] and Zhu [16] is briefly summarized in the next section.

6.1.1 Ashby and Zhu elongated cells

The idea at the basis of both Ashby and Zhu model consists in the artificial stretching along one direction of the regular unit cell with which the internal microstructure of expanded polymeric material is represented. Figure 6.1 shows a qualitative example of Ashby unit hexahedral cell elongated along one direction.

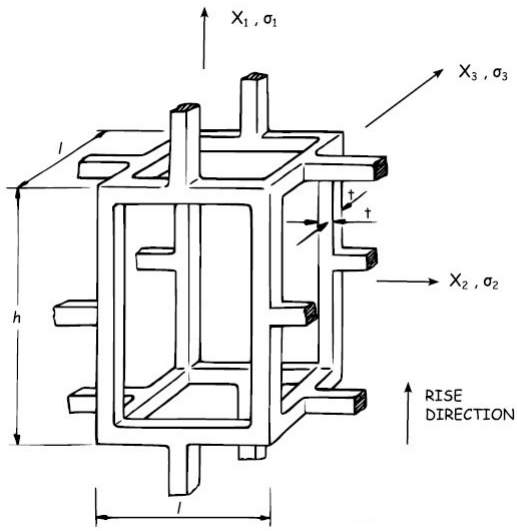

Figure 6.1: Ashby hexahedral unit cell artificially stretched along one direction (direction 1) used to study the effect of structural induced anisotropy in the morphology on macroscopic mechanical response. Image freely adapted from [3].

In analogy with the analysis presented in chapter 2, the characteristic lengths of the unit cell are:

- t: thickness of the beams constituting the unit cell;
- l: the total width and depth of the unit cell, which are the same since the unstretched cell is cubic;
- h: is the total height of the cell, arbitrarily variable according to the entity of applied stretch;

- 1, 2 and 3 are the main orthogonal directions of the reference coordinate system.

Moreover, Ashby defined a morpho-structural parameter, characterizing the morphology of the unit cell: the stretch ratio, $R = \frac{h}{l}$, also referred to as anisotropy ratio.

With this modification it is hence expected that the macroscopic mechanical response of the cell is different along direction 1, with an apparent stiffness E_1^*, and directions 2 and 3, along which an identical apparent stiffness $E_2^* = E_3^*$ is expected. The ratio between the apparent modulus measured along the stretch direction and orthogonal to it $\left(\frac{E_1^*}{E_2^*}\right)$ is defined as the anisotropy ratio, R.

By analysing the structure, exploiting the linear elastic beam theory in the range of finite elastic strains (as already performed in the case of the unstretched unit cell) an analytical expression for the apparent modulus in the stretch direction, normalized with respect to the constituent material Young modulus, E_S, can be computed:

$$\frac{E_1^*}{E_S} = C \left(\frac{t}{l}\right)^4 \frac{h}{l} \tag{6.1}$$

in which C is a generic constant that has to be determined through the fitting of experimental data [3].

Considering a load applied orthogonally to the stretch direction, the analytical expression for the apparent transverse stiffness, once again normalized with respect to the constituent material Young modulus, can be derived:

$$\frac{E_2^*}{E_S} = \frac{E_3^*}{E_S} = \frac{C}{2} \left(\frac{t}{l}\right)^4 \frac{l}{h} \left[1 + \left(\frac{l}{h}\right)^3\right] \tag{6.2}$$

Figure 6.2 displays the two different loading conditions with which equation 6.1 and 6.2 are derived.

The ratio between the apparent stiffness computed along the stretch and its orthogonal direction can be computed as a function of the

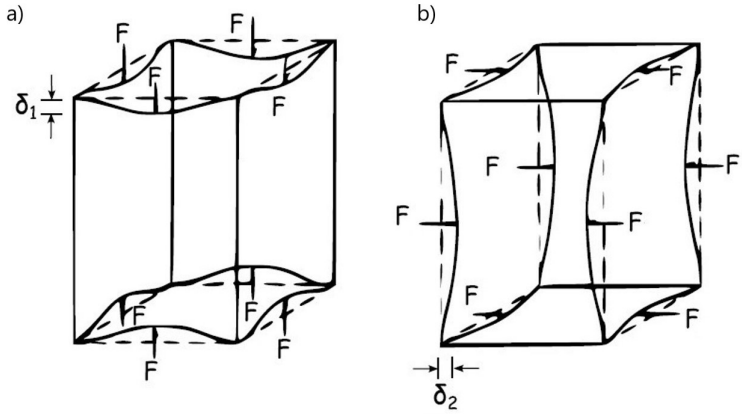

Figure 6.2: Linear elastic deformation of elongated hexahedral unit cell; a) stretch direction for which $\frac{E_1^*}{E_S}$ is computed and b) transverse direction for which $\frac{E_2^*}{E_S} = \frac{E_3^*}{E_S}$ is computed. Image freely adapted from [3].

stretch ratio, as given by:

$$\frac{E_1^*}{E_2^*} = \frac{E_1^*}{E_3^*} = \frac{2R^2}{1 + \frac{1}{R^3}} \tag{6.3}$$

From equation 6.3, a link between the apparent modulus ratio and cell anisotropy is found. Figure 6.3 displays a comparison between experimental data, collected from different scientific works on open cell foams, and the prediction obtained with the analytical expression reported by equation 6.3.

The graph demonstrates that the model gives a fair description of experimental data.

A similar approach is proposed also by Zhu in his analytical model [16], leading to the formulation of more complicate relationships due to the higher geometrical complexity of the tetrakaidekahedral unit cell considered, as shown in Figure 6.4. The unique geometric parameters necessary to identify the shape and size of the elongated cell are also defined: b, L and θ. The unit cell contains eight hexagonal faces, two horizontal square faces and four vertical diamond faces. The horizontal

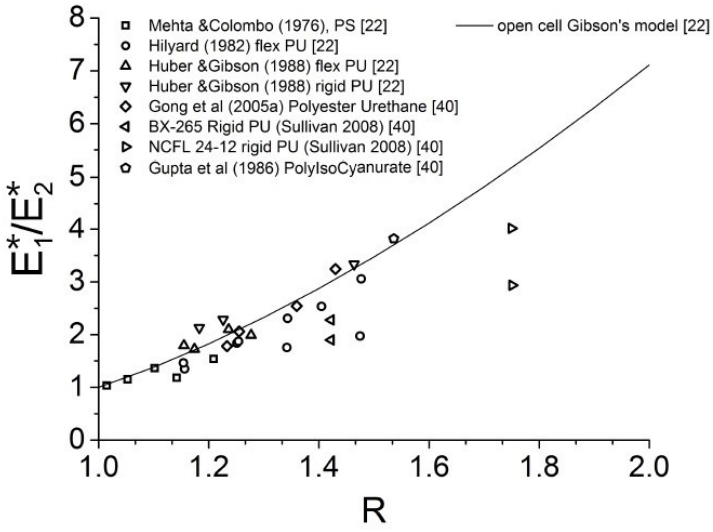

Figure 6.3: Apparent stiffness ratio as a function of stretch ratio for different open cell foams. Empty dots represent experimental data collected from different scientific works while the continuous black line represents the prediction of Ashby model. Figure freely adapted from [7] [13].

square faces have sides of length b and the diamond faces have sides of length L. The hexagonal faces have four sides with length L and two sides with length b. The angle θ defines the orientation of the hexagonal faces with respect to the rise direction as well as the obtuse angle of the vertical diamond faces, 2θ.

In this case, as proposed by Zhu and other authors, it is possible to derive analytical equations for the elongated unit cell as a function of three geometrical parameters (b, L and θ in the following example) instead of the two reported for the previous case.

For this kind of cell, considering H as the total height of the cell and D the total width and depth of the cell, aspect ratio can be defined as:

$$R = \frac{H}{D} = \frac{4L\ sin\theta}{2L\ cos\theta + \sqrt{2b}} \tag{6.4}$$

and, in addition, a transversal aspect ratio factor can be defined as

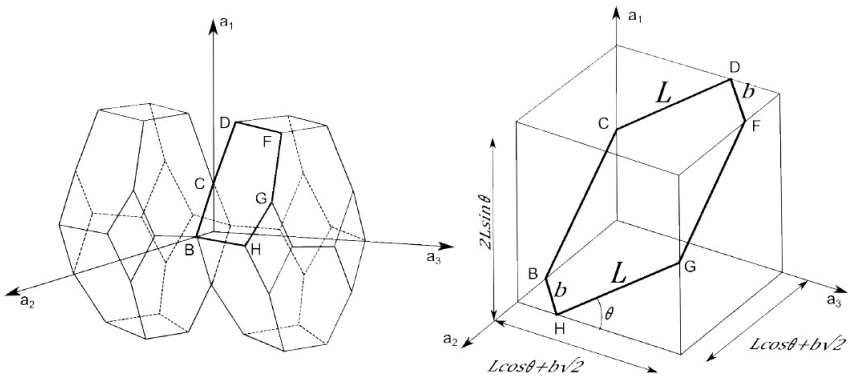

Figure 6.4: Unit tetrakaidekahedral cell used to skeletonize the internal microstructure of expanded polymeric material in Zhu analytical model; characteristic dimensions: b, L, and θ are reported in the right part of the figure. Image freely adapted from [13].

well:

$$Q = \frac{b}{L\ cos\theta} \tag{6.5}$$

Solving the structure analytically, exploiting the elastic beam theory, in a similar way to what performed by Gibson and Ashby in the previous example, an analytical expression of the apparent stiffnesses ratio can be computed:

$$\frac{E_1^*}{E_2^*} = \frac{E_1^*}{E_3^*} = \\ = \frac{R^2}{4} * \left[\frac{C_1 \left(2\bar{Q}^2 R^2 + \frac{63Q^3}{\sqrt{16+\bar{Q}^2R^2}} \right) + \left(\frac{\rho^*}{\rho_S} \right) \frac{8C_2 R\bar{Q}^3 \left(32+4Q\sqrt{16+\bar{Q}^2R^2} \right)}{\left(4Q+2\sqrt{16+\bar{Q}^2R^2} \right)\left(16+\bar{Q}^2R^2 \right)}}{16C_1 + \left(\frac{\rho^*}{\rho_S} \right) \frac{8C_2 R^3 \bar{Q}^5}{\left(4Q+2\sqrt{16+\bar{Q}^2R^2} \right)\left(16+\bar{Q}^2R^2 \right)}} \right] \tag{6.6}$$

in which:

$$\bar{Q} = 2 + \sqrt{2}Q \tag{6.7}$$

$$C_1 = \sqrt{3} - \frac{\pi}{2} \tag{6.8}$$

$$C_2 = \frac{20\sqrt{3} - 11\pi}{2\sqrt{3} - \pi} \tag{6.9}$$

As anticipated the analytical expression is far more complicated than the one proposed by Ashby, but it has the advantage to suitably adapt to a large variety of morphologies due to the possibility to tune two parameters (R and Q), during fitting of experimental data [13].

6.2 Materials and methods

6.2.1 Materials

The set of images representative of the internal microstructure of the expanded polymeric material, already presented in previous chapter, were considered. Moreover, a new material was added: an expanded polypropylene, made up of sintered expanded beads, whose nominal density is 120 $\mathrm{kg\,m^{-3}}$. This material is added to the thesis work with the aim of increasing the range of available morphologies. This material and its internal microstructure had been experimentally characterized in a previous study through mechanical testing and X-Ray computed tomography: is will be called, from here on, EPP120 [1]. The numerical approach of Representative Volume Element (RVE), applied on PET samples, was validated with the same procedure described in chapter 5 also for EPP120.

6.2.2 Structure analysis

The internal structure was investigated following the same procedures described in chapter 4, but adopting a different formulation of Mean Intercept Length algorithm, in the version proposed by Moreno and co-authors [12]. A similar approach to the one adopted by Gibson and Ashby was used but since the structures analysed in the present work are irregular and randomly distributed in space, variables equivalent to the characteristic lengths proposed by Ashby for regular structures were adopted in this case. Figure 6.5 displays the correspondence among the related quantities used to describe regular and irregular structures. In the case of regular hexahedral cells, Ashby proposed as characteristic lengths the thickness of cell walls, th, and the total length of the cell, L; in this case, on random structures, the average volumetric structure thickness, $\langle th \rangle$, and the mean volumetric equivalent diameter of the voids, $\langle D_{eq} \rangle$, are used. The two quanti-

ties were computed with a custom-developed code, made with *Matlab R2019b*, as already explained in chapter 4. The ratio between these two quantities is considered as the main scalar parameter describing the morphology of the microstructure.

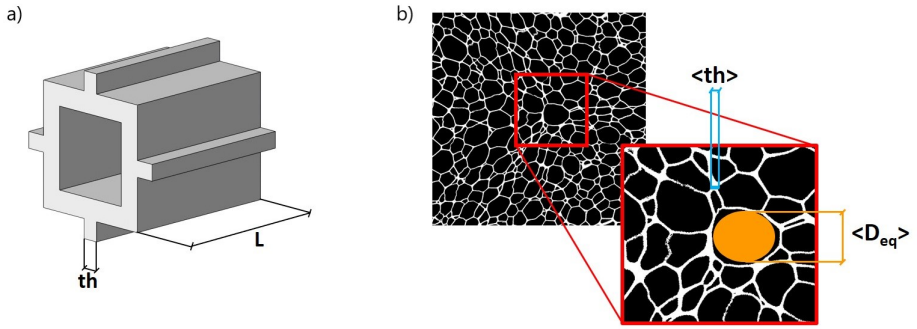

Figure 6.5: Characteristic dimensions of the microstructure: a) Ashby unit regular hexahedral cell: thickness of cell walls, th, and total length of the cell, L; b) randomly distributed structures: mean volumetric structure thickness, $\langle th \rangle$, and mean volumetric equivalent diameter, $\langle D_{eq} \rangle$.

6.2.3 Finite element modelling

Finite element simulations were performed on sub-domains following the same approach developed and presented in chapter 5. 75 sub-domains were selected from the available set of images, characterized by a fixed solid volume fraction, ϕ, varying from 10% up to 40% and grouped according to their solid volume fraction (in 5% bins) and variable morphology parameter ratio, $\frac{\langle th \rangle}{\langle D_{eq} \rangle}$. Constituent materials were considered linear elastic with the related constants reported in table 6.1.

Again, $C3D8$ linear cubic finite elements with full integration were used and the total number of elements varied from a minimum of $6 * 10^5$ up to a maximum of $2 * 10^6$, which corresponds to a number of free nodes that varied from $8 * 10^5$ up to $5 * 10^6$. As reported in previous chapters, all pre-processing and post-processing operations were performed on a

Table 6.1: Linear elastic parameters.

Material	Parameter	Value
PET	Young's modulus (E)	2900 MPa
	Poisson's ratio (ν)	0.4
PP	Young's modulus (E)	1300 MPa
	Poisson's ratio (ν)	0.3

personal computer with 2 cores and 16 GB RAM, while the actual finite element simulations were performed on a Linux machine with 24 cores and 49 GB RAM. Average CPU time needed for a single simulation varied between 5 and 28 hours depending on the total number of free nodes included in the finite element mesh.

6.2.4 Artificial image stretching

A custom-made algorithm, implemented in *Matlab R2019b*, was developed to artificially stretch along a single direction the set of images representing the structure contained in a selected sub-domain. This was performed while keeping the solid volume fraction of the selected sub-domain almost constant, to selectively modify the parameter describing structure morphology. Figure 6.6 displays a bidimensional example of the transformation of a generic sub-domain by the stretching algorithm.

Three sub-domains were selected, characterized by a solid volume fraction of 10%, 20% and 30%, respectively, and artificially stretched along one direction up to a maximum value of $50x$.The selected sub-domains belonged to the previously described PET 130 B, PET 100 A and PET 320 B samples. On each stretched sub-domain, the procedure adopted for finite element analysis, described in chapter 5, was applied. This step was performed to support observations performed on numerical results obtained on unstretched sub-domains representing experimentally available morphologies.

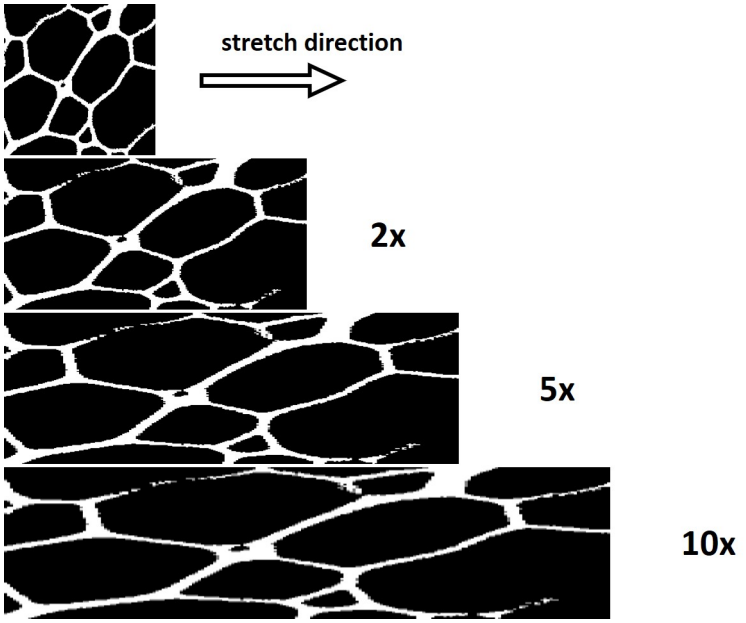

Figure 6.6: Bidimensional example of artificially stretched set of images representing a sub-domain; the sub-domain is stretched keeping the solid volume fraction constant and only modifying the parameter used to describe structure morphology.

6.3 Results and discussion

The first part of the results section describes the validation of the Representative Volume Element approach on the newly introduced sample, EPP120.

6.3.1 EPP120 model validation

Figure 6.7 shows a set of images obtained from X-Ray computed tomography, representing the internal microstructure of EPP120. In this case the global set is made of 1000 images with a spatial resolution of 3.33 µm. EPP 120 has a clearly different structure with respect to PET; this difference is strictly related to the different production process adopted (extrusion for PET and beads moulding and sintering for EPP120).

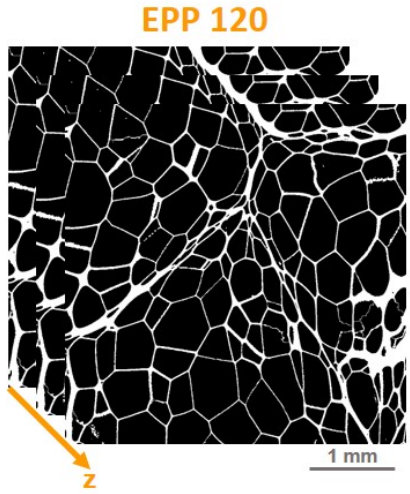

Figure 6.7: Set of images representing the internal microstructure of sample EPP120; from the images the expanded sintered beads structure is clearly visible, evidenced by the edges of beads touching each other.

Results, in terms of apparent stiffnesses, of the validation using the Representative Volume Element (RVE) approach on EPP120 are reported in figure 6.8.

Also, in this case, for the same reason mentioned in chapter 5, numerical results are systematically higher than experimental data; the agreement is still considered good enough to consider the approach valid also in the case of EPP120. The results of finite element simulations are able to describe the transversely isotropic macroscopic response of the expanded material, with one direction (X) along which the apparent stiffness is higher with respect to the other two (Y and Z). The dimension of the cubic RVE side adopted for this material is 250 pixel, corresponding to a total reconstructed volume of 0.833 mm^3. The two domains used for model validation belong to the bivariate distribution bin characterized by a solid volume fraction, ϕ, equal to 10% and a structural anisotropy degree (DA) equal to 0.36.

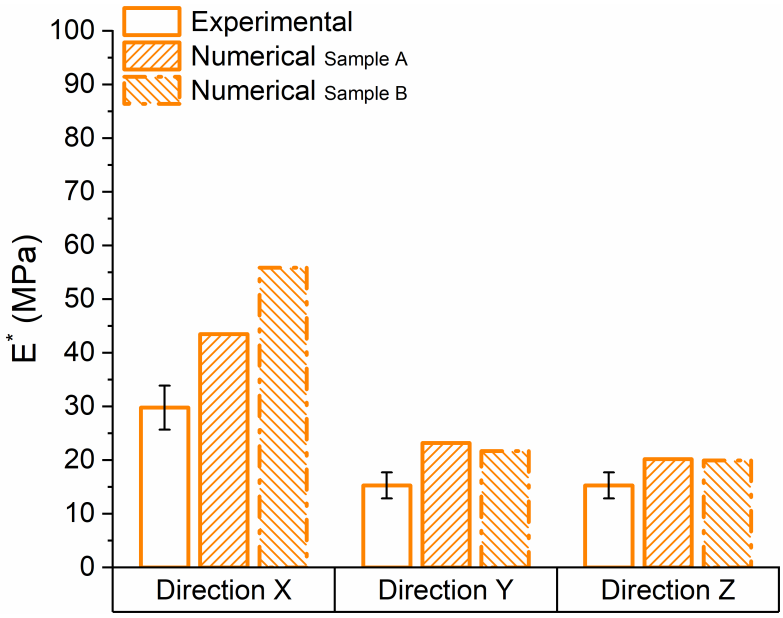

Figure 6.8: Comparison between apparent experimental and numerical stiffness evaluated along the three main orthogonal directions (X, Y and Z) of the foam EPP120. Average values and dispersion of five samples are reported for the experimental data; for numerical simulations, individual results obtained for each reconstructed sample are shown.

6.3.2 Morphology

Figure 6.9 shows the relationship found between the solid volume fraction, ϕ, and the characteristic dimensions used to quantify the morphology of the cells of the microstructure. A linear fit of the data, represented by the dashed red line in the plot, was performed and a power-law relationship similar to the one obtained in chapter 4 was identified:

$$\phi \approx \left(\frac{th}{D_{eq}}\right)^{n} \quad \text{with} \quad n = 1.36 \tag{6.10}$$

The value obtained for the exponent n is very close to the one given by Gibson and Ashby for a regular closed cell [3], equal to 1.5; the linear fit is considered valid from a statistical point of view since it has an r^2-value greater than 0.99. The similarity between this relationship and

the one found in the case of large volume analysis, presented in chapter 4, supports the representativeness of the sub-domains size selected for each analysed material.

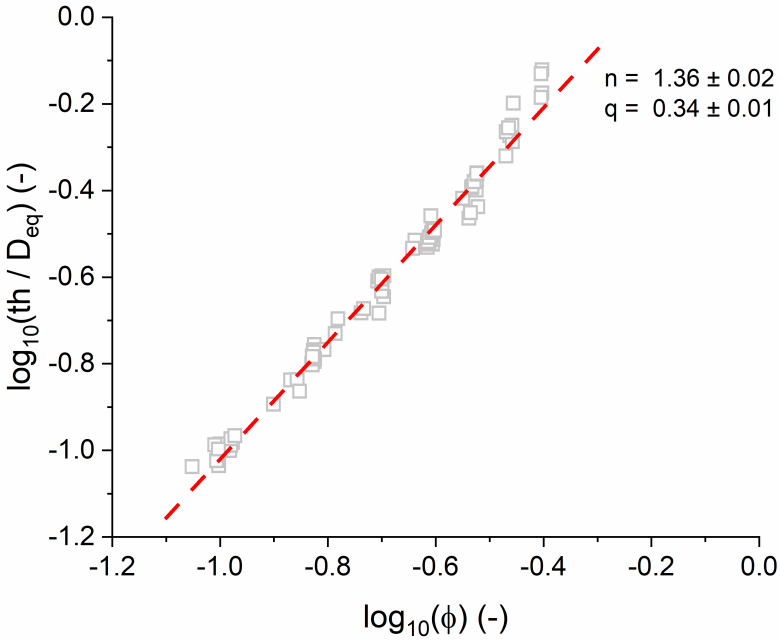

Figure 6.9: Double logarithmic plot of the ratio of mean volumetric structure thickness, th, and mean volumetric equivalent diameter of pores, D_{eq}, as a function of solid volume fraction, ϕ; the red dashed line represents a linear fit of the data and the two parameters n, line slope, and q, intercept are reported.

The results obtained from mechanical simulations performed on the sub-domains are shown in figure 6.10 in terms of mean value elements on the principal diagonal of the stiffness matrix: $C_{Mean} = \frac{C_{11}+C_{22}+C_{33}}{3}$. These are the terms directly involved in the response to uniaxial compression tests along the three main orthogonal directions of the cubic domain. Results are presented in term of stiffness matrix terms since no comparison with experimental data is reported and hence there is not the necessity to compute elastic constants to compare experimental and numerical results, avoiding the application of a specific elastic constitutive law (e.g. isotropic, orthotropic).

The results are grouped according to the relevant void volume fraction, which means that within a given group the only structural parameter that is changing is $\frac{th}{D_{eq}}$. Data show that, aside from the dependence (detailed in chapter 5) of the average apparent stiffness on the solid volume fraction, the investigated morphology variables have no influence on the average macroscopic mechanical response of expanded polymeric materials.

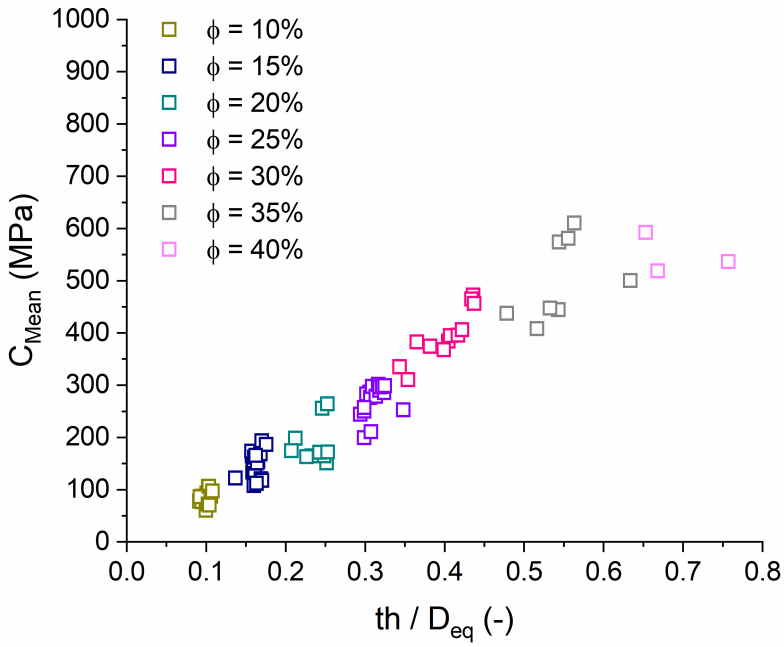

Figure 6.10: Average stiffness matrix component $C_{Mean} = \frac{C_{11}+C_{22}+C_{33}}{3}$ as a function of mean volumetric structure thickness, th, and mean volumetric equivalent diameter of voids, D_{eq}, ratio; results obtained on the different sub-domains are grouped as a function of solid volume fraction, ϕ, and are represented with different colours.

The independence of the average macroscopic mechanical response on microstructure morphology is confirmed by the results obtained on the artificially stretched sub-domains and reported in figure 6.11. In the graph the open symbols refer to the unstretched sub-domain while filled symbols represent the artificially stretched domains with

increasing stretched factor from $2x$ up to $50x$.

In this graph the independence of C_{Mean} on the ratio $\frac{th}{D_{eq}}$ is clearly visible; small fluctuations in the average values of each stretched sub-domains are related to small variations in the nominally constant solid volume fraction, in the order of 1% with respect to the initial value, introduced through the application of the stretching algorithm.

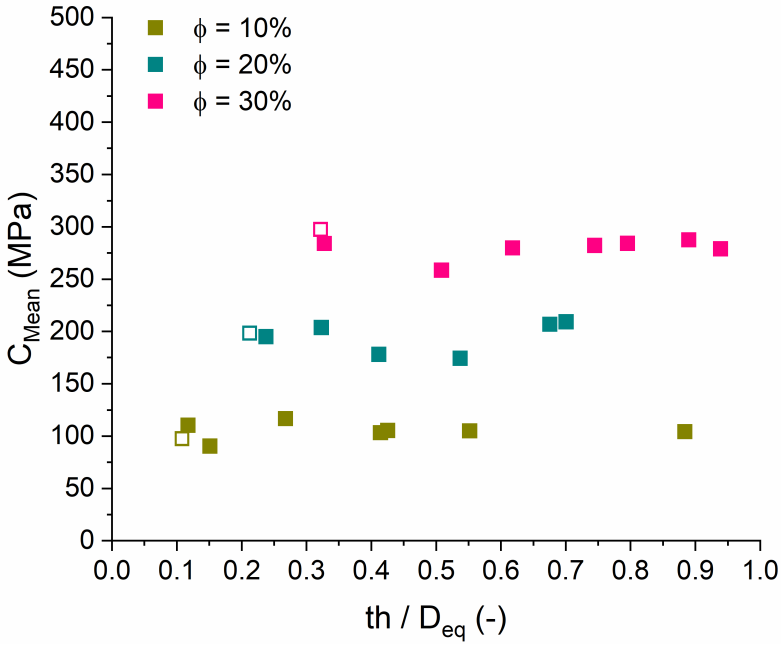

Figure 6.11: Average stiffness matrix component $C_{Mean} = \frac{C_{11}+C_{22}+C_{33}}{3}$ as a function of mean volumetric structure thickness, th, and mean volumetric equivalent diameter of voids, D_{eq}, ratio for three different sub-domains artificially stretched, keeping solid volume fraction almost constant. Open symbols refer to the unstretched sub-domains while full-coloured symbols refer to the stretched ones.

Moving on to a local analysis, the graphs in figure 6.12 display the stiffness matrix component, along one of the main orthogonal direction, C_{ii}, as a function of the ratio $\frac{th}{D_{eq}}$ computed along the same direction. It is clearly visible that an effect of morphology variation is appreciable only along the stretch direction; after an initial significant variation in

the stiffness matrix value as a function of the morphology ratio, the value tends to a plateau value even if the morphology parameter is still increasing. No significant variations can be detected along the other unstretched orthogonal directions.

This fact can lead to the conclusion that, with respect to the macroscopic mechanical response of expanded polymeric material, the information provided by the analysis of morphology can be equivalent to the one provided by the application of tensorial algorithms, such as Mean Intercept Length (MIL) and Autocorrelation function (ACF), already presented in chapter 4. Moreover, due to the small influence of morphology, even at high level of stretch values, its influence can be neglected, as a first approximation, in expanded polymeric foams macroscopic mechanical modelling. As previously said, if a tensorial algorithm is applied for structure investigation, the information provided by morphology analysis can be considered already contained in the eigenvalues and eigenvectors computed from the fabric tensors and the information can be three-dimensionally visualized, as performed in chapter 4, with a Rose diagram.

Finally, all the information acquired from morphology analysis, performed on the artificially stretched sub-domains, is summarized and plotted in figure 6.13. In this graph the y-axis represents the stiffness matrix component along the stretched direction, normalized with respect to the average values corresponding to the orthogonal unstretched directions. The same procedure was applied to the morphology parameters; the final quantity reported on the x-axis is called R for the sake of clarity. The dashed red line represents the prediction made with Ashby simple analytical model presented in the introduction paragraph [3]. Even if a relatively large scatter is visible, due to the irregularity of the structures and some numerical noise introduced with the stretching algorithm, the results are in fair agreement with the prediction made with the analytical model; this holds true even if the randomly distributed structure are summarized with simplified scalar

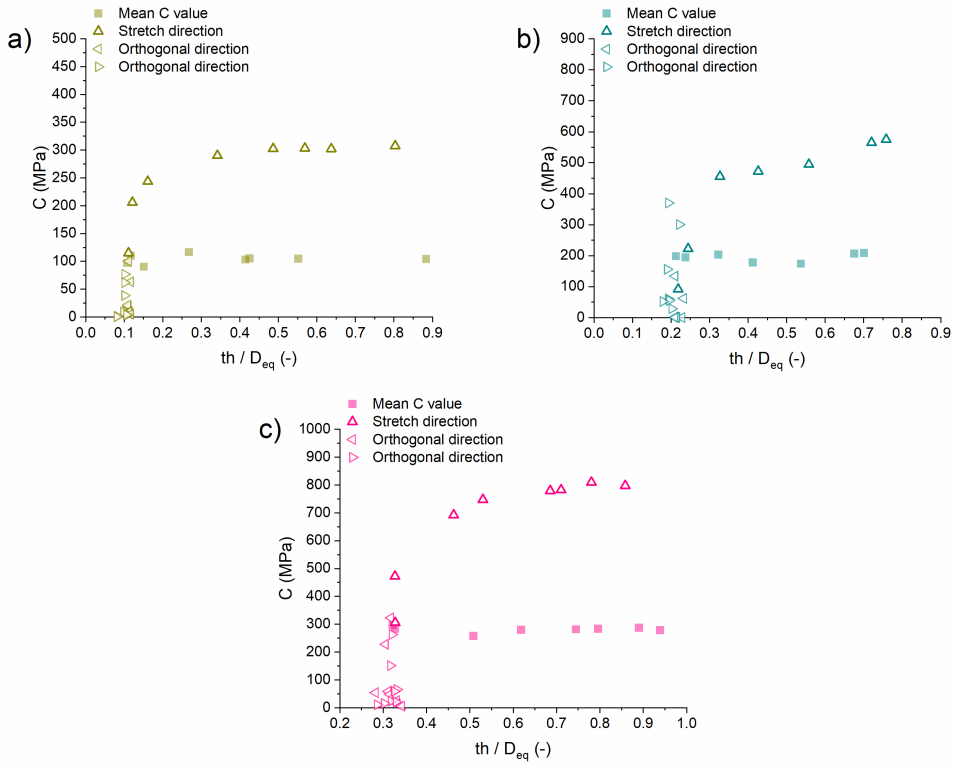

Figure 6.12: Stiffness matrix components, C_{ii}, as a function of morphology ratio computed along the same direction (X, Y or Z). Full coloured symbols represent average values, empty vertical triangles represent the values computed along the stretch direction and horizontal triangles represent the quantities computed along the orthogonal unstretched directions. Three examples are reported for three different values of solid volume fraction, ϕ: a) $\phi = 10\%$, b) $\phi = 20\%$ and c) $\phi = 30\%$.

quantities. Predictions of the Zhu model are not reported since the analytical expression contains a parameter strictly dependent on the hypothesis made to skeletonize the structure; these hypotheses are not applicable, in the case of random structures, since low structure regularity and related geometrical characteristic lengths are not uniquely detectable [13].

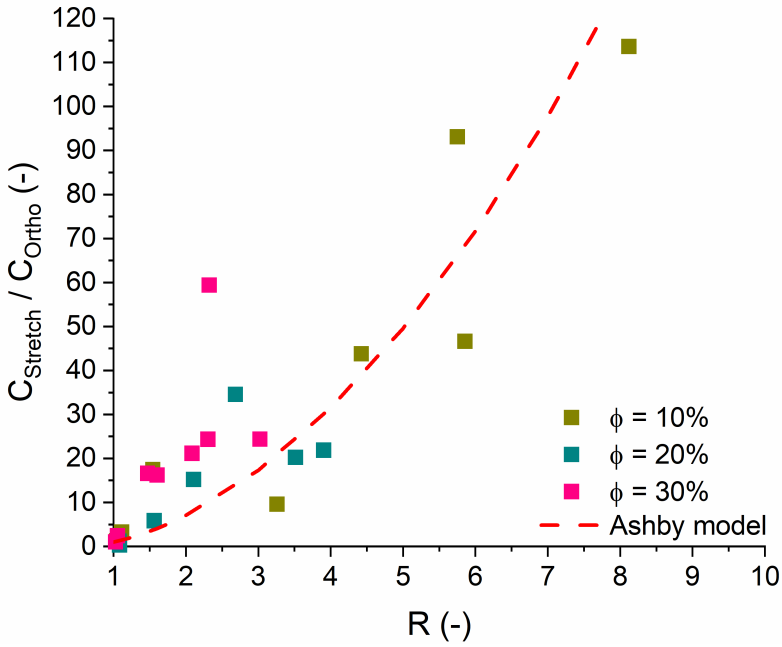

Figure 6.13: Normalized stiffness matrix value along the stretch direction with respect to the average value of stiffness matrix values along the two orthogonal unstretched directions as function of morphological parameter, R, computed as the ratio between $\frac{th}{D_{eq}}$ computed along the stretch direction and the average value of the same quantities computed along the orthogonal unstretched directions. Red dashed line represents the prediction made with Ashby analytical model.

6.4 Concluding remarks

In this chapter the influence of structure morphology on macroscopic mechanical properties of expanded polymeric material has been investigated through the application of numerical methods developed in previous chapters. A new material was introduced with the aim of increasing the range of experimentally available morphologies, and a custom-developed algorithm was employed to artificially generate an even larger variety of morphologies. An approach similar to the one proposed by Ashby was adapted to the study of irregular randomly distributed structures.

Morphology was found to yield only a local effect and not to display a significant correlation with the average global behaviour; hence, it can be considered a duplicate of the information derived from the application of tensorial algorithms, presented in chapter 5. Finally, it has been shown that the results obtained from randomly distributed structures, follow, as a first approximation, the prediction obtained from the Ashby analytical model, even if based on the assumptions of regular simple structures.

A further development of this morphology study could consist in a wider application of the stretching algorithm to validate the macroscopic mechanical behaviour observed on the selected and stretched subdomains reported in this chapter. Moreover, a rigorous equivalence between the information obtained through the application of tensorial algorithms for structure investigation and morphology analysis should be confirmed.

Since the considered morphology parameter does not seem to be essential and since the structure was investigated through the application of Mean Intercept Length (MIL) algorithm, thus computing the actual spatial distribution, the morphology parameter will be neglected in the next chapter, where a unique relationship between structure and macroscopic linear elastic constitutive laws is presented.

6.5 References

[1] L. Andena et al. “Compression of polystyrene and polypropylene foams for energy absorption applications: A combined mechanical and microstructural study”. en. In: *Journal of Cellular Plastics* 55.1 (Jan. 2019), pages 49–72. DOI: 10.1177/0021955X18806794. URL: http://journals.sagepub.com/doi/10.1177/0021955X18806794.

[2] Y. Chen, R. Das, and M. Battley. “Effects of cell size and cell wall thickness variations on the stiffness of closed-cell foams”. en. In: *International Journal of Solids and Structures* 52 (Jan. 2015), pages 150–164. DOI: 10.1016/j.ijsolstr.2014.09.022. URL: https://linkinghub.elsevier.com/retrieve/pii/S0020768314003692.

[3] L.J. Gibson and M.F. Ashby. *Cellular Solids*. en.

[4] L. Gong and S. Kyriakides. “Compressive response of open cell foams Part II: Initiation and evolution of crushing”. en. In: *International Journal of Solids and Structures* 42.5-6 (Mar. 2005), pages 1381–1399. DOI: 10.1016/j.ijsolstr.2004.07.024. URL: https://linkinghub.elsevier.com/retrieve/pii/S0020768304004317.

[5] L. Gong, S. Kyriakides, and W.Y. Jang. “Compressive response of open-cell foams. Part I: Morphology and elastic properties”. en. In: *International Journal of Solids and Structures* 42.5-6 (Mar. 2005), pages 1355–1379. DOI: 10.1016/j.ijsolstr.2004.07.023. URL: https://linkinghub.elsevier.com/retrieve/pii/S0020768304004305.

[6] L. Gong, S. Kyriakides, and N. Triantafyllidis. “On the stability of Kelvin cell foams under compressive loads”. en. In: *Journal of the Mechanics and Physics of Solids* 53.4 (Apr. 2005), pages 771–794. DOI: 10.1016/j.jmps.2004.10.007.

URL: https://linkinghub.elsevier.com/retrieve/pii/S0022509604001899.

[7] N. Huber. "Connections Between Topology and Macroscopic Mechanical Properties of Three-Dimensional Open-Pore Materials". en. In: *Frontiers in Materials* 5 (Nov. 2018), page 69. DOI: 10.3389/fmats.2018.00069. URL: https://www.frontiersin.org/article/10.3389/fmats.2018.00069/full.

[8] W.Y. Jang, A.M. Kraynik, and S. Kyriakides. "On the microstructure of open-cell foams and its effect on elastic properties". en. In: *International Journal of Solids and Structures* 45.7-8 (Apr. 2008), pages 1845–1875. DOI: 10.1016/j.ijsolstr.2007.10.008. URL: https://linkinghub.elsevier.com/retrieve/pii/S0020768307004118.

[9] J. Köll and S. Hallström. "Generation of periodic stochastic foam models for numerical analysis". en. In: *Journal of Cellular Plastics* 50.1 (Jan. 2014), pages 37–54. DOI: 10.1177/0021955X13503848. URL: http://journals.sagepub.com/doi/10.1177/0021955X13503848.

[10] J. Köll and S. Hallström. "Influence from polydispersity on the morphology of Voronoi and equilibrium foams". en. In: *Journal of Cellular Plastics* 53.2 (Mar. 2017), pages 199–214. DOI: 10.1177/0021955X16644892. URL: http://journals.sagepub.com/doi/10.1177/0021955X16644892.

[11] K. Li, X.L. Gao, and G. Subhash. "Effects of cell shape and cell wall thickness variations on the elastic properties of two-dimensional cellular solids". en. In: *International Journal of Solids and Structures* 42.5-6 (Mar. 2005), pages 1777–1795. DOI: 10.1016/j.ijsolstr.2004.08.005. URL: https://linkinghub.elsevier.com/retrieve/pii/S0020768304004536.

[12] R. Moreno, M. Borga, and O. Smedby. “Generalizing the mean intercept length tensor for gray-level images: Generalizing the mean intercept length tensor”. en. In: *Medical Physics* 39.7Part2 (July 2012), pages 4599–4612. DOI: 10.1118/1.4730502. URL: http://doi.wiley.com/10.1118/1.4730502.

[13] R.M. Sullivan, L.J. Ghosn, and B.A. Lerch. “A general tetrakaidecahedron model for open-celled foams”. en. In: *International Journal of Solids and Structures* 45.6 (Mar. 2008), pages 1754–1765. DOI: 10.1016/j.ijsolstr.2007.10.028. URL: https://linkinghub.elsevier.com/retrieve/pii/S0020768307004465.

[14] C. Tekoglu et al. “Size effects in foams: Experiments and modeling”. en. In: *Progress in Materials Science* 56.2 (Feb. 2011), pages 109–138. DOI: 10.1016/j.pmatsci.2010.06.001. URL: https://linkinghub.elsevier.com/retrieve/pii/S0079642510000393.

[15] H.X. Zhu, J.R. Hobdell, and A.H. Windle. “Effects of cell irregularity on the elastic properties of open-cell foams”. en. In: *Acta Materialia* 48.20 (Dec. 2000), pages 4893–4900. DOI: 10.1016/S1359-6454(00)00282-2. URL: https://linkinghub.elsevier.com/retrieve/pii/S1359645400002822.

[16] H.X. Zhu, J.F. Knott, and N.J. Mills. “Analysis of the elastic properties of open-cell foams with tetrakaidecahedral cells”. en. In: *Journal of the Mechanics and Physics of Solids* 45.3 (Mar. 1997), pages 319–343. DOI: 10.1016/S0022-5096(96)00090-7. URL: https://linkinghub.elsevier.com/retrieve/pii/S0022509696000907.

[17] H.X. Zhu and A.H. Windle. “Effects of cell irregularity on the high strain compression of open-cell foams”. en. In: *Acta Materialia* 50.5 (Mar. 2002), pages 1041–1052. DOI: 10.1016/S1359-6454(01)00402-5. URL: https://linkinghub.elsevier.com/retrieve/pii/S1359645401004025.

[18] P.K. Zysset. “A review of morphology–elasticity relationships in human trabecular bone: theories and experiments”. en. In: *Journal of Biomechanics* 36.10 (Oct. 2003), pages 1469–1485. DOI: 10.1016/S0021-9290(03)00128-3. URL: https://linkinghub.elsevier.com/retrieve/pii/S0021929003001283.

Chapter 7

Macroscopic linear elastic constitutive laws

In the following chapter a quantity to describe macroscopic mechanical anisotropy is proposed with the aim of uniquely assigning the most suitable set of linear elastic parameters to the inspected sample, considering structural information and mechanical results coming from finite element analysis. The information about the inspected structures is combined with the elastic constants, computed through finite element analysis, to obtain a closed system of equations. In this way elastic constants, necessary to describe the elastic macroscopic mechanical behaviour of expanded polymeric materials, can be identified from the knowledge of limited information about the geometrical structure. In the last part of the chapter the equations are applied to an example case, an open-cell polyurethane foam, on which some experimental tests have been conducted to measure the necessary quantities for the application of the defined equations.

7.1 Theoretical background

In the past decades many authors proposed different approaches to compute a mechanical anisotropy index starting from a generic stiffness or compliance tensor [14] [13] [5]. In some works, complex relationships have been developed, which link the elastic constants of a given transversely isotropic tensor to its nearest (in a sense that needs to properly defined) linear elastic counterpart [6] [12]. Very few works proposed an analytical approach that relates a generic tensor, representing in the most general case a triclinic material, to its nearest isotropic elastic tensor, due to the complexity of finding a closed relationship between the many elastic constants necessary to describe a triclinic material (21) and the two which are sufficient in the isotropic case [3] [2] [10]. Morin and collaborators recently proposed a general approach based on Euclidean distance to simply compute the distance between a generic tensor and its closest isotropic tensor; the distance is considered as the mechanical anisotropy index and a closed relationship between the starting tensor and the linear elastic constants, necessary to model a linear elastic isotropic solid is also provided [8]. The analytical steps necessary to demonstrate distance existence and uniqueness, are reported in the following paragraph.

7.1.1 Mechanical anisotropy index

The computation of a generic Euclidean distance for a given material, whose mechanical behaviour is described by a fourth-order stiffness tensor (or dually a fourth-order compliance tensor), can be derived starting from the scalar case, in which the properties of the involved functions are easier to define and demonstrate; then the distance can be generalized to the tensorial case [8].

The constitutive relation in one-dimensional linear elasticity is given by the classical Hooke's law, which relates the uniaxial stress, σ, and

strain, ε:

$$\sigma = E\,\varepsilon \quad \text{or dually} \quad \varepsilon = \frac{1}{E}\,\sigma \tag{7.1}$$

in which E is the Young modulus and its reciprocal the elastic compliance. The stored elastic energy per unit length, w, is classically given by

$$w = \frac{1}{2}\,\sigma\,\varepsilon \quad \text{or dually} \quad w = \frac{1}{2}\,\frac{1}{E}\,\sigma^2 \tag{7.2}$$

The final objective is to derive a distance function between two generic materials, characterized by stiffnesses that correspond to Young's moduli E_1 and E_2, or dually their compliances that correspond to the inverses of Young's moduli, which verifies the following properties:

1. The defining properties of a distance function must be checked $\forall E_1, E_2, E_3 \in \mathbb{R}^{>0}$, where $\mathbb{R}^{>0}$ denotes the set of strictly positive real numbers:

   (a) Distance has to be nonnegative:

   $$d(E_1, E_2) \geq 0 \tag{7.3}$$

   (b) Distance verifies the identity of indiscernible:

   $$d(E_1, E_2) = 0 \iff E_1 = E_2 \tag{7.4}$$

   (c) Distance has to be symmetric in the arguments:

   $$d(E_1, E_2) = d(E_2, E_1) \tag{7.5}$$

   (d) Distance respects the triangle inequality:

   $$d(E_1, E_2) \leq d(E_1, E_3) + d(E_2, E_3) \tag{7.6}$$

2. Then the distance function must be invariant under the operation of inversion in order not to favour the formulation in terms of

stiffness or compliance; this assumption leads, in the scalar case, to the following property:

$$d(E_1, E_2) = d\left(\frac{1}{E_1}, \frac{1}{E_2}\right) \tag{7.7}$$

The simplest distance between elastic moduli is based on the classical Euclidean metric, which is based on classical energy considerations and on the virtual working principle. The most commonly variants are:

1. **Primal Euclidean Distance**: this distance is obtained from the difference between the elastic energy stored by two different materials for an imposed loading strain, ε_0; in this case the stress states read:

$$\sigma_1 = E_1\,\varepsilon_0 \quad \text{and} \quad \sigma_2 = E_2\,\varepsilon_0 \tag{7.8}$$

and the difference between stored elastic energies is given by

$$w_1 - w_2 = \frac{1}{2}\,(\sigma_1 - \sigma_2)\,\varepsilon_0 = \frac{1}{2}\,(E_1 - E_2)\,\varepsilon_0^2 \tag{7.9}$$

The distance between the two elastic behaviours is given by the primal Euclidean distance, expressed in terms of the stiffnesses E_1 and E_2:

$$d_{primal}(E_1, E_2) = |E_1 - E_2| \tag{7.10}$$

2. **Dual Euclidean Distance**: similarly, to the primal Euclidean distance, this can be constructed from energetic consideration for an imposed loading stress, σ_0; in this case the strain states read:

$$\varepsilon_1 = \frac{\sigma_0}{E_1} \quad \textit{and} \quad \varepsilon_2 = \frac{\sigma_0}{E_2} \tag{7.11}$$

and the difference between elastic energies is given by

$$w_1 - w_2 = \frac{1}{2}\,(\varepsilon_1 - \varepsilon_2)\,\sigma_0 = \frac{1}{2}\,\left(\frac{1}{E_1} - \frac{1}{E_2}\right)\,\sigma_0^2 \tag{7.12}$$

It is thus possible to construct a dual Euclidean distance, expressed in terms of compliances:

$$d_{dual}(E_1, E_2) = \left| \frac{1}{E_1} - \frac{1}{E_2} \right| \tag{7.13}$$

Obviously, the two metrics do not give the same results since the values obtained and the units considered are not the same and hence the classical definition is not suitable to define a unique distance between two elastic behaviours. It is so of fundamental importance that the distance between two elastic materials has to be expressed in a non-dimensional form in order to be invariant under inversion.

To write the equation in a non-dimensional form, a scalar $E_0 > 0$ which has the dimension of a stiffness and acts as a gauge factor, is considered. A reduced non-dimensional elasticity law, with the gauge E_0, can thus be expressed:

$$\frac{\sigma}{E_0} = \frac{E}{E_0}\,\varepsilon \tag{7.14}$$

Hence, the distance has to be expressed in terms of dimensionless quantity $\frac{E}{E_0}$. The distance will consequently depend upon the choice made for the gauge factor, E_0: in particular, a given value of the gauge factor will generate a reduced elasticity law and will lead to some family of distances denoted by d^{E_0}.

A generalized-Euclidean distance can be introduced as a function of the gauge factor:

$$d_f^{E_0}\left(\frac{E_1}{E_0}, \frac{E_2}{E_0}\right) = \left| f\left(\frac{E_1}{E_0}\right) - f\left(\frac{E_2}{E_0}\right) \right| \tag{7.15}$$

where f is a strictly monotonic function on $\mathbb{R}^{>0}$; this allows $d_f^{E_0}$ to verify the fundamental properties of a distance function previously expressed.

Finally, to ensure the property of invariance by inversion:

$$d_f^{E_0}\left(\frac{E_1}{E_0},\frac{E_2}{E_0}\right)=d_f^{E_0}\left(\frac{E_0}{E_1},\frac{E_0}{E_2}\right) \tag{7.16}$$

a sufficient condition for the function f is that it should verify the property:

$$f(x)+f\left(\frac{1}{x}\right)=\alpha \quad \text{with} \quad \forall x\in\mathbb{R}^{>0} \tag{7.17}$$

where α is a constant. In the last equation the sign between the two function can be only plus; it can be shown that if minus sign is considered the function f cannot be strictly monotone on $\mathbb{R}^{>0}$.

Having defined the distance and its properties in a mono-dimensional case, the same concepts can now be generalized to the tensorial n-dimensional case. Since the tensors investigated are elastic tensors, the mathematical demonstration concerns mainly fourth-order and second-order tensors in a three-dimensional Cartesian space. The tensorial elasticity law relates the second-order stress and strain tensors, respectively $\underline{\boldsymbol{\sigma}}$ and $\underline{\boldsymbol{\varepsilon}}$, through linear relations:

$$\underline{\boldsymbol{\sigma}}=\underline{\underline{\boldsymbol{C}}}:\underline{\boldsymbol{\varepsilon}} \quad \text{and} \quad \underline{\boldsymbol{\varepsilon}}=\underline{\underline{\boldsymbol{S}}}:\underline{\boldsymbol{\sigma}} \quad \text{with} \quad \underline{\underline{\boldsymbol{C}}}:\underline{\underline{\boldsymbol{S}}}=\underline{\underline{\boldsymbol{S}}}:\underline{\underline{\boldsymbol{C}}}=\underline{\underline{\boldsymbol{I}}} \tag{7.18}$$

where $\underline{\underline{\boldsymbol{C}}}$ and $\underline{\underline{\boldsymbol{S}}}$ respectively denote the fourth-order stiffness and compliance tensors, and $\underline{\underline{\boldsymbol{I}}}$ is the fourth-order identity tensor. Elasticity tensors are positive-definite and posses major and minor symmetries:

$$C_{ijkl}=C_{jikl}=C_{ijlk} \quad \text{and} \quad C_{ijkl}=C_{klij} \tag{7.19}$$

and dually

$$S_{ijkl}=S_{jikl}=S_{ijlk} \quad \text{and} \quad S_{ijkl}=S_{klij} \tag{7.20}$$

The inner product for tensors, which is needed to define the norm of a tensor, reads:

$$\left\langle \underline{\underline{\boldsymbol{A}}},\underline{\underline{\boldsymbol{B}}}\right\rangle = A_{ijkl}B_{ijkl} \tag{7.21}$$

and from this follows the definition of the norm $\left\|\underline{\underline{\boldsymbol{A}}}\right\|$ of a tensor:

$$\left\|\underline{\underline{\boldsymbol{A}}}\right\| = \sqrt{\left\langle \underline{\underline{\boldsymbol{A}}}, \underline{\underline{\boldsymbol{A}}} \right\rangle} = \sqrt{A_{ijkl} A_{ijkl}} \tag{7.22}$$

To facilitate the calculations the tensors can be expressed according to Kelvin notation in elasticity and in addition fourth-order elasticity tensors in three dimensions can be equivalently expressed as second-order tensors in six dimensions while second-order symmetric tensors in three dimensions are equivalent to vectors of six dimensions. So, the elasticity tensors of stiffness (dually compliance), strain and stress are expressed in the following form:

$$\widehat{\boldsymbol{C}} = \begin{bmatrix} C_{1111} & C_{1122} & C_{1133} & \sqrt{2}C_{1123} & \sqrt{2}C_{1113} & \sqrt{2}C_{1112} \\ C_{1122} & C_{2222} & C_{2233} & \sqrt{2}C_{2223} & \sqrt{2}C_{2213} & \sqrt{2}C_{2212} \\ C_{1133} & C_{2233} & C_{3333} & \sqrt{2}C_{3323} & \sqrt{2}C_{3313} & \sqrt{2}C_{3312} \\ \sqrt{2}C_{1123} & \sqrt{2}C_{2223} & \sqrt{2}C_{3323} & 2C_{2323} & 2C_{2313} & 2C_{2312} \\ \sqrt{2}C_{1113} & \sqrt{2}C_{2213} & \sqrt{2}C_{3313} & 2C_{2313} & 2C_{1313} & 2C_{1312} \\ \sqrt{2}C_{1112} & \sqrt{2}C_{2212} & \sqrt{2}C_{3312} & 2C_{2312} & 2C_{1312} & 2C_{1212} \end{bmatrix} \tag{7.23}$$

and

$$\widehat{\boldsymbol{\sigma}} = \begin{bmatrix} \sigma_{11} \\ \sigma_{22} \\ \sigma_{33} \\ \sqrt{2}\sigma_{23} \\ \sqrt{2}\sigma_{13} \\ \sqrt{2}\sigma_{12} \end{bmatrix} \quad \text{and} \quad \widehat{\boldsymbol{\varepsilon}} = \begin{bmatrix} \varepsilon_{11} \\ \varepsilon_{22} \\ \varepsilon_{33} \\ \sqrt{2}\varepsilon_{23} \\ \sqrt{2}\varepsilon_{13} \\ \sqrt{2}\varepsilon_{12} \end{bmatrix} \tag{7.24}$$

With Kelvin notation, the elasticity law can be rewritten:

$$\widehat{\boldsymbol{\sigma}} = \widehat{\boldsymbol{C}} \cdot \widehat{\boldsymbol{\varepsilon}} \quad \text{and} \quad \widehat{\boldsymbol{\varepsilon}} = \widehat{\boldsymbol{S}} \cdot \widehat{\boldsymbol{\sigma}} \quad \text{with} \quad \widehat{\boldsymbol{C}} \cdot \widehat{\boldsymbol{S}} = \widehat{\boldsymbol{I}}_6 \tag{7.25}$$

where $\widehat{\boldsymbol{I}}_6$ is the $6\,x\,6$ identity matrix. The norm of the tensor alternatively reads:

$$\left\|\underline{\underline{\boldsymbol{C}}}\right\| = \left\|\widehat{\boldsymbol{C}}\right\| = \sqrt{\widehat{\boldsymbol{C}} : \widehat{\boldsymbol{C}}} = \sqrt{C_{IJ} C_{IJ}} \tag{7.26}$$

To extend the generalized-Euclidean distance from scalar to tensorial case, functions with four-order tensor arguments that enjoy major and

minor symmetries have to be defined. Since the tensors are expressed through the Kelvin notation, the function $\boldsymbol{f}$ of a positive-definite $6\,x\,6$ matrix needs only to be defined. The function $\boldsymbol{f}$ of a generic symmetric positive-definite matrix, $\widehat{\boldsymbol{A}}$, can be calculated in three steps:

1. Perform a diagonalization of matrix, $\widehat{\boldsymbol{A}}$, which provides a rotation matrix, $\widehat{\boldsymbol{R}}$, and a diagonal matrix $\widehat{\boldsymbol{D}}$ with the eigenvalues of $\widehat{\boldsymbol{A}}$ on its diagonal, such that $\widehat{\boldsymbol{A}} = \widehat{\boldsymbol{R}}^T\widehat{\boldsymbol{D}}\widehat{\boldsymbol{R}}$, where the transpose $\widehat{\boldsymbol{R}}^T$ of matrix $\widehat{\boldsymbol{R}}$ is defined by $R^T_{IJ} = R_{IJ}$;

2. Write down the new diagonal matrix $\widetilde{\boldsymbol{D}}$ by replacing each diagonal term λ_i of $\widehat{\boldsymbol{D}}$ with $f(\lambda_i)$;

3. Recombine $\widetilde{\boldsymbol{D}}$ and $\widehat{\boldsymbol{R}}$ to obtain the function f of matrix $\widehat{\boldsymbol{A}}$:

$$\boldsymbol{f}\left(\widehat{\boldsymbol{A}}\right) = \widehat{\boldsymbol{R}}^T\widetilde{\boldsymbol{D}}\widehat{\boldsymbol{R}} \tag{7.27}$$

   It is hence straightforward to note that the inverse of $\widehat{\boldsymbol{A}}$ can be constructed as:

$$\widehat{\boldsymbol{A}}^{-1} = \widehat{\boldsymbol{R}}^T\widetilde{\boldsymbol{D}}^{-1}\widehat{\boldsymbol{R}} \tag{7.28}$$

Thus, if the scalar function f is assumed to satisfy the property defined in equation 7.17, then the following result holds:

$$\boldsymbol{f}\left(\widehat{\boldsymbol{A}}\right) + \boldsymbol{f}\left(\widehat{\boldsymbol{A}}^{-1}\right) = \alpha\widehat{\boldsymbol{I}}_6 \tag{7.29}$$

where α is a constant.

The generalized-Euclidean distance in the tensorial case can then be obtained as a direct extension of the distance defined in the scalar case. The elasticity law is once again expressed in a non-dimensional form and the gauge factor $E_0 > 0$ is once again introduced; the elasticity law can so be expressed as follows:

$$\frac{\widehat{\boldsymbol{\sigma}}}{E_0} = \frac{\widehat{\boldsymbol{C}}}{E_0}\cdot\widehat{\boldsymbol{\varepsilon}} \quad \text{and} \quad \widehat{\boldsymbol{\varepsilon}} = \left(E_0\widehat{\boldsymbol{S}}\right)\cdot\frac{\widehat{\boldsymbol{\sigma}}}{E_0} \quad \text{with} \quad \frac{\widehat{\boldsymbol{C}}}{E_0}\cdot\left(E_0\widehat{\boldsymbol{S}}\right) = \widehat{\boldsymbol{I}}_6 \tag{7.30}$$

The generalized Euclidean distance thus reads:

$$d_f^{E_0}\left(\frac{\widehat{\boldsymbol{C}}_1}{E_0},\frac{\widehat{\boldsymbol{C}}_2}{E_0}\right)=\left\|\boldsymbol{f}\left(\frac{\widehat{\boldsymbol{C}}_1}{E_0}\right)-\boldsymbol{f}\left(\frac{\widehat{\boldsymbol{C}}_2}{E_0}\right)\right\| \tag{7.31}$$

and, as previously stated, if the function f satisfies the property expressed by equation 7.17, equation 7.31 holds and hence the distance is invariant by inversion:

$$d_f^{E_0}\left(\frac{\widehat{\boldsymbol{C}}_1}{E_0},\frac{\widehat{\boldsymbol{C}}_2}{E_0}\right)=d_f^{E_0}\left(\left(\frac{\widehat{\boldsymbol{C}}_1}{E_0}\right)^{-1},\left(\frac{\widehat{\boldsymbol{C}}_2}{E_0}\right)^{-1}\right) \tag{7.32}$$

The last step consists in providing closed-form expressions of strictly monotonic functions that ensure the property reported in equation 7.17. A subclass of functions can be constructed from arbitrary continuously differentiable functions g, whose properties need to be defined, such that:

$$f(x)=g(x)-g\left(\frac{1}{x}\right)+\frac{\alpha}{2}\quad\text{with}\quad\forall x\in\mathbb{R}^{>0} \tag{7.33}$$

Since the desired function is strictly monotonic, one has necessarily $f'(x)>0$ or $f'(x)<0$. Since $f'(x)=g'(x)+\frac{g'\left(\frac{1}{x}\right)}{x^2}$, the only restriction upon function g is that it is must be strictly monotonic. The constant α can then be chosen arbitrarily. Among the different strictly monotonic available functions, the most suitable candidate selected are:

- **Logarithmic function - log-Euclidean distance**: considering the following system

$$\begin{cases}g(x)=\frac{1}{2}ln(x)\\ \alpha=0\end{cases} \tag{7.34}$$

which leads to

$$f(x)=ln(x) \tag{7.35}$$

The associated distance for tensors, with the gauge E_0, is thus

given by:

$$d_{ln}^{E_0}\left(\frac{\widehat{\boldsymbol{C}}_1}{E_0},\frac{\widehat{\boldsymbol{C}}_2}{E_0}\right)=\left\|\boldsymbol{ln}\left(\frac{\widehat{\boldsymbol{C}}_1}{E_0}\right)-\boldsymbol{ln}\left(\frac{\widehat{\boldsymbol{C}}_2}{E_0}\right)\right\| \tag{7.36}$$

From the definition of the logarithm of a generic symmetric matrix, $\widehat{\boldsymbol{A}}$, with positive eigenvalues, it appears that:

$$\boldsymbol{ln}\left(\beta\widehat{\boldsymbol{A}}\right)=\boldsymbol{ln}\left(\beta\right)\widehat{\boldsymbol{I}}_6+\boldsymbol{ln}\left(\widehat{\boldsymbol{A}}\right)\quad\text{with}\quad\forall\beta>0 \tag{7.37}$$

Thus, the distance is independent from the gauge factor and reduces to:

$$d_{ln}\left(\widehat{\boldsymbol{C}}_1,\widehat{\boldsymbol{C}}_2\right)=\left\|\boldsymbol{ln}\left(\widehat{\boldsymbol{C}}_1\right)-\boldsymbol{ln}\left(\widehat{\boldsymbol{C}}_2\right)\right\| \tag{7.38}$$

- **Arctangent function - arctan-Euclidean distance**: the system in this case is

$$\begin{cases}g(x)=\frac{1}{2}\arctan(x)\\ \alpha=\frac{\pi}{2}\end{cases} \tag{7.39}$$

which leads to

$$f(x)=\arctan(x) \tag{7.40}$$

The associated distance for tensors is called the arctan-Euclidean distance and reads:

$$d_{\arctan}^{E_0}\left(\frac{\widehat{\boldsymbol{C}}_1}{E_0},\frac{\widehat{\boldsymbol{C}}_2}{E_0}\right)=\left\|\boldsymbol{arctan}\left(\frac{\widehat{\boldsymbol{C}}_1}{E_0}\right)-\boldsymbol{arctan}\left(\frac{\widehat{\boldsymbol{C}}_2}{E_0}\right)\right\| \tag{7.41}$$

In the scalar case, this kind of distance has a geometrical interpretation since it corresponds to the angle between the lines of slopes $\frac{E_1}{E_0}$ and $\frac{E_2}{E_0}$ on stress versus strain curves in the $\left(\varepsilon\,,\,\frac{\sigma}{E_0}\right)$ plane.

- **Power function - power-Euclidean distance**: the system

considered is

$$\begin{cases} g(x) = x^n \\ \alpha = 0 \end{cases} \tag{7.42}$$

where n is a complex number different from 0. This system leads to

$$f(x) = x^n - x^{-n} \tag{7.43}$$

The associated family of distances for tensors, with gauge E_0, called power-Euclidean distances result as follows:

$$d_n^{E_0}\left(\frac{\widehat{\boldsymbol{C}}_1}{E_0}, \frac{\widehat{\boldsymbol{C}}_2}{E_0}\right) = \left\| \left(\frac{\widehat{\boldsymbol{C}}_1}{E_0}\right)^n - \left(\frac{\widehat{\boldsymbol{C}}_2}{E_0}\right)^n + \left(\frac{\widehat{\boldsymbol{C}}_2}{E_0}\right)^{-n} - \left(\frac{\widehat{\boldsymbol{C}}_1}{E_0}\right)^{-n} \right\| \tag{7.44}$$

Once the distance is defined, together with its uniqueness, it can be applied to the research of the closest isotropic elasticity tensor with respect to an arbitrary given elastic tensor. This problem reduces to the minimization of the distance between the given tensor, $\widehat{\boldsymbol{C}}$, and the closest isotropic tensor, $\widehat{\boldsymbol{C}}_{iso}$. The isotropic tensor solution of the minimization problem will thus depend on the distance considered.

A general isotropic fourth-order stiffness tensor, $\widehat{\boldsymbol{C}}_{iso}$, can be written in the form:

$$\widehat{\boldsymbol{C}}_{iso} = 3k\hat{\boldsymbol{J}} + 2\mu\widehat{\boldsymbol{K}} \tag{7.45}$$

where k and μ are respectively the bulk modulus and shear modulus; $\hat{\boldsymbol{J}}$ and $\widehat{\boldsymbol{K}}$ are linearly independent isotropic tensors defined by:

$$\hat{\boldsymbol{J}} = \frac{1}{\sqrt{3}}\hat{\boldsymbol{I}}_3 \otimes \hat{\boldsymbol{I}}_3 \tag{7.46}$$

$$\widehat{\boldsymbol{K}} = \boldsymbol{I} - \hat{\boldsymbol{J}} \tag{7.47}$$

in which $\hat{\boldsymbol{I}}_3$ is the second-order identity tensor. It can be demonstrated is not reported for the sake of clarity, that the function $\boldsymbol{f}$ of an isotropic fourth-order tensor, expressed with Kelvin notation, is given by:

$$\boldsymbol{f}\left(\widehat{\boldsymbol{C}}_{iso}\right) = f(3k)\hat{\boldsymbol{J}} + f(2\mu)\widehat{\boldsymbol{K}} \tag{7.48}$$

The distance, between some arbitrary elasticity tensor and the closest isotropic one can be written as follows:

$$d_f^{E_0}\left(\frac{\widehat{\boldsymbol{C}}_1}{E_0},\frac{\widehat{\boldsymbol{C}}_2}{E_0}\right)=\left\|\boldsymbol{f}\left(\frac{\widehat{\boldsymbol{C}}}{E_0}\right)-f\left(\frac{3k}{E_0}\right)\widehat{\boldsymbol{J}}-f\left(\frac{2\mu}{E_0}\right)\widehat{\boldsymbol{K}}\right\| \tag{7.49}$$

The closest elasticity tensor minimizes this distance; the research is hence focused on the stationarity of $d_f^{E_0}$, or equivalently expressed $\left(d_f^{E_0}\right)^2$, as a function of the two elastic constants k and μ:

$$\begin{cases}\dfrac{\partial\left(d_f^{E_0}\right)^2}{\partial k}=0\\[2ex]\dfrac{\partial\left(d_f^{E_0}\right)^2}{\partial \mu}=0\end{cases} \tag{7.50}$$

Substituting the expression previously reported into the system, it can be rewritten as:

$$\begin{cases}f\left(\frac{3k}{E_0}\right)=\boldsymbol{f}\left(\frac{\widehat{\boldsymbol{C}}}{E_0}\right):\widehat{\boldsymbol{J}}\\ f\left(\frac{2\mu}{E_0}\right)=\frac{1}{5}\,\boldsymbol{f}\left(\frac{\widehat{\boldsymbol{C}}}{E_0}\right):\widehat{\boldsymbol{K}}\end{cases} \tag{7.51}$$

Since the scalar function f is supposed to be strictly monotonic, its inverse function, f^{-1} exists, at least numerically; the elastic constants k and μ of the closest isotropic tensor to $\widehat{\boldsymbol{C}}$ for the distance $d_f^{E_0}$ are thus given by:

$$\begin{cases}k=\frac{E_0}{3}\,f^{-1}\left(\boldsymbol{f}\left(\frac{\widehat{\boldsymbol{C}}}{E_0}\right):\widehat{\boldsymbol{J}}\right)\\ \mu=\frac{E_0}{2}\,f^{-1}\left(\frac{1}{5}\,\boldsymbol{f}\left(\frac{\widehat{\boldsymbol{C}}}{E_0}\right):\widehat{\boldsymbol{K}}\right)\end{cases} \tag{7.52}$$

7.2 Materials and methods

7.2.1 Materials

The material investigated in this chapter can be divided in two groups:

- *PET 80, PET 100, PET 130, PET 320* and *EPP120*: these materials were already experimentally characterized and used as a basis for numerical simulations in previous chapters; in the present chapter the results of structure analysis and mechanical results, coming from numerical simulations, will be used to implement the Euclidean distance described in the previous paragraph and consequently compute a mechanical anisotropy index. Moreover, these results are used to formalize a system of analytical equations which can be used to estimate elastic constants, starting from microstructural parameters, according to the most suitable linear elastic constitutive law able to describe the macroscopic mechanical behaviour of inspected samples.

- *PPI*: this is a newly introduced material, an open cell polyurethane foam whose nominal apparent density is 30 $\mathrm{kg\,m^{-3}}$. The material was produced by Adler Group and supplied in the form of sheets of nominal dimensions $250\,x\,150\,x\,20$ mm. No information about the formulation or production parameters is available.

This last material was introduced to prove the validity of the analytical equations developed based on the data obtained in previous chapter; hence, this material was also experimentally characterized with the aim of obtaining the necessary quantities for the present analysis.

7.2.2 Experimental methods

Experimental methods analogous to those reported in chapter 3 are presented for PPI material. The experimental protocols employed aim

at measuring the following quantities:

- *Constituent material density* (ρ_S): this quantity is measured through gas pycnometer analysis; the instrument used is once again *Pycnomatic ATC Thermo Scientific* gas pycnometer. Five cubic specimens of 20 mm side length were prepared with an hot-wire cutting machine; also, in this case, the samples were cut randomly along the sheet to increase the statistical validity of the results. Measurements were conducted in pure helium atmosphere (Helium 5.0, purity grade) at 23 °C and at an equilibrium pressure of 2 kPa. Small configuration, available on the instrument and corresponding to a measurement volume of 25 cm^3, was selected. Three consecutive measurements were performed on each specimen. Since the material is a completely open-cell foam the density of the bulk constituent material could be directly measured with this kind of test.

- *Constituent material modulus* (E_S): due to the relatively large dimensions of the structure, in the order of hundreds of micrometres, it was possible to manually cut, with the aid of a magnifying glass, single struts of nominal length 3 mm to perform quasi-static uniaxial tensile tests. Fifteen samples were manually prepared and the average cross-sections measured with the aid of an *Olympus BX-60* microscope in reflectance mode. The cross-section for experimental tensile test was considered, as a first approximation, ideally circular; the average cross-section area was subsequently confirmed with the results coming from structure analysis performed on the set of images obtained from X-Ray computed tomography. Samples were tested in uniaxial quasi-static tensile configuration with a dynamic mechanical analyser *RSA III TA Instruments* equipped with a 35 N load cell used in transient mode with crosshead displacement control. Tests were carried out in a controlled environment at 23 °C and 50% of relative

humidity. They were conducted up to a nominal strain of 100% by applying a nominal strain rate of 0.005 s^{-1}, which corresponds to a nominal crosshead displacement of 1 mm min^{-1}. For what concerns the topic of the present chapter only information at small strains, around 1%, was used; the large strain behaviour will be considered in the next chapter.

- *Foam macroscopic apparent stiffness* (E_i^*): foam macroscopic mechanical behaviour was inspected with a similar procedure reported in chapter 3. Quasi-static uniaxial compression tests were performed, in this case, on the same dynamic mechanical analyser *RSA III TA Instruments* used for uniaxial tensile test, with parallel plates configuration and once again under crosshead displacement control. Tests were carried out in a controlled environment at 23 °C and 50% of relative humidity. Cubic specimens, similar to the ones used for gas pycnometer analysis, were prepared with an hot-wire cutting machine. Three specimens were tested at 50% of nominal strain applying a nominal strain rate of 0.005 s^{-1}, which corresponds to a nominal crosshead displacement of 6 mm min^{-1}. Compression was performed along the three main orthogonal directions of the cubic specimens. Preliminary quasi-static uniaxial loading-unloading tests were conducted in the same conditions and no permanent deformation was detected at the end of the test; hence each specimen was tested along the three orthogonal directions, up to large strains; five minutes between each test were allowed to viscoelastic strain recovery. Also, in this case mechanical results at small strains (1%) will be used in the present chapter, while large strain results will be exploited in the next.

- *Microstructure inspection*: internal microstructure was once again analysed through X-Ray computed tomography, performed in collaboration with *ENEA, Division for Sustainable materials, Re-*

search centre of Brindisi. Acquisitions were performed using a *GE Phoenix Nanotom CT systems* fitted with a molybdenum target suitable for weakly absorbing materials. The accelerating voltage and the beam current of the X-Ray tube were set at 50 kV and 185 µA, respectively. The number of projections was 2400. Voxel size was set at 10 µm. The exposure time for each projection and the total scan time were 750 ms and 3 h, respectively. Volume reconstruction was carried out with the application *Phoenix datos|x 2*, with the same procedure described in chapter 4. The size of the resulting set of images was $1300\,x\,1300\,x\,1300$ voxels, corresponding to an investigated volume of 13^3 mm^3.

7.2.3 Numerical methods

The internal microstructure of material PPI was characterized with the methodologies and algorithms described in chapter 4.

Stiffness tensors, obtained from numerical simulations performed on PET and EPP materials, presented in chapter 5 and 6, were then analysed with a custom algorithm, developed with *Matlab R2019b*, which computes the Euclidean distance, $d_f^{E_0}$, and the corresponding elastic constants of the closest isotropic tensor.

7.3 Results and discussion

7.3.1 Structural and mechanical anisotropy

Figure 7.1 displays an example of the elastic constants of the closest isotropic tensor, with respect to the one obtained from finite element simulation, computed with the procedure described in the previous section. The results are shown in terms of Young modulus, E_{iso}, and shear modulus, G_{iso}. The example is referred to one sub-domain of PET 130 sample B, but similar results are obtained for all the other stiffness matrices. The figure reports values computed with the log-Euclidean distance and power-Euclidean distance, with exponent, n, equal to 1, $\frac{1}{2}$ and 2; arctan-Euclidean distance was excluded since for many stiffness matrices some singularity occurs during the computation of elastic constants. As stated in the theoretical paragraph, the log-Euclidean is the only distance independent from the normalization parameter E_0 while the other distance formulations strongly depend on this parameter, but they all converge into a single point. Results that follow, in terms of mechanical anisotropy index, are computed in a neighbourhood of this convergence point. Results about the dependence of power-Euclidean distance on the normalization parameter E_0 are not shown since the physical meaning of E_0 is still under investigation.

The Euclidean distance, generically indicated with the single symbol $d_f^{E_0}$ since around the convergence point all the distances give the same result, was computed and taken as a mechanical anisotropy index. Figure 7.2 shows the results obtained for all the stiffness matrices computed in previous chapters; mechanical anisotropy index is plotted as a function of structural anisotropy index, DA, computed through the application of Mean Intercept Length (MIL) algorithm. An apparent bilinear trend is reported in the graph with the change in the slope around a value for DA equal to 0.6. Again, this threshold corresponds to the different macroscopic mechanical behaviour and its associated linear elastic constitutive laws.

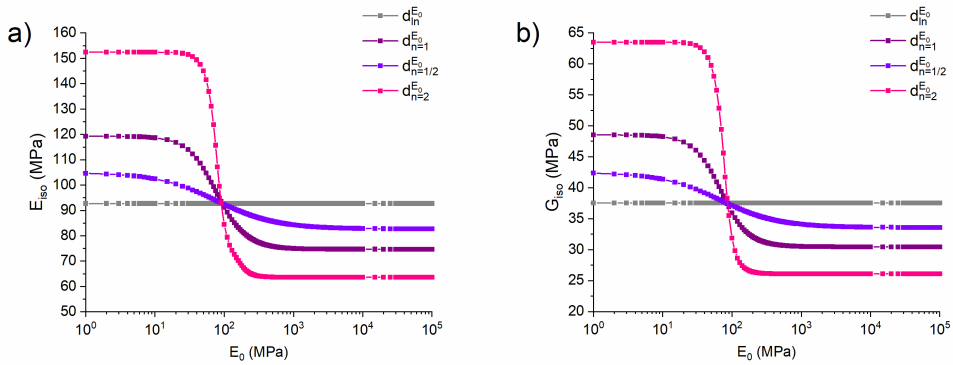

Figure 7.1: Elastic constants of the closest isotropic tensor computed with different definitions of Euclidean distance: a) Young modulus and b) shear modulus. The example refers to the stiffness matrix of a sub-domain of PET 130 sample B.

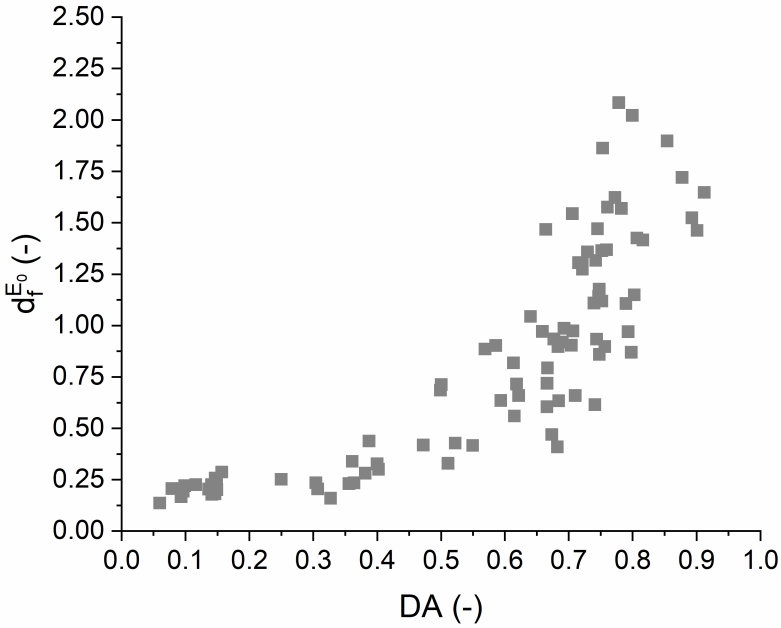

Figure 7.2: Euclidean distance, or alternatively called mechanical anisotropy index, $d_f^{E_0}$, as a function of structural anisotropy index, DA.

The result obtained and displayed in figure 7.2 was combined with the information coming from structural analysis in terms of eigenvalues

of the fabric tensor describing the spatial distribution of the material inside the inspected volume. In figure 7.3 the three eigenvalues of each analysed sub-domain, normalized with respect to their mean value, are plotted as a function of the structural anisotropy index of the corresponding sub-domain itself. It is clear from the graph that the three eigenvalues progressively diverge with increasing value of structural anisotropy index, DA. A first range, for DA values between 0 and 0.2, can be identified in which the three eigenvalues are almost equal. A second range can be identified exploiting the threshold found from data depicted in figure 7.2. Therefore, for DA values comprised between 0.2 and 0.6, two eigenvalues can be considered, as a first approximation, almost equal while the third is different from the others. The threshold at 0.6 is set exploiting the result obtained from mechanical anisotropy index analysis; without this analysis the threshold could not uniquely be set due to the dispersion of numerical data. The last range, DA values between 0.6 and 1, is comprehensive of all the sub-domains whose fabric tensor is characterized by three different eigenvalues. The uniquely identification of three different regions, as a function of DA, is coherent with the works of Cowin and other authors regarding cellular materials and their fabric tensor [3] [9] [12]. According to their work a cellular material exhibits a macroscopic mechanical response which can be analytically modelled as linear elastic as follows:

- *Three distinct eigenvalues* ($\lambda_1 \neq \lambda_2 \neq \lambda_3$): the material can be modelled with a linear elastic orthotropic constitutive law.
- *Two distinct eigenvalues* ($\lambda_1 = \lambda_2 \neq \lambda_3$): the material can be modelled with a linear elastic transversely isotropic constitutive law.
- *Three equal eigenvalues* ($\lambda_1 = \lambda_2 = \lambda_3$): in this case the material can be modelled with a linear elastic isotropic constitutive law.

The association between the found region, function of structural anisotropy index, and the corresponding linear elastic constitutive law

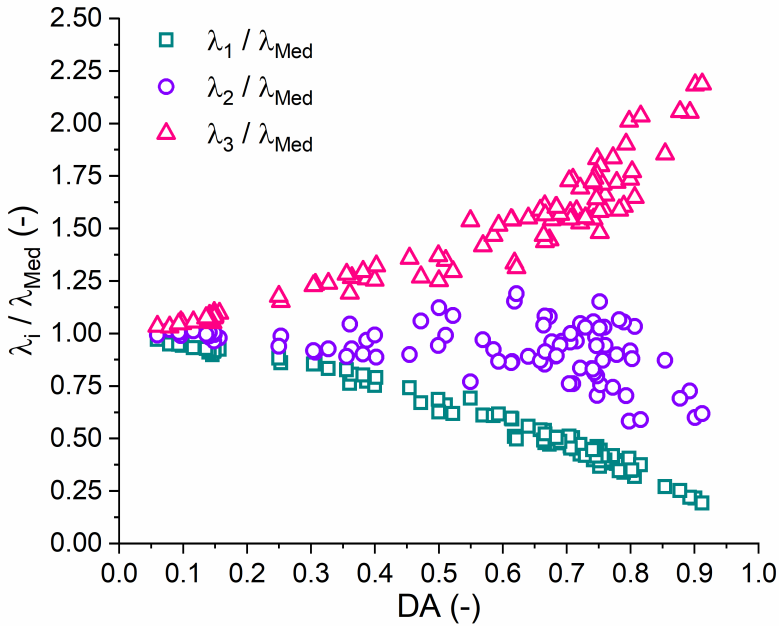

Figure 7.3: Fabric tensor eigenvalues normalized with respect to their mean value as a function of structural anisotropy index (DA).

is confirmed by inspecting the homogenized stiffness matrices. An example for each identified region is reported:

- $0 < DA < 0.2$ - *Isotropic constitutive law*:

$$\underline{\underline{C}} = \begin{bmatrix} 354.70 & 147.68 & 129.45 & 0.17 & 4.37 & 0.25 \\ 149.40 & 361.20 & 151.48 & 0.50 & 0.33 & 0.43 \\ 130.35 & 150.54 & 337.61 & 0.39 & 0.32 & 0.24 \\ 0.67 & 0.74 & 0.50 & 98.36 & 1.13 & -0.14 \\ 1.11 & 0.56 & 0.50 & 0.59 & 91.07 & 3.53 \\ -1.23 & -0.27 & 0.17 & 0.46 & 2.96 & 95.61 \end{bmatrix} \text{[MPa]}$$

the associated DA of the matrix is 0.11 and, besides the not exactly zero value of the non-principal components due to the numerical procedure and the irregularity of the structure, the two groups of components on the main diagonal, representing the

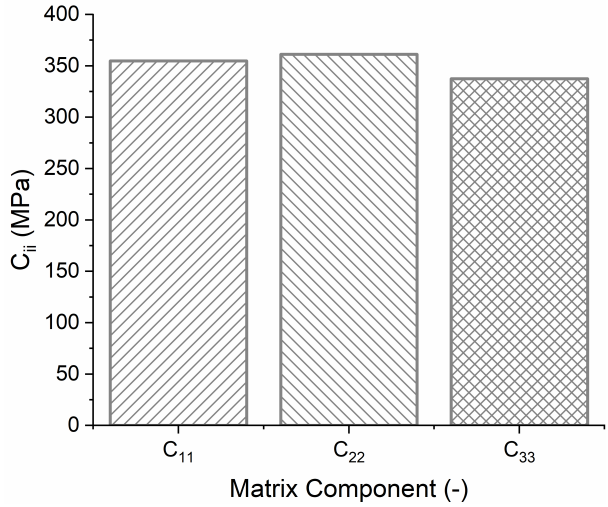

Figure 7.4: Orthogram comparing the components on the main diagonal of a stiffness matrix, C_{11}, C_{22} and C_{33} in the range of DA associated with macroscopic isotropic constitutive law.

direct effect of normal strains and shear strains, are almost the same, suggesting a macroscopic linear elastic isotropic behaviour.

- $0.2 < DA < 0.6$ - *Transversely isotropic constitutive law*:

$$\underline{\underline{C}} = \begin{bmatrix} 55.13 & 46.50 & 43.67 & 2.15 & -1.75 & 2.37 \\ 46.45 & 66.17 & 73.79 & 0.11 & 2.08 & -5.04 \\ 43.65 & 73.71 & 261.00 & -1.10 & -2.21 & 2.16 \\ 4.36 & 0.54 & -0.07 & 27.50 & -0.17 & -0.51 \\ -5.52 & 0.00 & -1.21 & -0.16 & 27.13 & 1.01 \\ 1.96 & -4.70 & 3.04 & 3.97 & 4.98 & 71.86 \end{bmatrix} \text{[MPa]}$$

the associated DA of the matrix is 0.52 and looking at the two groups of components on the main diagonal, for each group two terms are almost the same while the third is different, confirming the necessity to use a transversely isotropic constitutive law to describe the macroscopic mechanical behaviour of this kind of

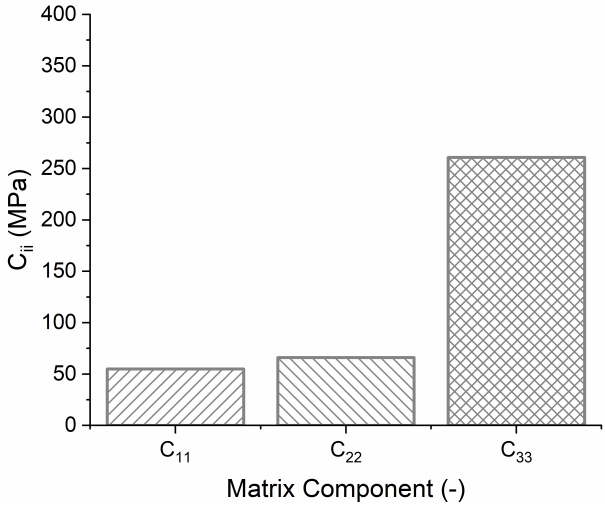

Figure 7.5: Orthogram comparing the components on the main diagonal of a stiffness matrix, C_{11}, C_{22} and C_{33} in the range of DA associated with macroscopic transversely isotropic constitutive law.

structures. As stated in the previous case, similar considerations on non-principal components can be made.

- $0.6 < DA < 1$ - *Orthotropic constitutive law*:

$$\underline{\underline{C}} = \begin{bmatrix} 53.05 & 40.52 & 34.75 & 1.66 & 14.51 & 1.00 \\ 40.39 & 381.93 & 49.96 & 1.58 & 15.19 & 3.53 \\ 34.80 & 49.90 & 185.91 & -5.17 & 20.49 & 1.64 \\ -4.88 & -0.56 & -6.49 & 52.97 & -1.91 & 16.60 \\ 18.19 & 14.86 & 25.83 & -0.86 & 22.32 & 1.38 \\ -4.20 & 0.09 & 0.16 & 13.99 & -1.80 & 69.24 \end{bmatrix} \text{[MPa]}$$

the associated DA of the matrix is 0.91 and in this case the elements constituting the two groups of main components are all different from one to another, suggesting the use of an orthotropic constitutive law. In this case, for DA values really close to 1, corresponding to the completely anisotropic structure case, some

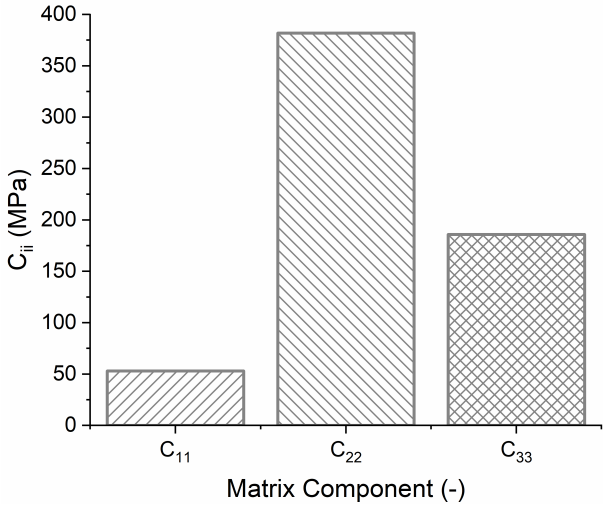

Figure 7.6: Orthogram comparing the components on the main diagonal of a stiffness matrix, C_{11}, C_{22} and C_{33} in the range of DA associated with macroscopic orthotropic constitutive law.

of the non-principal components are much greater than the one presented in the first two cases and cannot be attributed only to numerical issues. This fact can suggest that a more complex constitutive law than the orthotropic should be used for these extreme cases, but in the present work the highest level of linear elastic constitutive law complexity considered is the orthotropic one.

7.3.2 Macroscopic constitutive laws

Once the unique association between geometrical structure and suitable macroscopic linear elastic constitutive law was assessed, the elastic constants, computed from the stiffness matrices obtained from finite element simulations, were related to the morpho-structural parameters, coming from the image analysis of the sub-domains, to construct a set of analytical equations.

Figure 7.7 reports the relationships between the apparent Young moduli and structure parameters:

- *Figure 7.7-a)*: relationship between the average of apparent Young moduli $\left(E^*_{Mean} = \frac{E^*_{11}+E^*_{22}+E^*_{33}}{3}\right)$, normalized with respect to the bulk modulus of foam constituent material (E_S), as a function of solid volume fraction (ϕ).

- *Figure 7.7-b)*: relationship between the ratio of minimum and maximum apparent Young moduli $\left(\frac{E^*_{Min}}{E^*_{Max}}\right)$ as a function of the ratio between the minimum and maximum eigenvalues of the fabric tensor $\left(\frac{\lambda_{Min}}{\lambda_{Max}}\right)$.

- *Figure 7.7-c)*: relationship between the ratio of minimum and medium apparent Young moduli $\left(\frac{E^*_{Min}}{E^*_{Med}}\right)$ as a function of the ratio between the minimum and medium eigenvalues of the fabric tensor $\left(\frac{\lambda_{Min}}{\lambda_{Med}}\right)$.

For all the double-logarithmic plots a linear fitting of the data was performed. Due to the scatter of the data, the linear fitting was considered valid with a r^2-value greater than 0.9. In all cases the intercept of the fit turned out to be negligible; this finding leads to the formulation of power-law relationships of the type:

$$y = x^n \tag{7.53}$$

The same procedure was applied also to shear moduli and Poisson ratios and similar results were obtained. Results regarding shear moduli are reported in figure 7.8. The shear modulus of the constituent material was computed with the usual linear elastic isotropic relationship from the relevant Young modulus and Poisson ratio used in finite element simulation.

Figure 7.9 displays the results obtained for the apparent Poisson ratios.

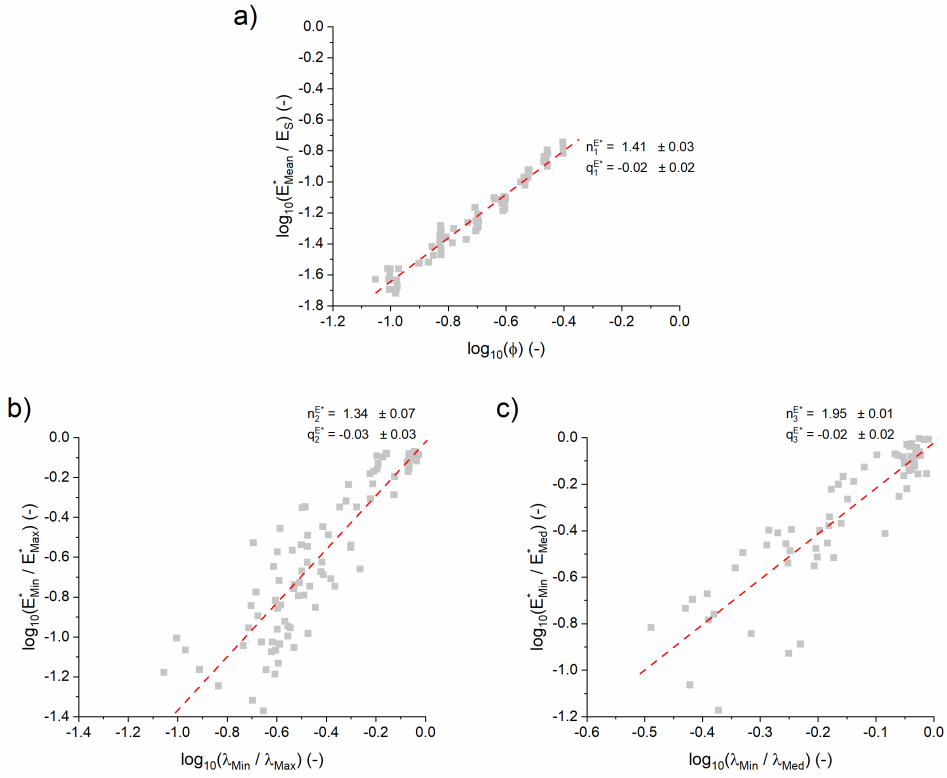

Figure 7.7: Double logarithmic plots of the relationships between apparent Young moduli, computed through finite element analysis, and morpho-structural parameters, computed through image analysis; a) mean apparent Young modulus $\left(E^*_{Mean} = \frac{E^*_{11}+E^*_{22}+E^*_{33}}{3}\right)$, normalized with respect to constituent material Young modulus (E_S), as a function of solid volume fraction (ϕ); b) ratio of minimum and maximum apparent Young moduli $\left(\frac{E^*_{Min}}{E^*_{Max}}\right)$ as a function of minimum and maximum fabric tensor eigenvalues $\left(\frac{\lambda_{Min}}{\lambda_{Max}}\right)$; c) ratio of minimum and medium apparent Young moduli $\left(\frac{E^*_{Min}}{E^*_{Med}}\right)$ as a function of minimum and maximum fabric tensor eigenvalues $\left(\frac{\lambda_{Min}}{\lambda_{Med}}\right)$. Red dashed lines represent linear fit results and related parameters obtained are also reported. **Note that different scales had to be used**.

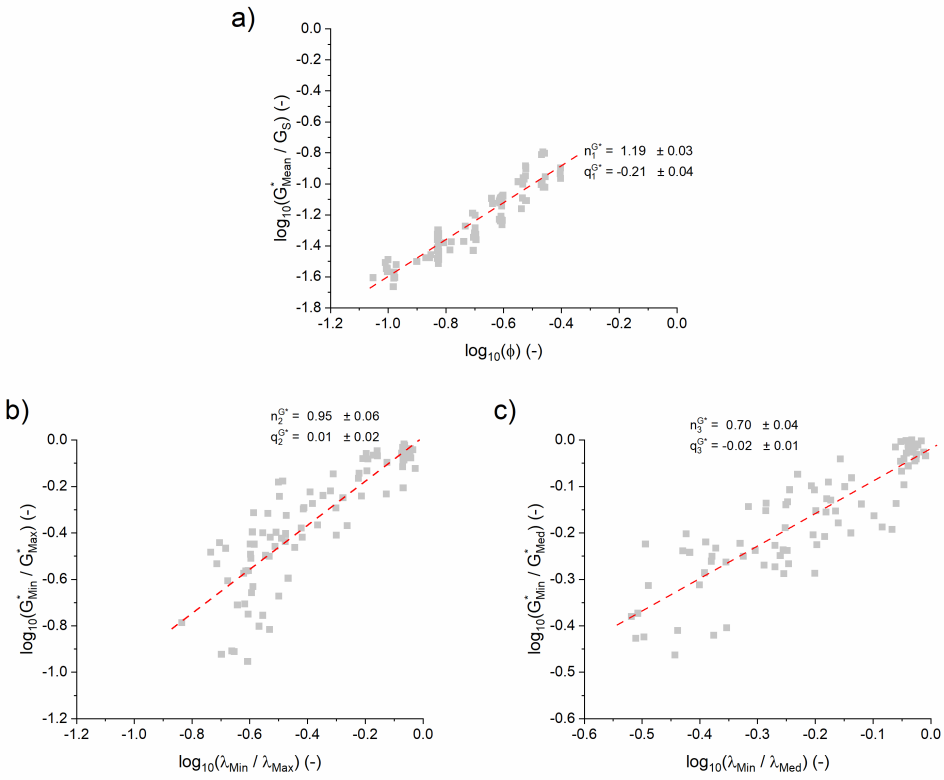

Figure 7.8: Double logarithmic plots of the relationships between apparent shear moduli, computed through finite element analysis, and morpho-structural parameters, computed through image analysis; a) mean apparent Shear modulus $\left(G^*_{Mean} = \frac{G^*_{12}+G^*_{13}+G^*_{23}}{3}\right)$, normalized with respect to constituent material shear modulus (G_S), as a function of solid volume fraction (ϕ); b) ratio of minimum and maximum apparent shear moduli $\left(\frac{G^*_{Min}}{G^*_{Max}}\right)$ as a function of minimum and maximum fabric tensor eigenvalues $\left(\frac{\lambda_{Min}}{\lambda_{Max}}\right)$; c) ratio of minimum and medium apparent shear moduli $\left(\frac{G^*_{Min}}{G^*_{Med}}\right)$ as a function of minimum and maximum fabric tensor eigenvalues $\left(\frac{\lambda_{Min}}{\lambda_{Med}}\right)$. Red dashed lines represent linear fit results and related parameters obtained are also reported. **Note that different scales had to be used**.

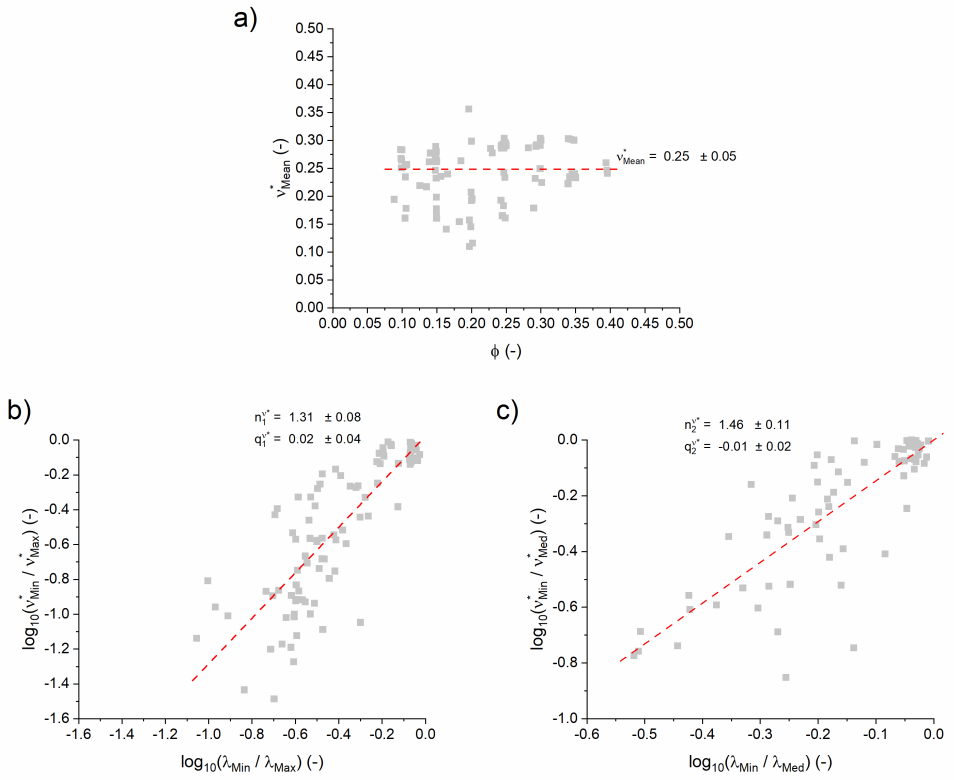

Figure 7.9: Double logarithmic plots of the relationships between apparent Poisson ratios, computed through finite element analysis, and morpho-structural parameters, computed through image analysis; a) mean apparent Poisson ratio $\left(\nu^*_{Mean} = \frac{\nu^*_{12}+\nu^*_{13}+\nu^*_{23}}{3}\right)$ as a function of solid volume fraction (ϕ); b) ratio of minimum and maximum apparent Poisson ratios $\left(\frac{\nu^*_{Min}}{\nu^*_{Max}}\right)$ as a function of minimum and maximum fabric tensor eigenvalues $\left(\frac{\lambda_{Min}}{\lambda_{Max}}\right)$; c) ratio of minimum and medium apparent Poisson ratios $\left(\frac{\nu^*_{Min}}{\nu^*_{Med}}\right)$ as a function of minimum and maximum fabric tensor eigenvalues $\left(\frac{\lambda_{Min}}{\lambda_{Med}}\right)$. Red dashed lines represent linear fit results and related parameters obtained are also reported. **Note that different scales had to be used**.

Combining the results shown in the present and previous sections, a system of equations can be assembled to estimate the elastic constants:

- $0 < DA < 0.2$ - *Isotropic homogenized material*: only two elastic constants have to be determined

$$\begin{cases} \frac{E^*_{Mean}}{E_S} = \frac{E^*}{E_S} = (\phi)^{n_1^{E^*}} & \text{with} \quad n_1^{E^*} = 1.41 \\ \frac{G^*_{Mean}}{G_S} = \frac{G^*}{G_S} = (\phi)^{n_1^{G^*}} & \text{with} \quad n_1^{G^*} = 1.19 \end{cases} \tag{7.54}$$

- $0.2 < DA < 0.6$ - *Transversely isotropic homogenized material*: five elastic constants have to be determined

$$\begin{cases} \frac{E^*_{Mean}}{E_S} = \frac{\frac{E^*_{Max}+2E^*_{Min}}{3}}{E_S} = (\phi)^{n_1^{E^*}} & \text{with} \quad n_1^{E^*} = 1.41 \\ \frac{E^*_{Min}}{E^*_{Max}} = \left(\frac{\lambda_{Min}}{\lambda_{Max}}\right)^{n_2^{E^*}} & \text{with} \quad n_2^{E^*} = 1.34 \\ \frac{G^*_{Mean}}{G_S} = \frac{\frac{G^*_{Max}+2G^*_{Min}}{3}}{G_S} = (\phi)^{n_1^{G^*}} & \text{with} \quad n_1^{G^*} = 1.19 \\ \frac{G^*_{Min}}{G^*_{Max}} = \left(\frac{\lambda_{Min}}{\lambda_{Max}}\right)^{n_2^{G^*}} & \text{with} \quad n_2^{G^*} = 0.95 \\ \nu^*_{Mean} = \frac{\nu^*_{Max}+2\nu^*_{Min}}{3} = 0.25 & \text{with} \quad \nu^*_{Min} = \frac{E^*_{Min}}{2G^*_{Min}} - 1 \end{cases} \tag{7.55}$$

- $0.6 < DA < 1$ - *Orthotropic homogenized material*: nine elastic constants have to be determined

$$
\begin{cases}
\dfrac{E^*_{Mean}}{E_S} = \dfrac{\frac{E^*_{Max}+E^*_{Med}+E^*_{Min}}{3}}{E_S} = (\phi)^{n_1^{E^*}} \quad \text{with} \quad n_1^{E^*} = 1.41 \\
\dfrac{E^*_{Min}}{E^*_{Max}} = \left(\dfrac{\lambda_{Min}}{\lambda_{Max}}\right)^{n_2^{E^*}} \quad \text{with} \quad n_2^{E^*} = 1.34 \\
\dfrac{E^*_{Min}}{E^*_{Med}} = \left(\dfrac{\lambda_{Min}}{\lambda_{Med}}\right)^{n_3^{E^*}} \quad \text{with} \quad n_3^{E^*} = 1.95 \\
\\
\dfrac{G^*_{Mean}}{G_S} = \dfrac{\frac{G^*_{Max}+G^*_{Med}+G^*_{Min}}{3}}{G_S} = (\phi)^{n_1^{G^*}} \quad \text{with} \quad n_1^{G^*} = 1.19 \\
\dfrac{G^*_{Min}}{G^*_{Max}} = \left(\dfrac{\lambda_{Min}}{\lambda_{Max}}\right)^{n_2^{G^*}} \quad \text{with} \quad n_2^{G^*} = 0.95 \\
\dfrac{G^*_{Min}}{G^*_{Med}} = \left(\dfrac{\lambda_{Min}}{\lambda_{Med}}\right)^{n_3^{G^*}} \quad \text{with} \quad n_3^{G^*} = 0.70 \\
\\
\nu^*_{Mean} = \dfrac{\nu^*_{Max}+\nu^*_{Med}+\nu^*_{Min}}{3} = 0.25 \\
\dfrac{\nu^*_{Min}}{\nu^*_{Max}} = \left(\dfrac{\lambda_{Min}}{\lambda_{Max}}\right)^{n_1^{\nu^*}} \quad \text{with} \quad n_1^{\nu^*} = 1.31 \\
\dfrac{\nu^*_{Min}}{\nu^*_{Med}} = \left(\dfrac{\lambda_{Min}}{\lambda_{Med}}\right)^{n_2^{\nu^*}} \quad \text{with} \quad n_2^{\nu^*} = 1.46
\end{cases}
\tag{7.56}
$$

Using the proposed set of equations, it is hence possible to estimate all the elastic constants necessary to describe the macroscopic mechanical behaviour of a given expanded polymeric material, based on partial information about the internal microstructure and material distribution in the volume inspected. It is then possible to assemble the stiffness matrix, or dually the compliance matrix, and consequently predict the macroscopic mechanical response of the material in a generic stress or strain state, limited to the linear elastic regime [11].

The exponents identified in the equations are substantially independent of the specific morphologies or microstructure inspected; this statement is supported by the fact that they were obtained by inspect-

ing expanded materials exhibiting very different internal microstructure and produced through different technologies.

As a final note, these equations can be used in both ways; by experimentally measuring some elastic constants it is possible to obtain information about the internal microstructure of the tested samples, in terms of scalar quantities, such as the solid volume fraction, but also on tensorial quantities, such as the eigenvalues of the fabric tensor and the related information about material distribution inside the tested volume.

7.3.3 PPI experimental results

In this section the experimental results obtained on PPI material will be briefly illustrated and they constitute the basis for the application of the proposed model, shown in the next section.

From gas pycnometer analysis the bulk density of the constituent material was measured as $1455.1 \pm 8.2\ \mathrm{kg\,m^{-3}}$.

Figure 7.10 displays the average nominal stress, $\sigma_{nominal}$, versus nominal strain, $\varepsilon_{nominal}$, curve computed from mechanical test performed on single material struts. The shaded area is the semi-dispersion at each fixed strain level for the fifteen structures tested. From the graph is possible to see that the mechanical behaviour of the constituent material is almost linear up to 30% nominal strain; small deviations from linearity may be caused by the irregular geometry of the samples tested. From this mechanical test secant Young modulus of constituent material (E_S) was computed as the ratio between the stress associated to a nominal strain of 0.5% and the strain itself. The resulting value was 14 ± 0.7 MPa.

Figure 7.11 displays the results obtained through mechanical testing of the expanded material along the three main orthogonal directions. It is clear from the graph on the left that the material exhibits a transversely isotropic behaviour: the small-strain response in two directions

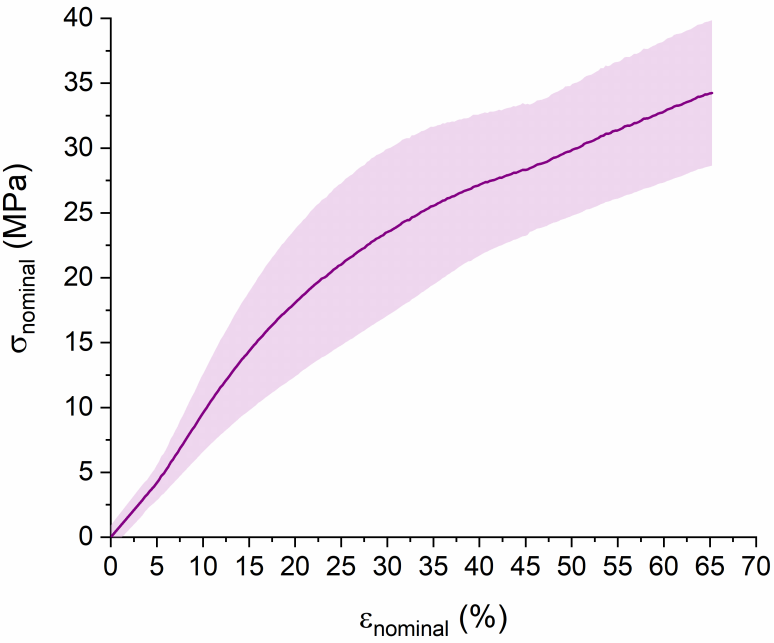

Figure 7.10: Mean nominal stress, $\sigma_{nominal}$, versus nominal strain, $\varepsilon_{nominal}$, curve of the tested single structures extracted from the expanded material.

is almost the same, while it is stiffer in the third one. Graph on the right shows the apparent stiffness, computed as before. The depicted semi-dispersions of the experimental data are once again reported.

Figure 7.12 shows the set of images, obtained through X-ray computed tomography analysis, representing the internal structure of PPI material. From the images the open-cell structure is clearly detectable; the cross-section of the foam struts resembles the typical plateau border geometry, widely adopted in literature to describe open-cell polyurethane foams [4] [1] [7].

Table 7.1 reports the results obtained from image analysis which were used in conjunction with the set of equations presented in the previous section.

The structural anisotropy degree value falls exactly within the range for which a macroscopic transversely isotropic mechanical behaviour is expected, confirming the considerations derived from the experimental

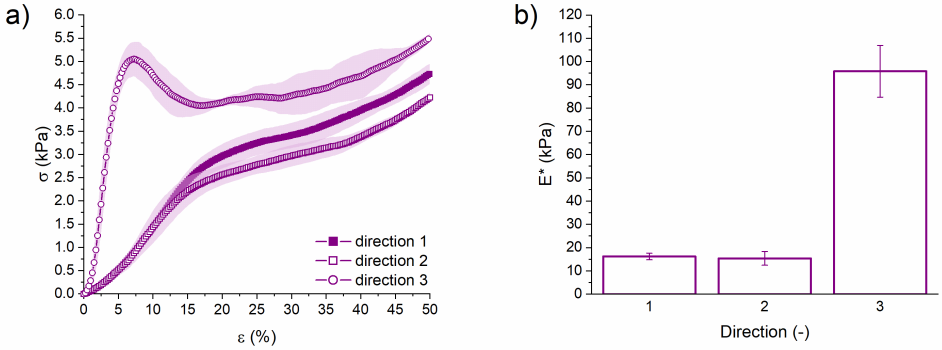

Figure 7.11: Experimental results of mechanical tests performed on the expanded polymeric samples; a) average nominal stress versus nominal strain of quasi-static uniaxial compression tests performed along the three main orthogonal direction of the cubic specimen; b) average apparent stiffnesses along the three main orthogonal directions of the tested specimens.

Figure 7.12: Binarized set of images representing the internal microstructure of PPI material obtained through X-ray computed tomography.

Table 7.1: Morpho-structural parameters computed from image analysis.

Parameter	
Solid volume fraction (ϕ)	2.79%
Mean structure thickness	107.46 µm
Structural anisotropy degree (DA)	0.4035
$\lambda_{Min}/\lambda_{Max}$	0.6072
$\lambda_{Min}/\lambda_{Med}$	0.6146

mechanical results.

7.3.4 Preliminary model validation

By exploiting the information obtained from structure analysis the elastic constants, necessary to describe the mechanical behaviour of a transversely isotropic solid, were computed. The two resulting apparent Young moduli were compared with the experimentally measured ones; the comparison is reported in figure 7.13. Error bars reported in the numerical estimation of the apparent stiffnesses were computed through error propagation while solving the system of equations. The agreement between experimental results and model prediction is quite good, considering that the closed-cell systems on which the equations were derived are completely different from the open-cell structure of PPI. This agreement supports the independence of the exponents identified within the proposed relations from the specific class of material inspected. Moreover, the prediction is able to clearly distinguish the apparent stiffnesses in the two directions.

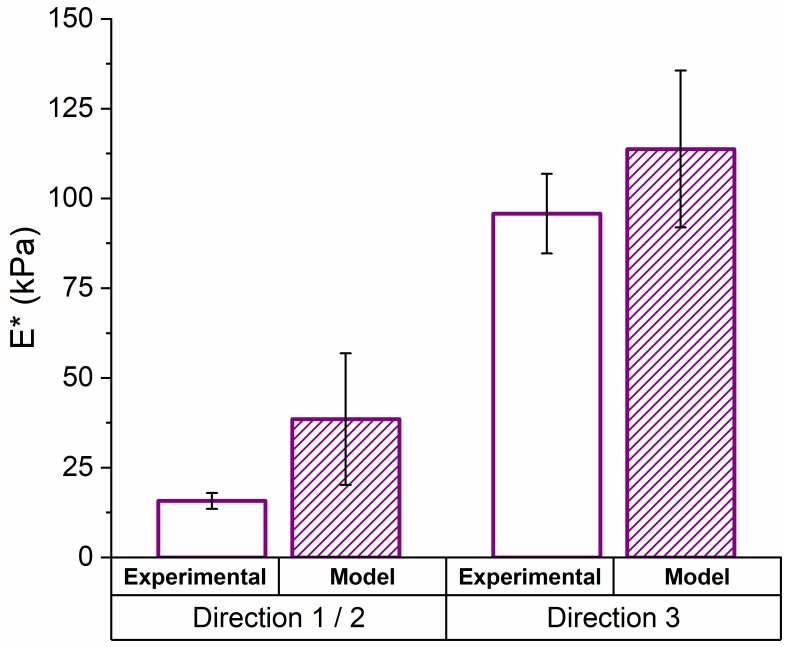

Figure 7.13: Comparison between apparent Young moduli experimentally measured with the one predicted using the set of analytical equations proposed. Error bars reported on the values predicted with the analytical equations are computed through error propagation during the resolution of the system.

7.4 Concluding remarks

In the present chapter a mechanical anisotropy index is proposed and combined with structural information, coming from X-Ray computed tomography, to provide a unique association between structural parameters and suitable macroscopic linear elastic constitutive models. Moreover, a system of equations, comprehensive of structural parameters and elastic constants, is proposed and its efficiency is demonstrated through its application to an open-cell expanded polymeric material, completely different from the closed-cell systems used to build the analytical relationships. These equations provide a powerful and efficient tool to estimate the elastic constants, knowing only limited information about the internal microstructure, and then allowing the estimation

of the entire stiffness matrix useful to investigate the linear elastic mechanical response in a generic stress or strain state. Moreover, from an industrial point of view, since X-Ray computed tomography is an expensive technique, both in terms of monetary and time resources, the proposed relationships can be exploited also in the opposite direction: by performing mechanical experiments on a given expanded material some internal microstructure characteristics can be inferred. The proposed relationships shall be further refined by increasing the quantity of available data and then properly validated by applying the set of equations to other experimentally available systems; additionally, synthetic structures with specific morpho-structural characteristics could be created by rapid prototyping techniques and subsequently tested. Such a reliable model could provide great help to the industry when designing new materials or optimizing existing ones.

7.5 References

[1] R. Bouix, P. Viot, and J. Lataillade. "Polypropylene foam behaviour under dynamic loadings: Strain rate, density and microstructure effects". en. In: *International Journal of Impact Engineering* 36.2 (Feb. 2009), pages 329–342. DOI: 10.1016/j.ijimpeng.2007.11.007. URL: https://linkinghub.elsevier.com/retrieve/pii/S0734743X08000791.

[2] S. C. Cowin. "Fabric dependence of an anisotropic strength criterion". en. In: *Mechanics of Materials* 5.3 (Sept. 1986), pages 251–260. DOI: 10.1016/0167-6636(86)90022-0. URL: https://linkinghub.elsevier.com/retrieve/pii/0167663686900220.

[3] S. C. Cowin. "The relationship between the elasticity tensor and the fabric tensor". en. In: *Mechanics of Materials* 4.2 (July 1985), pages 137–147. DOI: 10.1016/0167-6636(85)90012-2. URL: https://linkinghub.elsevier.com/retrieve/pii/0167663685900122.

[4] L. Gong, S. Kyriakides, and W.Y. Jang. "Compressive response of open-cell foams. Part I: Morphology and elastic properties". en. In: *International Journal of Solids and Structures* 42.5-6 (Mar. 2005), pages 1355–1379. DOI: 10.1016/j.ijsolstr.2004.07.023. URL: https://linkinghub.elsevier.com/retrieve/pii/S0020768304004305.

[5] S. Gong, Z. Li, and Y.Y. Zhao. "An extended Mori–Tanaka model for the elastic moduli of porous materials of finite size". en. In: *Acta Materialia* 59.17 (Oct. 2011), pages 6820–6830. DOI: 10.1016/j.actamat.2011.07.041. URL: https://linkinghub.elsevier.com/retrieve/pii/S1359645411005179.

[6] T.P. Harrigan and R.W. Mann. "Characterization of microstructural anisotropy in orthotropic materials using a second rank tensor". en. In: *Journal of Materials Science* 19.3 (Mar. 1984),

pages 761–767. DOI: 10.1007/BF00540446. URL: http://link.springer.com/10.1007/BF00540446.

[7] N.J. Mills. "The high strain mechanical response of the wet Kelvin model for open-cell foams". en. In: *International Journal of Solids and Structures* 44.1 (Jan. 2007), pages 51–65. DOI: 10.1016/j.ijsolstr.2006.04.014. URL: https://linkinghub.elsevier.com/retrieve/pii/S0020768306001235.

[8] L. Morin, P. Gilormini, and K. Derrien. "Generalized Euclidean Distances for Elasticity Tensors". en. In: *Journal of Elasticity* 138.2 (Mar. 2020), pages 221–232. DOI: 10.1007/s10659-019-09741-z. URL: http://link.springer.com/10.1007/s10659-019-09741-z.

[9] A. Odgaard et al. "Fabric and elastic principal directions of cancellous bone are closely related". en. In: *Journal of Biomechanics* 30.5 (May 1997), pages 487–495. DOI: 10.1016/S0021-9290(96)00177-7. URL: https://linkinghub.elsevier.com/retrieve/pii/S0021929096001777.

[10] N.I. Ostrosablin. "Transversely Isotropic Tensor Closest in Euclidean Norm to a Given Anisotropic Elastic Modulus Tensor". en. In: *Journal of Applied Mechanics and Technical Physics* 60.1 (Jan. 2019), pages 106–122. DOI: 10.1134/S0021894419010140. URL: http://link.springer.com/10.1134/S0021894419010140.

[11] B. Rietbergen and A. Odgaard. "Direct mechanics assessment of elastic symmetries and properties of trabecular bone architecture". en. In: (), page 6.

[12] Z. Tabor. "On the equivalence of two methods of determining fabric tensor". en. In: *Medical Engineering & Physics* 31.10 (Dec. 2009), pages 1313–1322. DOI: 10.1016/j.medengphy.2009.09.003. URL: https://linkinghub.elsevier.com/retrieve/pii/S135045330900191X.

[13] P.K. Zysset. “A review of morphology–elasticity relationships in human trabecular bone: theories and experiments”. en. In: *Journal of Biomechanics* 36.10 (Oct. 2003), pages 1469–1485. DOI: 10.1016/S0021-9290(03)00128-3. URL: https://linkinghub.elsevier.com/retrieve/pii/S0021929003001283.

[14] P.K. Zysset, R.W. Goulet, and S.J. Hollister. “A Global Relationship Between Trabecular Bone Morphology and Homogenized Elastic Properties”. en. In: *Journal of Biomechanical Engineering* 120.5 (Oct. 1998), pages 640–646. DOI: 10.1115/1.2834756. URL: https://asmedigitalcollection.asme.org/biomechanical/article/120/5/640/398235/A-Global-Relationship-Between-Trabecular-Bone.

Chapter 8

Image-based numerical tool for non-linear mechanical modelling

In the following chapter an image-based numerical tool designed to perform non-linear numerical simulations, again considering the real microstructure of expanded polymeric materials, is presented. The approach is firstly validated by performing linear finite element analysis and comparing the numerical results with experimental data presented in chapter 3. The approach is then applied to generate fictitious structures with different morpho-structural features to increase the range of available structures and hence to compare the relationships obtained with the RVE approach. Lastly, the algorithm is preliminary applied to non-linear simulations in which the attention is mainly focused on the efficiency, in terms of time and numerical resources (RAM and CPU), requested to perform simulations.

8.1 Introduction

One of the main open issues in the field of numerical modelling of expanded polymeric materials is the development of an efficient numerical tool useful to perform numerical simulations true to the complex real structure of this class. The main limitation is set by the large numerical resources required to perform finite element analysis on such a huge number of finite elements. This limitation has to be considered from two viewpoints: physical resources (e.g. RAM) and time necessary to conduct the simulation; the latter is typically very large and incompatible not only with industrial needs, but also with the academic research activities.

The main approaches usually adopted in the literature consist in the simplification of the internal microstructure, usually performing some skeletonization process with regular solids, as presented in chapter 2 [2] [21]; moreover, an additional simplification on the finite element type, decreasing the degree of freedom in the element deformation mechanisms, has to be included to shorten the requested simulation time and to reduce the physical resources necessary to solve the simulation [1] [18]. In the case of open-cell foams, the most widely used element is the Timoshenko beam, used by many authors to represents the internal structures of the simulated foam, and the junction points between structures are usually simplified with a nodal mass approach, which consists in artificially attributing the entire mass of the junction point to a single node at the end of the beam [7] [8] [6]. This approach is surely efficient from a numerical point of view, but results in an excessive simplification of the real structure of expanded polymeric materials, thus producing a very stiff macroscopic mechanical response compared to the real behaviour [4].

In recent years new approaches have been proposed in the literature, mainly based on level sets [9] [13] [17] [18] or Voxel finite element approaches [11] [12]; specific details on the related methods are not

reported here since they are beyond the scope of the present thesis, but interested readers can find useful references at the end of this chapter. These two approaches are numerically very efficient and moreover they are able to reproduce the real internal structure of the simulated material, starting from a set of images reproducing the internal structure. The main issue resides in convergence problems when non-linear simulations are performed, since these methods require at least a partial knowledge of internal deformation mechanisms since a so-called "advancing law" has to be provided to update at each simulation step the level set map. This issue is usually faced following a trial and error approach, formulating different "advancing laws" until the agreement between experimental and numerical data are satisfactory. This empirical way of setting the model parameters typically limits the validity of the obtained results to the specific system under investigation, thus giving a descriptive instead of a predictive model.

The method proposed in the following chapter is an image-based method, which considers the real geometry of internal microstructure, but greatly reduces the numerical resources necessary to perform finite element analysis. The approach works on an optimization of the high-resolution set of images, artificially reducing their original resolution, while preserving the essential morpho-structural features detected through image analysis.

8.2 Materials and methods

8.2.1 Materials

In this chapter the sets of images already obtained will be referred to, in particular those representing the internal structure of PET and PPI samples. PET samples will be used in the first part for the validation of the newly developed algorithm. In the second part PET and PPI samples will be used to perform non-linear mechanical simulations.

Experimental curves used in the following sections are also the ones already presented in previous chapters.

8.2.2 Structure analysis

Since the whole set of images is considered for numerical simulations the methods for structure analysis, already presented in chapter 4, will be used and briefly recalled.

Mean volumetric structure thickness and pores size were investigated to identify foams' internal cells characteristic dimensions. The mean volumetric structure thickness was calculated using the algorithm of Hildebrand and Rüegsegger [5] implemented in the custom-made *Matlab* algorithm while the labelling analysis tool of *Avizo* was used for cell measurements.

The analysis of anisotropy was accomplished using two custom made algorithms. The first one was implemented in *Matlab* to compute MIL on the set of images, according to the procedure proposed in chapter 4 [16]. The second one was implemented using the *VTK library* to compute spatial autocorrelation function [20]. In both approaches, MIL and ACF, a least square fitting algorithm was employed to fit the ellipsoid represented in the rose diagram; the number of orientations chosen for both analyses was 2049.

8.2.3 Peano's algorithm

Image conversion into finite element mesh is performed once again through the application of the marching cube algorithm [14], presented in chapter 5. As already discussed, straightforward application of the algorithm to the entire set of high-resolution images would result in a huge finite element mesh, with a number of elements in the order of 10^7 - 10^8, whose computational cost would not be affordable. A new algorithm was developed and implemented in a custom code, implemented in *Matlab R2019b*, to reduce this cost, while preserving the essential morpho-structural characteristics of the imaged specimens in the whole reconstructed volume. This simple two-parameters algorithm is freely inspired to the Peano's theory of n-order tensors reduction, hence referred to as Peano's algorithm, and is very efficient from a computational point of view.

The two employed parameters are:

- P: represents the cubic sub-domain side-length in which the 3D tensor, representing the set of binarized images, is subdivided. This is called Peano's number and it assumes positive integer values major or equal to 1. Obviously for $P = 1$ the image set remains exactly the same. All the defined sub-regions will collapse in a new single voxel with a length size equal to the old resolution (3 µm, in this work) multiplied by P. This product gives the characteristic length scale of the representative volume element of the homogenized medium used to compute the elastic properties.

- Th: is a threshold. The collapsed region will result in a new voxel representing solid material (Boolean value equal to 1) or its absence (Boolean value equal to 0) according to this parameter. If the ratio of "solid" voxels to the total number of voxels within a given sub-region is greater than Th the new voxel will be solid (Boolean equal to 1) or vice versa empty (Boolean equal to 0).

Starting from high-resolution CT data and by properly tuning the above described parameters the same CT inspected volume can be converted into a finite element mesh with a manageable size.

8.2.4 Finite element modelling

The combination of Peano's and marching cubes algorithms was exploited to generate 20 different finite element meshes of equivalent total volume, imported in the commercial code *ABAQUS 2018* to perform mechanical finite element simulations. 8 structures represent the real foam PET samples (2 per density) experimentally tested, whose results were presented in chapter 3; the other 12 represent fictitious structures generated with Peano's algorithm by altering solid fraction, mean structure thickness and anisotropy of the real ones. The meshes are made up of a number of cubic linear elements (C3D8) varying from 150000 to 820000. Initially the constitutive material law adopted is once again linear elastic, with the values reported in table 8.1.

Table 8.1: Linear elastic constants adopted for linear simulation of PET samples.

Parameter	Value
Young's modulus (E)	2900 MPa
Poisson's ratio (ν)	0.4

Displacement boundary conditions were applied to simulate a uniaxial compression test, up to a nominal strain value of 1%. Constrained displacements were enforced on one face along the compression direction while on the opposite face a total displacement, corresponding to the final aforementioned strain level, was applied.

For all the reconstructed geometries three simulations reproducing experimental compression tests along the three main orthogonal directions were conducted and the apparent Young moduli, E^*, were computed.

In the second part of the work, non-linear mechanical simulations were conducted on reconstructed geometries, always optimized with Peano's algorithm, representing the tested specimens of PET and PPI samples. Constitutive law adopted in this case are: perfectly elastic-plastic behaviour for PET samples, since it is widely reported in the literature that the non-linear compressive mechanical behaviour of PET exhibits a shear-yielding mechanism [19] [15]; for PPI, since an almost linear behaviour up to 30% of nominal strain has been showed for the constituent material in chapter 7, a linear elastic isotropic constitutive law is adopted. Parameters used are summarized in table 8.2 and 8.3.

Table 8.2: Mechanical parameters adopted for non-linear simulation of geometries representing real samples whose constituent material is PET.

Parameter	Value
Young's modulus (E)	2900 MPa
Poisson's ratio (ν)	0.4
Plastic strain (ε_y)	0
Plastic stress (σ_y)	200 MPa

Table 8.3: Mechanical parameters adopted for non-linear simulation of geometries representing real samples whose constituent material is PPI.

Parameter	Value
Young's modulus (E)	14 MPa
Poisson's ratio (ν)	0.3

The yield threshold for PET was taken from literature data obtained on PET fibres and is consequently higher than the one reported in literature for bulk PET (70 MPa); this choice is made on the assumption that the material within the foam samples is highly oriented [10].

Boundary conditions adopted for non-linear simulations are the same adopted for the linear case, except for the total displacement,

which in this case corresponds to a nominal strain of 10%. Only for real tested specimens, one simulation for each reconstructed mesh was performed.

Both linear and non-linear simulations were run on a Linux machine with 24 cores and 49 GB RAM; the average CPU time needed for a single linear simulation varied between 2 and 4 hours, depending on the total number of finite elements in the mesh, while the average time for non-linear simulations ranged between 8 and 16 hours, always according to the number of finite elements and in this case also according to the complexity of the constitutive law adopted.

8.3 Results and discussion

8.3.1 Peano's algorithm validation

Mesh optimization is a crucial aspect of image-based approaches which aim to convert the set of images, acquired from X-Ray computed tomography analysis, into a finite element mesh that represents the real structure of the sample scanned, as already pointed out many times in the previous chapters. Figure 8.1 displays the effectiveness of the new custom-made developed algorithm in greatly reducing the number of elements needed to reconstruct the entire volume inspected with the tomography. The number of elements is plotted as a function of Peano's number (P) and threshold variation (Th), the two parameters of the adopted algorithm. Data in the graph refer to PET 320 sample B, but similar results were obtained for other inspected specimens.

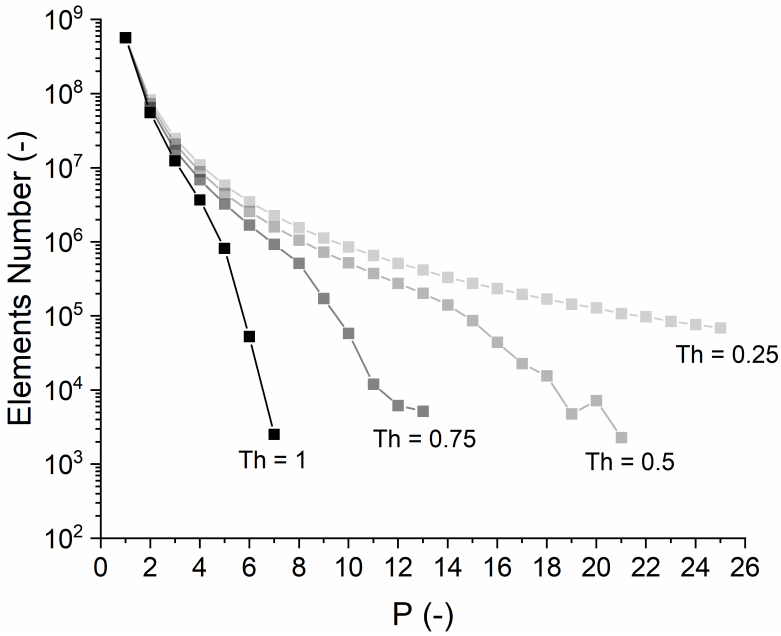

Figure 8.1: Total number of elements required to reconstruct the entire volume inspected with X-Ray computed tomography as a function of Peano's algorithm parameters: threshold (Th) tuning and Peano's number (P).

The reduction of the number of elements required to reconstruct the geometry must be achieved while preserving at the same time the essential morpho-structural characteristics of the relevant inspected sample. Figure 8.2 clearly shows how it is possible, with a proper tuning of the two aforementioned parameters, to maintain the values of fundamental morpho-structural characteristics of the specimen reasonably close to their original values. Considering the reported example (with data obtained from PET 320 sample B), the choice of values 10 for P and 0.5 for Th ensures that relevant structural parameters are not varied by more than 5% with a three order of magnitude reduction of the total element number from 568973091 to 520081. One of the main advantages of the proposed algorithm resides in the very limited computational resources required. Its usefulness is strictly related to the quality of the original set of images: the higher its initial resolution, the higher the usefulness of applying the algorithm with the aim of reducing the elements number without altering too much the morphological characteristics of the inspected samples. Conversely, starting from a low-resolution set of images, the usefulness of applying the algorithm decreases since a lower number of finite elements is necessary to convert the images and moreover, starting with low accurate information on microstructure the application of Peano's algorithm leads to a consequent additional reduction in the accuracy of structure description.

After the application of Peano's algorithm the resulting volume is subsequently processed with the marching cubes one to convert it into the finite element mesh; this result represents an ideal compromise between element number and faithfulness to the original morpho-structural characteristics. The resolution of the marching cube algorithms obviously matched that of the image set reduced using Peano's. An example of finite element mesh reconstruction is reported in figure 8.3; the geometries shown refer to samples B of each density inspected for PET material.

The optimally tuned parameters of the Peano's algorithm are re-

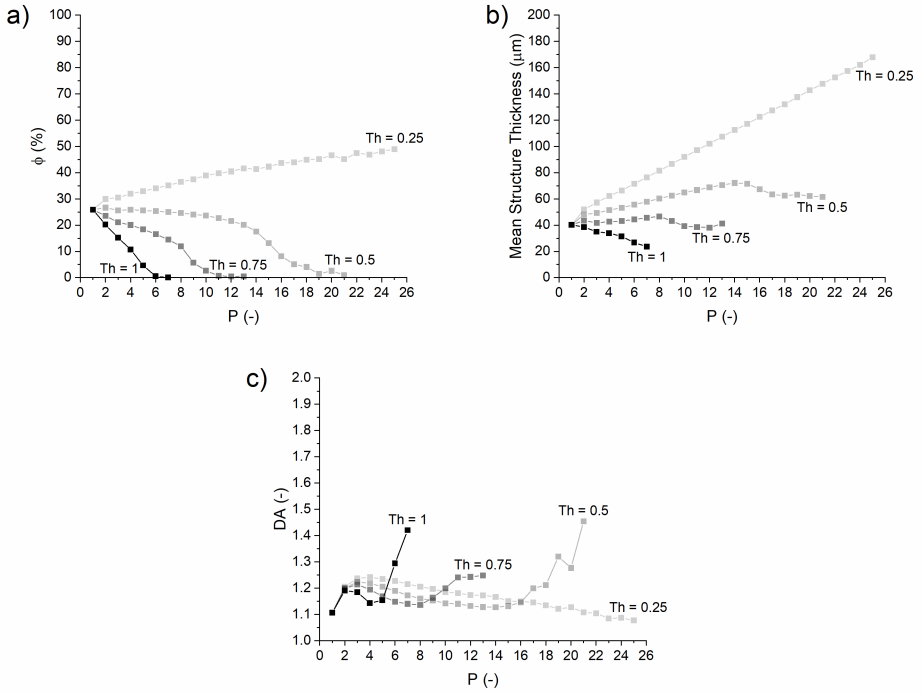

Figure 8.2: Effect of Peano's algorithm variables on the main morpho-structural parameters of PET 320 sample B: a) solid volume fraction (ϕ); b) mean volumetric structure thickness; c) structural degree of anisotropy (DA).

ported in table 8.4 for each sample, together with the element number before and after its application; new final resolution used in the marching cubes algorithm is also listed. P was set to 10 in all cases, while the optimal value of Th was 0.4 for PET 80, and 0.5 for the higher densities; the very narrow parameter range identified for materials having significantly different morphological characteristics proves the robustness of the method.

Figure 8.4 summarizes the comparison of the original and modified morpho-structural characteristics. It is clear that only minor variations in terms of solid volume fraction (ϕ) and degree of anisotropy occurred; the main difference between the original and reduced size structures is in the mean volumetric structure thickness, but it is considered acceptable

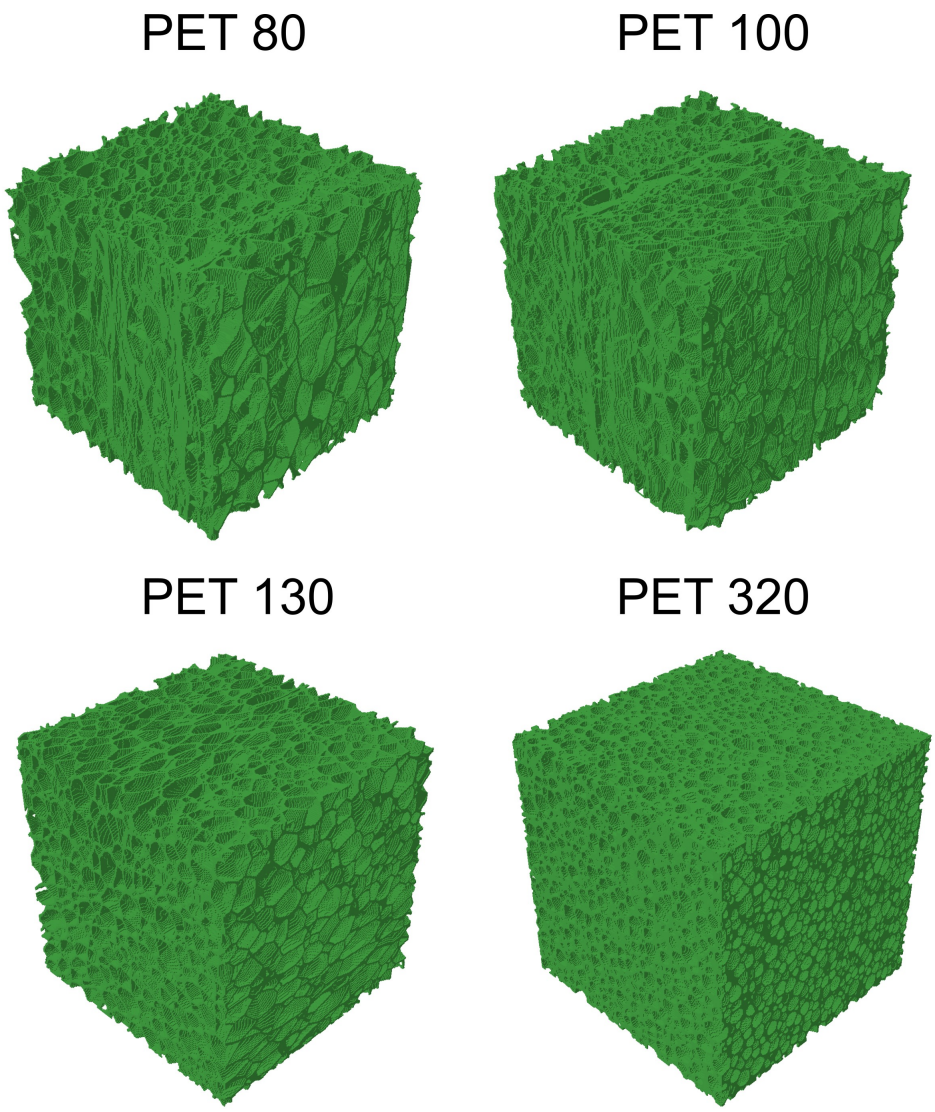

Figure 8.3: Finite element mesh reconstruction after the application of Peano's algorithm to the set of images obtained through tomography. All the geometries shown refers to sample B of the corresponding density for material PET.

since it has been shown in chapter 6 that this structural parameter has a minor influence on the macroscopic mechanical behaviour of expanded polymeric materials. Obviously, the reduction of the spatial resolution is accompanied by a coarser representation of existing structures: the

Table 8.4: Results of mesh optimization performed by applying Peano's algorithm using the listed optimal parameters. The spatial resolution of the original set of images was 3 µm.

Sample	Original number of elements	Reduced number of elements	P	Th	Modified resolution [µm]
PET 80 A	369997393	323934	10	0.4	30
PET 80 B	282556706	318097	10	0.4	30
PET 100 A	456845460	345770	10	0.5	30
PET 100 B	470968553	402227	10	0.5	30
PET 130 A	377427402	297431	10	0.5	30
PET 130 B	308986233	343174	10	0.5	30
PET 320 A	643671877	599183	10	0.5	30
PET 320 B	658234174	629510	10	0.5	30

thinner ones are either deleted or made thicker. Nevertheless, a good tuning of Peano's parameters preserves the essential features of the investigated structure, despite a huge reduction in the total finite element number and related free nodes (about three orders of magnitude). This reduction is essential, as already stated, to reduce the computational burden of the analysis to levels which are compatible with the currently available numerical resources (in terms of RAM, CPU and CPU time).

Linear numerical simulations of the mechanical testing of the reconstructed meshes were performed according to the methods described in previous sections. Relevant results focused on the determination of the foams' apparent stiffness (E^*), determined as the slope at the origin of the nominal stress versus nominal strain plot.

In figure 8.5 a comparison is made between the experimental data obtained along the three main orthogonal directions on all tested samples, already presented in chapter 3, and numerical simulations on the reconstructed geometries representing the originally inspected samples (two for each inspected density of material PET). It is clear from the graph that the numerical results generally overestimate the experimental ones, in a similar way to the Representative Volume Element (RVE) approach presented in chapter 5, especially for lower densities. With the present approach, reasons explaining this fact reside

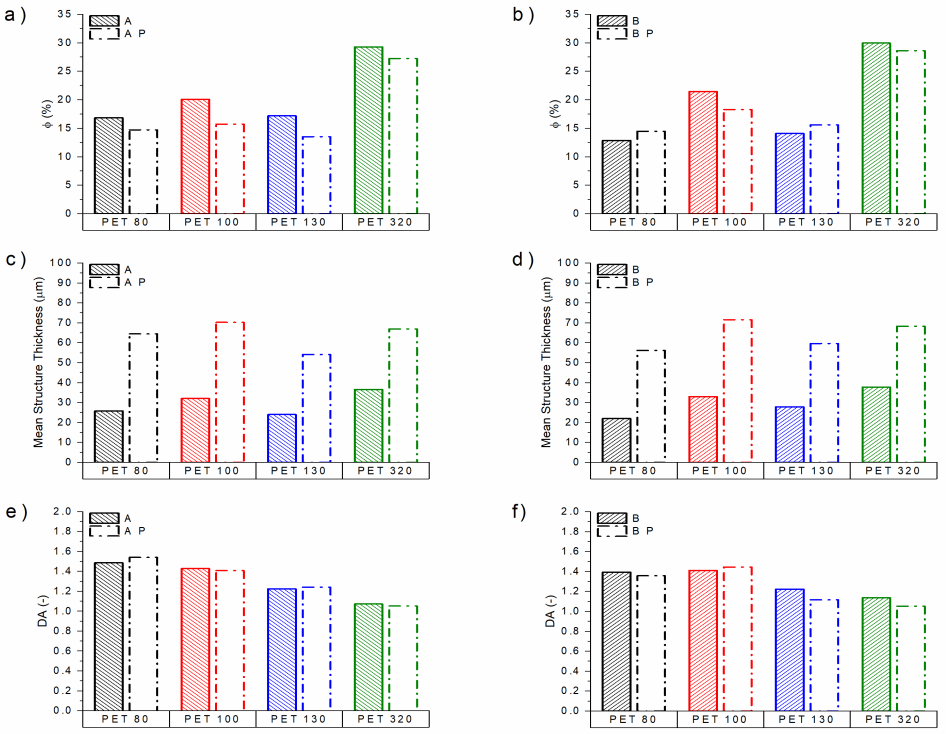

Figure 8.4: Comparison between morpho-structural characteristics before and after application of Peano's algorithm (P); comparison is done for sample A (a), c) and e)) and B (b), d) and f)) for each inspected density of material PET. Solid volume fraction (ϕ) (a) and b)), mean volumetric structure thickness (c) and d)) and structural degree of anisotropy (DA) (e) and f)) are reported.

in the great number of variables that affect the final results of numerical simulation: the structural variability of individual samples (still smaller than the real macroscopic ones), the application of binarization to the set of images and also Peano's algorithm which introduces small but sensible changes in the structure. All these factors combined with the very high sensitivity of the apparent stiffness (E^*) to solid volume fraction, especially for very low values (as already demonstrated in chapter 5), limit the ability of this approach to closely match experimental data.

Despite the mismatch between experimental and numerical data, for

the reasons discussed, the results are considered acceptable; the macroscopic mechanical response along the three main orthogonal directions for all the inspected densities is well descripted by the numerical approach. Absolute values are not in good agreement for all the reported cases for the variations in structure description reported in the previous paragraphs.

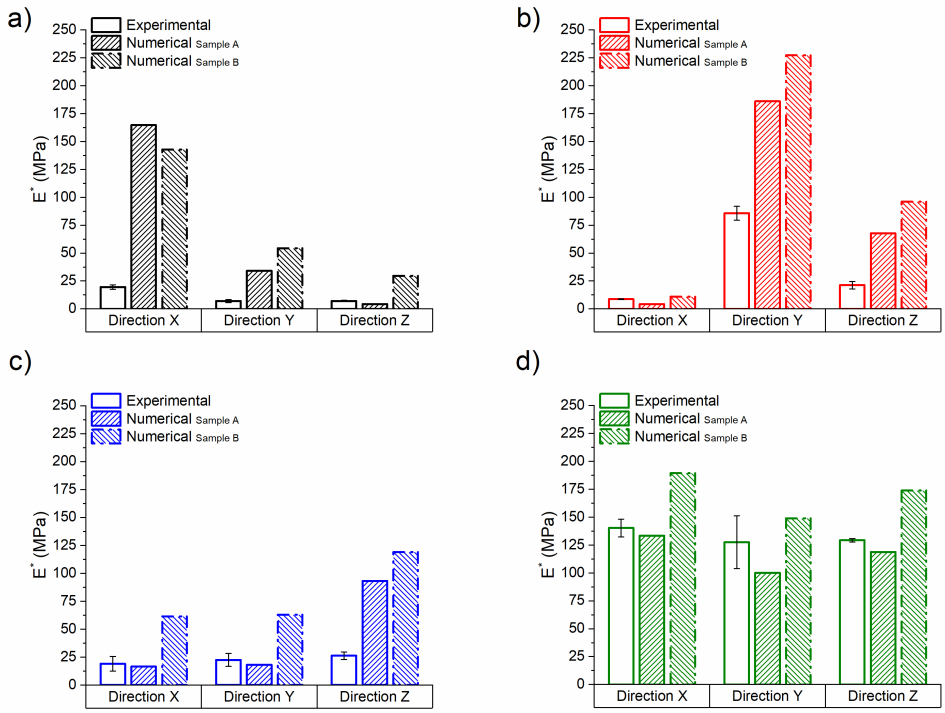

Figure 8.5: Comparison between experimental apparent stiffness and numerical apparent stiffness evaluated along three main orthogonal directions (X, Y and Z) for a) PET 80 samples A and B, b) PET 100 samples A and B, c) PET 130 samples A and B and d) PET 320 samples A and B. Experimental data shows average values and dispersion of five samples for each foam density; for the numerical simulations, individual results obtained for each reconstructed sample are shown.

Peano's algorithm, besides its ability to generate reduced structures from the real ones, can also be exploited to generate fictitious structures

by properly tuning the algorithm's parameters. In the present chapter 12 fictitious structures were generated starting from the real PET 320 sample B to broaden the range to be analysed beyond the limits enforced by the currently available foaming techniques. Some examples of these reconstructed fictitious structures are reported in figure 8.6.

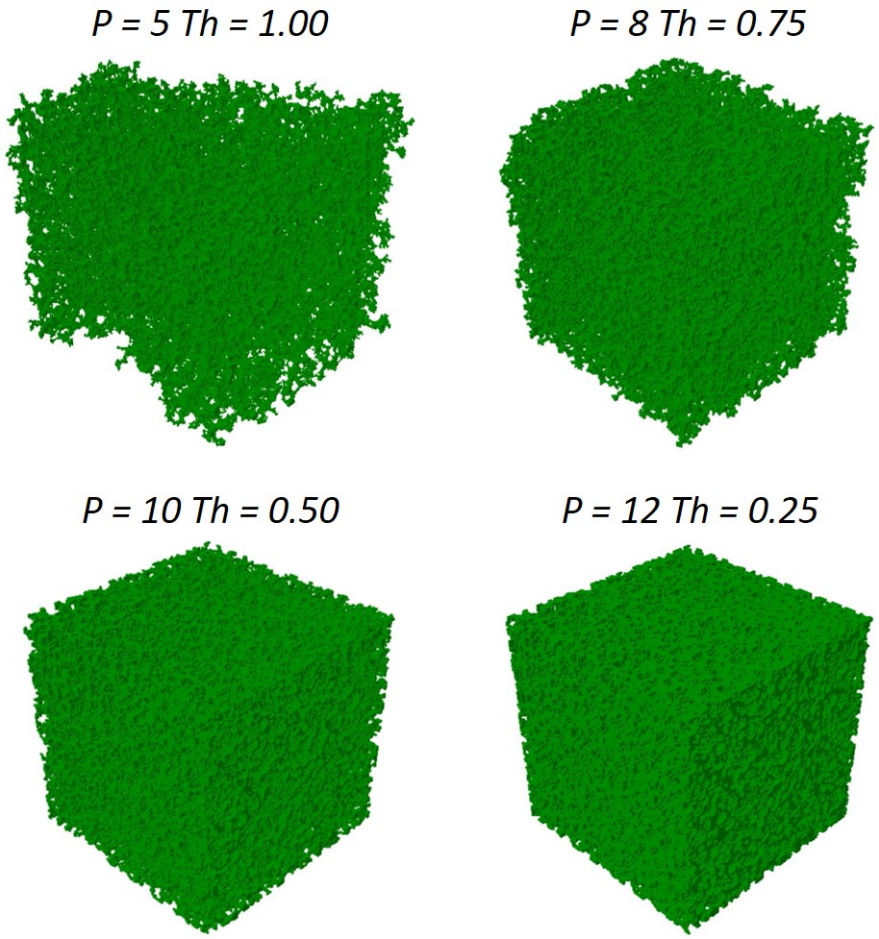

Figure 8.6: Examples of fictitious structures reconstructed with different set of values of Peano's algorithm parameters, P and Th.

In real foams, it is very difficult to control individual features, with changes in the production process typically influencing several parameters (e.g. wall thickness, cell size) at once. The generation of fictitious structures allows to single out the individual contribution

of each individual morphological characteristic to the macroscopic mechanical properties of the foam. This capability was exploited by generating structures spanning a much broader range of solid volume fraction with respect to the real ones and compare the results obtained with this newly developed approach with respect to the ones obtained with Representative Volume Element approach already shown and discussed in chapter 5.

The results, both experimental and numerical, were combined with those obtained by analysing the fictitious structures generated thanks to Peano's algorithm. Taking advantage of a much broader range of void volume fraction $(1-\phi)$ examined, a very clear bilinear trend of the apparent stiffness can be identified also in this case, as shown in figure 8.7, confirming and enhancing the results presented in chapter 5. The mean apparent stiffness $\left(E^*_{Mean} = \frac{E^*_X + E^*_Y + E^*_Z}{3}\right)$ of each sample was, also in this case, normalised with respect to the reference amorphous PET bulk modulus. A marked change in slope is again clearly visible at about 80% of void volume fraction. The very large variation in the sensitivity of the stiffness to the void volume fraction, or dually solid volume fraction, confirmed once again the existence of a transition in the main foam deformation mechanism, moving from a volumetric, axially dominated to a surface, bending dominated one.

The change in the deformation mechanisms, for void volume fractions greater than 80%, is once again supported and confirmed by the different homogenized deformation components, quantified through the numerical application of Gurson model [3], as explained in chapter 5. In figure 8.8 the two homogenized strain components, volumetric and surface, are reported as a function of void volume fraction. For void volume fractions higher than 80% the macroscopic deformation mechanism is almost completely due to surface deformation, index of a prevailing global bending deformation mechanism. For smaller values the two deformation mechanisms coexist, while for void volume fraction value inferior to 40% the volumetric strain component is predominant

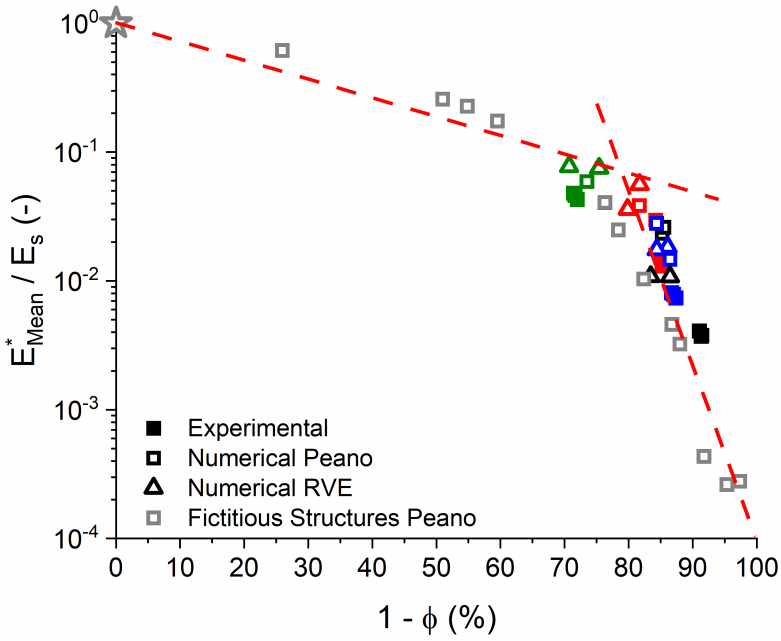

Figure 8.7: Normalized mean apparent stiffness $\left(\frac{E^*_{Mean}}{E_S}\right)$ as a function of void volume fraction $(1-\phi)$. Filled coloured symbols represent experimental mechanical tests and empty coloured symbols are the numerical simulations performed on the structures reconstructed from the relevant images sets; empty grey symbols are the results obtained from fictitious structures, while grey star represents bulk amorphous PET. Red dashed lines highlight bilinear trend of the data.

with respect to the surface one. This leads to the assimilation of the expanded material macroscopic mechanical behaviour, with void volume fractions value lower than 40%, to that of a porous solid and no more of a cellular solid. For completeness, the graph also reports also the two points, orange and green stars, which represent the deformation components of bulk PET. A red dashed line represents the macroscopic strain imposed in linear finite element simulations.

Figure 8.9 displays a qualitative example of volumetric strain distribution across the simulated volume of two different samples characterized by a void volume fraction higher and lower than the identified threshold value of 80%. In both cases the macroscopically imposed com-

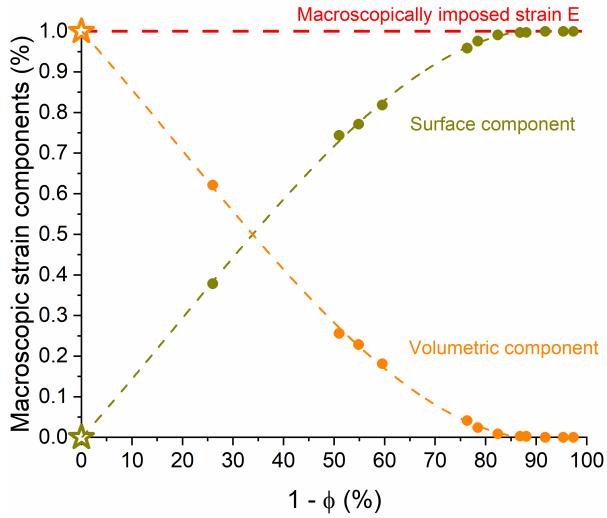

Figure 8.8: Deformation components of the simulated sub-domains as a function of void volume fraction; the two contributions derive from the numerical application of Gurson model. Dashed red line represents macroscopic strain applied as a boundary condition in finite element modelling.

pressive strain is equal to 1%. It is clear from the depicted contour plot that volumetric strains are highly localised and inhomogeneous around voids and the inhomogeneities are more pronounced for the case with the highest void volume fraction value, where surface strain are predominant, according to the results reported in figure 8.7. Moreover, for the two geometries reported the total volumetric strain is equal to 0.43% and 0.95% for the higher and lower void volume fraction, respectively, proving once again the existence of different deformation mechanisms for the two identified regimes. Figure 8.9, conversely, clearly shows the difficulties to visually inspect and interpret the mechanical results obtained from the simulations performed on such complex geometries and so justifies the choice of adopting an homogenization model to extract lumped parameters from simulations.

Finally, the relation between mechanically observed and structurally determined anisotropy was explored. Despite a certain degree of scatter visible in figure 8.10, a good correlation, similar to the one reported in

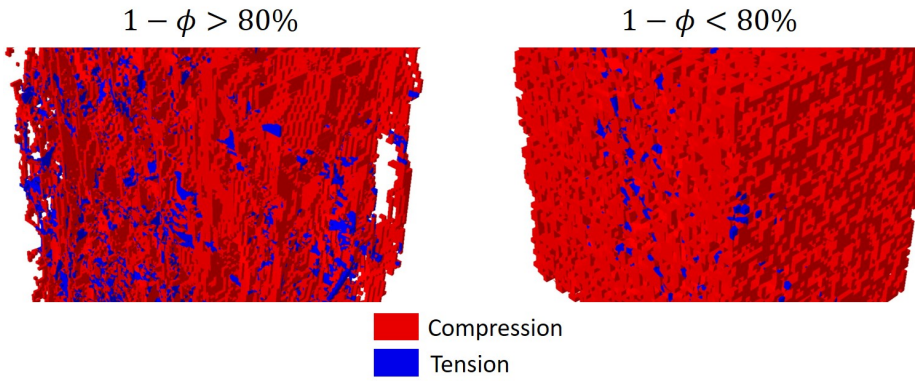

Figure 8.9: Maximum principal volumetric deformation contour plot for two different geometries obtained through Peano's algorithm. Geometry on the left exhibits a void volume fraction higher than 80% and the one on the right lower than 80%. Compressive volumetric strain are represented in red, while tensile volumetric strain are represented in blue.

previous chapters, was found between the ratio of maximum to minimum apparent stiffness $\left(\frac{E^*_{Max}}{E^*_{Min}}\right)$ for the real samples and the corresponding ratio of the maximum and minimum eigenvalues $\left(\frac{\lambda_{Max}}{\lambda_{Min}}\right)$, evaluated with both Mean Intercept Length (MIL) and Autocorrelation function (ACF) algorithms. The similar result obtained using both algorithms supports the thesis of some authors, which state that ACF and MIL can give equivalent results, providing that enough texture features are considered during the analysis. Since similar results in terms of spatial material distribution are provided by MIL and ACF algorithms, in terms of fabric tensor eigenvalues (λ_i), similar relations, already presented in chapter 7 for MIL algorithm, could be constructed also for ACF algorithm strengthening the equivalence between the two tensorial algorithm in describing the macroscopic mechanical behaviour of expanded polymeric material starting from spatial material distribution.

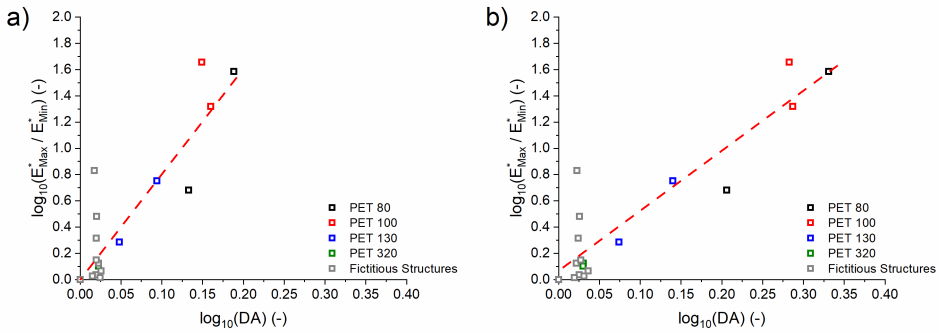

Figure 8.10: Ratio of maximum to minimum apparent stiffness $\left(\frac{E^*_{Max}}{E^*_{Min}}\right)$ and computed structural degree of anisotropy (DA) for a) Mean Intercept Length algorithm and b) autocorrelation function algorithm. Empty coloured symbols represent numerical simulations on the structure reconstructed from images sets optimization and empty grey symbols are the results obtained from fictitious structures.

8.3.2 Algorithm comparisons

Table 8.5 summarizes a comparison, based on different numerical aspects, of the two image-based approaches applied along the present thesis.

The comparison between the two algorithms reported in the table is performed fixing the volume reconstructed and simulated (0.9^3 mm^3) and is clearly shown how Peano's algorithm require less numerical resources with respect to the Representative Volume Element approach and, moreover, with the first approach non-linear simulation are not feasible with the available numerical resources. In a similar way, the comparison could be performed fixing the maximum numerical resources available (49 GB RAM and 23 CPUs) and looking at the maximum volume simulated: 0.9^3 mm^3 for RVE approach and 3.9^3 mm^3 for Peano's algorithm approach, showing once again the usefulness of Peano's algorithm application to reduce the computational cost required to simulate a large volume, more representative of the real experimentally tested samples. The maximum volume simulated reported, is specific of the

Table 8.5: Technical comparison between the image-based algorithms applied in the present thesis work.

	Representative Volume Element (RVE)	**Peano's algorithm**
Geometry description - **Accuracy**	Tomographic resolution - High resolution CT scans	Tomographic resolution - Reduced resolution
Geometry reconstruction - **Pre-processing**	$\approx$ 10 minutes Personal Computer (8 GB RAM, 1 CPU)	$\approx$ 10 minutes Workstation (32 GB RAM, 2 CPUs)
Minimum average numerical resources **Linear simulation** **Post-processing**	Cluster - (40 GB RAM, 24 CPU)	Cluster - (16 GB RAM, 8 CPUs)
Minimum average numerical resources **Non-linear simulation** **Post-processing**	Not feasible with available numerical resources	Cluster $\approx$ 24 hours for 100 iterations (49 GB RAM, 23 CPUs)
Specific **boundary condition**	Symmetry / Periodic / Quasi-Periodic	Not required
Homogeneization scheme	Required	Not required

set of images and related resolution used in the present work, but with larger inspected volume and through the application of the same procedure described above for Peano's algorithm, larger volume could be reconstructed and simulated. Moreover, through the mesh optimization process it is possible to reconstruct the mesh with an adequate number of finite elements that allows to perform non-linear finite element simulations in a reasonable amount of time and with a relatively limited request of numerical resources.

Non-linear mechanical simulation results will be shown in the next section, where the main objective of this result is still mainly focused on the efficiency of the designed Peano's algorithm, more than on the agreement between experimental and numerical results. As just said, all the following results are obtained in a reasonable amount of time (less than one day) and with limited numerical resources (high-end workstation) employed.

8.3.3 Non-linear simulation results

Figure 8.11 displays a qualitative comparison between the undeformed and the deformed reconstructed volume, proving once again the difficulties to visually inspect the results obtained from simulations on such complex geometries.

Figure 8.12 displays the results obtained from non-linear mechanical finite element simulations conducted on the finite element mesh optimized using Peano's algorithm, compared with experimental data presented in chapter 3. For both dataset, nominal strain, $\varepsilon_{nominal}$, is computed as the average displacement divided by the initial length of the tested sample, while nominal stress, $\sigma_{nominal}$, is computed as the total force divided by the nominal area of the sample. The shaded area around experimental data is computed as the semi-dispersion of the three tested specimens at fixed nominal strain level. Experimental data for a relatively small range of nominal strains (with respect to the 50% reached during uniaxial compression) is reported to better compare it with numerical data.

A basic resolution scheme for finite element (*ABAQUS static general*), with full-integration linear solid elements (C3D8) and a perfectly elastic-plastic behaviour of constituent bulk material were adopted. It is clear from the graph that a relatively good agreement is obtained for all the simulated densities; all the results were obtained in a relatively short amount of time (16 hours maximum) and with a reasonably limited amount of numerical resources (see table 8.5), proving the efficiency and accuracy of Peano's optimization algorithm.

Similar results are presented in figure 8.13 for PPI. In this case the finite element mesh was optimized by setting the two parameters of Peano's algorithm as follows: $P = 5$, $Th = 0.5$. In this case the material was treated as isotropic linear elastic, in accordance with the results of experimental tests, conducted on a single structure, presented in chapter 7. Also, in this case a fair agreement between experimental

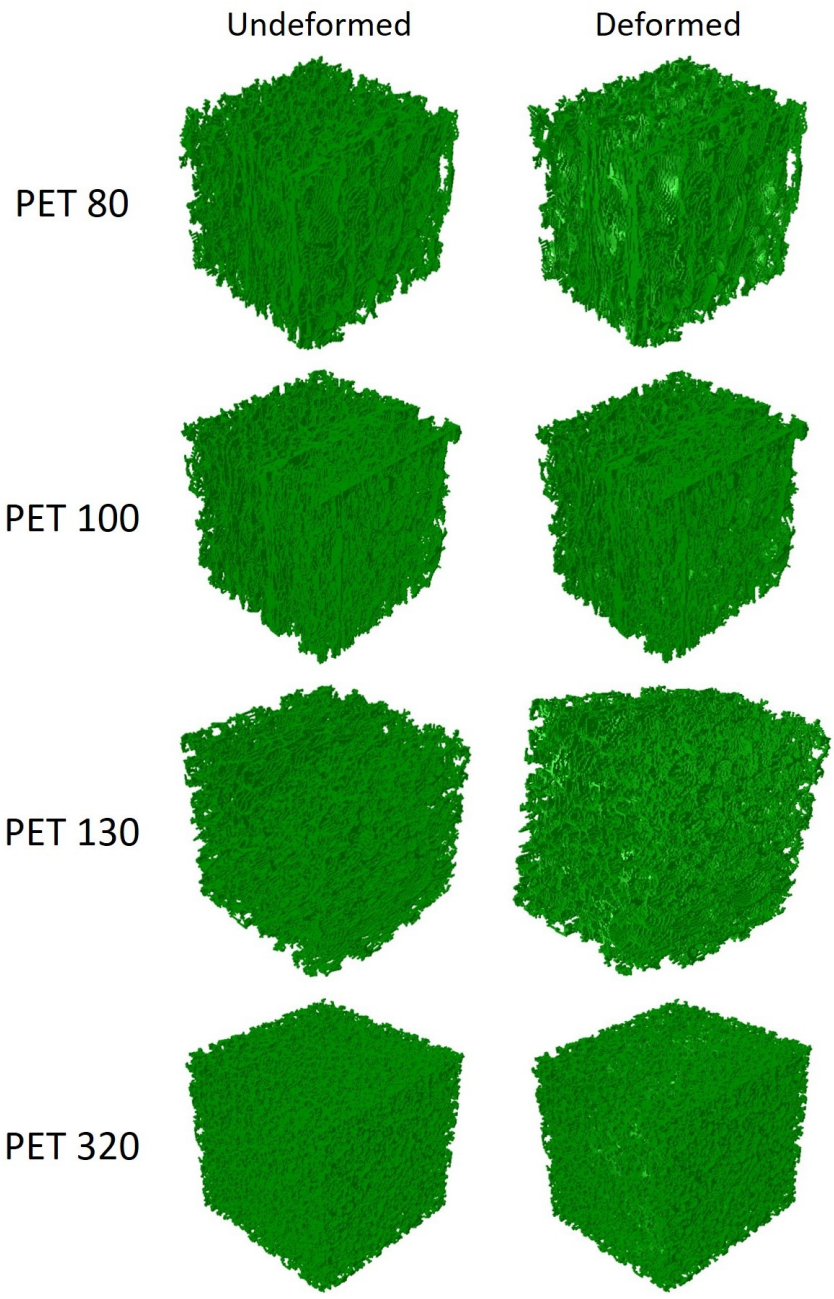

Figure 8.11: Qualitative comparison between undeformed and deformed volume reported for each simulated volume obtained from PET set of images. The most deformed regions in the compressed reconstructed volume are highlighted.

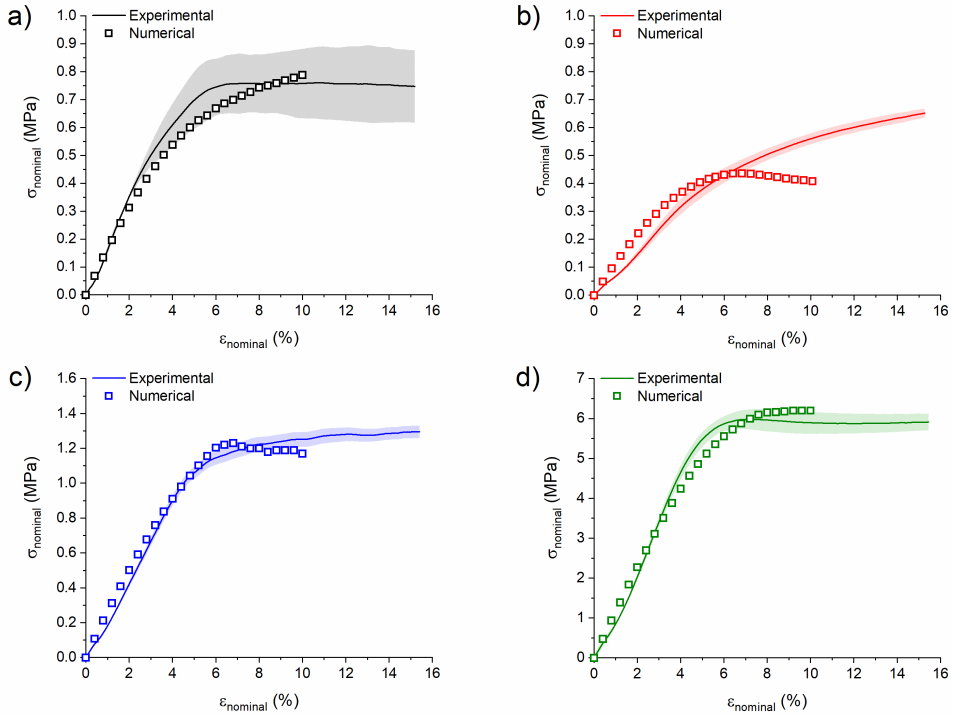

Figure 8.12: Nominal stress versus nominal strain curves obtained from experimental quasi-static uniaxial compression test and from finite element simulation reproducing the same mechanical test conducted on the optimized reconstructed finite element mesh. Comparison between experimental and numerical results is presented for all the tested materials: a) PET 80, b) PET 100, c) PET 130 and d) PET 320.

and numerical results was obtained. A smaller amount of time and numerical resources were required compared to PET since the solid volume fraction of PPI material was considerably lower, around 3%: hence, fewer finite elements were necessary to reconstruct the whole geometry.

In all the cases simulations are conducted up to 10% of nominal strain since it is reasonable to assume, also looking at the complete experimental curves, that in this range of strain no internal contact between structures occur and hence is not implemented in finite element

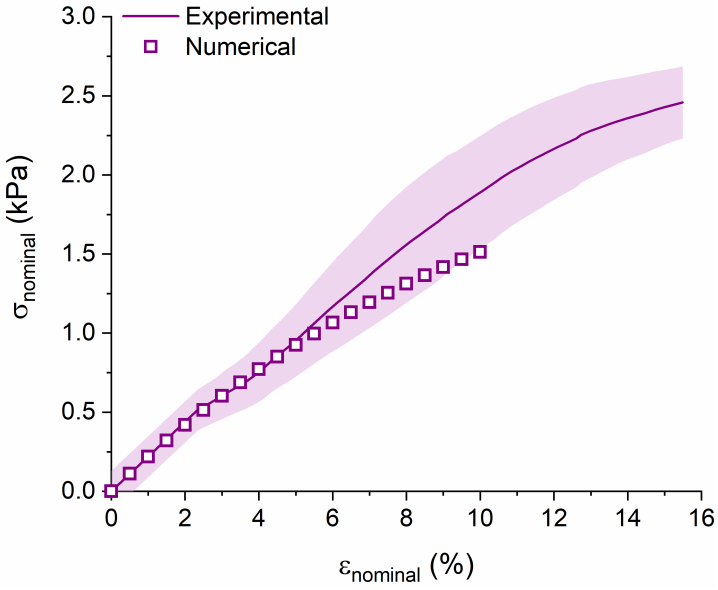

Figure 8.13: Nominal stress versus nominal strain curves obtained from experimental quasi-static uniaxial compression test and from finite element simulation reproducing the same mechanical test conducted on the optimized reconstructed finite element mesh. Comparison between experimental and numerical results is presented.

simulations. This fact is supported by the fact that the characteristic plateau of the macroscopic mechanical response of expanded polymeric material is just started at the end of the analysed nominal strain range.

Surely, if non-linear finite element simulations has to be conducted up to a larger value of nominal strain internal contact should be implemented and moreover, as evident from PPI results, also a more accurate description of constituent material mechanical behaviour has to be implemented, since in the non-linear macroscopic mechanical response range, non-linear aspect of constituent material, such as yielding phenomena or viscoelastic nature of polymers, become more and more predominant, together with internal structure modification, with respect to finite linear simulations where the main contribution to the macroscopic mechanical behaviour of foams comes from the structure.

8.4 Concluding remarks

In this chapter a newly developed image-based approach was presented. It was validated through linear elastic finite element analysis, performed in the small strain deformation range, and subsequent comparison with experimental results and with the alternative Representative Volume Element approach. The optimization algorithm has then proven its efficiency in both linear and non-linear finite element analysis, providing a powerful tool for numerical simulations. This approach not only allows to reproduce the macroscopic mechanical behaviour of experimentally tested material including the real structure into the simulation, but allows, with the proper tuning of algorithm parameters, to generate fictitious structures to enlarge the range of morpho-structural properties tested and not experimentally available; this feature supports the quest for macroscopic general relationships between structural parameters, bulk constituent material mechanical behaviour and the macroscopic mechanical response of the expanded polymeric material.

The approach found a good validation in linear finite element simulations, but much has to be done to improve its effectiveness in the case of non-linear behaviour. Some preliminary results were reported, with the aim of demonstrating the numerical efficiency of the developed approach, but other aspects will have to be considered in the future, such as internal contact between structures or a more suitable mechanical behaviour of the constituent material considering other features, above all the intrinsic viscoelastic nature of polymers. These steps are of fundamental importance for the development of the research to finally formulate a macroscopic non-linear constitutive law, describing different mechanical aspects of expanded polymeric material in a similar way to what has been performed for linear elastic macroscopic mechanical behaviour, presented in previous chapters.

8.5 References

[1] D. Garoz et al. “Consistent application of periodic boundary conditions in implicit and explicit finite element simulations of damage in composites”. en. In: *Composites Part B: Engineering* 168 (July 2019), pages 254–266. DOI: 10.1016/j.compositesb.2018.12.023. URL: https://linkinghub.elsevier.com/retrieve/pii/S1359836818337776.

[2] L.J. Gibson and M.F. Ashby. *Cellular Solids*. en.

[3] A.L. Gurson. “Continuum theory of ductile rupture by void nucleation and growth: Part I - Yield criteria and flow rules for porous ductile media”. en. In: *Continuum theory of ductile rupture by void nucleation and growth: Part I - Yield criteria and flow rules for porous ductile media* 39 (Sept. 1975), page 63.

[4] P. Henyš, L. Čapek, and J. Březina. “Comparison of current methods for implementing periodic boundary conditions in multi-scale homogenisation”. en. In: *European Journal of Mechanics - A/Solids* 78 (Nov. 2019), page 103825. DOI: 10.1016/j.euromechsol.2019.103825. URL: https://linkinghub.elsevier.com/retrieve/pii/S0997753818308453.

[5] T. Hildebrand and P. Rüegsegger. “A new method for the model-independent assessment of thickness in three-dimensional images”. en. In: *Journal of Microscopy* 185.1 (Jan. 1997), pages 67–75. DOI: 10.1046/j.1365-2818.1997.1340694.x. URL: https://onlinelibrary.wiley.com/doi/abs/10.1046/j.1365-2818.1997.1340694.x.

[6] N. Huber. “Connections Between Topology and Macroscopic Mechanical Properties of Three-Dimensional Open-Pore Materials”. en. In: *Frontiers in Materials* 5 (Nov. 2018), page 69. DOI: 10.3389/fmats.2018.00069. URL: https://www.frontiersin.org/article/10.3389/fmats.2018.00069/full.

[7] J. Jiao and N. Huber. "Deformation mechanisms in nanoporous metals: Effect of ligament shape and disorder". en. In: *Computational Materials Science* 127 (Feb. 2017), pages 194–203. DOI: 10.1016/j.commatsci.2016.10.035. URL: https://linkinghub.elsevier.com/retrieve/pii/S0927025616305481.

[8] J. Jiao and N. Huber. "Effect of nodal mass on macroscopic mechanical properties of nanoporous metals". en. In: *International Journal of Mechanical Sciences* 134 (Dec. 2017), pages 234–243. DOI: 10.1016/j.ijmecsci.2017.10.011. URL: https://linkinghub.elsevier.com/retrieve/pii/S0020740317317010.

[9] K. Kapoor and M.D. Sangid. "Initializing type-2 residual stresses in crystal plasticity finite element simulations utilizing high-energy diffraction microscopy data". en. In: *Materials Science and Engineering: A* 729 (June 2018), pages 53–63. DOI: 10.1016/j.msea.2018.05.031. URL: https://linkinghub.elsevier.com/retrieve/pii/S0921509318306798.

[10] E.T.J. Klompen et al. "Modeling of the Postyield Response of Glassy Polymers: Influence of Thermomechanical History". en. In: *Macromolecules* 38.16 (Aug. 2005), pages 6997–7008. DOI: 10.1021/ma050498v. URL: https://pubs.acs.org/doi/10.1021/ma050498v.

[11] V. Kouznetsova, M.G.D. Geers, and W.A.M. Brekelmans. "Multi-scale constitutive modelling of heterogeneous materials with a gradient-enhanced computational homogenization scheme". en. In: *International Journal for Numerical Methods in Engineering* 54.8 (July 2002), pages 1235–1260. DOI: 10.1002/nme.541. URL: http://doi.wiley.com/10.1002/nme.541.

[12] V.G. Kouznetsova, M.G.D. Geers, and W.A.M. Brekelmans. "Multi-scale second-order computational homogenization of multi-phase materials: a nested finite element solution strategy". en. In: *Computer Methods in Applied Mechanics and Engineering*

193.48-51 (Dec. 2004), pages 5525–5550. DOI: 10.1016/j.cma.2003.12.073. URL: https://linkinghub.elsevier.com/retrieve/pii/S0045782504002853.

[13] J. Liu, H. Yu, and A.C. To. "Porous structure design through Blinn transformation-based level set method". en. In: *Structural and Multidisciplinary Optimization* 57.2 (Feb. 2018), pages 849–864. DOI: 10.1007/s00158-017-1786-1. URL: http://link.springer.com/10.1007/s00158-017-1786-1.

[14] W.E. Lorensen and H.E. Cline. "Marching cubes: a high resolution 3D surface construction algorithm". en. In: *Marching cubes: a high resolution 3D surface construction algorithm* 21 (July 1987), page 7.

[15] H.G.H. van Melick, L.E. Govaert, and H.E.H. Meijer. "Localisation phenomena in glassy polymers: influence of thermal and mechanical history". en. In: *Polymer* 44.12 (June 2003), pages 3579–3591. DOI: 10.1016/S0032-3861(03)00089-2. URL: https://linkinghub.elsevier.com/retrieve/pii/S0032386103000892.

[16] R. Moreno, M. Borga, and O. Smedby. "Generalizing the mean intercept length tensor for gray-level images: Generalizing the mean intercept length tensor". en. In: *Medical Physics* 39.7Part2 (July 2012), pages 4599–4612. DOI: 10.1118/1.4730502. URL: http://doi.wiley.com/10.1118/1.4730502.

[17] R.J.M. Smit, W.A.M. Brekelmans, and H.E.H. Meijer. "Prediction of the mechanical behavior of nonlinear heterogeneous systems by multi-level finite element modeling". en. In: *Computer Methods in Applied Mechanics and Engineering* 155.1-2 (Mar. 1998), pages 181–192. DOI: 10.1016/S0045-7825(97)00139-4. URL: https://linkinghub.elsevier.com/retrieve/pii/S0045782597001394.

[18] K. Terada et al. “Simulation of the multi-scale convergence in computational homogenization approaches”. en. In: *International Journal of Solids and Structures* 37.16 (Apr. 2000), pages 2285–2311. DOI: 10.1016/S0020-7683(98)00341-2. URL: https://linkinghub.elsevier.com/retrieve/pii/S0020768398003412.

[19] T.A. Tervoort et al. “A Constitutive Equation for the Elasto-Viscoplastic Deformation of Glassy Polymers”. en. In: (), page 23.

[20] M.J. Wald et al. “Spatial autocorrelation and mean intercept length analysis of trabecular bone anisotropy applied to in vivo magnetic resonance imaging: Spatial autocorrelation and mean intercept length analysis”. en. In: *Medical Physics* 34.3 (Feb. 2007), pages 1110–1120. DOI: 10.1118/1.2437281. URL: http://doi.wiley.com/10.1118/1.2437281.

[21] H.X. Zhu, J.F. Knott, and N.J. Mills. “Analysis of the elastic properties of open-cell foams with tetrakaidecahedral cells”. en. In: *Journal of the Mechanics and Physics of Solids* 45.3 (Mar. 1997), pages 319–343. DOI: 10.1016/S0022-5096(96)00090-7. URL: https://linkinghub.elsevier.com/retrieve/pii/S0022509696000907.

Chapter 9

Conclusions

This PhD thesis presented the development and optimization of different numerical tools. Their main aim was the inspection and accurate quantification of the internal microstructure parameters and their subsequent correlation with the macroscopic mechanical behaviour of relevant expanded polymeric materials. The final objective was the achievement of analytical relationships correlating structure and mechanical parameters. This goal was fully met in the range of predominantly linear elastic behaviour, where an analytical set of equations was obtained; relevant applications include for example acoustical and thermal insulation. Structure parameters were uniquely correlated to the elastic constants of a macroscopic constitutive law built on structural analysis, suitable to describe the mechanical behaviour of the inspected sample. This system of equations can be a useful tool for applications, since it allows for the optimization of the macroscopic mechanical properties of an expanded product while designing its internal microstructure or vice versa it could be used to obtain information on the internal structure performing simple mechanical tests on the produced samples, as reported in the previous chapters of this thesis for selected materials. In both ways, the set of equations can provide significant time and cost savings during the development of new products.

Another fundamental aspect faced during the present thesis work

was the development of an efficient numerical tool able to perform non-linear finite element analysis, also considering the real internal structure of a large volume of expanded material; in fact, a volume large enough to be considered representative of the whole material. The potential implications of this model extend its use to several applications in which foam properties are typically exploited, including packaging and protective devices. Simulations, performed in a reasonable amount of time (within a single day) and limited numerical resources (a typical high-end workstation) can provide useful information on the macroscopic behaviour at relatively high strains under different loading conditions for a newly developed product.

From a research point of view, the developed numerical tools provide a valuable addition to the approaches already reported in the scientific literature, and they constitute a step forward towards the full understanding of the synergistic effect between internal structure and constituent material mechanical behaviour of this class of materials. Specifically, these or similar tools are a necessary step for the construction of homogenized material model, similar to the one presented for describing linear elastic behaviour, also in the non-linear case. These models, thanks to the new production technologies available, such as 3D printing technology, could be easily validated realizing purposely designed structures that can be tested experimentally to validate the macroscopic relationships formulated in the present work.

Acknowledgements

Since all the persons I wish to thank are Italian, I think it should be better to change language and style ...

Un ringraziamento ufficiale e sentito va a Fabio de Pascalis e Michele Nacucchi del centro ricerche ENEA di Brindisi per l'eccellente collaborazione scientifica instaurata durante lo sviluppo del lavoro di tesi; grazie per la professionalità dimostrata e per il fondamentale supporto scientifico nella realizzazione delle acquisizioni tomografiche e durante lo sviluppo e ottimizzazione degli algoritmi per l'analisi delle strutture.

Passando ora al lato Politecnico, il primo grande ringraziamento è d'obbligo nei confronti del prof. Vena Pasquale, mio primo mentore scientifico. Grazie per la fiducia dimostratami già a partire dall'assegnazione del tema di tesi magistrale, tema a lei molto caro, ma soprattutto per aver raccomandato la mia professionalità e potenzialità al gruppo di ricerca che mi ha "adottato" durante questi anni e ovviamente (pare scontato, ma non lo è) grazie per tutti gli insegnamenti dei quali ho già fatto tesoro prezioso.

A proposito del gruppo di ricerca di adozione, il PolyEngLab, ovviamente un doveroso ringraziamento va ovviamente a tutti.

In primis al mio relatore, l'Ing. Luca Andena: ancora prima di intraprendere la mia tesi di dottorato lo ringrazio per la fiducia accordatami nell'assegnazione dell'assegno di ricerca, "adottando" un povero ingegnere biomedico e lanciandolo a testa bassa nel mondo dell'ingegneria dei materiali. Grazie soprattutto per l'elevata indipendenza accordatami in questi anni durante le mie ricerche, considerato anche questo come un segno di grande fiducia e un fattore che mi ha fatto crescere molto velocemente nell'ambito lavorativo e mi ha insegnato a districarmi agevolmente nella giungla dipartimentale. Grazie per la pazienza dimostrata durante le mie peregrinazioni scientifiche e non, che spesso esulavano dal mio cammino scientifico strettamente legato al lavoro di tesi! Ultimo, ma non certo per importanza, la pazienza

dimostrata nella correzione del mio pessimo inglese, purtroppo ognuno ha il suo tallone d'Achille e in questo caso ricade sulla lingua anglofona!

All'ing. Francesco Briatico-Vangosa grazie per tutte le conversazioni metafisico-scientifiche che spesso mi servivano a scollegare il cervello dagli intoppi numerici e che mi hanno aiutato sicuramente a rischiarare la mente consentendomi di tornare ad affrontare i miei problemi scientifici con un'ottica rinnovata; ovviamente oltre alle chiacchierate "side-work" grazie per tutti gli insegnamenti in ambito reologico e soprattutto per l'involontaria spinta iniziale, durante i miei primi mesi di percorso nell'ingegneria dei materiali; ad ogni material-cavolata che usciva dalla mia bocca, il tuo monito costante era: "Devi studiare di più!". Credimi che anche se involontario è uno stimolo che mi ha spronato molto a fare meglio!

Alla prof. Claudia Marano il ringraziamento più grande va sicuramente sul lato umano: grazie per aver spesso ascoltato le mie "inutili" filippiche sulla cosmogonia del dipartimento e del lavoro e aver sempre avuto una parola di conforto e incoraggiamento. Ovviamente lato scientifico ti ringrazio per avermi fatto scontrare più e più volte con i grandi problemi che il mondo degli elastomeri pone a noi (ormai mi ci metto anche io) ingegneri dei materiali! Speriamo di riuscire a risolverne qualcuno insieme in futuro!

Al prof. Roberto Frassine un grazie per quelli che io chiamo "insegnamenti alla Bob"; all'apparenza strani e totalmente incoerenti, ma che se analizzati a posteriori in realtà sono molto semplici da interpretare e da applicare in seguito! Insegnamenti che sicuramente mi torneranno utili in qualsiasi team di lavoro mi troverò in futuro, anche se con il mio carattere, difficili da mettere in pratica al 100%. Oltre al lato politico, ovviamente lo ringrazio anche per aver arricchito il mio bagaglio scientifico, anche in questo caso in modo un po' strano (LP^3 torna sempre), diciamo pratico! Con un colpo di coda, penso grazie all'effetto osmosi, sei anche riuscito ad insegnarmi qualcosa di meccanica della frattura.

Ultimo membro "anziano" del gruppo, non certo per importanza,

il mito Oscar Bressan, un Tecnico di laboratorio con la T maiuscola. Grazie per tutti i tuoi insegnamenti pratici! Anche solo guardandoti lavorare, con la tua metodicità e puntigliosità, si può imparare davvero molto; si ruba il tuo lavoro con gli occhi e da buon "ladro scientifico" ne ho rubato davvero tanto! Grazie e soprattutto grazie anche per il bel rapporto lavorativo che si è creato tra noi in questi anni, complice anche tutte le faticate che ci siamo fatti cercando di risolvere e portare a termine le commesse impossibili e sappiamo quante ce ne sono arrivate sul collo!

In ultimo ringrazio tutti i giovani che sono ancora presenti o che negli anni sono passati nel gruppo: assegnisti, dottorandi, post-doc, tesisti e ospiti. Siete davvero troppi per potervi nominare tutti, ma ognuno di voi ha lasciato qualcosa e spero anche io di aver lasciato qualcosa a voi. Ad alcuni di voi (il Notaio, Gianca e Shiva) va sicuramente un ringraziamento in più avendo sopportato tutte le mie manie e follie da buoni colleghi di ufficio; grazie davvero per la pazienza.

In fine, non certo per importanza, ringrazio veramente di cuore il "capostipite" del gruppo di ricerca che mi ha accolto, Prof. Andrea Pavan. Grazie per tutti i consigli e gli Insegnamenti che già a partire dall'assegno di ricerca mi ha trasmesso, oltre quelli scientifici anche quelli morali e di professionalità. Il suo esempio, come persona e come professionista, lo porterò sempre con me gelosamente custodito. Grazie davvero di tutto!

Al di là del gruppo, c'è però anche un dipartimento e un Politecnico intero dove ho incontrato molte persone, le quali non posso fare a meno di ringraziare.

In cima a tutta la lista c'è sicuramente il prof. Valter Carvelli; sempre pronto a dare un consiglio ed un supporto di sua spontanea volontà, anche quando non richiesto! Un gesto che sicuramente ho molto apprezzato perché oltre a sbloccare la scienza, solleva molto il morale. Grazie di cuore Valter!

Ringrazio di cuore anche l'ing. Giancarlo Locati; la tua infinita

conoscenza dei materiali polimerici con un ottica industriale è stata per me un prezioso bagaglio di conoscenza che mi ha insegnato, oltre a tanta scienza, anche ad affrontare certi problemi e sfide scientifiche in un'ottica un po' diversa e per certi aspetti distante dal taglio rigoroso del mondo scientifico; un taglio aziendale, forse un po' più grossolano e praticone (direbbero i grandi scienziati), ma sicuramente efficace ed efficiente per molti aspetti. Grazie anche per tutte le chiacchierate scientifico-filosofiche che abbiamo condiviso durante i primi mesi del mio assegno; sono state per me un ottimo punto di partenza per addentrarmi nel mondo delle materie plastiche!

Ringrazio ora, quelli che mi piace definire i miei angeli custodi del dipartimento: Katia, Rosella, Marcella, Giusy (prima o poi ci mangeremo il famoso piatto di minchiette ai quattro formaggi), Gilly e il mitico Mirko (e il suo fidato compagno, zio pinolinopinolinopinolino). Grazie per tutti i consigli, le chiacchiere, le risate e le incazzature che abbiamo condiviso in questi anni! Come si è soliti dire, il viaggio è meno pesante se hai dei buoni compagni con cui condividerlo, e devo dire che al sottoscritto è andata di lusso!

Un ultimo ringraziamento va a tutti gli altri ragazzi, dottorandi e assegnisti, incontrati in dipartimento; anche in questo caso siete davvero troppi per essere nominati singolarmente (sia mai che dimentico qualcuno), ma anche in questo caso ognuno di voi è stato un componente fondamentale del mio percorso, soprattutto i compagni di sigaretta XD!

Lato personale, pare scontato, ma per me non lo è assolutamente, ringrazio di cuore i miei fantastici genitori, Laura e Vittorio, i miei primi veri insegnanti e sempre sinceri mentori. Grazie per aver supportato e sopportato la scrittura di BEN 3 tesi e soprattutto il caratterino del sottoscritto da 30 anni a questa parte!

Alla conclusione di un viaggio è risaputo che ogni persona, nel bene o nel male, lascia qualcosa sul nostro cammino; il mio bagaglio esce più pesante, ma non difficile da trasportare; arricchito da tutte le esperienze che questi anni hanno messo sul mio cammino... e ovviamente...

Il bello deve ancora venire! Give me a roar!